HOST GALAXY PROPERTIES OF CA II AND NA I QUASAR ABSORPTION-LINE SYSTEMS

by

Brian Cherinka

B.S. in Physics, University of Florida, 2003

M.S. in Physics and Astronomy, University of Pittsburgh, 2005

Submitted to the Graduate Faculty of

Kenneth P. Dietrich School of Arts and Sciences in partial

fulfillment

of the requirements for the degree of

Ph.D

University of Pittsburgh

2012

UNIVERSITY OF PITTSBURGH

KENNETH P. DIETRICH SCHOOL OF ARTS AND SCIENCES

This dissertation was presented

by

Brian Cherinka

It was defended on

December 12, 2011

and approved by

R. Schulte-Ladbeck, Ph. D., Professor

A. Kosowsky, Ph. D., Professor

D. Naples, Ph. D., Professor

S. Rao, Ph. D., Professor

R. Croft, Ph. D., Professor

Dissertation Director: R. Schulte-Ladbeck, Ph. D., Professor

HOST GALAXY PROPERTIES OF CA II AND NA I QUASAR ABSORPTION-LINE SYSTEMS

Brian Cherinka, PhD

University of Pittsburgh, 2012

Many questions remain within the areas of galaxy formation and evolution. Understanding the origin of gas in galaxy environments, whether as tidal debris, infalling High Velocity Clouds, galaxy outflows, or as gaseous material residing in galaxy disks, is an important step in answering those questions. Quasar absorption-lines can often be used to probe the environments of intervening galaxies. Traditionally, quasar absorption-lines are studied independently of the host galaxy but this method denies us the exploration of the connection between galaxy and environment. Instead, one can select pairs of known galaxies and quasars. This gives much more information regarding the host galaxy and allows us to better connect galaxy properties with associated absorbers.

We use the seventh data release of the Sloan Digital Sky Survey to generate a sample of spectroscopic galaxy-quasar pairs. We cross-correlated a sample of 105,000 quasars and ∼800,000 galaxies to produce ∼98,000 galaxy-quasar pairs, with the quasar projected within 100 kpc of the galaxy. Adopting an automated line-finding algorithm and using the galaxy redshift as a prior, we search through all quasar spectra and identify Ca II and Na I absorption due to the intervening galaxy. This procedure produced 1745 Ca II absorbers and 4500 Na I absorbers detected at or above 2σ. Stacking analysis of a subset of absorbers at $z > 0.01$, with significances at or above 3σ, showed strong Ca II and Na I features around external galaxies.

Using the same subset of absorbers at $z > 0.01$, we looked for correlations between absorber and galaxy properties and examined differences in galaxy properties between the

absorbers and non-absorbers. We found no correlations with absorber strength or differences between many galaxy properties at the 3σ level. The lack of correlations and differences between absorbers and non-absorbers suggest a ubiquitous nature for Ca II and Na I around all types of galaxies, with the absorbers showing no geometric preference within galaxy halos. This suggests a possible origin as leftover debris from past mergers that has been redistributed within the halo over time.

The main results are presented in Chapters 3 and 4, with complimentary work presented in Chapter 5.

TABLE OF CONTENTS

LIST OF TABLES

LIST OF FIGURES

PREFACE

This has been a long road, but well worth it. I am certainly a different person now than when I began, hopefully for the better.

I wish to thank my advisor Regina Schulte-Ladbeck. I am very fortunate to have been working with her, and have benefited greatly from her knowledge and experience. I am grateful for her constant encouragement, and guidance, and I look forward to our continued collaborations.

I also want to thank the other members of my thesis committee for providing useful insight, offering suggestions, and reviewing my thesis manuscript along my journey.

I would like to thank Jeff Newman and Michael Wood-Vasey for the many helpful discussions about statistics, astronomy, education, and visualization that I have had with them during my time here.

I wish to thank my family for their support. I am eternally grateful for all they have given me.

Finally, I would like to thank all of my friends. Without you I would not be who I am today. You have enriched my life beyond what I originally thought possible, and expanded my mind. You withheld judgement and accepted me for who I am, as true friends do. You remained my friends throughout difficult times and I appreciate everything you have done for me.

1.0 INTRODUCTION

Here I provide a brief introduction into the topics necessary to understand the work that makes up my thesis. This introductory chapter begins with a description of large-scale structure and galaxy formation, as well as our current understanding of how galaxies acquire the gas that fuels and governs their lives. I discuss the importance of quasar absorption lines, their connection with the galaxies responsible for them. I then go on to describe the physics of absorption line formation and the mechanism by which we probe the gas within galaxies via observations of quasars. Finally, I discuss details of Calcium and Sodium, two atomic elements that present themselves as strong optical absorption lines that have been used to probe the Milky Way and nearby external galaxies.

1.1 GALAXY FORMATION

Our current picture of the Universe is one consisting of three main components today: baryonic matter, dark matter, and dark energy. Figure 1.1 shows how the energy-density budget of the Universe breaks down today and in the distant past. Today, the Universe is made up mostly of dark energy (72%), and dark matter (23%), with only about ∼4% consisting of baryonic matter (Komatsu et al., 2011; Larson et al., 2011; Jarosik et al., 2011). Dark energy is the name of the component that is currently causing the accelerating expansion of the Universe (Riess et al., 1998; Perlmutter et al., 1999). The simplest model of dark energy is the cosmological constant, Λ, associated with an inherent energy density to the Universe, and characterized by a negative equation of state that acts to accelerate the expansion (Carroll et al., 1992; Schmidt et al., 1998). Dark matter is an unseen matter com-

ponent that acts to hold galaxies and clusters together via gravity (Oort, 1932; Zwicky, 1937; Rubin et al., 1980; Clowe et al., 2006). Current evidence posits it as being cold (velocities that are non-relativistic), non-baryonic, and only interacting via the weak force and gravity (Bertone et al., 2005). The baryon component is made up of all matter and energy that we can see today (e.g., gas, dust, stars, radiation, etc.).

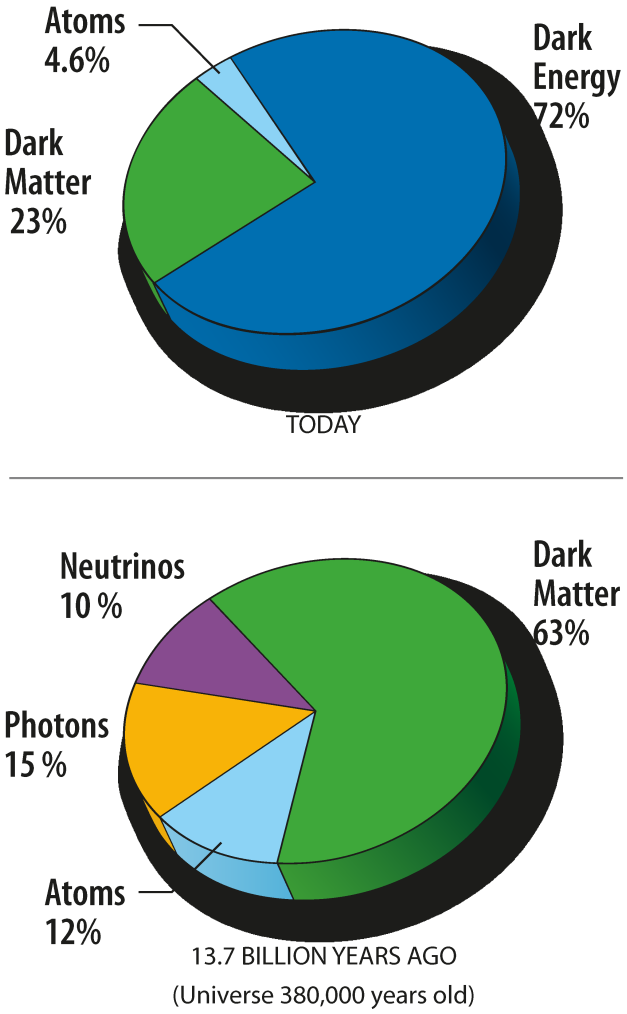

Figure 1.1 Top: The present day contribution of each component to the overall energy density of the Universe. Bottom: The breakdown 13.7 Gyr ago. Credit: NASA / WMAP Science Team (Komatsu et al., 2011; Larson et al., 2011; Jarosik et al., 2011)

This framework is sometimes referred to as the Λ-Cold Dark Matter model, or the Λ-CDM model. In this framework, the Universe started out in a hot, dense state with matter uniformly distributed throughout the Universe. Figure 1.2 shows a picture of the Cosmic

Microwave Background (Alpher et al., 1948; Dicke et al., 1965; Penzias & Wilson, 1965a,b), a microwave image of the Universe as it existed 13.7 Gyr ago, highlighting the uniformity of the matter distribution in the early Universe (Komatsu et al., 2011; Larson et al., 2011). The color scale shows the small fluctuations in temperature ($\lesssim 10^{-5}$ Jarosik et al. (2011)) which reflect the small-scale matter density perturbations that are the seeds of galaxy formation. The red regions represent slight over-densities in the matter distribution, while the deep blue regions are slight under-densities. As the Universe expands, these over- and under- dense regions are amplified via gravity, and grow into the structure we see today. Over time, this growth of structure produced a web-like filamentary structure, with dense clusters at the intersections of the filaments and voids interspersed in-between.

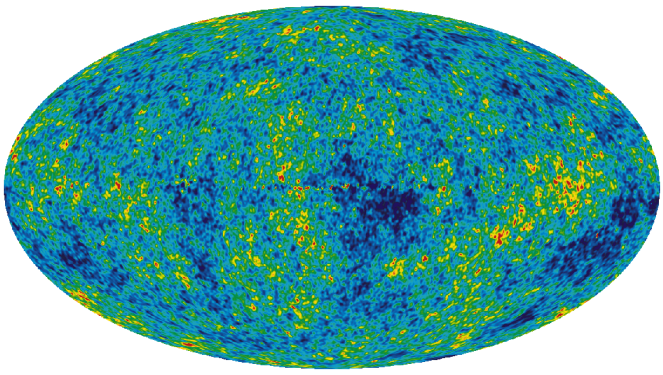

Figure 1.2 A full sky map of the Cosmic Microwave Background from the 5-year WMAP results. Credit: NASA / WMAP Science Team (Komatsu et al., 2011; Larson et al., 2011; Jarosik et al., 2011)

Figure 1.3 shows an N-body simulation of dark matter particles from the Millennium Simulation (Springel et al., 2005). This is a simulation using 10^{10} particles to follow the dark matter distribution within a 500 h^{-1} Mpc^3 volume. The panels show the linear growth of dark matter structure through gravitational interactions over time, from 13.5 Gyrs ago (z=18.3, upper left) to today (z=0, bottom right), and the subsequent development of the clusters, filaments, and voids. As the baryons also interact gravitationally, they trace the underlying dark matter distribution, collapsing into filaments, and then flowing along those filaments

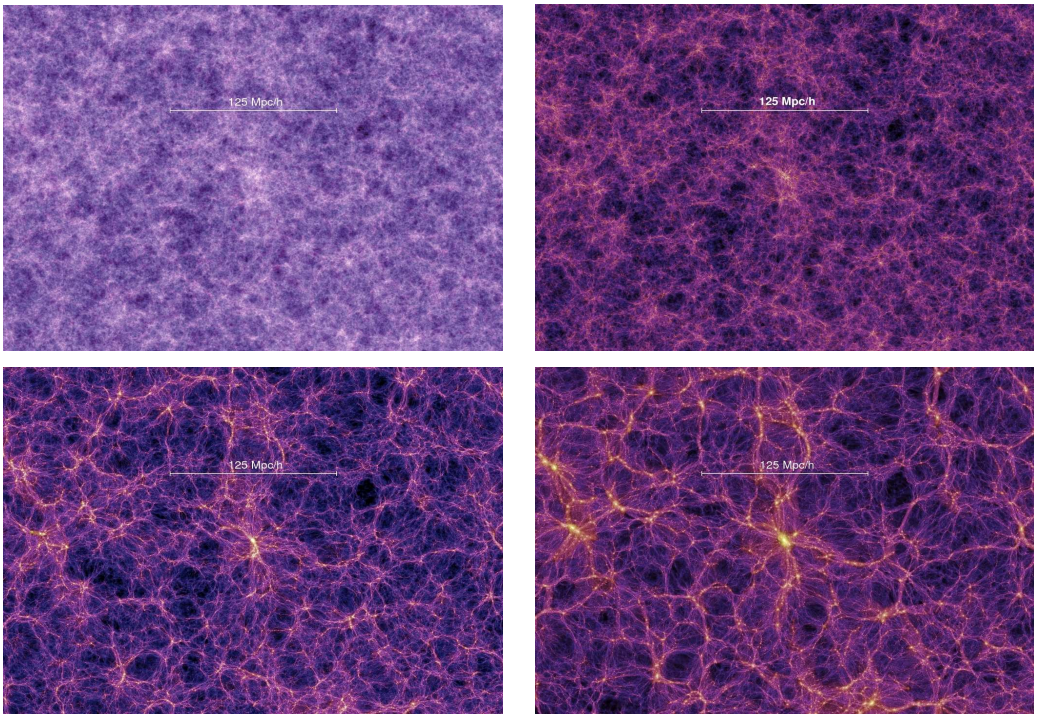

Figure 1.3 A dark matter simulation from the Millennium Simulation. From top left to bottom right: redshift slices are depicted at z=18.3, 5.7, 1.4, and 0.0, respectively. The bar shows a length scale of 125 Mpc/h. http://www.mpa-garching.mpg.de/galform/virgo/millennium/

to the nearest cluster. In this way, galaxies are formed first as small structures and are built up hierarchically, through mergers, into larger and larger structures. Within the deepest potential wells, located at the intersections of filaments, there are dense galaxy clusters and superclusters, while more isolated systems live in the filaments and voids. Figure 1.4 shows the observed galaxy distribution as measured by the Sloan Digital Sky Survey (SDSS), out to a redshift of 0.14, with the pattern of large-scale structure as predicted by current theory.

In order to quantify how the Universe went from a uniform matter distribution to the clumpy Universe we see today, extensive work has been done over the past four decades in creating a semi-analytic model of galaxy formation. The model of galaxy formation synthesized by White & Frenk (1991) includes many aspects which are important in galaxy formation, namely cold dark matter, gas cooling, star formation, and feedback. Within the current

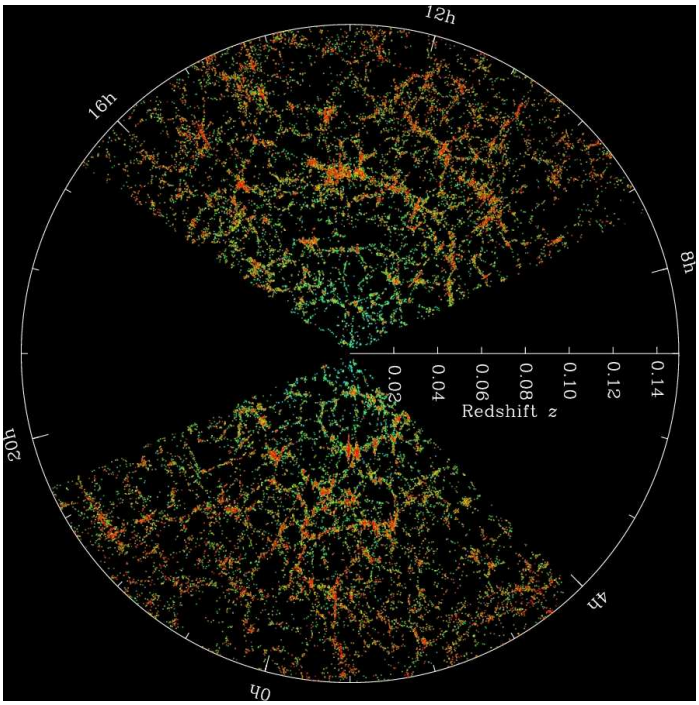

Figure 1.4 Slices through the SDSS 3-dimensional map of the distribution of galaxies. Earth is at the center, and each point represents a galaxy, typically containing about 100 billion stars. Galaxies are colored according to the ages of their stars, with the redder, more strongly clustered points showing galaxies that are made of older stars. The outer circle is at a distance of two billion light years. The region between the wedges was not mapped by the SDSS because dust in our own Galaxy obscures the view of the distant universe in these directions. Both slices contain all galaxies within -1.25 and 1.25 degrees declination. Credit: M. Blanton and the Sloan Digital Sky Survey.

framework, galaxy formation is a two stage process (White & Rees, 1978), which starts with the formation of a dark matter halo, through a dissipationless, gravitational collapse. A dark matter halo is a construct that is in a state of near-equilibrium, self-supported against gravity by the random motions of its constituents, characterizing the transition between matter expanding with the Hubble flow and matter that is not. Peebles (1980) outlined how structure forms from linear perturbations from an initially smooth Gaussian distribution. Press & Schechter (1974) characterized the abundance of dark matter halos of different masses that arises using linear perturbation theory, along with halo formation histories, often

described as merger tree.

The second stage is the formation of the galaxy itself. Galaxies form inside dark matter halos through the cooling and condensation of baryons (Hoyle, 1953; Rees & Ostriker, 1977; Silk, 1977). As baryons cool and enter the dark matter halos, they are shock-heated to the virial temperature of the halo where they become pressure-supported against gravitational collapse. The hot baryons diffusely fill the halo out to the virial radius, and gradually cool through line emission or Bremsstrahlung radiation. As the baryons cool, and lose pressure support, they collapse onto the central region of the halo, forming a rotationally supported galactic disk.

Recent work (Dekel & Birnboim, 2006; Kereš et al., 2005, 2009) has expanded the standard picture of galaxy formation to include a 'cold'-mode of gas accretion, as well as a 'hot'-mode. At high redshifts, when low-mass systems dominate, the cold-mode is the dominant mode of gas accretion. In this picture, cold gas ($T<10^5$K) flows into galaxy halos along dense filaments and does not undergo shock-heating as it enters the halo. Without being shock-heated, the gas penetrates deep into the halo, depositing directly onto the central galaxy where it can begin to cool into a disk and form stars. As galaxies grow through mergers, a transition occurs once the galaxy reaches a mass $\sim 10^{10.3} M_{\odot}$, or the halo mass reaches $\sim 10^{12} M_{\odot}$, where the gas is now shock-heated to the virial temperature as it enters the halo and is no longer able to penetrate deep into the halo. The heated gas then gradually cools onto the central region of the halo. This mechanism is referred to as the hot-mode of gas accretion. Once this transition mass is reached, the hot-mode of gas accretion becomes the dominant mode in which galaxies acquire their gas. Thus the cold-mode dominates at high redshift and in low density environments today whereas the hot-mode dominates in high-density environments today, like groups and clusters, where the halo has had time to grow above $10^{12} M_{\odot}$.

AGN and stellar feedback processes can complicate the gas acquisition process. Galaxy outflows can disrupt the inflow of cold gas into the halo while transporting gas and metals from the interstellar medium (ISM) of galaxies back out into the surrounding medium. Supernova driven winds have been invoked to explain the lack of observed faint dwarf galaxies compared to that predicted by semi-analytic galaxy models (Benson et al., 2003). Supernova

driven winds help drive cold gas out of dwarf galaxies, disrupting their ability to form stars. AGN feedback acts to heat up surrounding cold gas slowing the gas-cooling process thereby preventing star formation.

The most direct way of probing cool gas in the ISM of galaxies as well as in the surrounding environment is through quasar absorption lines.

1.2 QUASAR ABSORPTION LINE SYSTEMS

In the early 1960's, a new class of objects was being observed that had stellar-like appearances but whose spectra were clearly distinct from stars. These objects were dubbed 'quasi-stellar objects', or QSOs. Similar objects observed with radio emission were similarly named quasars ('quasi-stellar radio sources'). The first quasar discovered was 3C273 by Cyril Hazard in 1963 (Hazard et al., 1963) and a spectrum was obtained by Martin Schmidt (Schmidt, 1963). The spectrum indicated that the object was located at a large cosmological distance. For these objects to be located at cosmological distances and still remain brightly visible in the sky, they had to be some of the most luminous objects in the Universe, with luminosities $\sim 10^{48}$erg/s. Their extreme luminosities and point-like appearance on the sky are due to a very active nucleus at the center of the host galaxy that outshines the rest of the host. Much work has been done on the intrinsic properties of quasars and their connections with Active Galactic Nuclei (AGN) in general.

For the purpose of this thesis however, quasars act only as background light sources. As light from the quasar travels towards us, it passes through intervening material along the way. The intervening gas can absorb a portion of the light, imprinting the quasar spectrum with an absorption line. Figure 1.5 shows a cartoon diagram of a quasar, with its light passing through some intervening gas of a galaxy lying between itself and Earth. The bottom shows the spectrum of the quasar with many absorption lines from the intervening gas imprinted on the spectrum. We can use the presence (and type) of these lines to learn about the environment in which the lines arise, often times independently from the galaxy responsible for that environment. Quasar absorption lines can be a useful tool in probing the gaseous

environments around galaxies, which in turn improves our understanding of the nature of galaxy evolution over time.

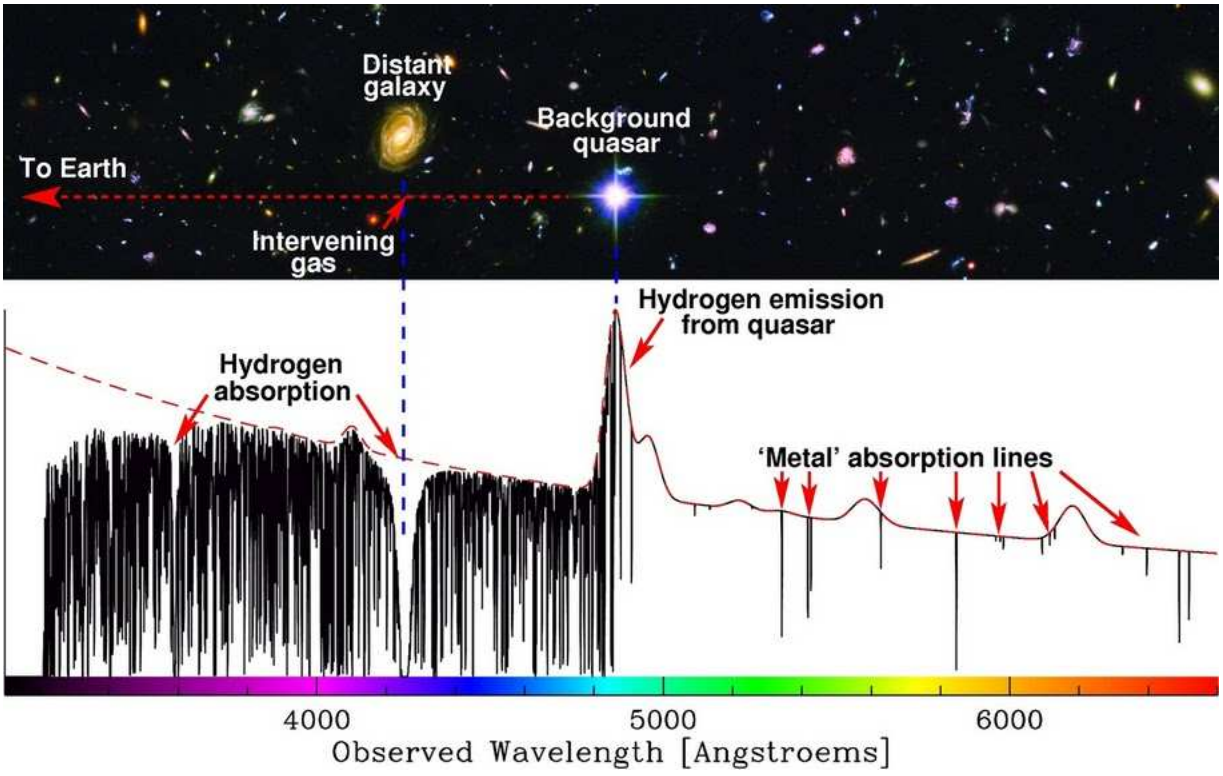

Figure 1.5 A cartoon diagram of a quasar spectrum depicting how material from an intervening galaxy becomes imprinted onto the spectrum of a quasar. We can use this imprint as a means to probe the physical environment in which the absorption lines arise. Credit: Mike Murphy, Swinburne University of Technology.

Quasar absorption lines provide a wealth of information on the physical conditions of gaseous structures along random lines of sight through the Universe. Many absorption lines have been observed, such that they are classified into systems which one can then study statistically as a whole population. The Damped Lyman-α Absorbers (DLAs) are a particularly important class of absorbers (Kulkarni, 2007; Prochaska et al., 2008) as they are the largest HI column density absorbers ($N_{HI} \geq 10^{20.3}\mathrm{cm}^{-2}$), trace the cosmic abundance of neutral gas, and give us insight on star-formation processes and gas processing in galaxies. Simulations (Gardner et al., 2001; Nagamine et al., 2007; Okoshi & Nagashima, 2005; Johansson & Efstathiou, 2006) and observations (Le Brun et al., 1997; Chen & Lanzetta, 2003; Rao et al., 2003; Rao et al., 2011; Christensen et al., 2007) of DLAs paint a picture

of the strongest Hydrogen columns dominated by dwarf galaxies at high redshift evolving to a population at low redshift consisting of a mixed bag of galaxies that cover a range of properties. The sub-DLAs and Lyman-limit systems have column densities of $N_{HI} \geq 10^{19}\text{cm}^{-2}$ and $N_{HI} \geq 10^{17}\text{cm}^{-2}$ respectively and probe neutral and ionized gas in the ISM (Kulkarni et al., 2010; Prochaska et al., 2010). The Lyman-α forest lines have column densities around $N_{HI} \geq 10^{15}\text{cm}^{-2}$ and represent the more diffuse component of the Hydrogen absorbers (Kollmeier et al., 2003; Pieri et al., 2010). The two broad absorption-line troughs marked with 'Hydrogen absorption' in Figure 1.5 are DLA lines. The dense swathe of lines seen blueward of the quasar Hydrogen emission-line are Lyman-α forest lines, and represent neutral Hydrogen gas clouds located through the intergalactic medium. Also depicted are numerous metal absorption-lines present in the quasar spectrum. Metal-line absorption systems complement the DLAs in our understanding of the gaseous processes in galaxies, through a slightly different window than the HI absorbers. Metal-line absorption systems have been used to probe such galaxy properties as metallicities, dust depletions, star-formation activity, velocity structure, to name a few and can probe all gas phases of the interstellar and intergalactic medium (Kulkarni et al., 2005; Nestor et al., 2007; Prochaska et al., 2011; Tripp et al., 2008; Tumlinson et al., 2005, 2011). There are numerous strong metal absorption-line systems seen in quasar spectra, mostly in rest-frame ultraviolet wavelength regions. See Verner et al. (1994) for a detailed list.

Since quasar absorption systems can be studied independently of the galaxy, this often results in a gap in our understanding of how galaxies and their environments are connected. There are two main approaches in uncovering this connection between the absorber host galaxy and the absorbing gas seen in quasar spectra. The first, more traditional, approach involves selecting quasar absorption line systems through observations of spectra of quasars, which, in the past, have been selected by their distinctive bright point-like appearance on the sky. This method is independent of the absorber host galaxy, as the line is found first, with follow-up imaging to locate the host galaxy. However, this approach has failed to produce a large body of galaxy/quasar pairs, as high-redshift observations fail to identify the galaxies responsible for the absorption, primarily because of the relative contrast between the brightness of the quasar and that of the galaxy as well as the relationship between angular size and

redshift. With no identification, then for most absorption systems this prevents any analysis of the host properties other than what can be gleaned from the absorption lines themselves. While some classes of absorbers have had a modicum amount of success in identification of their host environments, e.g. Mg II and O VI, this problem affects all quasar absorption line systems. While low-redshift observations make it easier to observe the absorber host galaxy, there are still only a small number of known DLA galaxy/quasar pairs (Rao et al., 2003; Rao et al., 2011; Chen & Lanzetta, 2003; Le Brun et al., 1997; Zwaan et al., 2005). Thus while the quasar absorption-line systems have been studied in great detail (see for example Wolfe et al., 2005; Rauch, 1998, (for a review of DLAs and forest lines)), their connection to the galaxies and the environments in which they reside remains unclear.

The second approach in uncovering the connection between the absorbing gas and the absorber host galaxy is by searching for known low-redshift galaxies with quasars projected along lines of sights towards the galaxy. One well known example of this approach of identifying the galaxy/quasar pair and subsequent absorption line system is the dwarf galaxy SBS 1543+593. This galaxy/quasar pair was first discovered by Reimers & Hagen (1998) and was extensively studied both in absorption and emission by Bowen et al. (2005), Schulte-Ladbeck et al. (2004), and Schulte-Ladbeck et al. (2005). Ideally, one would like to observe multiple quasars projected near or behind one particular foreground galaxy. This allows detailed comparisons of the absorbing gas along multiple lines-of-sight through the galaxy. This technique however requires a foreground galaxy to have a large angular extent so its cross section covers a greater area for random sightlines, increasing the probability of having multiple quasars projected behind it. The angular size thus constrains the foreground galaxy to be of extremely low-redshift, making these systems rare and difficult to find. Crampton et al. (1997) identified 16 AGN behind the Magellanic Clouds selected via their X-ray emission and 146 quasar candidates behind nearby galaxies. Kozłowski & Kochanek (2009) identified 5000 possible quasar candidates behind the Magellanic Clouds using a mid-IR color selection scheme.

Few previous attempts have been made at generating galaxy/quasar pair catalogs. A catalog of over 400 galaxy/quasar pairs with angular separations $<10'$ was compiled by Burbidge et al. (1990). Bukhmastova (2001) compiled a catalog from the literature of 8382

galaxy/quasar pairs separated by <150 kpc at the galaxy redshift. While these surveys typically provide a large number of galaxy/quasar pairs, the lack of homogeneous data prohibits a full understanding of absorber gas properties and their connections with the host galaxies. Previous catalogs of galaxy-quasar pairs have often only provided separation information, while the Ca II and Na I absorption systems that have been detected in identified external galaxies were discovered on an individual basis, making it difficult to construct a coherent picture of the galaxy-absorber relationship. The work in this thesis seeks to generate a new sample of a large number of galaxy/quasars pairs identified from the Sloan Digital Sky Survey. Armed with a large sample of identifiable galaxy/quasars pairs, statistical analysis can be used to gain insight into the galaxy-environment connection for both the Ca II and Na I classes of absorption line systems.

1.3 THE INTERSTELLAR MEDIUM

To fully understand the formation and subsequent evolution of galaxies, one needs to understand the physical conditions within and around said galaxies. The general structure of gas and dust residing between the stars in a galaxy is referred to as the interstellar medium (ISM) of a galaxy. The ISM was first 'identified' in the early 20^{th} century when narrow absorption lines of Ca II and Na I were discovered in the spectra of binary stars that were different than the broadened lines seen in stellar atmospheres. These lines appeared as 'stationary' lines in the stellar spectra, distinguishing themselves from the typical Doppler shifted lines seen in the binary's cyclical orbit. Later, it was found that the size of star clusters diminished slower with distance than their brightnesses, indicating the presence of a medium responsible for extincting the light. The ISM was originally thought to be a homogeneous, diffuse medium, but higher resolution spectra taken of the Ca II and Na I 'stationary' lines revealed multiple cloud components pointing more towards a clumpy ISM. From the 40's onward, much work has been done in refining our understanding of the ISM. Today, our picture has grown to include a multi-phase medium consisting of five distinct thermal phases existing together in a quasi-steady state equilibrium. This medium is made up of gas ranging from cold molecular

Table 1.1 The Five Phases of the ISM, adapted from Kwok (2007); Frisch (2001)

Phase	Temp [K]	n [cm^{-3}]	State of Hydrogen	Volume	Form
H_2	∼0-50	$>10^3$	H_2	∼0.05%	clumpy cores
CNM	∼80-100	∼50	HI	∼1-4%	sheets and filaments
WNM	∼8000	∼0.5	HI	∼30%	boundaries of photodisassociation areas
WIM	∼6-12,000	∼0.1	HII	∼25%	diffuse photoionized regions
HIM	$>10^6$	$<10^{-2}$	HII	∼50%	bubbles,fountains outside plane

gas in dense cloud complexes to very hot ionized gas existing as bubbles and filaments lying above and below the Galaxy plane. Table 1.1 provides a brief description of the phases of the ISM.

1.3.1 Element Abundances and Dust Depletion

To really understand the physical conditions of the ISM in galaxies, we need to know the total abundance of the elements that we study. We describe the abundance of an element in terms of its gas-phase abundance, as most elements exist in the gas-phase in the ISM. The depletion of an element describes the difference between the observed abundance and its expected total cosmic abundance. It is usually given as

$$\delta(X) = [X_{gas}/H] = \log\left(\frac{X}{H}\right)_g - \log\left(\frac{X}{H}\right)_\odot \tag{1.1}$$

where $\log\left(X/H\right)_\odot$ is the elemental abundance in the sun. The solar abundance is usually adopted as a good approximation to the cosmic abundance. The amount of gas missing from the gas-phase is often attributed to being deposited onto the surfaces of dust grains.

Interstellar dust is an additional component of the ISM. Dust is a solid phase consisting of mainly silicate and graphite grains ranging in size from μm to molecular scales. Persisting in all but the hottest phases of the ISM, dust is important in the chemistry of the ISM, the extinction of light, and the gas-phase depletions of elements. Dust is approximately 100 times less abundant than gas in the Milky Way, making up ∼0.1% of the baryonic mass of the Milky Way. Elements are typically classified as either refractory or volatile elements,

based on their condensation temperature. The condensation temperature is the temperature at which 50% of the element has been removed from the gas-phase. Refractory elements consist of elements with a condensation temperature higher than the 'common' rock-forming elements of iron, silicon, and magnesium, around ∼1300 K for solar system abundances. Volatile elements are those elements with condensation temperature less than this.

1.4 ABSORPTION LINE FORMATION

As light passes through a cloud of gas in the ISM, the intensity of light that comes out the other side depends on the absorption and emission properties of the cloud. For a given volume element, the net change in intensity of light that survives through the cloud is

$$dI_\lambda = j_\lambda dl - \kappa_\lambda \rho I_\lambda ds \tag{1.2}$$

where $j_\lambda dl$ represents the change in intensity due to emission from the medium and $\kappa_\lambda \rho I_\lambda ds$ is the change in intensity due to absorption by the medium. Here, j_λ is the emission coefficient, κ_λ is the mass absorption coefficient, and ρ is the matter density of the particular gas cloud. Considering the absorption component alone from Equation 1.2, $\kappa_\lambda \rho I_\lambda ds$ measures the incremental extinction of light over some distance ds, and is sometimes written as

$$dI_\lambda = -I_\lambda d\tau_\lambda \tag{1.3}$$

where

$$d\tau_\lambda = \kappa_\lambda \rho ds. \tag{1.4}$$

τ_λ is the total optical depth through the cloud, or the total amount of extincted light across the cloud length L:

$$\tau_\lambda = \int_0^L \kappa_\lambda \rho ds \tag{1.5}$$

From an observational standpoint, we have no knowledge of the cloud element that the light passes through. We only receive information on the total path length traveled by the light through the cloud, thus it is sensible to talk only in terms of integrated quantities such as

τ_λ. τ_λ is dependent on both the wavelength of light as well as the matter properties of the gas cloud. Solving Equation 1.3 for I_λ yields the equation of radiative transfer considering absorption only

$$I_\lambda = I_o \exp\left(-\tau_\lambda\right) \tag{1.6}$$

1.4.1 Line Broadening and the Voigt Profile

Atomic and molecular lines from bound-bound transitions are not infinitely sharp and have finite widths due to a variety of mechanisms that broaden the line profile. The first type of broadening is natural broadening. This is due to the fact that there is a finite lifetime for any transition to occur. From the energy/time Heisenberg uncertainty principle, this implies that energy levels in a given transition have some finite spread to them. The result is a spread in the wavelength that a transition occurs at, giving the line some finite width. The profile that describes such a broadening is that of a Lorentzian, characterized by a narrow peak with broad wings.

Another, and usually dominant, type of line broadening is Doppler broadening. Doppler broadening occurs because of random motions of the atoms in the absorbing cloud. The ensemble of atoms in the cloud are governed by a Maxwellian velocity distribution. Due to these random motions, some of the atoms will have line-of-sight velocities directed towards us, and others directed away. This results in a slight Doppler shift which translates into shifts in the wavelengths at which the transition occurs. Since the velocity distribution of the absorbing gas is Gaussian, this makes the core of the line profile Gaussian as well. The Doppler broadening is often characterized by the Doppler parameter, b, and is given by

$$b = \sqrt{\frac{2kT}{m}} \tag{1.7}$$

The overall profile shape of an absorption line is a convolution of the Lorentzian and Gaussian distributions described above, called the Voigt profile.

The prior two cases describe broadening intrinsic to the atomic makeup and velocity distribution of the gas. An additional source of broadening results from our observations through a given telescope instrument. The instrument has a finite resolution which acts to

redistribute the photon counts falling within pixels smaller than the size of the instrumental resolution. Absorption lines narrower than this resolution element will effectively become 'broadened' to the size of the resolution element at that wavelength. These lines are said to be 'unresolved'. The shape of the line profile of unresolved lines will not accurately reflect the number of atoms in the gas and thus cannot be related to the physical conditions of the gas. The amount of information on the physical conditions that can be gleaned from absorption lines depends on the both the resolution of the instrument and the level of saturation in the lines.

1.4.2 Equivalent Width and the Curve of Growth

The equivalent width is the total strength of an absorption line and is defined as

$$W = \int_{-\infty}^{\infty} (1 - \frac{I_\lambda}{I_o}) d\lambda \tag{1.8}$$

where I_λ is the line flux at a given wavelength, and I_o is the flux of the continuum. For a given absorption profile, the equivalent width can be represented as the width of a column that extends from the normalized line profile continuum to zero intensity (see Figure 1.6). The equivalent width is an observable quantity measured directly from the spectrum and can be related to more fundamental physical properties such as the gas column density and velocity distribution through the curve of growth. Recalling Equation 1.6, the equivalent width can also be written as

$$W = \int_{-\infty}^{\infty} [1 - \exp(-\tau_\lambda)] d\lambda \tag{1.9}$$

The curve of growth (Carroll & Ostlie, 1996; Kwok, 2007) is a relationship between the column density of the absorbing gas and the equivalent width of the absorption line for a given ion. It consists of three regimes which describe how the equivalent width of a profile

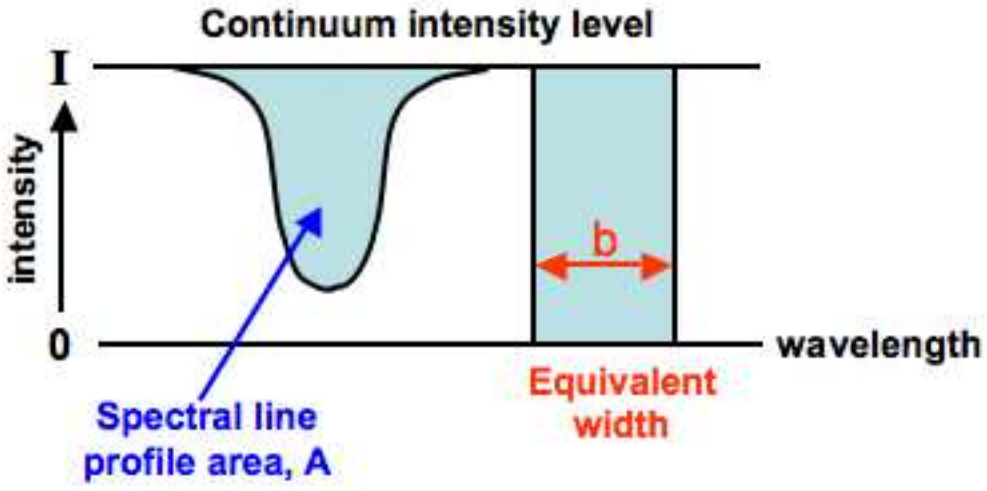

Figure 1.6 A cartoon diagram of an absorption line profile. The shaded area under the line profile is the equivalent width. To the right is a column of equal area extending from the continuum down to zero. In this figure, A=b is the equivalent width of the line. Credit: COSMOS - The SAO Encyclopedia of Astronomy

grows as a function of the column density and/or the velocity distribution of the gas. The three regimes are the:

$$\begin{aligned} \textbf{Linear}: &\quad W \propto N \\ \textbf{Logarithmic}: &\quad W \propto b\sqrt{\ln\left(N/b\right)} \\ \textbf{SquareRoot}: &\quad W \propto \sqrt{N} \end{aligned} \tag{1.8}$$

For gas at small column densities ($\lesssim 10^{14}$ cm^{-2}), or equivalently small optical depth ($\tau<<1$), the Voigt profile is dominated by the Doppler core. As the column density of the gas increases, photons are continuously removed from the beam as the strength of the line profile continues to grow. The equivalent width is independent of the velocity distribution of the gas and grows linearly with the column density. This regime is the 'linear' part of the curve of growth. As the column density of gas continues to increase, the gas reaches a point where photons are no longer able to be absorbed in the core. The absorption line at this point is said to be saturated. At this stage, the equivalent width becomes degenerate with the column density. Any photons incident upon the gas go into increasing the velocity

distribution of the gas, thus the flat part of the curve of growth depends heavily on the Doppler parameter, b. As the column density continues to increase above $\sim 10^{19} \mathrm{cm}^{-2}$, the damping wings of the Lorentzian profile begin to dominate the line profile. At this point, the equivalent width again becomes dependent on the column density, growing with a square root dependence. This is the 'square root' part of the curve of growth. The central panel of Figure 1.7 shows the curve of growth for the Ly-α transition of Hydrogen, highlighting the three regimes. The top plot shows how the line profile grows with increasing gas column density, first in the line core, followed by saturation, and then in the wings. The solid curves in the top panel match the solid points on the curve of growth shown in the central panel.

1.5 OPTICAL ABSORPTION LINES

There is a wealth of absorption lines used to study the environment in and around galaxies, such as the Damped Ly-α line, the doublets of Mg II, C IV, S IV, and O VI, or the Fe III triplet, to name just a few. However, the majority of these line have rest-frame UV wavelengths. The SDSS is wide-field survey observing the sky primarily in the optical wavelength region (Stoughton et al., 2002). The SDSS spectral coverage is from 3800-9200 Å. Sloan is also a low redshift survey, peaking at z=0.1 with a tail out to z of 0.5. Thus, most of the strong absorption lines are eliminated as probes for the ISM of SDSS galaxies. For example, Mg II, one of the longer UV wavelength lines at 2800 Å, does not shift into Sloan's spectral coverage until z=0.36, well into the tail of the SDSS galaxy distribution. Two strong absorption lines that do have rest-frame wavelengths in the optical are Ca II and Na I. These two lines fall within the spectral coverage of SDSS and can be observed within the entirety of the SDSS galaxy distribution. For this reason we use Ca II and Na I as our diagnostic tool for the environments in low-redshift galaxies in SDSS.

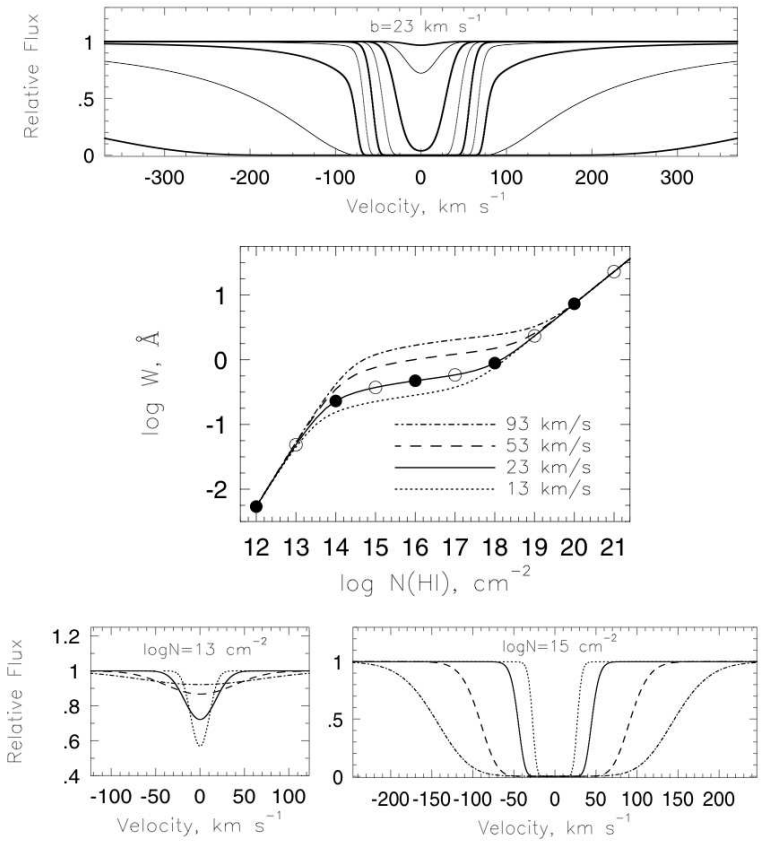

Figure 1.7 Illustration of the different regimes of the curve of growth. The middle panel shows the curve of growth for the Ly-α transition, relating the equivalent width, W, of the absorption profile to the column density, $N(HI)$. The different curves represent four different values of the Doppler parameter: b = 13, 23, 53, and 93 km s^{-1}. The upper panel shows absorption profiles with Doppler parameter b = 23 km s^{-1} for the series of neutral hydrogen column densities $N(HI)$ = 10^{12} - 10^{20} cm^{-2}. The thick (thin) curves correspond to the filled (open) points on the b = 23 km s^{-1} curve of growth (middle panel), starting at $N(HI) = 10^{12}$ cm^{-2}. For $N(HI) < 10^{13}$ cm^{-2}, known as the linear part of the curve of growth, the equivalent width does not depend on b. The lower left panel shows that, at fixed $N(HI)$, the depth of the profile is smaller for large b, such that the equivalent width remains constant. On the flat part of the curve of growth, profiles are saturated and the equivalent width increases with b for constant $N(HI)$. For $N(HI) > 10^{20}$ cm^{-2}, the profile develops damping wings, which dominate the equivalent width. Taken from Figure 3 of Charlton et al. (2000).

1.5.1 Ca II

Calcium (Ca) is an alkali earth metal with an atomic number of 20. The ground state of Ca is [Ar]$4s^2$. It lies in a closed-shell state with two electrons in the 4s orbital. Ca II is the first ionized state of Calcium. As it has one unpaired electron in the 4s orbital, it has an angular spin quantum number of S=1/2, and therefore a multiplicity equal to 2S+1 = 2, producing a doublet. The doublet occurs at wavelengths $\lambda\lambda$ 3934.77,3969.59 Å, which correspond to a transition from the $4^2S_{\frac{1}{2}}$ state to the $4^2P_{\frac{3}{2}}$,$4^2P_{\frac{1}{2}}$ state, respectively, in the LS coupling scheme. The λ3934.77 Å line of Ca II is often labeled *K*, while the λ3969.59 Å line is labeled *H*. At these rest-frame wavelengths, the Ca II line can be observed in a redshift range 0-1.3, a range spanning the entire SDSS galaxy distribution. The oscillator strength of an ion represents the transition probability of an electron in that particular excited state. For the Ca II K and H lines, the oscillator strengths are 0.65 and 0.32, respectively, or roughly a factor of 2 relative to each other. This means that in the optically thin case, the K line will always be twice as strong as the H line.

Calcium is considered an alpha element, that is, it can be created from lighter elements by fusion with a Helium nucleus. The dominant, stable, isotope of interstellar calcium is ^{40}Ca. It is primarily produced within the hydrostatic, oxygen and silicon burning shells of massive stars ($\gtrsim$8-11 $M_\odot$), but can also come from the decay of ^{40}K (Woosley & Weaver, 1995; Timmes et al., 1995).

Ca II has an ionization energy of ∼11.8 eV, which corresponds to a wavelength of ∼1051 Å. Neutral Hydrogen ionizes at 13.6 eV. Thus the ionization energy of a particular ion can tell you which phase of the ISM it should primarily probe. Since the ionization energy of Ca II is <13.6 eV, it should probe the cold and warm neutral gas component of the ISM in galaxies. However, with such a low ionization energy, it is not the dominant state of Calcium and is considered only a trace species. As most of the volume of the ISM is occupied by the HIM, most of the Calcium is in the doubly ionized state of Ca III. Ca III has an ionization energy of ∼47 eV. With such a high ionization energy for Ca III, the total abundance of Ca in the ISM can be approximated as

$$\mathrm{N(Ca) = N(Ca\ I) + N(Ca\ II) + N(Ca\ III).} \tag{1.10}$$

In most cases however, the Ca I component is usually neglected as it can only exist in dense cold environments, heavily shielded from ionizing photons by dust.

Ca is a highly refractory element and thus is heavily depleted onto dust grains. Refractory elements are elements with 50% condensation temperatures above the condensation temperatures of the most common rock-forming elements of Mg, Fe, and Si (∼1340 K). For solar system abundances at a total pressure of 10^{-4} atm, the condensation temperature for Ca is ∼1517 K. In the solar system Ca is considered one of the elements contributing to the major element condensates. A major element condensate is one consisting of elements that form the bulk of the rock-forming material in the solar system and act as host phases for other elements to condense on. These condensates do not need any prior material and are usually the first minerals to form from the solar nebula. The initial phase that Ca condenses on is Hibonite, $CaAl_{12}O_{19}$, at a temperature of ∼1659 K.

1.5.2 Na I

Sodium (Na) is an alkali metal with an atomic number of 11. The ground state of Na is [Ne]$3s^1$. The ground state of Na is also sometimes referred to as Na I, representing the neutral state of sodium gas. Like Ca II, Na I has one unpaired electron in its outermost orbital, thus producing a doublet. The doublet occurs at $\lambda\lambda$ 5891.58,5897.56 Å, corresponding to a transition between the $3^2S_{\frac{1}{2}}$ state and the $3^2P_{\frac{3}{2}}$,$3^2P_{\frac{1}{2}}$ states, for the 5891.58 line ad 5897.56 line, respectively. The Na I doublet is also referred to as the Fraunhofer D-line, or the D1,D2 lines. The Fraunhofer lines are prominent absorption lines first seen in the optical spectrum of the Sun, labeled A-K, systematically categorized and studied by Joseph von Fraunhofer. The 'D' designation has now come to refer to the transition between the ground state and the first excited state of any of the alkali metal elements. Given the rest-frame wavelength of Na I, this ion can be observed out to redshifts of 0.6, given the SDSS spectral coverage. Thus Na I can also be observed within the entire SDSS spectroscopic galaxy population.

Interstellar Na I mainly comes from the carbon burning shell of massive stars ($\gtrsim$8-11 $M_\odot$) (Woosley & Weaver, 1995; Timmes et al., 1995). The stable isotope ^{23}Na is the primary product but the final abundance depends on the excess amount of neutrons. It can

also be produced from the neutron capture of ^{22}Ne in the helium burning shell.

Na I has an ionization energy of 5.1 eV, which corresponds to a wavelength of ∼2431 Å. With such a low ionization energy, Na I is thought to probe the interiors of dense cold clouds in the ISM. Na I is also considered a trace species in that Na I is not the dominant ionization state for sodium. The first ionization state of Na, Na II, has an ionization energy ∼45 eV. With such a high ionization energy, higher ionized states of Na become rare, making Na I and Na II the dominant contributors to the total Na abundance, given as

$$\mathrm{N(Na) = N(Na\ I) + N(Na\ II).} \tag{1.11}$$

With a 50% condensation temperature of ∼958 K, Na I is a moderately volatile element, and thus, does not exhibit heavy depletion onto dust. Its depletion is also relatively independent of gas density. Na is considered a trace element in the solar system. Trace elements do not condense as 'pure' phases. They condense by forming solid solutions onto pre-existing materials that have already condensed out of the solar nebula. The host phase for Na is Feldspar. The dissolving compound which facilitates the reaction is $NaAlSi_3O_8$.

1.5.3 In the Milky Way

Ca II and Na I have been studied extensively in the Milky Way (Welsh et al., 2009b; Welsh et al., 2010), in High (HVC) and Intermediate Velocity Clouds (IVC), and in the Local Group (Ferlet et al., 1985a; Vladilo et al., 1993) for some time now. Welsh et al. (2010) mapped out the 3-D density distribution of Ca II and Na I gas using hundreds of sightlines within 300 pc of the Sun. They found that Na I predominantly exists in clumpy dense environments while Ca II is more diffuse existing in both the cold and warm neutral media as well as the warm ionized medium. The average EWs of Ca II and Na I within this region is ∼0.5 Å and average NaI/CaII ratios along the observed sightlines ranged from 0.1-100. Given the effects that dust and specific ionization conditions have on the amount of Ca II gas in a local environment, it is rather difficult to obtain accurate measurements of N(Ca II), although not impossible. Wakker & Mathis (2000) found a direct relationship between Ca II and H I for sightlines through HVCs and IVCs. A direct relationship between Na I and H I

was found from sightlines through the Milky Way (Ferlet et al., 1985b) and also found by Wakker & Mathis (2000) in the halo environment, although with large scatter.

To get an accurate estimate of the total amount of gas, one needs to take into account interstellar dust, since much of an element may be depleted onto dust grains. The exact conditions in which elements are removed from, or returned, to the gas-phase has been studied for a long time. A relationship was observed in the cloud ζ Oph between the relative depletion of an element from the gas-phase and the condensation temperature of the element. Based on these observations, Field (1974); Field & Cameron (1975) first developed the idea that element depletions were dominated by the original grain-formation mechanisms. This was later extended by Barlow (1978) to include the trapping of elements by absorption onto dust grains and the return of elements to the gas-phase through shock sputtering. The last two processes are dynamic processes and thus are dependent on the density of the local environment. Phillips et al. (1982) found that the strength of the dependence of depletion on density varies from element to element and can be used to probe the importance of each process. Phillips et al. (1984) found that the depletion of Ca onto dust was heavily dependent on the density of the local environment while Na depletion remained relatively constant with gas density. The dependence of the depletion factor on density highlights the importance of gas-grain interactions in the ISM. They found that the Ca depletion dependence on density was indicative of Ca's predominance of depletion onto silicate grains due to their high adsorption binding energy, whereas most other refractory elements are depleted onto both silicate and graphite grains. The lack of dependence of Na on density is due to Na's inability to accrete onto grains in diffuse environments. The lack of accretion is due to either shock-heating of the gas resulting in grain destruction or chemical processes that release Na from the grain surface.

The ratio of N(Na I) to N(Ca II), Na I/Ca II for short, can be used as a probe of the physical conditions in the local environment. The exact value of the ratio depends on the amount of dust in the system, along with the local environment conditions. Typical values seen for NaI/CaII in the Milky Way vary from 0.1-100. The dramatic variation seen in the ratio depends on the physical conditions of the absorbing medium as well as the extent to which Ca II is released into the gaseous phase from shocks. Observations by Bertin et al.

(1993); Crawford, I. A. (1992); Welty et al. (1996); Welsh et al. (2009b,a) have shown that in the WNM, NaI/CaII generally takes on low values (<1.0), while in the CNM, NaI/CaII takes on high values (>100). In the CNM, where the gas densities become appreciable, Ca is heavily depleted onto dust, as shown by Barlow (1978) and Phillips et al. (1984), driving the ratio to high values. In the WNM, where the gas densities are not as high, Ca is not as depleted, resulting in much lower NaI/CaII ratios. Siluk & Silk (1974); Routly & Spitzer (1952) also showed that low values for NaI/CaII can result from Ca II being released from grains from high-velocity (>30 km s^{-1}) interstellar shocks. So a low NaI/CaII ratio can either indicate warm, low density gas conditions or the presence of high-velocity shocks.

In practice it is difficult to distinguish between ionization effects or dust as the primary reason of the variation in the NaI/CaII ratio. However, in the WNM, around a temperature of ∼7000 K, the NaI/CaII ratio becomes independent of the electron density and can be used to trace the degree to which Ca is depleted onto dust. Ionization modeling of dust-free gas in the WNM has shown that the NaI/CaII ratio is roughly constant at log(NaI/CaII)∼ −1.6. As such, any variation seen in the ratio in the WNM can be attributed to variations in the local dust depletion in the environment.

1.5.4 In External Galaxies

Ca II has been detected in external galaxies since the late 70's. Before large surveys like the SDSS, Ca II absorption systems were identified on an individual case by case basis. Around 17-22 Ca II systems were detected with identified external galaxies between the late 70's and the mid 90's (Boksenberg & Sargent, 1978; Boksenberg et al., 1980; Blades, J. C. et al., 1981; Bergeron et al., 1987; Womble et al., 1990; Bowen, 1991; Womble, D. S. et al., 1991; Womble, 1993). Womble et al. (1992) constructed a mini-review of the known Ca II systems at the time. They found no correlations with the strength of absorption with impact parameter for close pairs (<22 kpc). They also found that the Ca II absorbers are more prevalent in morphologically disturbed galaxies, based on a crude visual classification into one of three groups, while the non-detections were more prevalent in the isolated, undisturbed galaxies. Zych et al. (2007) found five Ca II absorbers with associated galaxies in the SDSS selected

on the presence of Mg II. They found that the Ca II absorbing galaxies were metal-rich, luminous blue galaxies with large star-formation rates.

Ca II systems without identified hosts have been studied recently in much more detail than those with identified galaxies. Wild & Hewett (2005a) and Wild et al. (2006a,b, 2007) studied a sample of 38 Ca II absorbers at high redshifts ($0.84<z<1.3$) and found that strong absorbers, those with EW>0.2 Å, might be a subset of the DLA absorber population. They are also some of the dustiest absorbers, much more so than the DLAs or the Mg II populations of absorbers. Hewett & Wild (2007) imaged a subset of the Wild et al. (2006a) strong Ca II absorbers in the K-band to look for host galaxies. While not spectroscopically confirmed, they found an excess of luminous galaxies within 50 kpc of the absorbers, with a mean separation of 24 kpc and an absorber cross-section larger than the more established Mg II population.

Richter et al. (2011) studied a sample of 23 weak intervening Ca II absorbers at high resolution. As a complement to the strong Ca II absorbers studied by Wild & Hewett (2005b) and Wild et al. (2006a, 2007), Richter et al. (2011) found that the weaker Ca II systems extend much farther out from their host systems into the halo and circumgalactic environments and represent HVC analogs. For a subset of those selected by their strong neutral Hydrogen, they found a tight relationship between Ca II and H I similar to that found by Wakker & Mathis (2000).

The literature on interstellar Na I is even more sparse than Ca II. Before the SDSS, only a handful of Na I absorption lines systems had been identified in external galaxies (Junkkarinen & Barlow, 1994; Wilson & Penston, 1979; Kunth, D. & Bergeron, J., 1984; Womble et al., 1990). With the SDSS, while identified individual systems have remained few in number, a more comprehensive analysis has been undertaken through statistical analysis. In addition to the work of this thesis, Chen et al. (2010) recently conducted an analysis on interstellar Na I through the stacking of ∼140,000 galaxy spectra from the SDSS DR7, in the redshift range 0.05-0.18. Since Chen et al. (2010) use galaxy spectra, they are effectively probing the inner 3-12 kpc of galaxies, while our work probes a much larger area around the galaxy and is a good complement to their work. Richter et al. (2011) found five Na I absorber systems from their sample of 23 Ca II absorbers at low redshifts (<0.5). Two multi-

component high redshift systems (~ 1.1) were detected at high resolution in the background of a gravitationally-lensed quasar (Kondo et al., 2006). In the cases of Richter et al. (2011) and Kondo et al. (2006) however, the galaxies giving rise to the absorption have not been identified.

With Ca II and Na I sightlines through both the plane and the halo of the Milky Way, as well as within the Local Group, the connection between the Galaxy and absorbing environment can be studied. This however is limited to the very local Universe. The question that still remains is how are galaxies in general connected to the Ca II and Na I absorption environments at higher redshifts.

1.6 OUTLINE

The work in this thesis is motivated by precisely this question. With the vast numbers of galaxies and quasars found in the Sloan Digital Sky Survey (SDSS), the SDSS is an ideal place to look for low-redshift galaxy/quasars pairs in a practical and straightforward manner, which can be used to study quasar absorption-line systems arising from known galaxies with redshifts between $0<z<0.5$. With SDSS as well, much more galaxy information is provided for our pairs than typically has been in the past with such large pair catalogs. In general the work in this thesis describes the construction of galaxy-quasar pair catalogs and the subsequent identification of Ca II and Na I absorbers within those pairs. The analysis performed consists of examining correlations between absorber properties and galaxies properties, as well as looking for significant differences in galaxy properties between galaxies hosting Ca II or Na I absorption and those that do not.

Chapter 2 represents the initial stages of this thesis work. We had started working with the SDSS Data Release 4 and upgraded to Data Release 5 for galaxies and Data Release 6 for quasars. After briefly describing the Sloan survey, we discuss the construction of a sample of 154 galaxy-quasar pairs that are closely separated within an angular radius of $1'$ and within twice the galaxy optical radius. The automated absorption-line finding algorithm we adopt is discussed in Section 2.3. We use this algorithm to search for Ca II and Na I

absorption lines in the resulting pair catalog. We find 13 Ca II and 9 Na I absorption systems at significances ≥ 2 around external galaxies. The analysis of the absorbers indicate that the Ca II absorbers primarily consist of blue, late-type disk galaxies, located at smaller impact parameters, compared with the non-absorbing galaxies. With the exception of a weak $g-r$ color difference, we find no significant differences between Na I absorbing galaxies and non-absorbers. The work presented in this large has largely been superseded by the work in Chapters 3 and 4.

While the work described in Chapter 2 was ongoing, SDSS released their final data release, DR7. To have the most up-to-date sample available, we decided to redo the sample construction and analysis using the DR7 sample of galaxies and quasars. Many techniques were also revised from the previous analysis and implemented with this new sample. Chapter 3 describes this work and represents the most recent and final dataset on which the rest of the analysis in this thesis is based. With the DR7, we constructed a sample of ∼98,000 galaxy-quasar pairs separated within a physical radius of 100 kpc. Using the same automated line finder, we identify 1749 Ca II absorbers and ∼4500 Na I absorption systems at significances ≥2. The rest of the chapter describes the analysis of a visually selected subset of these systems. We visually identify 92 Ca II absorbers and 16 Na I absorbers at significances $\geq$ 2. The majority of the identified absorbers have equivalent widths, LSR velocities, and impact parameters that strongly suggest they are most likely sightlines through the Milky Way, Local Group, or Virgo Cluster instead of being associated with external (e.g. $z > 0.01$) galaxies. The bonafide visually-identified Ca II absorbers belonging to external galaxies are blue, luminous, disk galaxies located at small impact parameters, consistent with what we find in the DR5/6 sample, as well as what has been seen in the literature so far, suggesting that Ca II absorption is more commonly found in star-forming galaxies at low redshift. Both of these subsets greatly enhance the numbers of detected Ca II and Na I absorption systems around identified low redshift external galaxies. The work described in this chapter is detailed in Cherinka & Schulte-Ladbeck (2011).

In Chapter 4, we address the issue of the robustness of the automated absorption-line finding algorithm and estimate the number of contaminants in the absorber sample due to false identifications of non-absorbers. The results of this analysis suggest a high false

positive rate for absorbers selected at significances greater than 2, but not for absorbers with significance greater than 3. We thus select a subset of absorbers at $z \geq 0.01$ and significance greater than 3 on which to perform the rest of the analysis. Using this sample of 19 Ca II and 36 NaI SDSS DR7 galaxy-quasar pairs, we perform and discuss the stacking analysis and the comparison between the absorber and non-absorber galaxy populations. We stack the identified absorbers found by our line-finding algorithm and show the presence of strong Ca II and Na I absorption, even within spectra that were rejected by eye. The stack of non-absorbers shows no presence of Ca II and the weak presence of Na I absorption. Correlating the absorber strength with various galaxy properties, we find no correlations between the Ca II K or Na I rest equivalent width and any galaxy property. We also compare samples of absorbing and non-absorbing galaxies. We find no significant differences for either the Ca II or the Na I absorber galaxies. The fraction of both Ca II and Na I absorbers is small ($\sim$5%) for b <10 kpc, and less than one percent at larger separations. The fraction within 10 kpc increases for 0.1-1 L* galaxies. Both the Ca II and Na I absorbers appear to be uniform in their distributions within spherical galaxy halos, with no strong indication of pure disk or outflow contributions.

In Chapter 5 we discuss future work that can be done, highlighting recent follow-up work of neutral Hydrogen observations of two Ca II absorber galaxies from the DR5/6 sample, with the quasar projected within twice the optical radius of the galaxy. Both systems are candidates to be DLAs based on the strength of their Ca II absorption. We find both galaxies to be M^*_{HI} galaxies, with gas-mass fractions representative of disk galaxies. Both candidates fall well within the range of HI properties from the expected $z = 0$ DLA population (Zwaan et al., 2005; Rosenberg & Schneider, 2003). We also find both systems to belong in groups, suggesting a common phenomenon for the DLA environment. This follow-up work is published in Cherinka et al. (2009).

2.0 ABSORBERS IN SDSS DR5/6

This chapter describes the early stages of my thesis work using the SDSS Data Releases 5 and 6. Over the course of this work many techniques were refined or changed. Chapters 3 and 4 describes my latest work, using the SDSS DR7, with a slightly different sample construction and a refined analysis. Section 2.1 briefly describes details of the Sloan Digital Sky Survey, the survey from which all of my work in this chapter, as well as chapters 3 and 4, is derived. Section 2.2 describes the selection criteria used to create the parent sample of galaxy/quasar pairs from SDSS DR5/6. Section 2.3 describes the automated line finding routine used to identify Ca II and Na I absorption-line systems in both DR5/6 and DR7. In sections 2.4 we discuss the resulting absorber sample generated from the DR5/6 sample of galaxy/quasar pairs. The analysis of the absorber sample is presented in sections 2.5 and 2.6. A summary of the results is presented in Section 2.7.

2.1 THE SLOAN DIGITAL SKY SURVEY

The Sloan Digital Sky Survey (SDSS) is a recently completed survey that has, over the past ten years, revolutionized the way astronomy is done. A 2.5 m telescope located at the Apache Point Observatory in New Mexico, running from 2001-2009, the SDSS has obtained images of one-quarter of the sky down to an r-band magnitude of $\sim$22. After seven major data releases, the SDSS has obtained photometry for hundreds of millions of objects and spectra for a million of those imaged. Table 2.1 summarizes the survey details for the SDSS data releases used in this thesis.

Photometric data is collected in an array of thirty 2048x2048 pixel CCDs laid out in six

Table 2.1 SDSS Survey Details

	Photometric Catalog		Spectroscopic Catalog	
Catalog	Sky Coverage [sq. deg.]	# of objects	Sky Coverage [sq. deg.]	# of objects
DR5	8000	215 million	5740	Total: 1,048,960 Galaxies: 674,749 Quasars: 90,611 Stars: 215,733 Sky: 55,555
DR6	9583	287 million	7425	Total: 1,271,680 Galaxies: 790,860 Quasars: 103,647 Stars: 287,071 Sky: 68,770
DR7	11663	357 million	9380	Total: 1,640,960 Galaxies: 929,555 Quasars: 121,273 Stars: 464,261 Sky: 97,398

colmuns of five CCDs each. Each row contains one of the five filters, r, i, u, z, g, used by the SDSS. The survey operates the instrument in drift scan mode, with the CCDs slowly reading out data as objects move along the columns. It takes an object 54 seconds to cross a CCD chip, such that a 54 second exposure is taken in each filter, resulting in 5 images per object. The camera images all objects within its field-of-view down to $r\sim22$.

After the images are taken, targets are selected for follow-up spectroscopy. There are three main classes that are targeted: galaxies, quasars, and luminous red galaxies. For galaxies, selection for spectroscopy is based on satisfying several criteria. The first is the selection of galaxies with a Petrosian magnitude, $r_{\rm P}$, <17.7, where the Petrosian magnitude is the magnitude contained within the Petrosian radius. The Petrosian radius is defined as the radius in which the Petrosian ratio reaches a limiting value of 0.2, where the Petrosian ratio, at some radius r, is defined as

$$R_P(r) = \frac{\int_{0.8r}^{1.25r} dr' 2\pi r' I(r') / [\pi(1.25^2 - 0.8^2) r^2]}{\int_0^r dr' 2\pi r' I(r') / (\pi r^2)} \tag{2.1}$$

and represents the ratio of the integrated surface brightness in an annulus around radius r over the integrated surface brightness within r. Additional criteria in the selection of galaxies for spectroscopy are a difference between point spread function and model magnitudes of >0.3, and a Petrosian half-light surface brightness $\mu_r<24.5$ mag arcsec^{-2}. While quasars have a stellar-like appearance in images, their spectral energy distributions (SEDs) are quite different than stars, thus making them distinguishable from stars in color-color or color-magnitude plots. Quasars are selected as those objects that lie 4σ away from the stellar locus in the u-g, g-r, and r-i color spaces, and have $15<i<19$. High-redshift quasars are selected in the same manner but in a redder color space of g-r, r-i, and i-z. Once objects pass the appropriate criteria for targeting, spectroscopic observations are carried out. Details for the spectroscopic target selection process is outlined in Strauss et al. (2002) for galaxies and Richards et al. (2002) for quasars.

The spectroscopic data are collected on four CCDs using two spectrographs, each with a blue and red channel. Spectra are collected and fed to the spectrographs via 640 fibers hooked into an aluminum plate of fixed size. Each fiber has a 3″ diameter and the entire plate covers a 3° field of view. For each spectrum, three fifteen minute exposures are taken until a median $(S/N)^2$ per pixel of ∼15 is reached in the g and i bands. The wavelength range of the spectra is 3800 Å to 9200 Å, with a resolution ranging from 1800 at the blue end to 2200 at the red. Wavelengths in the SDSS are binned with a constant logarithmic dispersion, thus fixing the pixel size at 69 km s^{-1}. The instrumental dispersion varies from ∼0.9 Å/pix at the blue end to ∼2.1 Å/pix at the red end. The number of pixels per resolution elements in SDSS is 2.35. This gives an instrumental resolution of about ∼160 km s^{-1}.

Once taken, each exposure is then bias-subtracted, flat-fielded, and flux-calibrated. The counts in each exposure are placed on the same scale and the wavelength scale is rebinned to a polynomial in log λ. The exposures are then merged into a single spectrum. As the counts are intrinsically Poisson distributed, the number of counts roughly goes as $N \sim 1/(\sigma_{flux}/flux)^2$. For a typical 1-d reduced and calibrated spectrum, the median number of counts per pixel is around ∼73, for quasar spectra. See Stoughton et al. (2002) for details on the spectroscopic data reduction procedure.

2.1.1 Catalog Issues

- **Fiber Collisions**

  An issue that affects the construction of both our DR5/6 and DR7 samples of galaxy-quasar pairs is the 55″ fiber collision problem in SDSS. On a given tile in SDSS, there are a maximum of 592 possible fibers for placement onto a viable target. The spacing between each fiber on a tile is 55″. Targets that lie less than 55″ from each other are spectroscopically unobservable unless recovered with overlapping tiles on the sky. About 6% of all SDSS targets are missed in this manner (Blanton et al., 2003a). With approximately 1.1 million objects targeted for spectroscopy, 6% corresponds to ∼66000 objects. This however does not necessarily imply that the incompleteness of close pairs

is ∼6%. The spectroscopic incompleteness of our sample in particular (close pairs within 100 kpc) will be addressed in a future paper. At the mean redshift for SDSS galaxies ($z \sim 0.1$), 55″ corresponds to ∼101 kpc. For the majority of our galaxies, we are searching well within the fiber collision radius.

- **Spectrophotometric Calibration**

  Beginning with the SDSS Data Release 6 and continuing with the Data Release 7, improvements were made to both the photometric and spectroscopic calibrations. With DR6, improvements were made to the pipeline that extracts and calibrates the one-dimensional spectra. A new spectrophotometric flux scale as well as improved wavelength calibrations were adopted. With DR7, additional improvements were made to the wavelength calibration and to the spectroscopic flats used for flat-fielding. Improvements were also made to the algorithm controlling the rejection of discrepant points, which prior to DR7, would occasionally reject and remove a spectral emission line feature. See Adelman-McCarthy et al. (2008) and Abazajian et al. (2009) for details. These differences between DR5/6 and DR7 ultimately resulted in the loss of some absorber candidates when we moved from the DR5/DR6 parent sample to the DR7 parent sample, as discussed in Section 2.4.3.

2.2 PARENT SAMPLE CONSTRUCTION

Here we describe the construction of our catalog of galaxy-quasar pairs using the SDSS Data Releases 5 and 6.

2.2.1 Sample Selection

Selecting a sample of galaxy/quasar pairs requires the generation of galaxy and quasar lists from the SDSS and a matching algorithm to find the intersection of both lists. In their seminal work on galaxy/quasar pairs, Burbidge et al. (1990) originally searched for pairings with an angular separation of 10′ on the sky. At the mean redshift of SDSS spectroscopic

galaxies around 0.1 (Stoughton et al., 2002), 10′ corresponds to ∼1000 kpc in the standard ΛCDM cosmology (using H_o=71 km/s, Ω_m=0.27, and Ω_Λ=0.73 (Hinshaw et al., 2009)). We adopt this cosmology for the remainder of this section, as well as for all analysis pertaining to the SDSS DR5/6 sample of galaxy-quasar pairs. We judged a matching radius of 10′ as excessive for our purpose, given that the impact parameters of known Ca II and Na I absorbing galaxies are less than about 25 kpc (see Chapter 3, sections 3.1.2.1 and 3.1.2.2). We therefore adopted a matching radius of 1′, or 110 kpc at z_{gal}=0.1. To construct a sample of SDSS quasars, we adopted the algorithm of Schneider et al. (2005). Schneider's algorithm uses three SQL queries to construct the quasar catalog. The first query is a union of primary objects targeted as quasar candidates and primary objects not targeted as quasar candidates but had spectra that were classified as either quasar or unknown, or had a $z \geq 0.6$. The second and third queries were designed to recover non-primary objects with quasar spectra or objects mapped to a photometric object in the TARGET database but not in the BEST database (see Schneider et al. (2005) for details). We ran the algorithm on the SDSS DR5 sample and it returned a sample of 207,000 photometric and spectroscopic quasars. It should be noted that the algorithm from Schneider et al. (2005) is broad in its scope so it includes not only photometric and spectroscopic quasars but other objects as well. Schneider et al. (2005) made further cuts to produce the final clean quasar catalog that is now accessible in the SDSS.

Table 2.2 Galaxy/Quasar Catalog

Galaxy	z_{gal}	Quasar	z_{qso}	b [″]	b [kpc]	r_{petro} [″]	r_{petro} [kpc]	$b/r_{\rm Petro}$
SDSS J000508.89+002610.6	0.08451±0.00015	SDSS J000508.85+002608.3	0.6680±0.0021	2.39	3.74	3.66 ±0.14	5.7 ±0.2	0.65± 0.03
SDSS J000512.73+000805.3	0.26340±0.00015	SDSS J000512.18+000802.9	1.1210±0.0012	8.53	34.37	5.47 ±0.35	22.1±1.4	1.56± 0.10
SDSS J001233.41+010014.2	0.08543±0.00009	SDSS J001233.34+010010.3	1.2132±0.0010	3.99	6.32	3.58 ±0.26	5.7 ±0.4	1.11± 0.08
SDSS J003339.85-005522.3	0.21242±0.00010	SDSS J003340.21-005525.5	0.9378±0.0018	6.28	21.54	7.76 ±7.65	26.6±26.2	0.8 ± 0.8
SDSS J004316.15+001035.6	0.14352±0.00017	SDSS J004316.50+001045.1	0.5799±0.0006	10.93	27.27	6.51 ±0.19	16.2±0.5	1.68± 0.05
SDSS J004515.67-011317.8	0.10551±7.38242	SDSS J004515.44-011317.7	1.5942±0.0025	3.45	6.59	9.14 ±0.41	17.5±0.8	0.38± 0.02
SDSS J004604.12+000710.8	0.05745±0.00011	SDSS J004603.29+000729.5	2.5557±0.0018	22.52	24.77	18.02 ±-999	19.8±-999	1.25± -999

Note. —
List of the 154 Galaxy/Quasar Pairs. Included for each pair are the redshifts, the impact parameter between the galaxy and quasar in ″ and kpc, the r-band Petrosian radius of the galaxy in ″ and kpc, and the $b/r_{\rm Petro}$ ratio. Physical distances are calculated at the location of the host galaxy. '-999' means no error is available. The full catalog is available in Appendix A2.

We then cross-correlated our quasar sample with the SDSS DR6 photometric galaxy sample, which consists of ∼174 million galaxies, and searched for galaxy/quasar pairs with a separation of ≤60". The separation is large enough to cover the effective cross-sectional area for most absorption-line systems. The disadvantage with this cutoff is at low redshifts, where we only cover the inner <10 kpc for galaxies below z<0.01. For SDSS galaxies, this means we lose possible pairs of quasars with large, low-redshift galaxies. This search resulted in ∼3 million galaxy/quasar pairs consisting of both photometric and spectroscopic galaxies and quasars. To narrow down the sample to pairs of interest, we placed several cuts on the sample. The first cut required both the quasar and galaxy to have spectroscopic data available, as we are interested in performing absorption-line and emission-line analyses. This cut was made by ensuring $z_{QSO} > z_{gal}$ and $z_{QSO} - z_{gal} > \sqrt{\sigma^2_{z_{QSO}} + \sigma^2_{z_{gal}}}$. This returned 16,279 galaxy/quasar pairs. Often times, SDSS targets were spectroscopically observed multiple times by meeting criteria for several target selection algorithms (i.e. Main Galaxy Sample, Luminous Red Galaxy Sample, etc.) or by being reobserved when falling in an overlapping tile region. As a result, a galaxy or quasar may have one object id but multiple spectroscopic object ids. Of the 16,279 galaxy/quasar pairs, there are 7,693 unique pairs. The second cut we applied to the 16,279 galaxy/quasar pairs was to require that the quasar lie within twice the r-band Petrosian radius of the galaxy (defined in Section 2.1). As the goal is to connect galaxy properties with those of quasar absorption line systems, we selected those quasars with a projected distance near to the galaxy. A cut at two Petrosian radii was chosen because we reasonably expect HI column densities to exceed the DLA limit out to distances several times the optical radius as shown by HI maps of local spirals (Cayatte et al., 1994; Broeils, A. H. & Rhee, M.-H., 1997) and dwarfs (Rosenberg et al., 2006; Swaters et al., 2002). We were then left with ∼600 galaxy/quasar pairs. For each pair with multiple quasar or galaxy spectra, we keep the spectra with the highest S/N. Removing the duplicates in this manner reduced the sample from ∼600 to ∼350 unique galaxy/quasar pairs. A third cut was applied through a visual inspection on the remaining sample to ensure that the resulting pairs were actual galaxy/quasar pairs. Appendix 5.2.2.4 shows our SQL code for the initial sample construction plus the first two cuts. After visual inspection, the sample was reduced to 154 galaxy/quasar pairs. Pairs rejected typically consisted of 1.) objects

that were targeted as quasar candidates which follow-up spectroscopy revealed to be HII regions, a patchy region of the galaxy, or some kind of merger event, 2.) objects with an 'Unknown' spectral classification that did not match the typical quasar spectrum at the redshift indicated, 3.) a diffraction spike from a nearby star, or 4.) a meteor or satellite streak.

In summary, the final sample consists of 154 galaxy/quasar pairs that meet the following criteria:

1. Both the galaxy and quasar have been spectroscopically observed and $z_{QSO} > z_{gal}$

2. The quasar is projected within twice the Petrosian r-band radius

3. The galaxy/quasar pair survives visual inspection.

Table B1 in Appendix B lists the final sample of 154 galaxy/quasar pairs. Figure 2.1 shows the distribution of impact parameters and r-band Petrosian radii of the unique (7693) galaxy/quasar pairs after the 60″ and redshift cutoffs were applied. As seen in Figure 2.1, there are two distinct regions absent of galaxy/quasar pairs located at large and small Petrosian radii and at small impact parameters. The void at large $r_{\rm Petro}$ and small b is due to Sloan's inability to correctly identify large galaxies photometrically (Stoughton et al., 2002; Abazajian et al., 2009). At $r_{\rm Petro} < 1''$, there are no galaxy/quasars pairs as atmospheric seeing limits the sizes of galaxies observed in Sloan.

2.2.2 Caveats

There are several caveats regarding the final sample of objects that will be addressed here:

- Our sample is an optically selected sample, thus it suffers from the Malmquist bias. As the SDSS is a magnitude-limited survey (Strauss et al., 2002), the selection of galaxies in the SDSS favors giant disk galaxies preferentially over dwarf or low surface brightness galaxies. The SDSS's photometric limiting magnitude is r=23, while they place a cut on spectroscopic targets of the main galaxy sample at $r_{\rm Petro}$ =17.77 and on the luminous

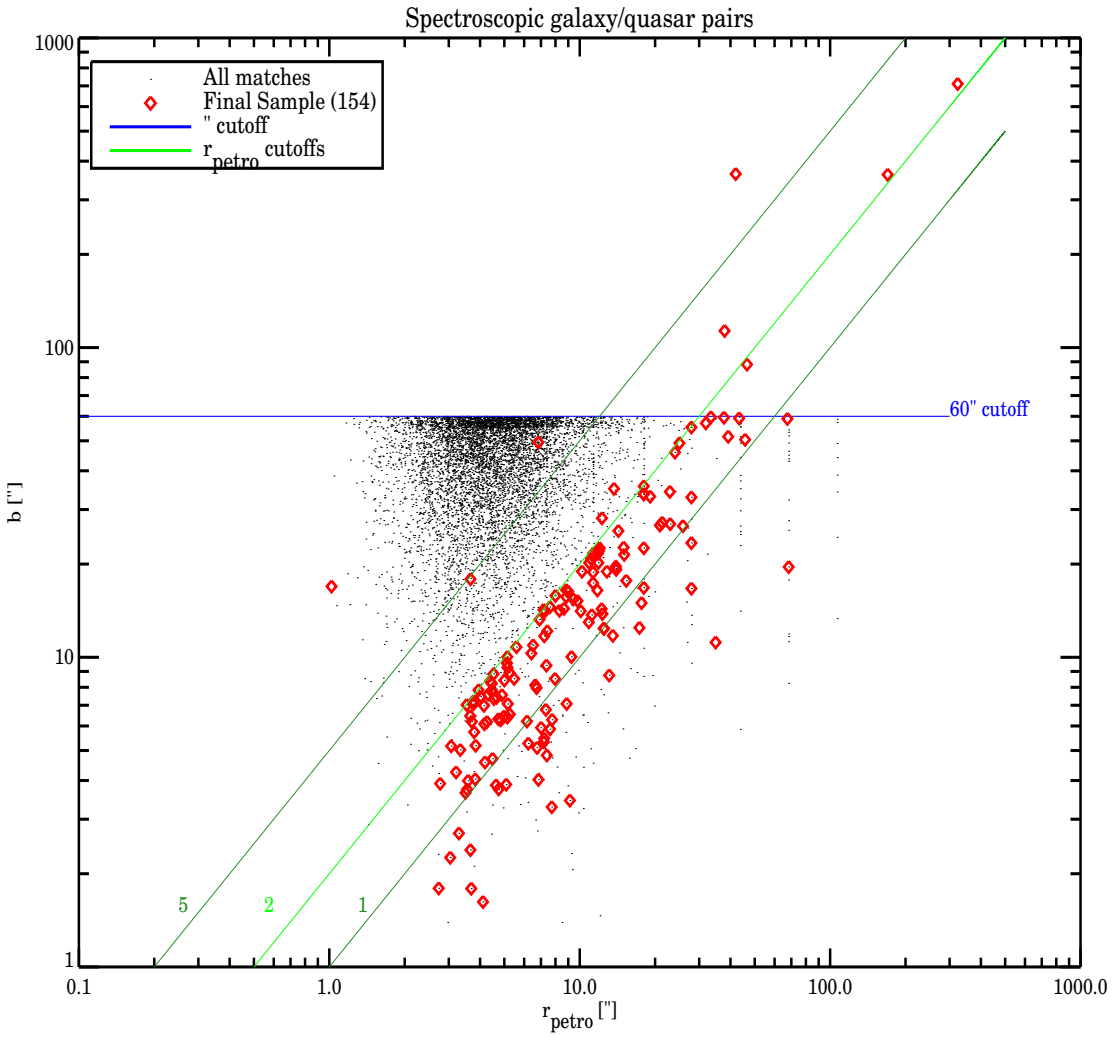

Figure 2.1 Impact parameter vs r-band Petrosian radius for the entire spectroscopic galaxy/quasar sample. The red diamonds designate the objects in the final sample, after the three cuts were applied. The horizontal blue line is the 1st applied cut of 60″. The diagonal light green line is the 2nd applied cut of twice the Petrosian radius. The 1 and 5 x Petrosian radius lines are shown to the right and left for reference. The red diamonds above the 60″ and 2×Petrosian radius cutoffs are discussed in section 2.1. The black points below the 2xPetrosian radius cutoff, but not enclosed by a red diamond are those objects rejected with the 3^{rd} applied cut of visual confirmation.

red galaxy sample at $r_{\rm Petro}$=19.5. In addition to the galaxy population being biased towards the bright end, there is also the effect of quasars that may exhibit absorption from

an intervening galaxy which is below the magnitude limit of the SDSS, and is thus not visible. Given our requirement for a visible galaxy, our selection method misses these potential pairs. Since the traditional selection method of quasar absorption-line systems selects systems independent of the galaxy, our selection method may be considered complementary to the traditional method.

- During the visual inspection stage, some objects flagged as galaxies by SDSS were seen to actually be child objects connected to a larger parent low-redshift, bright galaxy. We then updated the original galaxy in the galaxy/quasar pair to the parent galaxy and impact parameters were recalculated using the parent galaxy center, resulting in impact parameters that exceeded 60″ or $b/r_{\rm Petro} > 2$.
- As is well documented (Stoughton et al., 2002; Abazajian et al., 2009), these large, low-redshift, bright galaxies tend to have their photometric fluxes and scale sizes underestimated due to systematic errors in the sky subtraction procedure. Blanton & Hogg (2009) have compiled a catalog of low redshift galaxies consisting of SDSS DR6 MAIN galaxies that meet the cuts from Blanton et al. (2005) plus all NED[1] galaxies (circa July 2008) with $z < 0.05$. They have redone the photometry to achieve better estimates of the fluxes and sizes for these galaxies. We adopt their preliminary measurements for fluxes, the r-band Petrosian radius, and the r-band Petrosian R50 and R90 radii, for those galaxies in our catalog matched in theirs. There is one galaxy in our sample, NGC 4631, that should be in their catalog as it is a NED galaxy with $z < 0.05$ but is not. We therefore have no corrected estimate for the r-band Petrosian radius of this galaxy. We include this galaxy in the sample but exclude this galaxy during the analysis of the trends of the Ca II and Na I absorbers with Petrosian radius.
- Three galaxies in the catalog had either misidentified redshifts from their spectra or no redshift available due to it being a low-z bright galaxy with no spectrum taken. SDSS J022606.84-001655.9 had a misidentified redshift of z=0.0004. We adopt the NED redshift of 0.407±0.001 for this galaxy. SDSS J024240.70-000047.9 has no reported SDSS redshift. This galaxy was identified as NGC 1068 and we adopted the NED redshift of 0.00379±0.00001. This galaxy was selected into our sample via caveat 2. Fi-

[1]NASA Extragalactic Database http://ned.ipac.caltech.edu/

nally, SDSS J123636.73+141333.1 also had a misidentified redshift of z=0.00014. It was identified as VCC 1682, a part of the Virgo Cluster. We adopt a redshift of 0.0034±0.0006, calculated from the average of the distance moduli values given for VCC 1682 in Young & Currie (1995).

2.3 ABSORPTION LINE IDENTIFICATION

Upon construction of the SDSS sample of galaxy-quasars pairs, the next step is the identification of Ca II and Na I absorption-line systems in the spectra of quasars. As we are ultimately interested in host galaxy properties of absorption-line systems, we use the SDSS redshift of the galaxy to constrain the parameter space in which we search for absorbers. We adopted the automated line finder of the Hubble Space Telescope (HST) Quasar Absorption Line Key Project (Schneider et al., 1993) which is optimized to look for weak, unresolved quasar absorption lines. We follow the prescription as outlined in Churchill (2009, in prep.). The prescription searches for significant unresolved features by stepping through the spectrum weighting each pixel by the Instrumental Spread Function (ISF), a Gaussian that describes how the pixel counts are redistributed below the limiting resolution of the instrument. The ISF, Φ, is defined as

$$\Phi(\lambda' - \lambda) = \frac{1}{2\pi\sigma} \exp\,[-\frac{(\lambda' - \lambda)^2}{2\sigma^2}] \tag{2.2}$$

In practice, the ISF is discretized as a Gaussian model, P_i, symmetric about a pixel i, that spans $M = 2J0 + 1$ elements, where $J0 = 2p$, and p is the number of pixels per resolution element. The discretized ISF is given as

$$P_i = \exp\,[-x_{kj}^2] / \sum_{i=1}^{M} \exp\,[-x_{kj}^2] \tag{2}$$

$$x_{kj} = \frac{\lambda_k - \lambda_j}{\sigma_j^{ISF}}$$

normalized to ensure conservation of counts within the region spanned by the ISF. In the above, $\sigma_j^{ISF} = \lambda_j \;/\; (2.35\; R)$ is the Gaussian width of the ISF at pixel j, where R is the

spectral resolution, and $k = j + (i-1) - J0$ is the wavelength index relative to the central pixel j.

Before running the line finder algorithm we flux normalize each quasar spectrum. We first divide each quasar spectrum by a global continuum fit calculated from the flux array and normalized flux array stored in the 'spSpec' 1D spectral fits file. In some cases the sought-after doublets were superimposed on a broad emission line in the quasar's spectrum. We thus re-defined a local continuum anchored to the quasar's normalized spectrum within a 100 Å region centered around the expected doublet location based on the associated galaxy's emission-line redshift.

Our implementation of the procedure is outlined as follows:

1. **Weight the Flux Decrement in each Pixel by the ISF:**

   The weighted equivalent width and uncertainty in pixel j is defined as

$$ew_j = -\frac{\Delta\lambda_j}{P^2}\sum_{i=1}^{M} P_i D_k \tag{2.4}$$

$$\sigma_{ew_j} = \frac{\Delta\lambda_j}{P^2}\left(\sum_{i=1}^{M} P_i^2 \sigma_{D_k}^2\right)^{1/2} \tag{2.5}$$

   where

$$P^2 = \sum_{i=1}^{M} P_i^2 \tag{2.6}$$

   D_k = 1-(I_k/I_k^c) is the flux decrement in pixel k, and $\Delta\lambda_j$ = 0.5×(λ_{j+1}-λ_{j-1}) is the wavelength dispersion in pixel j.

2. **Search the Spectrum for Pixels Satisfying the Condition:**

   For each quasar spectrum, we identify any individual pixels within the search region with

$$\frac{ew_j}{\sigma_{ew_j}} \leq -N_\sigma \tag{2.7}$$

   where N_σ is a user-specified significance threshold. We chose $N_\sigma = 2.0$ as our significance threshold. If no pixel is detected with $\frac{w_j}{\sigma_{w_j}}$≤-2.0, then a flag is set indicating 'No Detections'. If a pixel is detected at the edge of the search region with $\frac{w_j}{\sigma_{w_j}}$≤-2.0, then a flag is set indicating 'Outside Pixel'. This pixel is then rejected as being truly associated with the host galaxy, as the search region is centered on the strong line of the doublet.

3. **Determine the Pixels Spanned by Feature i:**

   For a given pixel that satisfies the above condition, we identify the start and end pixels of feature i by scanning the spectrum blueward and redward of pixel j until the conditions

$$\frac{ew_j^-}{\sigma_{ew_j^-}} \geq -1.0 \quad ; \quad \frac{ew_j^+}{\sigma_{ew_j^+}} \geq -1.0 \tag{2.8}$$

   are met. This defines a candidate line feature.

4. **Determine the Significance of the Candidate Feature:**

   Once the pixel span of feature i has been identified, the observed equivalent width, EW, and uncertainty, σ_{EW}, of feature i are

$$EW_i = \sum_{k=j^-}^{j^+} e_k \tag{2.9}$$

$$\sigma_{EW_i}^2 = \sum_{k=j^-}^{j^+} \sigma_{e_k}^2 \tag{2.10}$$

   where $e_k = \Delta\lambda_k D_k$ is the unweighted equivalent width in pixel k, and $\sigma_e = \Delta\lambda_k \sigma_{D_k}$ is the uncertainty in e_k. The final step is to calculate the significance, S, of feature i and check that it satisfies the required significance threshold.

$$S_i = \frac{EW_i}{\sigma_{EW_i}} \quad ; \quad S_i \geq N_\sigma \tag{2.11}$$

   If the candidate feature satisfies the above criterion, then it is kept as a candidate absorption line. If the feature fails the significance test, a flag is set indicating 'Line Not Significant'.

5. **Velocity Threshold Check:**

   Once a candidate line is identified, we check to see if the line is located within 500 km s^{-1} from the expected line location based on the emission-line redshift of the galaxy. Typical values for velocities seen in galaxy rotation curves are in the range 200-300 km s^{-1}s (Rubin et al., 1985), while outflow velocities reach up to ∼500 km s^{-1} (Heckman et al., 2000). If the candidate feature lies ≥±500 km s^{-1} from the galaxy's systemic velocity, a flag is set indicating 'Large Velocity Difference'.

6. **Weak Line Doublet Check:**

   Once a candidate feature is identified that passes our significance and velocity thresholds, we then search for the weaker doublet line in the expected region given the galaxy's identified redshift and the predicted separation from the stronger doublet line. We require the weaker line to have a significance consistent with the region allowed from the doublet ratio. If the candidate line fails the significance test, a flag is set indicating 'Weak Line Not Detected'.

7. **Doublet Consistency Check:**

   Lastly, if the weaker doublet line is detected, we perform two checks to ensure the doublet is consistent with a being a 'physical' redshifted doublet. We check that the wavelength of the weaker line is consistent with the predicted location based off the stronger line, and we also check that the doublet ratio (within errors) is consistent with what is expected for Ca II and Na I doublet systems. For optically thin gas, the ratio of the primary and secondary lines of Ca II and Na I is 2:1, while for saturated lines, the doublet ratio approaches 1:1. We use this allowed region to define the acceptable strengths of the weaker, Ca II H line, i.e., the Ca II H line rest equivalent width must be, at least, half as strong as that of the Ca II K line and, at most, equal in strength to that of the Ca II K line. If the doublet fails these conditional checks, a flag is set indicating 'Not Good Doublet', otherwise a flag is set indicating 'Good Doublet'.

2.4 SDSS DR5/6 ABSORBER SAMPLE

After running the automated line finder on our sample of 154 pairs, we find 13 Ca II absorbing systems and 9 Na I absorbing systems that meet our significance and velocity thresholds. Of these systems, 4 were found to have both Ca II and Na I. The Ca II and Na I systems consist of a mix of those flagged as 'Good Doublet' and 'Weak Line Not Detected'.

One drawback with this method of locating lines is that it does not handle closely separated lines, as is the case with the Na I doublet. The line finder typically blends the two lines together as one feature. Due to this, we manually measure equivalent widths (EW) with

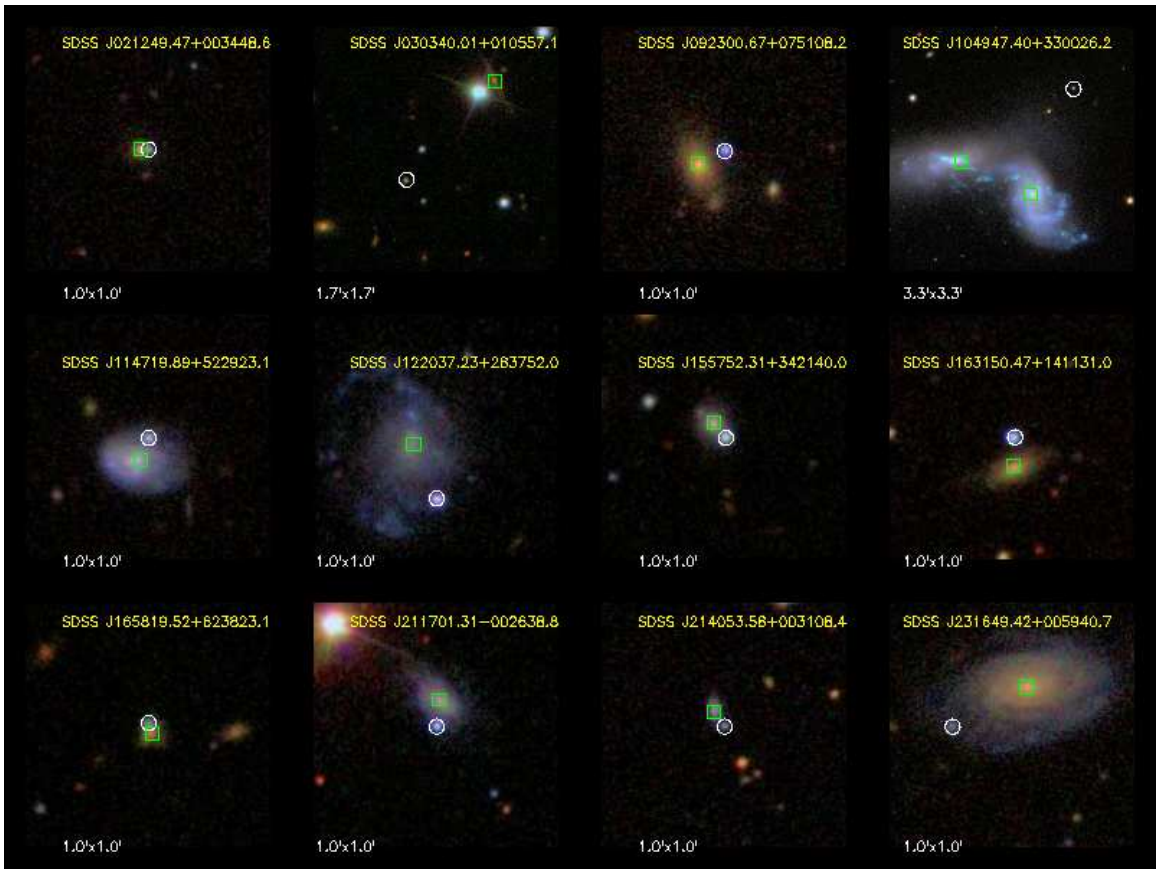

Figure 2.2 Color images of the Ca II absorbers. The white circles indicate the location of the quasar. Green squares indicate the location of the galaxy. The quasar name is shown at the top of each image and the image size is shown at the bottom.

IRAF for all of the Na I and Ca II lines by fitting a Gaussian profile to the line. The two lines of the Ca II doublet were fitted separately while the Na I doublet was deblended into the two components. Comparison of the full width at half maximum (FWHM) as measured from the Gaussian IRAF fitting with the FWHM of the SDSS resolution element indicates that our absorbers are a mix of resolved and unresolved lines. However, as is often the case with absorption lines systems, the resolved lines may actually consist of multiple cloud components. The errors on the EWs consist of errors from the continuum fitting plus errors from the statistical noise fluctuations. The errors due to continuum fitting were calculated by shifting the continuum by a fraction of the noise in the continuum. For the errors due to statistical noise fluctuations, we adopt the formula from Bowen (1991). For undetected lines,

we calculate 3σ upper limits from Bowen (1991), adjusted to include errors in the placement of the continuum. For the undetected Ca II and Na I lines, we adopt a value of 1.0 Å for the intrinsic galaxy FWHM, based on an average value of all the measured weaker doublet lines in our dataset. The measurements from the ISF-weighted linefinder are shown in Tables 2.3 and 2.4, while the measurements from the IRAF Gaussian fitting are shown in Tables 2.5 and 2.6. Table 2.7 lists the doublet ratios for the Ca II and Na I absorbing samples, where applicable. All the doublet ratios are consistent with being physical systems, i.e. a doublet ratio between 1 and 2. Where a doublet ratio could not be calculated, we test whether the upper limit on the second line in the doublet is consistent with the expected equivalent width given that of the first line.

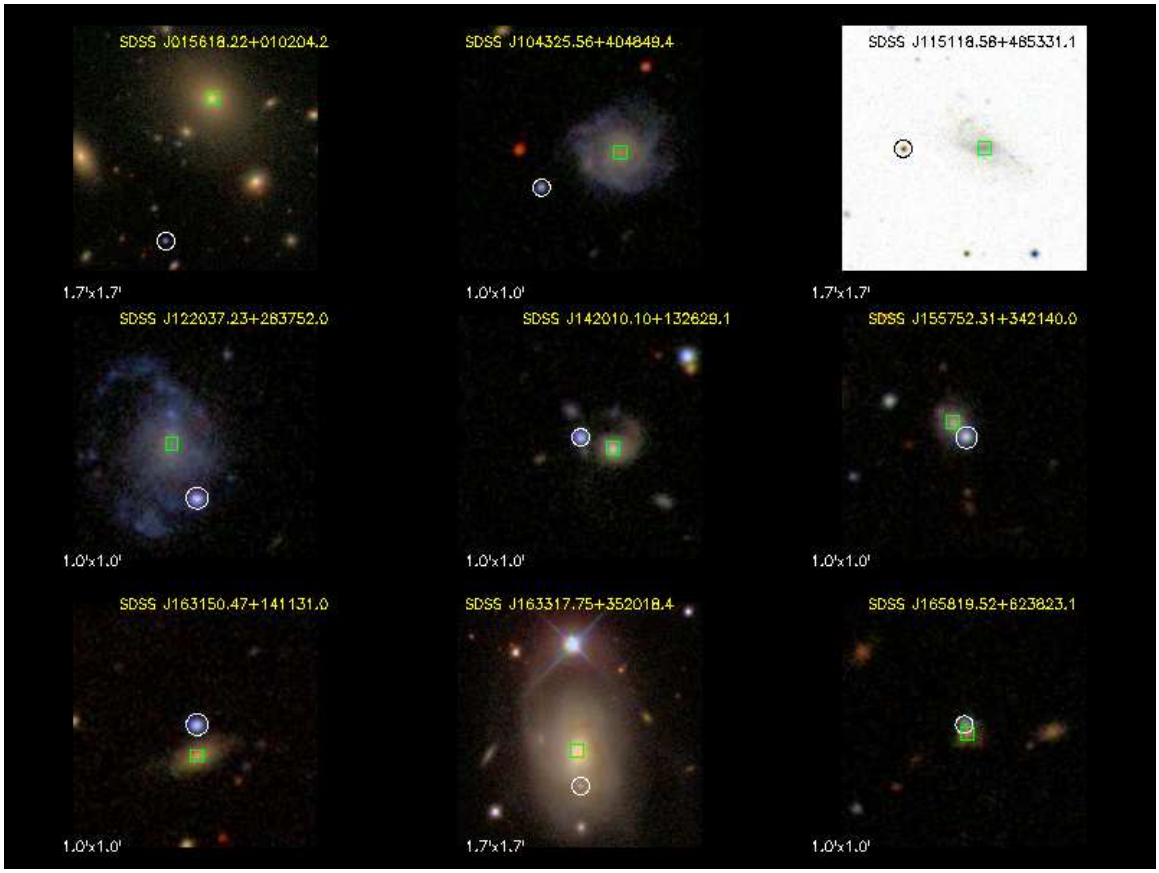

Figure 2.3 Color images of the Na I absorbers. The labeling is the same as in Figure 2.2.

Table 2.3 Line Finder Output of Ca II absorbing systems

Galaxy	z_{SDSS}	rEW[λ3934.77] [Å]	$z_{\lambda1}$	$\Delta\ v_{\lambda1}$ [km s^{-1}]	$SL_{\lambda1}$	rEW[λ3969.59] [Å]	$z_{\lambda2}$	$\Delta\ v_{\lambda2}$ [km s^{-1}]	$SL_{\lambda2}$
SDSS J021249.59+003448.7	0.16380±0.00020	1.3±0.6	0.1634±0.0005	-120±120	2.31	<1.5	–	–	–
SDSS J030337.58+010638.7	0.15595±0.00016	4.1±1.9	0.1551±0.0005	-255±150	2.18	<2.1	–	–	–
SDSS J092301.03+075105.1	0.10388±0.00015	0.42±0.18	0.1040±0.0004	36 ±120	2.32	<0.4	–	–	–
SDSS J104949.75+325903.1	0.00541±0.00001	0.31±0.13	0.0055±0.0004	27 ±120	2.36	<0.3	–	–	–
SDSS J104955.07+325926.9	0.00572±0.00010	0.32±0.13	0.0055±0.0004	-66 ±120	2.46	<0.3	–	–	–
SDSS J114720.19+522918.6	0.04757±0.00008	1.1±0.4	0.0474±0.0005	-51 ±150	2.91	0.9±0.4	0.0471±0.0005	-141±150	2.45
SDSS J122037.63+283803.2	0.02762±0.00011	0.26±0.13	0.0276±0.0003	-6 ± 90	2.01	<0.3	–	–	–
SDSS J155752.51+342142.7	0.11367±0.00006	0.5±0.2	0.1140±0.0004	99 ±120	2.32	0.5±0.2	0.1142±0.0004	159±120	2.04
SDSS J163150.46+141124.6	0.13102±0.00016	0.44±0.18	0.1310±0.0004	-6 ±120	2.40	0.31±0.18	0.1315±0.0004	144±120	1.78
SDSS J165819.50+623821.3	0.28042±0.00018	0.7±0.3	0.2802±0.0006	-66 ±180	2.07	<0.7	–	–	–
SDSS J211701.26-002633.7	0.05792±0.00009	0.9±0.3	0.0580±0.0004	24 ±120	2.99	<0.7	–	–	–
SDSS J214053.72+003111.7	0.10851±0.00009	6.1±2.9	0.1076±0.0006	-273±180	2.13	9.2±9.0	0.1078±0.0006	-213±180	1.02
SDSS J231648.38+005948.8	0.06895±0.00016	1.9±0.9	0.0696±0.0005	195±150	2.25	<1.7	–	–	–

Note. — Upper limits are 3σ upper limits on line equivalent width.

Table 2.4 Line Finder Output of Na I absorbing systems

Galaxy	z_{SDSS}	rEW[λ5891.58] [Å]	$z_{\lambda1}$	Δ $v_{\lambda1}$ [km s^{-1}]	$SL_{\lambda1}$	rEW[λ5897.58] [Å]	$z_{\lambda2}$	Δ $v_{\lambda2}$ [km s^{-1}]	$SL_{\lambda2}$
SDSS J015617.64+010249.2	0.07809±0.00017	1.4±0.6	0.0778±0.0005	-87±150	2.15	<1.5	–	–	–
SDSS J104323.72+404848.9	0.07482±0.00015	6.3±2.2	0.0744±0.0005	-126±150	2.91	<6.8	–	–	–
SDSS J115115.25+485331.0	0.02564±0.00011	1.3±0.6	0.0249±0.0004	-222±120	2.08	<1.3	–	–	–
SDSS J122037.63+283803.2	0.02762±0.00011	1.0±0.2	0.0281±0.0006	144±180	4.06	<0.4	–	–	–
SDSS J142009.64+132626.7	0.14150±0.00020	0.6±0.3	0.1407±0.0004	-246± 90	2.47	<0.6	–	–	–
SDSS J155752.51+342142.7	0.11367±0.00006	0.9±0.3	0.1143±0.0008	189±240	3.15	<0.4	–	–	–
SDSS J163150.46+141124.6	0.13102±0.00016	2.0±0.4	0.1313±0.0007	84±210	4.69	<0.9	–	–	–
SDSS J163317.74+352001.5	0.03454±0.00015	2.4±0.7	0.0342±0.0007	-102±210	3.26	<1.6	–	–	–
SDSS J165819.50+623821.3	0.28042±0.00018	0.8±0.4	0.2797±0.0007	-216±210	2.36	0.4±0.4	0.2808±0.0007	114±210	1.05

Note. — Upper limits are 3σ upper limits on line equivalent width.

With traditional absorption line measurements in which no host galaxy information is known, it is common practice to require multiple ions from one redshift to be present to validate the line's authenticity, or at the very least, to require both lines in a doublet of one particular ion. While we take the line's location at the known galaxy's redshift as one indicator of authenticity, we also assign a quality rating between 0-4 as a measure of the line's authenticity based on the traditional method of absorption line measurements. The last column in Table 2.7 refers to this quality indicator.

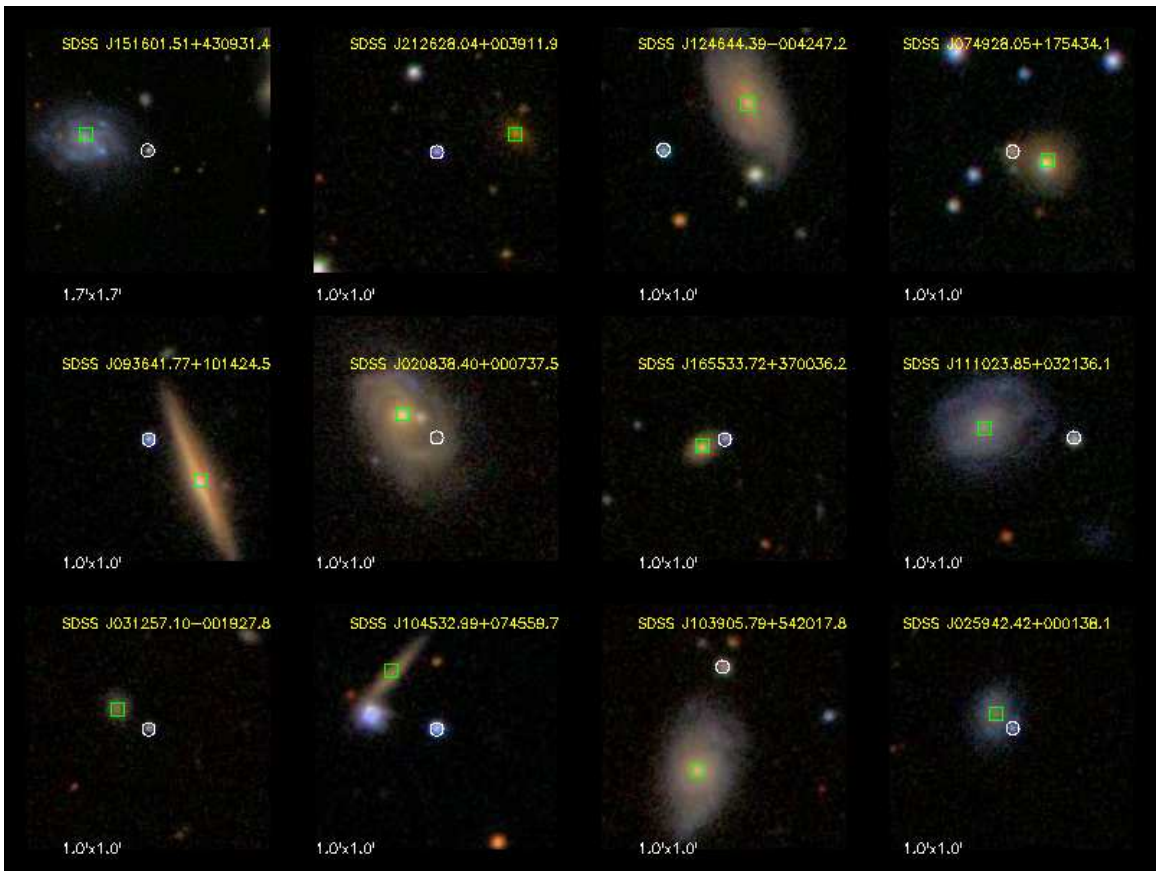

Figure 2.4 Color images for a subset of the non-absorbers (with no Ca II or Na I found by the line finder). The labeling is the same as in Figure 2.2

Table 2.5 IRAF measurements of CaII absorbing galaxies

Galaxy	z_{SDSS}	rEW[λ3934.77] [Å]	$z_{\lambda1}$	$\Delta\ v_{\lambda1}$ [km s^{-1}]	rEW[λ3969.59] [Å]	$z_{\lambda2}$	$\Delta\ v_{\lambda2}$ [km s^{-1}]
SDSS J021249.59+003448.7	0.16390±0.00020	1.4±0.7	0.16336±0.00001	-162±60	<1.7	–	–
SDSS J030337.58+010638.7	0.15595±0.00016	4.2±0.9	0.15515±0.00002	-240±48	<1.2	–	–
SDSS J092301.03+075105.1	0.10387±0.00015	0.44±0.17	0.10397±0.00001	27±45	<0.5	–	–
SDSS J104949.75+325903.1	0.00540±0.00001	0.40±0.12	0.00548±0.00002	21±6	<0.5	–	–
SDSS J104955.07+325926.9	0.00570±0.00010	0.40±0.12	0.00548±0.00002	-72±30	<0.5	–	–
SDSS J114720.19+522918.6	0.04757±0.00008	1.3±0.3	0.04750±0.00020	-21±60	0.4±0.2	0.04739±0.00008	-54±33
SDSS J122037.63+283803.2	0.02760±0.00011	0.3±0.1	0.02768±0.00001	18±33	<0.4	–	–
SDSS J155752.51+342142.7	0.11367±0.00006	0.5±0.2	0.11398±0.00002	93±18	0.5±0.2	0.11399±0.00004	96±21
SDSS J163150.46+141124.6	0.13102±0.00016	0.51±0.13	0.13097±0.00001	-15±48	0.31±0.11	0.13081±0.00001	-63±48
SDSS J165819.50+623821.3	0.28042±0.00018	0.6±0.3	0.28065±0.00001	69±54	<0.7	–	–
SDSS J211701.26-002633.7	0.05792±0.00009	1.0±0.4	0.05802±0.00003	30±27	<1.0	–	–
SDSS J214053.72+003111.7	0.10851±0.00009	6.6±1.2	0.10773±0.00004	-234±30	5.4±3.3	0.10838±0.00008	-39±36
SDSS J231648.38+005948.8	0.06895±0.00016	2.0±0.7	0.06957±0.00005	186±51	<2.0	–	–

Note. — The line equivalent width errors, as well as 3σ upper limits, include statistical error and continuum fitting errors.

Table 2.6 IRAF measurements of NaI absorbing galaxies

Galaxy	z_{SDSS}	rEW[λ5891.58] [Å]	$z_{\lambda1}$	$\Delta\ v_{\lambda1}$ [km s^{-1}]	rEW[λ5897.56] [Å]	$z_{\lambda2}$	$\Delta\ v_{\lambda2}$ [km s^{-1}]
SDSS J015617.64+010249.2	0.07809±0.00017	1.7±0.5	0.07767±0.00002	-126±51	<1.4	–	–
SDSS J104323.72+404848.9	0.07482±0.00015	6.4±1.2	0.07452±0.00001	-90±45	<3.4	–	–
SDSS J115115.25+485331.0	0.02564±0.00011	1.5±0.4	0.02474±0.00001	-270±33	0.8±0.3	0.02466±0.00001	-294±33
SDSS J122037.63+283803.2	0.02762±0.00011	0.91±0.14	0.02769±0.00001	21±33	0.35±0.10	0.02754±0.00002	-24±33
SDSS J142009.64+132626.7	0.14150±0.00020	0.78±0.16	0.14065±0.00002	-255±60	0.46±0.16	0.14064±0.00002	-258±60
SDSS J155752.51+342142.7	0.11367±0.00006	0.6±0.4	0.11386±0.00010	57±36	0.45±0.11	0.11392±0.00010	75±36
SDSS J163150.46+141124.6	0.13102±0.00016	0.8±0.2[a]; 2.4±0.3[b]	0.1312±0.0007	54±216	<2.2	–	–
SDSS J163317.74+352001.5	0.03454±0.00015	2.0±1.0	0.03425±0.00003	-87±46	<0.7	–	–
SDSS J165819.50+623821.3	0.28042±0.00018	0.50±0.17	0.27916±0.00001	-378±54	0.42±0.18	0.27890±0.00001	-456±54
		0.42±0.14	0.28019±0.00001	-69±54	0.4±0.2	0.28007±0.00001	-105±54

Note. — The range of the Na I equivalent width after subtracting out the blended z=1.577 Fe II λ2586.65 line, considering both the a.) optically thin and b.) saturated cases for the Fe II line. See the note on SDSS J163150.46+141124.6 in Section 2.4.1.

Figures 2.2-2.4 show the Ca II and Na I absorbing galaxy-quasar pairs, as well as a sample of pairs where no absorption was identified. Figures 2.5 and 2.6 show the Ca II and Na I absorption lines plotted in velocity space. We describe a few notes on particular Ca II and Na I absorption lines in the following section.

2.4.1 Notes on Individual Absorbers

Here we comment on several absorbers. The IAU names are those of the SDSS galaxies.

- **The Ca II absorbers SDSS J030337.58+010638.7 and SDSS J214053.72+003111.7**
  For both of these absorbers, the observed Ca II line position lies in the Ly-α forest of their respective quasars, adding an additional level of uncertainty to the validity of the lines. For SDSS J0303, the absorber was given a quality rating of 0, due to the sole detection of the strong line of Ca II, and the upper limit on the weaker line is inconsistent with the expected EW from the strong line. This detection could be due to the Ly-α forest at $z \sim 2.7$. The absorber SDSS J2140 was given a quality rating of 2, meaning the full Ca II doublet was detected. The doublet ratio is consistent with being a physical system. This line could be due to the Ly-α forest at $z \sim 2.6$, however since the full Ca II doublet was detected, the chance of two Ly-α forest clouds causing both lines seems unlikely.

- **The Ca II absorber associated with QSO SDSS J104947.40+330026.2**
  For the Ca II feature found in the spectrum of SDSS J104947.40+330026.2, there are two possible galaxy contributors. Examination of the SDSS image shows two low redshift interacting galaxies projected near the quasar. One galaxy, NGC 3395, is at a redshift of 0.00541±0.00001. The other galaxy is NGC 3396, at a redshift of 0.00572±0.00010. We treat this system as two individual galaxy/quasar pairs for all further analysis. Many previously identified Ca II absorbers have been attributed to arising in interactions. One of the absorbers from Womble et al. (1990) was associated with an irregular galaxy while Bergeron et al. (1987); Carilli & van Gorkom (1987); Carilli et al. (1989) suggest that the absorption seen in the galaxies ESO1327-2041,NGC 3067,and Klemola 31 is due to disrupted gas from galaxy interactions.

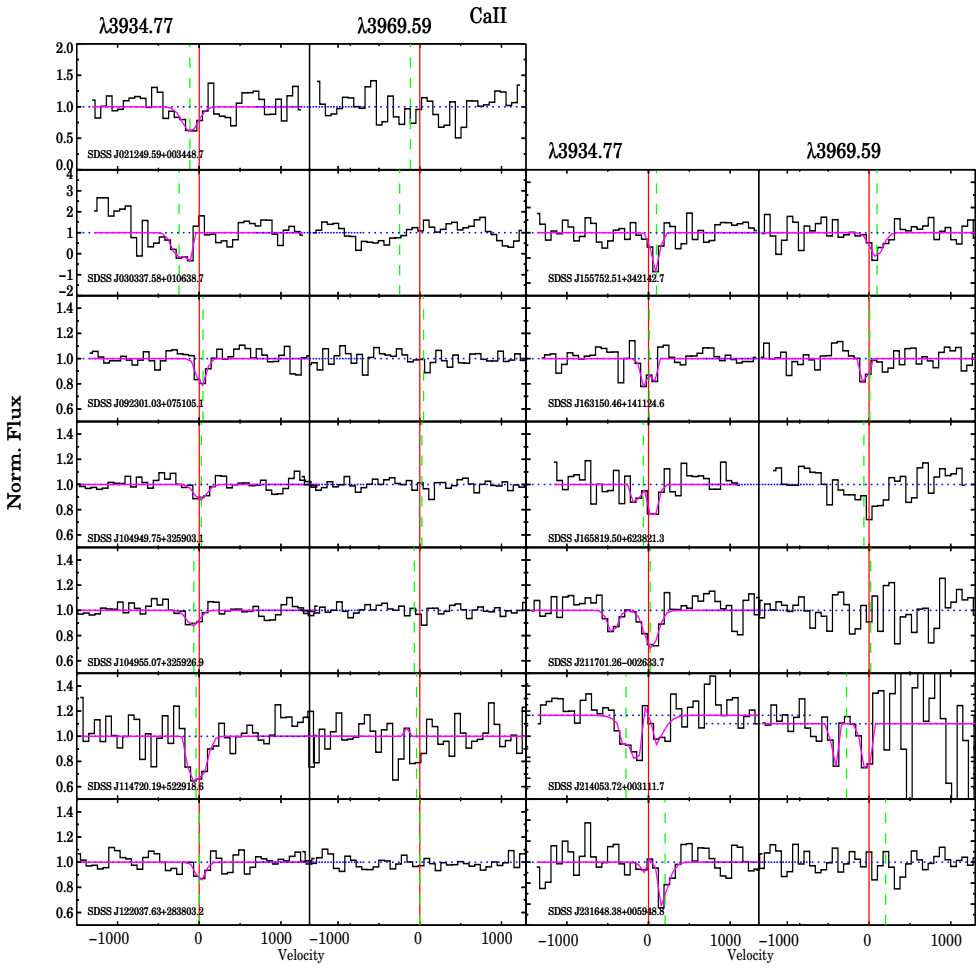

Figure 2.5 Spectral plots for the 3934.77 Å and 3969.59 Å line of the Ca II doublets in our sample. Each spectrum has been normalized to a continuum of 1. The x-axis is in velocity space, centered on the expected line position based on the absorber galaxy redshift, marked with the red vertical line. The green-dashed vertical line marks the position of the Ca II line as found by the ISF-weighted line finder. The magenta line is a multi-component Gaussian fit to the line. The blue-dotted line shows the normalized continuum. For the 3969Å line, spectra with no fit are those in which the line was undetected by the line finder. The galaxy absorber name is displayed in the lower left corner.

- **The z=0.0748 Na I absorber SDSS J104323.72+404848.9**

  The Na I line identified at z = 0.07452±0.00001 lies in an extremely noisy part of the

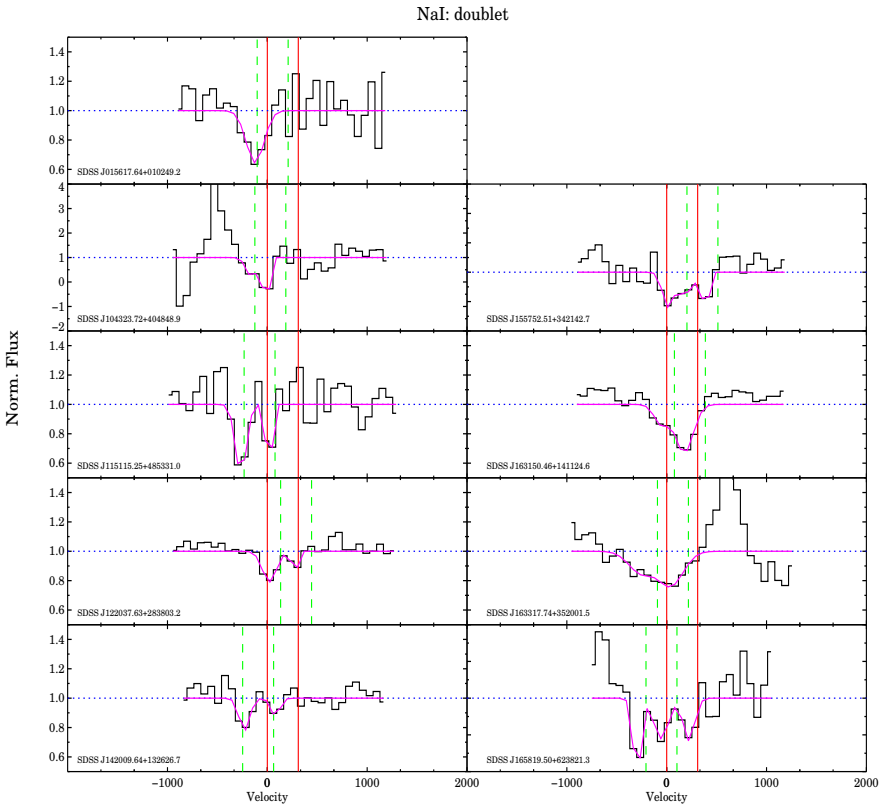

Figure 2.6 Spectral plots for the Na I doublets in our sample. The lines are the same as in Figure 2.5.

QSO spectrum and has received a quality of 1. Examination of the QSO spectrum reveals a very similar feature at 6315Å in similar size and shape to the supposed Na I feature. This additional feature makes the validity of the Na I line suspect, however we include the line in our sample and further analysis as to not introduce any bias in the rejection. It should also be noted that the detected Na I absorption line lies blue-ward of the Ly-α emission line of the quasar. The quasar has a redshift of 4.9.

- **The z=0.02762 Na I absorber SDSS J122037.63+283803.2**

  Upon inspection of the feature in the QSO spectrum, the Na I feature identified by the line finder at z=0.0281±0.0006 is seen to be a blend of the two Na I components situated at the expected absorber redshift. Therefore, we use IRAF to deblend the two lines giving a line redshift and velocity difference between the absorption line and galaxy

Table 2.7 Doublet Ratio Measurements and Line Assessments for the Ca II and Na I Absorbers

Ca II Absorbers						
Galaxy	Doublet Ratio	σ_{DR}	(rEW$_1$-σ_{rEW_1})/2.0	(rEW$_1$+σ_{rEW_1})	rEW$_2$	Quality
SDSS J021249.59+003448.7	–	–	0.4	2.1	<1.7	1
SDSS J030337.58+010638.7	–	–	1.7	5.1	<1.2	0
SDSS J092301.03+075105.1	–	–	0.13	0.6	<0.5	1
SDSS J104949.75+325903.1	–	–	0.13	0.5	<0.5	1
SDSS J104955.07+325926.9	–	–	0.13	0.5	<0.5	1
SDSS J114720.19+522918.6	3.3	2.3	–	–	–	2
SDSS J122037.63+283803.2	–	–	0.10	0.4	<0.4	3
SDSS J155752.51+342142.7	1.0	0.6	–	–	–	4
SDSS J163150.46+141124.6	1.6	0.7	–	–	–	3
SDSS J165819.50+623821.3	–	–	0.15	0.8	<0.7	3
SDSS J211701.26-002633.7	–	–	0.3	1.4	<1.0	1
SDSS J214053.72+003111.7	1.2	0.8	–	–	–	2
SDSS J231648.38+005948.8	–	–	0.6	2.7	<2.0	1
Na I Absorbers						
Galaxy	Doublet Ratio	σ_{DR}	(rEW$_1$-σ_{rEW_1})/2.0	(rEW$_1$+σ_{rEW_1})	rEW$_2$	
SDSS J015617.64+010249.2	–	–	0.6	2.2	<1.4	1
SDSS J104323.72+404848.9	–	–	2.6	7.6	<3.4	1
SDSS J115115.25+485331.0	1.9	0.9	–	–	–	2
SDSS J122037.63+283803.2	2.6	0.8	–	–	–	3
SDSS J142009.64+132626.7	1.7	0.7	–	–	–	2
SDSS J155752.51+342142.7	1.3	1.0	–	–	–	4
SDSS J163150.46+141124.6	–	–	0.3-1.0	1.0-2.7	<2.2	3
SDSS J163317.74+352001.5	–	–	0.5	3.0	<0.7	1
SDSS J165819.50+623821.3	1.19	0.6	–	–	–	2
	1.08	0.7	–	–	–	3

Note. —
Columns 2 & 3 are the doublet ratio and the error on the doublet ratio. They must satisfy the condition DR+σ_{DR} > 1.0 and DR−σ_{DR} < 2.0. If a doublet ratio could not be calculated, columns 4 & 5 assess whether the 3σ upper limit on the 2^{nd} line in the doublet is consistent with the EW of the 1^{st} line. Column 4 is the absolute minimum EW the 2^{nd} line could be given the optically thin limit. Column 5 is the absolute maximum the 2^{nd} line could be given the optically thick limit. Column 6 is the 3σ upper limit on the 2^{nd} line. Column 7 is a quality indicator. A quality of 4 means that the full doublet was detected for both Ca II and Na I. A quality of 3 means that one line was measured in both Ca II and Na I. A quality of 2 means that the full doublet was detected in only one ion, either Ca II or Na I. A quality of 1 means that only one line of one doublet was detected and the upper limit on the 2^{nd} line is consistent with being within the range of values given by the equivalent width of the first line. A quality of 0 means that only one line of one doublet was detected and the upper limit on the 2^{nd} line is not consistent with the range of values given by the first line. The bold-faced galaxies are those in which both the Ca II and Na I was detected.

systemic redshift of z=0.02769±0.00001, Δv=21±33 km s^{-1}, and z=0.02754±0.00002, Δv=-24±33 km s^{-1} for the primary and secondary Na I lines, respectively.

- **The z=0.11367 Na I absorber SDSS J155752.51+342142.7**

  As with SDSS J122037.63+283803.2, examination of the Na I line identified by the line finder revealed it to be a blend of both lines in the actual Na I doublet, located at the expected absorber postion. We again use IRAF to deblend the lines, giving z = 0.11386±0.00010, Δv=57±36 km s^{-1}, and z=0.11392±0.00010, Δv=75±36 km s^{-1}, for the primary and secondary line, respectively.

- **The z=0.13102 Na I absorber SDSS J163150.46+141124.6**

  The Na I line identified at z = 0.1313±0.0007 is actually blended with the Fe II λ2586.65 component of the Fe II $\lambda\lambda$2586.65,2600.17 doublet from an absorbing system located at z = 1.577. The Na I doublet and Fe II λ2586.65 line lie at 6666.18 Å while the Fe II λ2600.17 lies at 6701.73 Å. The observed equivalent widths of the Na I+Fe II λ2586 blend and the Fe II λ2600 lines are 3.01±0.3 Å, and 2.22±0.16 Å, respectively. To estimate the equivalent width of the Na I doublet, we subtract out the component of the equivalent width due to the Fe II λ2586.65 line. The Fe II λ2600.17 line is the stronger line in the doublet with an oscillator strength of 0.224. The oscillator strength of the Fe II λ2586.65 line is 0.065. We use the ratio of $\frac{\lambda_1^2 f_1}{\lambda_2^2 f_2}$ to estimate the equivalent width of the Fe II λ2586.65 line (Churchill, 2009).

  We consider two cases for the strength of the Fe II λ2586.65 line, one in the ideal optically thin limit, with $\frac{\lambda_1^2 f_1}{\lambda_2^2 f_2} = 0.287169$, and the saturated case with $\frac{\lambda_1^2 f_1}{\lambda_2^2 f_2} = 1$. The subscripts 1 and 2 here refer to the λ2586.65, and λ2600.17 lines, respectively. For each case, we estimate the expected equivalent width of the Fe II λ2586.65 line using $EW_1 = \frac{\lambda_1^2 f_1}{\lambda_2^2 f_2}\, EW_2$. In the optically thin case, we derive an $EW_{\lambda 2586.65} = 0.64\pm0.05$ Å. For the saturated case, we derive an $EW_{\lambda 2586.65} = 2.22\pm0.16$ Å. This gives an equivalent width for the Na I doublet of 0.79±0.14 Å in the optically thin case and 2.37±0.3 Å in the saturated case. We report these values in Table 2.6.

- **The z=0.0345 Na I absorber SDSS J163317.74+352001.5**

  For the Na I line identified by the line finder at z = 0.0342±0.007, we find, after visual inspection, that the line is located near the [O III] λ4959 emission line from the quasar,

located at 6107 Å. The Na I feature is significant compared to the noise in the continuum and there does not appear to be any absorption associated with the [O III] line. The second line in the doublet is not detected but it is within the expected range of EW's from the first line. However, given the large EW of the Na I line and the expected positions of the doublet lines seen in Figure 2.6, it is possible that the Na I lines are blended. Another possibility is that there are multiple components along the sightline that, due to the low resolution of the SDSS, are blended into one broad feature.

- **The z=0.28042 Na I absorber SDSS J165819.50+623821.3**

  Examination of the Na I features in the QSO spectrum reveals three possible lines of Na I, two of which are at the expected absorber redshift, and a third located at shorter wavelengths from the other two, at z=0.27916±0.00001. The line finder identified a blend of the first two lines seen in the spectrum as the primary Na I line, thus we use IRAF to deblend the lines and consider two possible doublets for this system, one consisting of the first and second lines, and another consisting of the second and third lines. Measurements for both doublets are listed in Table 2.6. For the first doublet, the primary Na I line is located at z=0.27916±0.00001 and has a velocity offset from the expected absorber position of -378±54 km s^{-1} while the secondary line is located at z=0.27890±0.00001 with Δv = -456±54 km s^{-1}. The second possible doublet is located closer to the expected absorber position, with the primary line at z=0.28019±0.00001, Δv = -69±54 km s^{-1}, and the secondary line at z=0.28007±0.00001, and Δv = -105±54 km s^{-1}.

2.5 ABSORBER ANALYSIS

We briefly present a summary of the properties of our sample with details of the analysis presented below. Our sample of 154 galaxy/quasar pairs consists of roughly ∼60% spectroscopically identified late-type disk galaxies and ∼40% spectroscopically identified early-types. The median impact parameter between the galaxy and quasar at z_{gal} is 17±11 kpc. The galaxies in the sample have a mean redshift of (μ,σ)=(0.12,0.09). The mean B-band absolute magnitude is (μ,σ)=(-19.4,1.4). The mean B-band luminosity in units of L_B^* is

(μ,σ)=(0.6,0.5) L_B^*. The mean inclination is (μ,σ)=(50°,16°), and mean rest-frame $g-r$ color (shifted to $z \sim 0.1$) is (μ,σ)=(0.8,0.3). σ here refers to the 1σ standard deviation in the distribution.

2.5.1 Optical Properties

Basic optical properties were calculated for our galaxy sample (in the standard ΛCDM cosmology). Absolute SDSS magnitudes and luminosities were calculated from the SDSS g and r photometry for each galaxy, corrected for galactic extinction (Schlegel et al., 1998), and k-corrected using Blanton's **kcorrect v4.32** (Blanton & Roweis, 2007). We do not correct for internal extinction. The $g-r$ colors have been band-shifted to rest-frame colors at $z = 0.1$. The Johnson-Morgan-Cousins absolute B-band magnitude and luminosity were also calculated for each galaxy using the Smith et al. (2002) transformation laws. Table B2 lists the SDSS g and r apparent magnitudes, along with the absolute B-band magnitude and the B-band luminosity in L^*, using M_B^*=-20.9 from Marinoni et al. (1999).

To better understand how quasar absorbers relate to galaxy structure and the environments in which they reside, it is necessary to have a more detailed galaxy classification than the standard red/blue separation. Therefore, we have performed a manual spectroscopic and a combined photometric/morphological classification on our galaxy sample. The spectroscopic classification was done by comparing the galaxy's spectrum to a sample of nearby (z=0.0004-0.03) galaxy spectra (Kennicutt, 1992) and assigning a class that best matches the observed spectrum. Kennicutt (1992) constructed a spectral atlas of nearby galaxies of low-to-high spectral resolution which had also been previously photometrically identified. Errors in the spectroscopic classification arise from the ambiguity in the visual identification of the galaxy spectra when it doesn't match a specific spectral class. The photometric/morphological classification uses a visual classification of morphology from Sandage & Bedke (1988) and NED combined with the photometric calibrators of $u-r$ color and concentration index in the r and i bands as rough indicators of morphology (Park & Choi, 2005). Errors in the photometric/morphological classification are again in the visual classification of morphology. For both classification schemes, if a galaxy type was

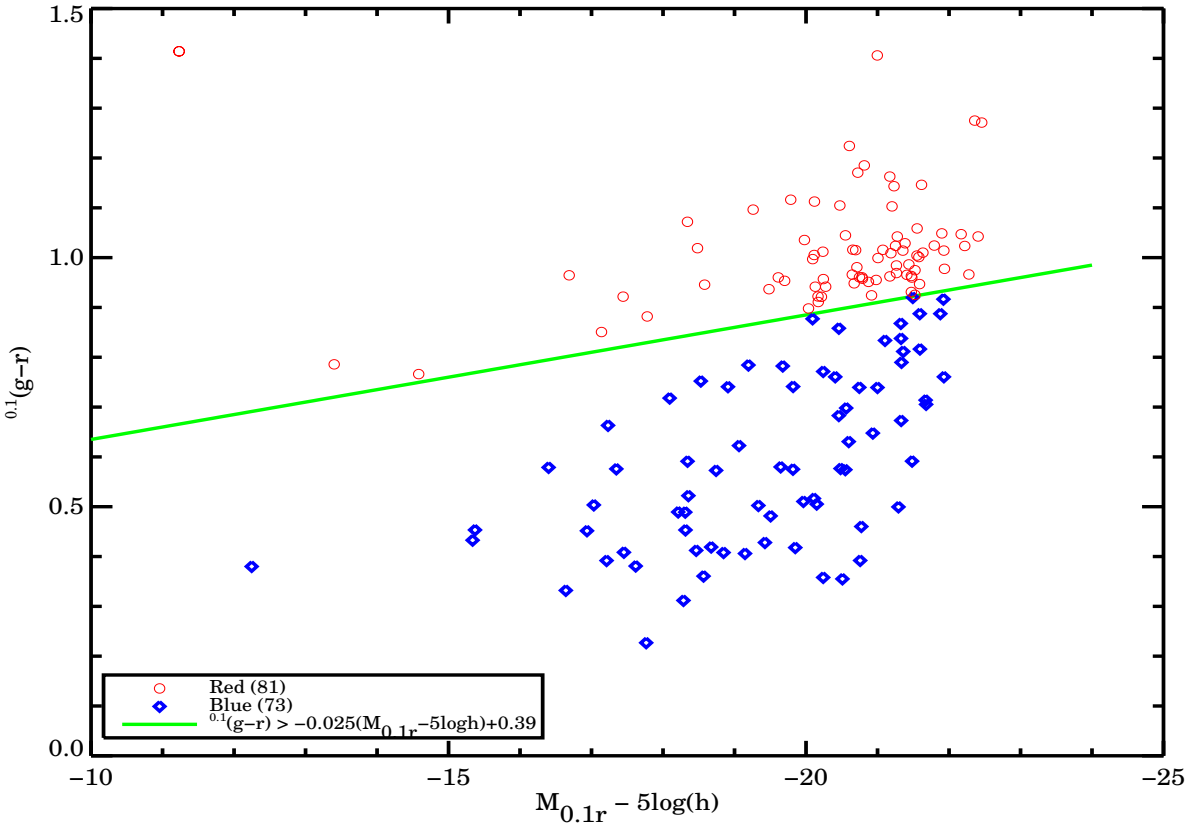

Figure 2.7 Plot of the $g - r$ color against SDSS r-band absolute magnitude. The green line corresponds to the average of the red and blue galaxy cutoffs of Yan et al. (2006). Applying the cuts divides our sample into 81 red galaxies, and 73 blue galaxies.

ambiguous between one type and the next (e.g. Sa and Sb), it was placed in the intermediate category (e.g. Sab). Spectra that could not be classified were labeled as Unknown. We also split our sample into a sample of red and blue galaxies based on the observed bimodality of galaxies in color space (Strateva et al., 2001; Blanton et al., 2003b). Figure 1 of Yan et al. (2006) shows this split for all spectroscopic SDSS galaxies between z of 0.05 and 0.1. We adopt a similar cutoff to Yan et al. (2006) in separating our galaxies into red and blue samples. Figure 2.7 shows a similar plot to Figure 1 of Yan et al. (2006) with our sample. Our sample splits into 81 red galaxies and 73 blue galaxies. Table B2 lists the assigned type class for both classification schemes for each galaxy as well as the Red/Blue color classification from Yan et al. (2006). Figures 2.8 and 2.9 show histograms of the two classification schemes with the red/blue sample split overplotted on top. From the figures, one can see that our classification schemes are in agreement with the more established red/blue split. Table 2.9 lists the percentage breakdown by type. From the spectroscopic classification, the galaxies in our sample mainly consist of Sa and Sc-type spirals with a large contribution of E/S0's as well.

Table 2.8 Galaxy Properties for Final Sample

Galaxy	z_{gal}	g^a	r^a	M_B	L_B $[L^*]$	SpecType	MorphType	Color
SDSS J000508.89+002610.6	0.08451±0.00015	18.237± 0.012	17.122± 0.007	-18.77± 0.05	0.14± 0.01	0.5	0.5	Red
SDSS J000512.73+000805.3	0.26340±0.00015	19.225± 0.026	17.819± 0.012	-21.41± 0.13	1.59± 0.19	2.0	0.5	Red
SDSS J001233.41+010014.2	0.08543±0.00009	19.629± 0.034	18.979± 0.022	-17.65± 0.08	0.05± 0.00	4.0	3.0	Blue
SDSS J003339.85-005522.3	0.21242±0.00010	19.354± 0.036	18.730± 0.025	-20.49± 0.09	0.69± 0.06	4.0	4.0	Blue
SDSS J004316.15+001035.6	0.14352±0.00017	17.840± 0.009	16.744± 0.006	-20.73± 0.04	0.86± 0.04	0.5	0.5	Red
SDSS J004515.67-011317.8	0.10551±7.38242	17.616± 0.015	17.335± 0.013	-20.42± 0.05	0.64± 0.03	4.0	4.0	Blue

Note. —
List of the galaxy optical properties in the final sample of 154 pairs. Each galaxy lists the redshift, g and r-band Sloan apparent magnitudes, B-band absolute magnitude, the B-band luminosity in units of L^*, our spectroscopic and morphological classification, and the assigned color based on the cut of Yan et al. (2006). The full catalog is available in the Appendix B.
a - galaxy magnitude corrected for Galactic extinction

2.5.2 Comparison and Robustness Tests

There remained with us a concern that the automated line finder did not exceed a 3σ detection for any of the Ca II systems. We therefore further tested the validity of the lines found by the ISF-weighted line finder in two ways: a bootstrap test on our sample with synthetic spectra, and a line significance level (SL) comparison test with a sample of Ca II absorbers from Wild & Hewett (2005b); Wild et al. (2006a).

1. **Monte Carlo Test**

   The aim of this test was to assess the probability that the lines found by the line finder are real or due to a random noise spike. To carry out this test, we performed a bootstrap test on the entire 154 quasar spectra. For each quasar spectrum, we produce 10,000 random realizations of that spectrum, generated by randomly sampling a new flux value, at each pixel, from a Gaussian distribution taking the original flux and flux error values as the mean and standard deviation, respectively. On each realized spectrum, we ran the ISF-weighted line finder over the same region as in the original, recording the significances of all lines found above 1σ. For each spectrum, we then examine the resulting distribution of line significances and compare with what is expected by chance, from a standard Gaussian distribution. If the ratio of the number of 2σ detections to 1σ detections in the distribution exceeds 0.15625, the ratio expected by chance, then the line found by the line finder can be statistically ruled out as being due to a random noise spike. The results of the test, seen in Figure 2.11, show that the Ca II and Na I samples are statistically consistent with being real lines.

2. **Comparison to the Samples of Wild & Hewett (2005b) and Wild et al. (2006a)**

   To test if the measurements from the line finder we adopt are consistent with other Ca II samples, we test the line finder on a sample of high-redshift ($0.84<z<1.3$) Ca II absorbers from Wild & Hewett (2005b) and Wild et al. (2006a), referred to here as the "Wild" sample. The Wild Ca II absorbers were found using a matched-filter approach (Hewett, P. C. et al., 1985). The matched-filter approach first creates a difference spectrum between the original spectrum and a filtered version. The difference spectrum is then iteratively stepped through with a template Gaussian doublet constructed to match

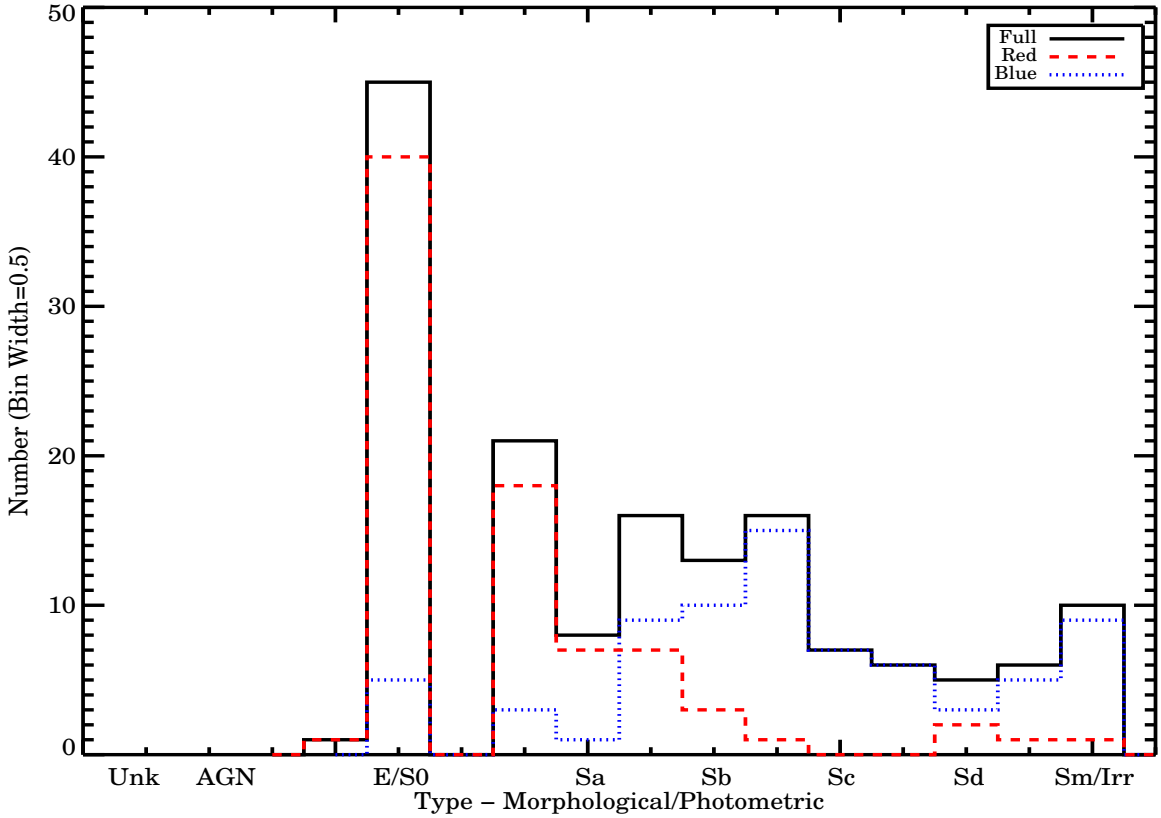

Figure 2.8 Histogram of galaxy type determined from the Photometric/Morphological classification scheme. The black line is the full sample of 154 galaxies. The red-dashed and blue-dotted histograms are the type distributions of the red and blue sample defined via the g-r color separation in Figure 2.7.

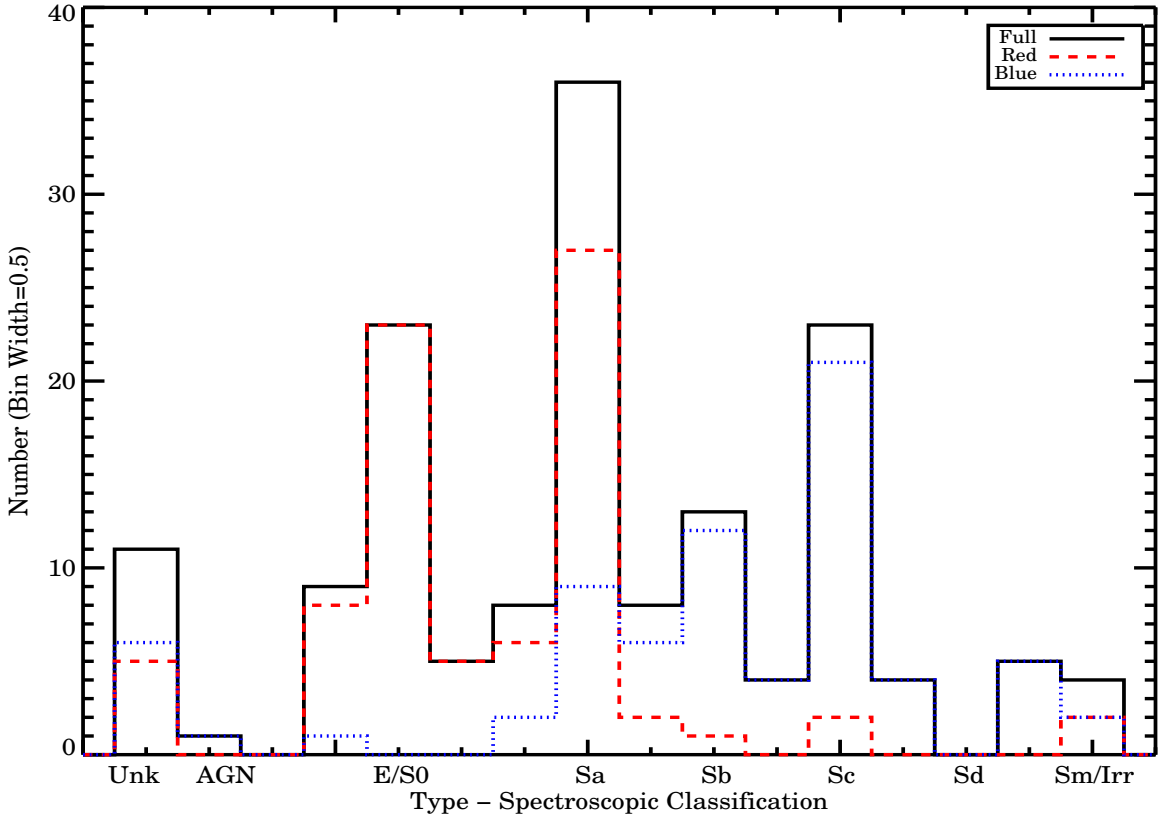

Figure 2.9 Histogram of galaxy type determined from the Spectroscopic classification scheme. The black line is the full sample of 154 galaxies. The red-dashed and blue-dotted histograms are the type distributions of the red and blue sample defined via the $g - r$ color separation in Figure 2.7.

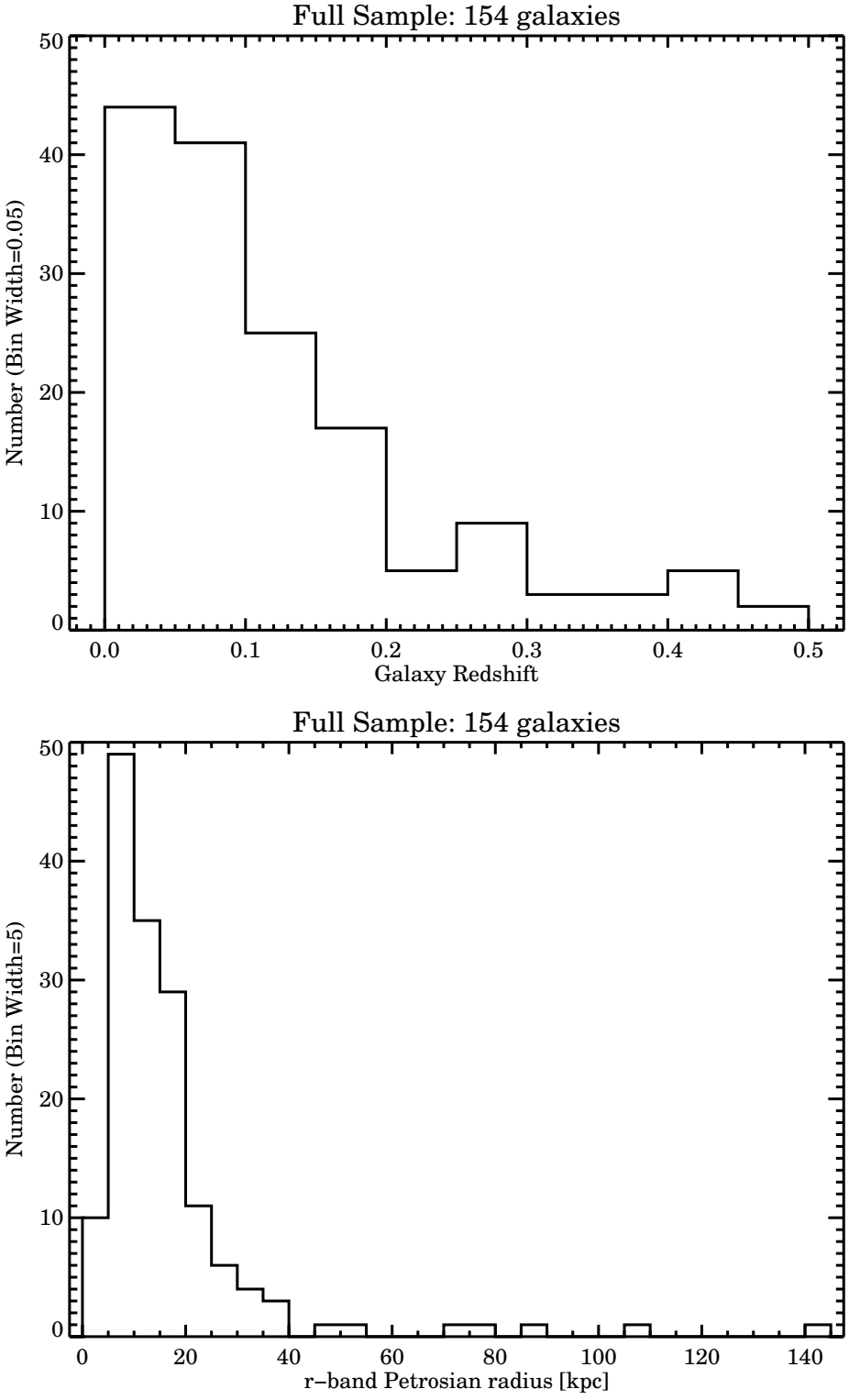

Figure 2.10 Distributions of galaxy redshift and r-band Petrosian radii for all 154 galaxies in the sample.

Table 2.9 Classification Breakdown

Type	Photometric/Morphological (154)	Spectroscopic (154)
Unknown	–	7.1% (11)
AGN	–	0.6% (1)
E	0.6% (1)	5.8% (9)
E/S0	29.2% (45)	14.9% (23)
S0	0.0% (0)	3.2% (5)
S0/Sa	13.6% (21)	5.2% (8)
Sa	5.2% (8)	23.4% (36)
Sa/Sb	10.4% (16)	5.2% (8)
Sb	8.4% (13)	8.4% (13)
Sb/Sc	10.4% (16)	2.6% (4)
Sc	4.5% (7)	14.9% (23)
Sc/Sd	3.9% (6)	2.6% (4)
Sd	3.2% (5)	0.0% (0)
Sd/Sm	3.9% (6)	3.2% (5)
Sm/Irr	6.5% (10)	2.6% (4)

Note. — Percentage breakdown of both galaxy classification schemes according to type. The number of galaxies in each bin is given in parantheses.

a Ca II doublet with a doublet ratio of 2:1 or 1:1 and the appropriate wavelength separation. They cross-correlate the template with the difference spectrum and the highest correlation results in a found doublet. They also required the Ca II systems to have a corresponding Mg II $\lambda\lambda$2796.35,2803.53 doublet. Equivalent widths and errors were then calculated from the fit parameters of a Gaussian fit using a maximum-likelihood routine. The significances of their Ca II lines, as calculated from their equivalent width and error measurements reported in Table 1 of Wild & Hewett (2005b), range from 2-10.

In order to compare the significances of our Ca II lines with theirs, we need to determine their Ca II line significances as measured by our line finder. Therefore we ran the ISF-weighted line finder on their sample and recorded the significance of each line as measured by the line finder. The line finder found all of the Ca II lines from the Wild sample but measured lower significances (1.5<SL<5) than those reported by Wild & Hewett (2005b). These significances are not inconsistent with those that we measure for our Ca II absorbers. The top plot of Figure 2.12 compares the SL output from the ISF-weighted line finder for the two samples. The two distributions are consistent with one

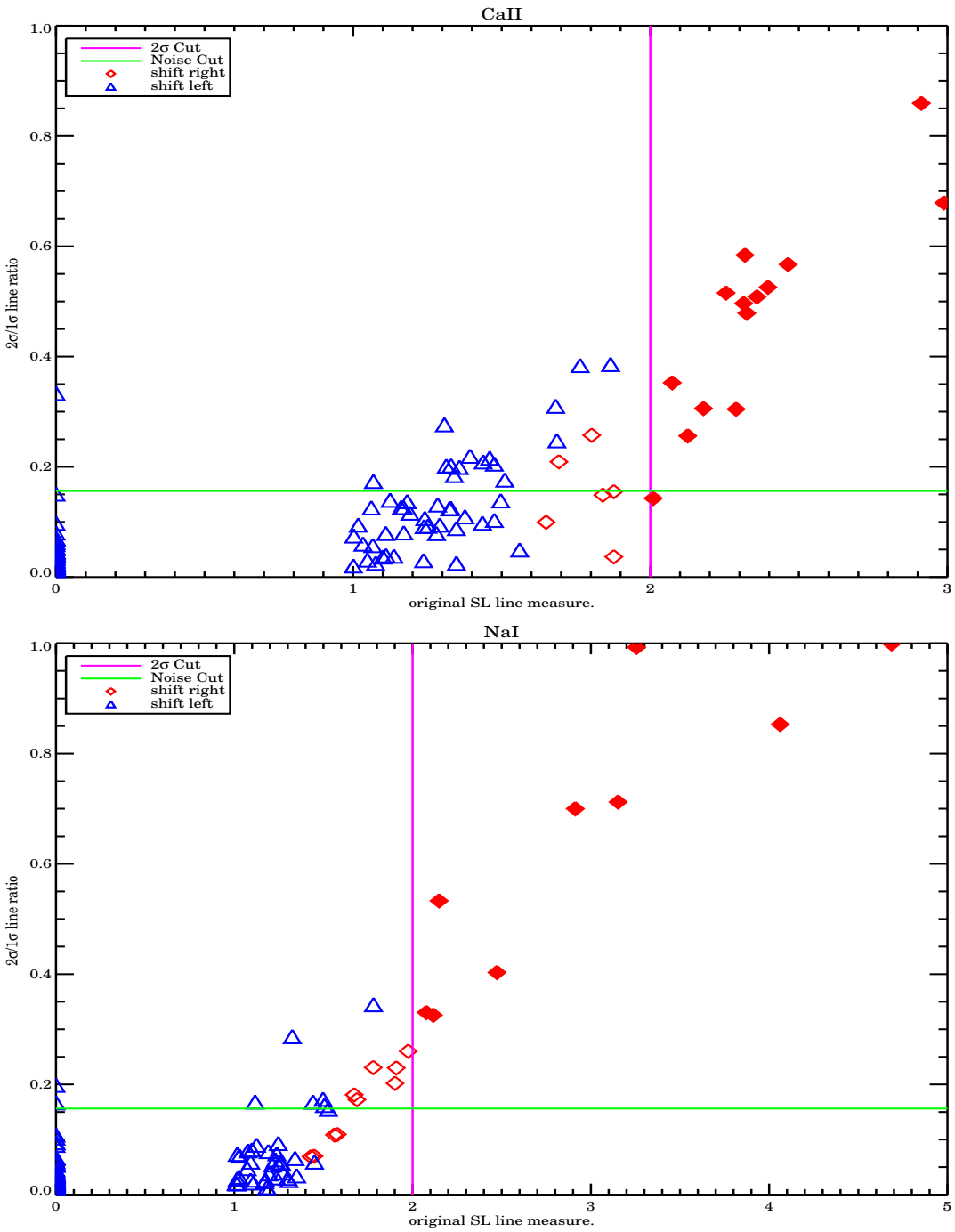

Figure 2.11 Ratio of the number of 2σ to 1σ events against the original line significance level(SL) measurement for each spectrum in the sample of 154 pairs. The Y-axis gives the ratio of the number of 2σ line detections to 1σ line detections from the distribution of randomly-realized spectra. The X-axis gives the line significance level as originally measured by the ISF-weighted line finder on the true spectrum. The region at and below the horizontal green is the region excluded by chance, the cutoff at 0.15625, the $\frac{2\sigma}{1\sigma}$ ratio for a standard Gaussian. The vertial magenta line is our 2σ cutoff for each sample. The red diamonds represent where the original SL measurement is located to the right of the mean of the simulated distribution while blue triangles represent a shift to the left of the mean. The filled red are the Ca II and Na I absorption lines.

another. Their distribution extends more to the tails due to a larger sample size and being located systematically at higher redshifts, and thus in a cleaner part of the SDSS spectrum than our Ca II sample. Our Ca II sample does not include any absorbers with a SL < 2.0, as we cut off the search at the 2σ level, indicated by the vertical magenta line.

As the line significances for the Wild sample are calculated from reported measurements determined by a Gaussian fit, it perhaps makes more sense to compare SL measurements calculated in a similar manner. We therefore remeasured the equivalent widths of the Wild sample using the same IRAF techniques that we used in our measurements and again compared the two SL distributions. The bottom plot of Figure 2.12 shows the two distributions. The two distributions are in good agreement with each other, with similar means and spreads. For comparison, we also plot the distribution of SL values of the Wild Ca II sample, calculated using the values given in Table 1 of Wild & Hewett (2005b). We find that both our Ca II SL distribution and our measured SL's of the Wild sample are in good agreement with the calculated Wild SL distribution. We assume that the difference in heights between the two Wild distributions reflect the differences between the two methods for Gaussian fitting. The differences in heights and spread between our Ca II sample and the Wild sample are from low statistics and our applied 2σ cutoff.

Thus we conclude from this test that the Ca II lines found by the ISF-weighted line finder that make up our sample and the measurements it reports are consistent with measurements returned by the line finder made on Ca II samples from the literature. The results returned by the IRAF measurements for our Ca II sample are also consistent with similar IRAF measurements made Ca II samples from the literature.

2.6 DISCUSSION

Here we discuss results on the Ca II and Na I sample when compared with the nonabsorbers in the galaxy/quasar sample. For each absorber sample, we compare to the respective

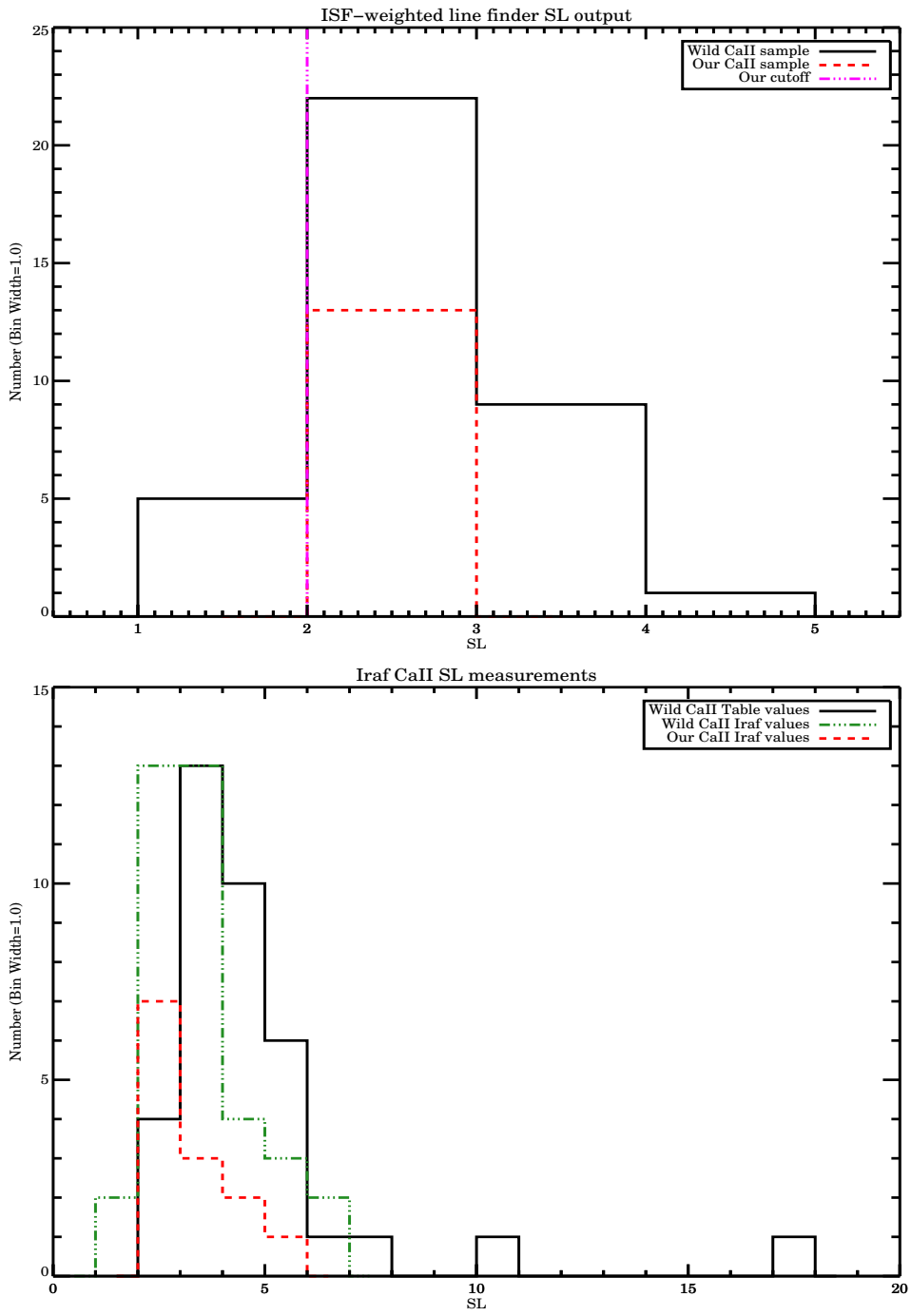

Figure 2.12 Comparison of Ca II line significance levels between our sample and that of Wild & Hewett (2005b); Wild et al. (2006a). The top plot shows the SL distributions from the ISF-weighted line finder and the bottom plot shows the SL distributions as calculated from the IRAF Gaussian fitting. The black histogram is the Ca II sample from Wild & Hewett (2005b). The red-dashed histogram is our Ca II sample. The magenta-dashed-dot line represents our 2σ cutoff applied in our search algorithm. In the bottom plot, black represents the SL values calculated from Table 1 in Wild & Hewett (2005b), while green-dashed-dot represents the SL values of Wild's Ca II sample as measured by our Gaussian fitting. Red-dashed again represents the SL values of our Ca II sample, measured via a Gaussian fit.

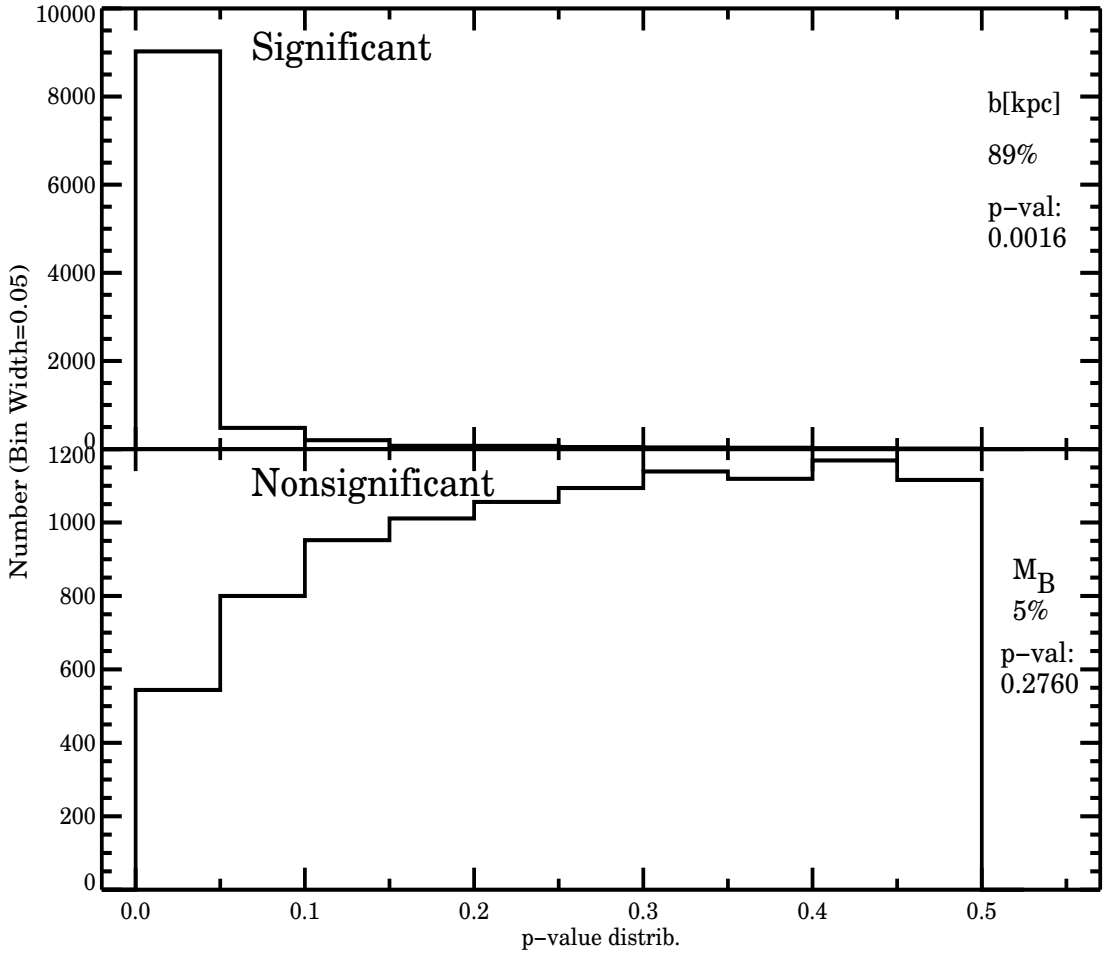

Figure 2.13 The p-value distributions of impact parameter and B-band absolute magnitude for the Ca II absorbers, indicating a significant or "Not Drawn" (top) and non-significant or "Drawn" (bottom) difference between the Ca II subsample and the non-Ca II absorber sample of galaxy/quasar pairs. The percentages listed indicate the percentage of p-values less than 0.05. If 50% or more of the p-values lie below 0.05, then the samples are significantly different at the 95% confidence level. Each panel also lists the median p-value for that distribution.

galaxy/quasar pairs where no absorption was found from that ion. For all galaxy properties, we test for any statistically significant differences between the two distributions. We perform a Mann-Whitney U test, which tests for significant differences in the means of two distributions. The U test is a nonparametric test that is fairly robust, has relatively high power, does not rely on a particular binning of the data, and works well down for small sample sizes.

To assess the range of p-values returned by the U test, we bootstrap both samples 10,000 times and run the statistical test on all realizations. Examination of the resulting distribution of p-values, as well as the median p-value returned, yields information on the validity of the p-value. If the median p-value is below 0.05, and 50% of the p-values in the distribution are below 0.05, then the median p-value returned can be trusted and the absorber distribution is significantly different at the 95% confidence level. Figure 2.13 shows two examples of the p-value distributions, for the Ca II impact parameter and B-band absolute magnitude, indicating the difference between a significant and non-significant result. Figures 2.14-2.17 compare the distributions of the Ca II and Na I samples with the sample of non-absorbing pairs for a variety of galaxy properties. The absorber properties shown to be significantly different than the nonabsorber sample at the 95% confidence level, and thus not drawn from the same population, are labeled as "Not Drawn", while the absorber properties shown not to be significantly different from the nonabsorber sample are labeled as "Drawn".

For fourteen galaxy/quasars pairs, the observed Ca II or Na I wavelengths lie in the Ly-α forest of the associated quasars, with two detections of Ca II absorption and one of Na I (see Section 2.4.1). To assess whether the inclusion of these pairs in our statistical analysis affects the results by contaminating the absorber and nonabsorber samples, we removed them from the sample and reran the analysis. We find that there is no significant difference in the results of the analysis.

2.6.1 Ca II Absorbers

For the Ca II absorbers, the results of the U test show that the two distributions are significantly different for impact parameter, the ratio of impact parameter to r-band Petrosian

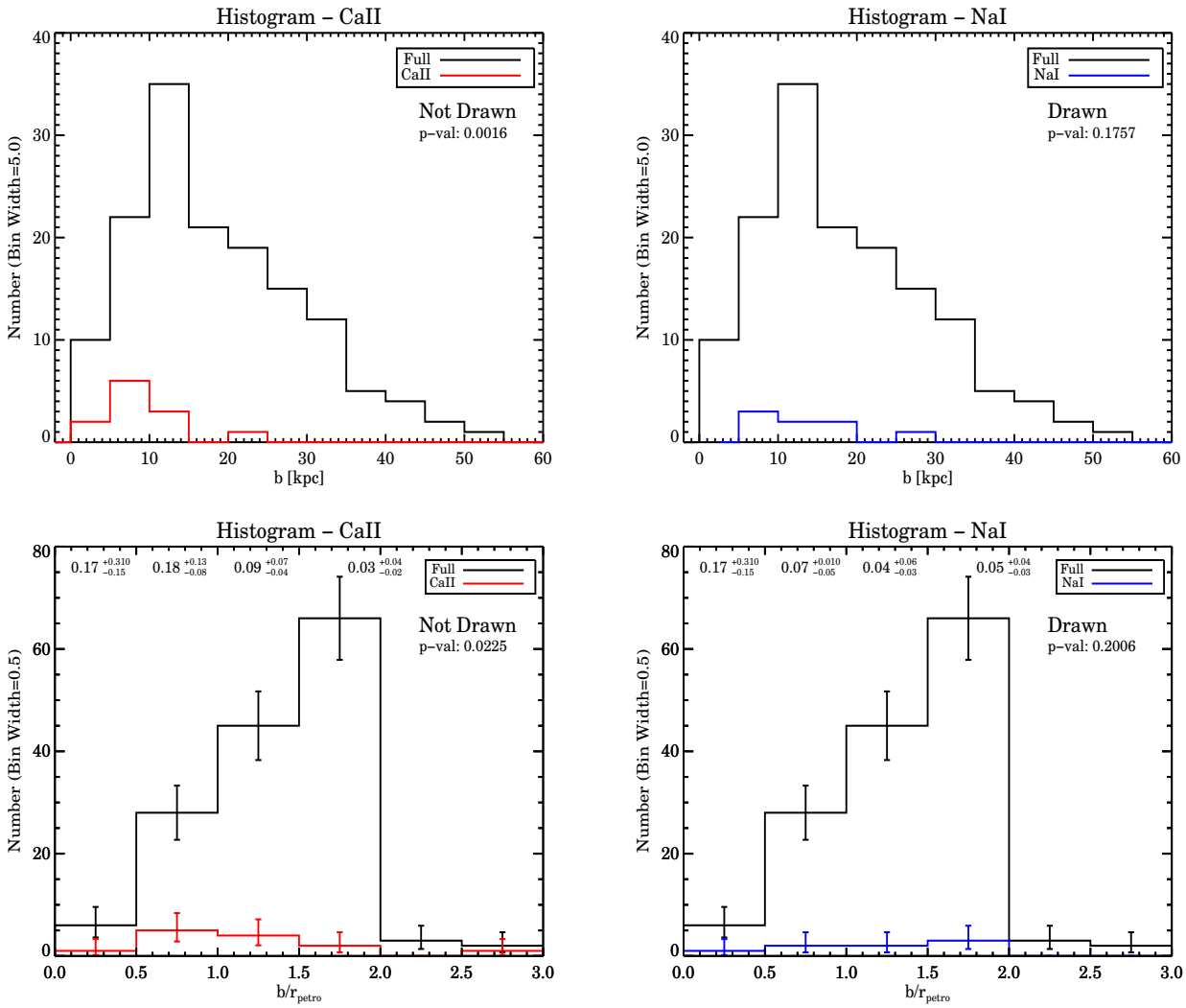

Figure 2.14 Distributions of impact parameter in kpc and the ratio of impact parameter to r-band Petrosian radius for the Ca II (left) and Na I (right) samples, respectively. The histograms have been cut off at b=60 kpc and a $b/r_{\rm Petro}$=3 for illustrative purposes. For the impact parameter distributions, there is one absorber off the scale of the plot for both Ca II and Na I. All the plots also indicate whether the absorber subsample is drawn from the overall sample of galaxies with "Drawn" or "Not Drawn". "Not Drawn" indicates a significant difference between the two samples.

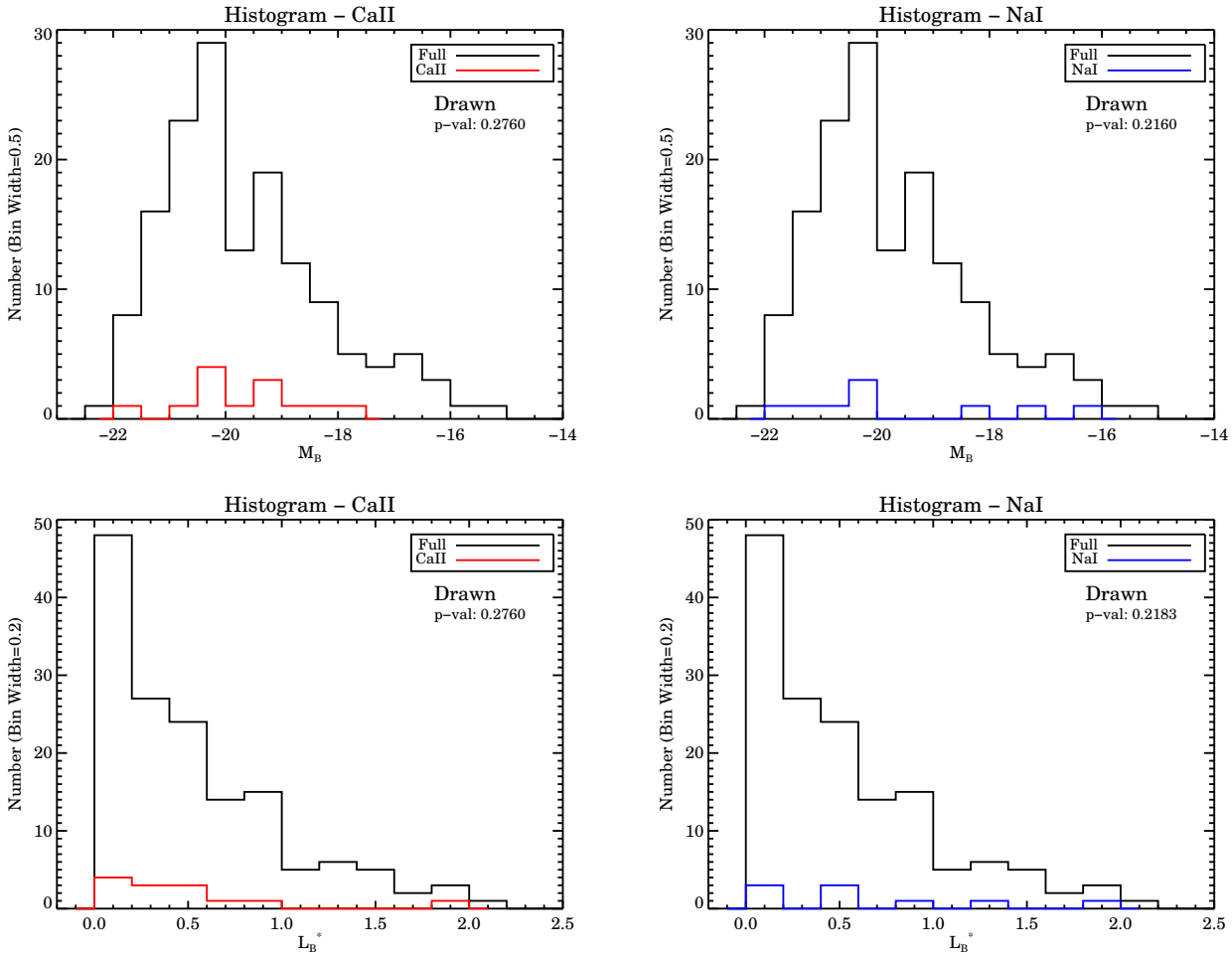

Figure 2.15 Distributions of B-band absolute magnitude and B-band luminosity in units of L_B^* for the Ca II (left) and Na I (right) samples, respectively.

radius, rest-frame $g-r$ color, and the morphological classification. The distributions for absolute B-band magnitude, L_B^* luminosity, inclination, and the spectroscopic classification were shown to not be significantly different between the two samples. These results give us some insight in to how the Ca II galaxy/quasar pairs relate to the overall sample. Figure 2.14 shows the distributions for impact parameter and $b/r_{\rm Petro}$ ratio. We find that the Ca II absorbers are located closer to the host galaxy compared to the non-absorbers, with the fraction of Ca II absorbers decreasing with increasing distance from the host galaxy. The median impact parameter is 7.7±4.6 kpc. This is similar to the impact parameters found by Womble (1993) (16±4 kpc)[2] and Zych et al. (2007) (7.0±8.4 kpc)[3]. Hewett & Wild (2007) found a larger impact parameter distribution (24±2 kpc) for systems found at large redshifts, although the validity of the identified host galaxies has not been verified. From the $g-r$ color distribution in Figure 2.17, and the morphological and spectroscopic classifications in Figure 2.16, we find that the majority of the Ca II absorbers appear to be more correlated with bluer, late-type spirals. The fact that the Ca II absorbers are significantly different than the non-absorbers in their morphological classification but not their spectroscopic classification indicates that a fraction of the non-Ca II absorbers may consist of red spirals. However this may simply be due to redshift effects. Wild & Hewett (2005b) found that the Ca II absorbers were some of the dustiest absorbers, with an average $E(B-V) \sim 0.1$, similar to those seen in star-forming galaxies at $z \sim 2-3$ (Shapley et al., 2001, 2005). In this context, it is curious that our Ca II absorbing galaxies show no significant difference in inclination compared to the non-absorbers.

2.6.2 Na I Absorbers

For the Na I absorbers, the results of the U test show that the Na I absorbers are significantly different than the non-absorbers in rest-frame $g-r$ color (they are bluer), but are not significantly different with respect to any of the other parameters. The $b/r_{\rm Petro}$ ratio distribution in Figure 2.14 shows that while the ratios for the Na I absorbers aren't significantly different than the rest of the galaxies, there is a slight decrease in the relative fraction of

[2]Impact parameters have been recalculated using the cosmology adopted in this paper.
[3]Median value calculated using data from their Table 5

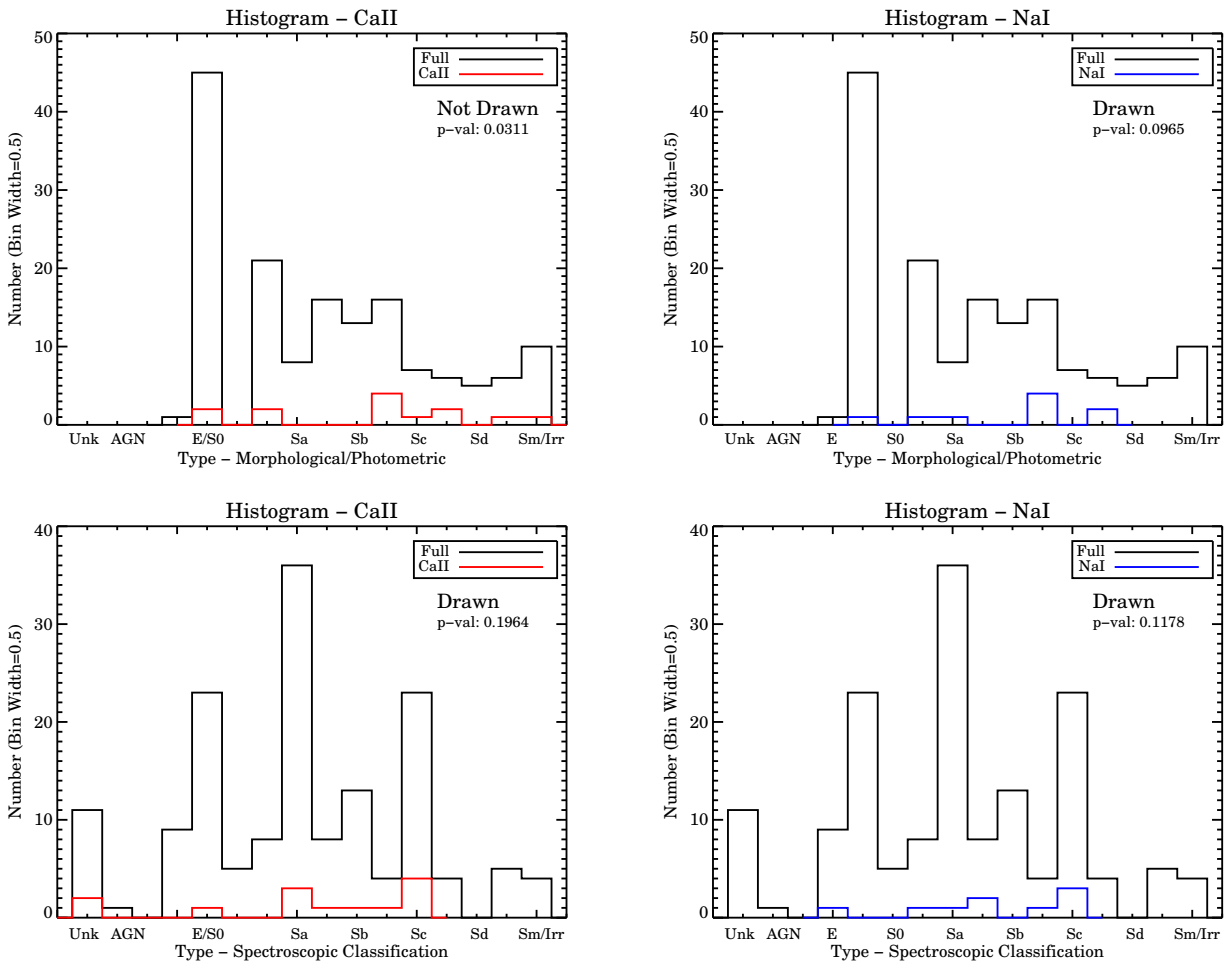

Figure 2.16 Distributions of morphological/photometric classification and spectroscopic classification for the Ca II (left) and Na I (right) samples, respectively.

Na I absorbers with increasing distance from the host galaxy. The median impact parameter for the Na I absorbers is 14.8±9.5 kpc. The single Na I galaxy/quasar pairs found by Junkkarinen & Barlow (1994),Womble et al. (1990), and Kunth, D. & Bergeron, J. (1984) have similar impact parameters of 11.4, ∼18, and 13.7 kpc, respectively[2]. Figures 2.15-2.17 show the Na I absorbers appear to be galaxies with properties consistent with the overall sample of galaxies.

2.7 SUMMARY

We introduce a sample of 154 galaxy/quasar pairs constructed from the SDSS spectroscopic galaxy and quasar catalogs, where the quasar lies projected within twice the Petrosian r-band radius of the galaxy and has a greater redshift than the galaxy. Previous low-redshift galaxy/quasar catalogs, while finding numerous pairs, have large impact parameters between the galaxy and quasar limiting the usefulness of the quasar as a probe of the gaseous material associated with the disk of the galaxy. Our catalog is the first catalog of low-redshift galaxy/quasar pairs with small impact parameters between the galaxy and quasar. It provides the advantage of direct observations of the host galaxy properties, along with the absorber gas situated along the quasar sightline.

We have searched for Ca II and Na I absorption in the quasar spectra at the redshifts of the associated galaxies, and identified thirteen Ca II absorbers and nine Na I absorbers, four of which have both Ca II and Na I. While these systems pass the statistical tests for being significant lines given the low resolution of the SDSS, higher resolution spectroscopy will no doubt more accurately determine the true multi-component nature of these absorption line systems.

We performed a statistical comparison between the Ca II and Na I absorbers with the overall sample of pairs. The Ca II absorbers appear to be blue, late-type spirals located at impact parameters close to the host galaxy. This is consistent with the Ca II host galaxy properties seen in Zych et al. (2007). The Ca II absorbers we present here significantly increase (13/17 systems, ∼75%) the number of Ca II absorbers with known host galaxies.

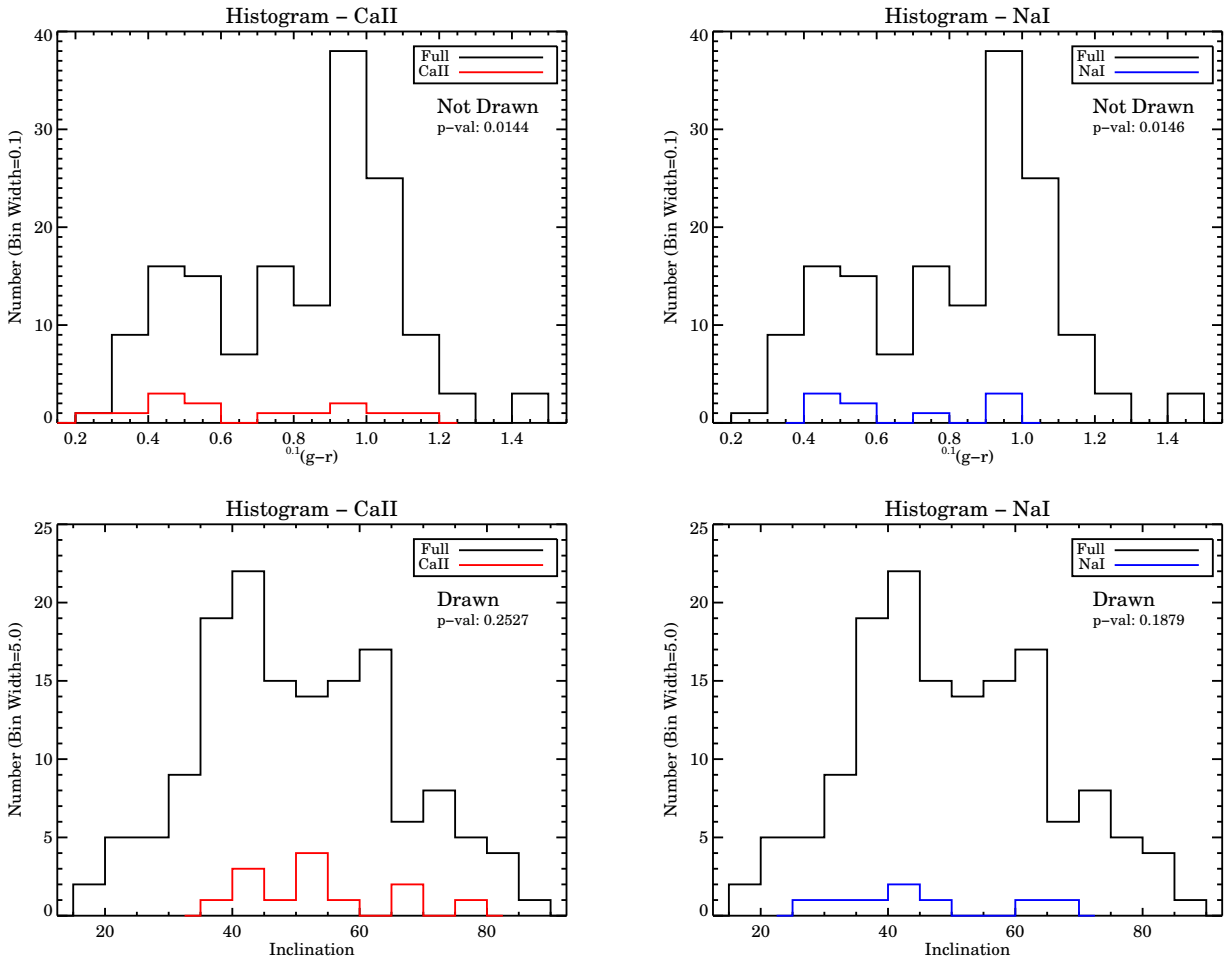

Figure 2.17 Distributions of rest-frame $g-r$ color and inclination for the Ca II (left) and Na I (right) samples, respectively. All $g-r$ colors have been band-shifted to a rest-frame at z=0.1.

The Na I absorbers, on the other hand, show only a significant difference with the overall sample in rest-frame $g-r$ color, although there exists a slight trend of decreasing fraction with increasing distance. Our sample significantly increases (9/4 systems, $\sim$225%) the number of Na I absorption systems at low redshift with direct detections of the absorber host galaxy. While there have been some Ca II and Na I absorbers identified among external galaxies, the small numbers prevented any statistical analysis of the absorbers themselves. While our sample size is small, we add a significant number of new systems with identifiable host galaxies and begin to build a larger sample which we can study statistically.

3.0 ABSORBERS IN SDSS DR7

Over the course of my work with SDSS DR5/6, DR7, the last data release of SDSS Phase-II, was released. As this was the most up-to-date dataset available, it was decided to redo the galaxy-quasar pair catalog using SDSS DR7 to provide the most relevant pair catalog for my work. Over the course of the analysis in Chapter 2, refinements were made to both the construction of the pair catalog, and the identification of Ca II and Na I absorption lines, resulting in a different sample from that described in Chapter 2. As the work in this chapter uses DR7, the pair catalog generated and the subsequent analysis supercedes that of Chapter 2. Section 3.1 discusses the selection of the DR7 SDSS galaxy and quasar samples, as well as the construction of the pair catalog. Section 3.2 describes the creation of the DR7 Ca II and Na I absorber samples generated using the same automated line finder described in Section 2.3. We analyze a subset of absorbing systems that passed visual inspection in Section 3.3. Upon visual inspection of the Ca II and Na I absorber samples, many absorbers were found to be indistinguishable from more local absorber sightlines. For these systems, it is unclear whether the absorber is truly associated with the galaxy indicated in the pair or if it is associated with Galactic gas, with Intermediate and High Velocity Clouds in the Milky Way halo, or associated with the Virgo Cluster. We apply several additional criteria to the visually inspected systems in order to select out a subset of absorbers more likely to be extragalactic in nature. These systems are discussed in Section 3.4. We briefly summarize the overall results in Section 3.5. Additional analysis of the DR7 Ca II and Na I absorber samples occurs in Chapter 4.

3.1 PARENT SAMPLE CONSTRUCTION

The SDSS-DR7 quasar catalog provides the parent quasar sample (Schneider et al., 2010). This catalog of bona fide quasars, that have redshifts checked by eye, and luminosities and line widths that meet the formal quasar definition, contains 105,783 spectroscopically confirmed quasars, and represents the final product of the SDSS-I and SDSS-II quasar survey. The quasar catalog uses a cosmology with H_o=70 km s^{-1}, Ω_m=0.3, and Ω_Λ=0.7, which we adopted for the remainder of this section, as well as for all analysis pertaining to the SDSS DR7 sample of galaxy-quasar pairs.

For the DR7, we decided to use the SDSS SpecPhoto view to provide the parent galaxy sample. The SpecPhoto table includes only those objects where the SpecObj is a sciencePrimary, and the BEST PhotoObj is a PRIMARY object and the object has clean spectra. We selected from this table all objects that were morphologically typed as a galaxy (type = galaxy) and have the spectrum of a galaxy (specClass = galaxy). This returned 798,948 galaxy spectra.

Table 3.1 SDSS DR7 Parent Sample of 97468 Galaxy-Quasar Pairs

Galaxy	z_{sdss}	Quasar	z_{QSO}	100 kpc Scale	b	b	inCa	inNa	CaFlag	NaFlag	VC_{CaII}	VC_{NaI}
				[′]	[′]	[kpc]						
[1]	[2]	[3]	[4]	[5]	[6]	[7]	[8]	[9]	[10]	[11]	[12]	[13]
SDSS J000005.53-011258.9	0.03170±0.00009	SDSS J235958.66-011225.3	1.77180	2.63	1.80	68.63	1	1	N	N	-	-
SDSS J000006.67+003016.7	0.10916±0.00015	SDSS J000006.53+003055.2	1.82460	0.84	0.64	76.84	1	1	N	N	-	-
SDSS J000027.97-002653.4	0.07897±0.00015	SDSS J000030.37-002732.4	1.80550	1.12	0.88	79.24	1	1	N	N	-	-
SDSS J000031.98-103322.0	0.07713±0.00015	SDSS J000035.75-103305.3	1.21820	1.14	0.97	84.75	1	1	N	N	-	-
SDSS J024910.78-074924.6	0.00457±0.00001	SDSS J024945.00-075626.9	1.58460	17.69	11.02	62.28	1	1	Q	N	4	-
SDSS J024910.78-074924.6	0.00457±0.00001	SDSS J024950.68-075949.9	0.97360	17.69	14.36	81.17	1	1	N	Q	-	7
SDSS J024910.78-074924.6	0.00457±0.00001	SDSS J024957.31-075617.0	2.16360	17.69	13.42	75.84	1	1	N	N	-	-
SDSS J025346.70-072344.0	0.00449±0.00001	SDSS J025407.68-074023.0	0.73160	18.00	17.44	96.88	1	1	N	N	-	-
SDSS J025346.70-072344.0	0.00449±0.00001	SDSS J025414.61-073435.4	1.47220	18.00	12.87	71.51	1	1	N	Q	-	4
SDSS J025346.70-072344.0	0.00449±0.00001	SDSS J025420.59-073745.5	2.16710	18.00	16.35	90.80	1	1	Q	N	3	-
SDSS J122037.63+283803.3	0.02764±0.00011	SDSS J122037.22+283752.0	2.20420	3.00	0.21	6.92	1	1	N	A	-	1
SDSS J141745.62+162509.3	0.24229±0.00015	SDSS J141746.03+162512.2	1.71690	0.44	0.11	25.26	1	1	A	N	1	-

Note. — The columns are 1-SDSS galaxy name, 2-SDSS galaxy redshift, 3-SDSS quasar name, 4-SDSS quasar redshift, 5-The 100 kpc search radius scale in arcmin, 6-impact parameter in arcmin, 7-impact parameter in kpc, 8&9-flags indicating the inclusion (1) or exclusion (0) due to Ly-α forest contamination, 10&11-flags indicating absorber candidate (A), questionable candidate (Q), non-detection (N), interloping doublet (D), removal due to sky line (S), 12&13-flags indicating our visual classification of the absorber or questionable candidate (see the FITS header in Appendix C for a legend). The full version of the table is online at http://iopscience.iop.org/1538-3881/142/4/122/ (Cherinka & Schulte-Ladbeck, 2011).

3.1.1 Parent Sample Definition

We identified all pairs for which

1. the quasar's spectrum is projected within 100 kpc of a galaxy's spectrum and
2. the quasar's spectrum has a redshift which is larger than the galaxy's, $z_{QSO} > z_{gal}$, by an amount equal to the total redshift error, σ, of the galaxy and the quasar, $z_{QSO} - z_{gal} > \sqrt{\sigma^2_{z_{QSO}} + \sigma^2_{z_{gal}}}$.

Steps 1 and 2 yielded 97489 pairs of galaxy/quasar spectra. We refer to these pairs as the galaxy-quasar parent sample. The full list of pairs is available for download as a FITS table with the online version of Cherinka & Schulte-Ladbeck (2011), a sample of which is provided in Table 3.1. Prior to the absorber selection we also apply an additional constraint on the parent sample where

3. we remove cases in which intervening Lyα forest lines potentially cause misidentification.

We perform step 3 for both Ca II and Na I, thus creating two parent samples, one of 95651 pairs (Na I) and one of 81912 pairs (Ca II). For the remainder of this section we discuss the overall parent sample of 97489 pairs.

3.1.2 Parent Sample Characteristics

Figure 3.1 shows the redshift distributions of the galaxy and quasar spectra in the parent sample of 97489 pairs. The mean redshift of the galaxies is (μ,σ)=(0.00649,0.00005), and the mean redshift of the quasars is (μ,σ)=(1.6,0.8). We see that, indeed, the distribution of QSOs lies mostly behind that of the galaxies. Figure 3.2 displays the impact parameter distribution of the pairs. We find an increasing number of pairs as the impact parameter increases. This distribution is expected given the large number of low-redshift galaxies seen in Figure 3.1. The 100 kpc search radius around these low-redshift galaxies produces a much larger search area on the sky, from which a greater number of sightlines will be observed. The mean impact parameter of the distribution is (μ,σ)=(66,24) kpc.

The spectra which define the galaxy-quasar parent sample do not necessarily belong to unique galaxy/quasar pairs. There are two reasons for this. First, the SDSS database

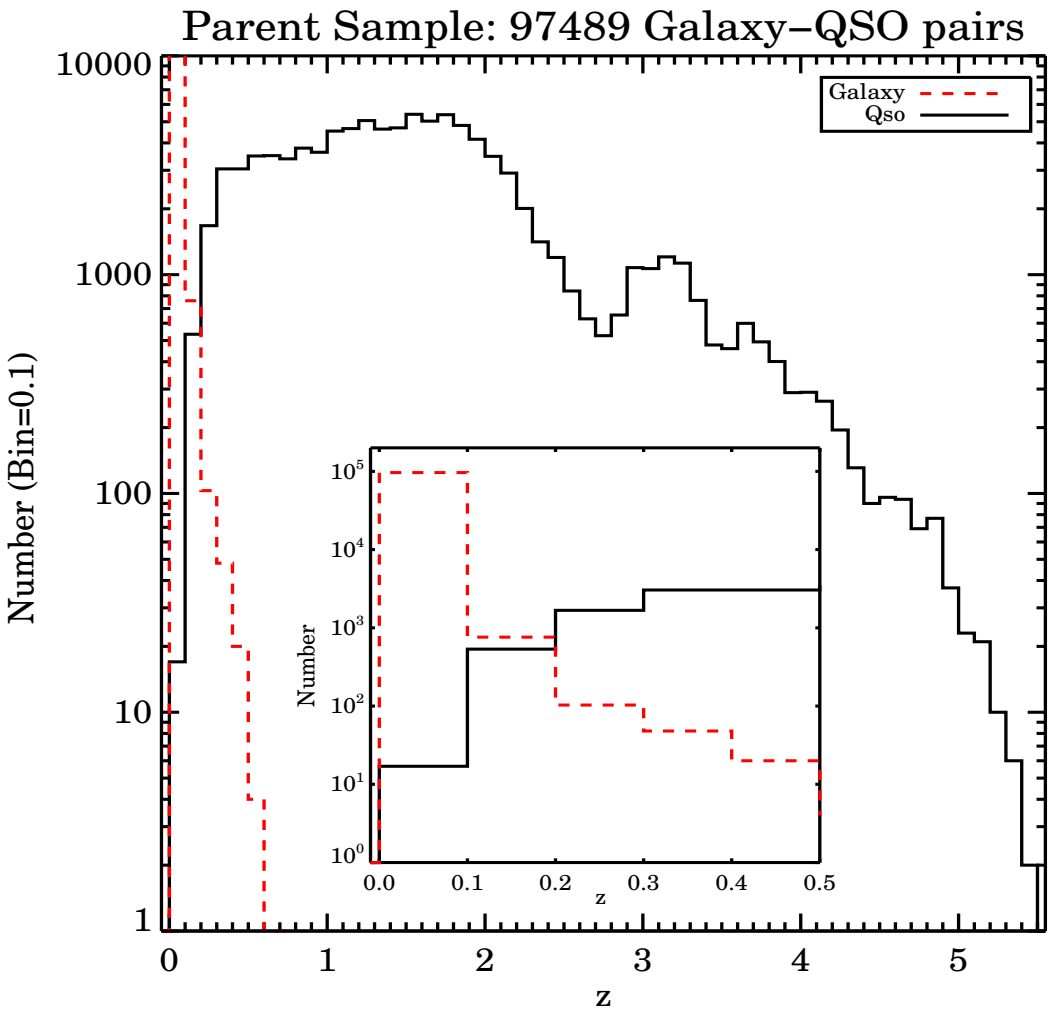

Figure 3.1 Shown here are the redshift distributions for the parent galaxy and quasar sample. As expected given our catalog constraints, the distribution of quasars does indeed lie behind the distribution of galaxies.

contains multiple spectra for some galaxies. A typical example is a nearby star-forming galaxy for which the SDSS targeted its nucleus plus one or more bright H II regions. Second, some nearby galaxies cover such a large area on the sky that they intercept two or more quasar sight-lines. If the coverages of multiple nearby galaxies overlap, then it is also possible to have more than one galaxy intercept the same quasar sightline.

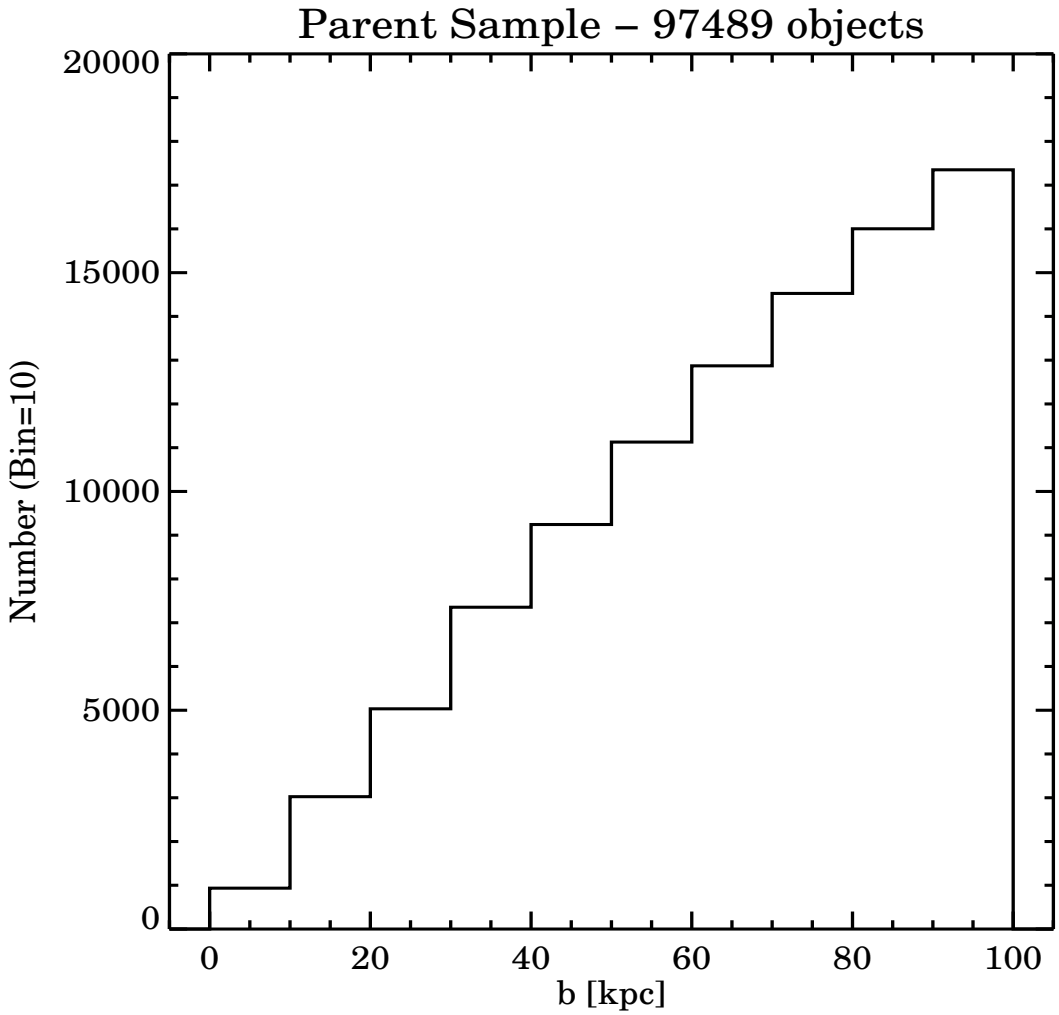

Figure 3.2 Shown here is the distribution of impact parameter in kpc of the parent galaxy-quasar sample. The large number of pairs seen at large impact parameters is due to the much larger projection of the 100 kpc search radius on the sky for low-redshift galaxies, facilitating the detection of many more sightlines.

3.2 SDSS DR7 ABSORBER SAMPLE

With the DR7 dataset, we made one cut on the parent sample of 97489 pairs prior to the automated line search, namely, we eliminated cases in which intervening Lyα forest lines would potentially cause misidentifications. This reduced the parent sample to 95651 (Na I) and 81912 (Ca II) pairs. Visual inspection of the candidate detections later showed a small

number of possible intervening Mg II, Fe II, or C IV systems that interfered with a positive identification of the doublet lines. Using the same automated line finding algorithm discussed in Section 2.3, we searched the Ca II and Na I parent samples and created three candidate line lists.

3.2.1 Ca II Doublet Sample

The first list contained Ca II doublets. The automated line finder identified 146623 candidate features out of 81912 pairs. As the line finder performs a search on a pixel-by-pixel basis, it is possible that in cases where there are two or more neighboring pixels that satisfy the significance threshold, the same candidate feature will be identified, thus producing a duplicate feature in the line list. Out of the 146623 candidate features, 40244 consist of duplicate features. Of the remaining 106379 candidate features, the number of systems broken down by flag is as follows:

- **No Detections** - 30994
- **Outside Pixel** - 3346
- **Line Not Significant** - 49922
- **Large Velocity Difference** - 14226
- **Weak Line Not Detected** - 6082
- **Not Good Doublet** - 60
- **Good Doublet** - 1749

For the Ca II doublet list, we only consider those candidate features with the 'Good Doublet' flag set as our absorber sample. The remaining 104630 candidate features are thus considered non-detections. With the remaining 1749 candidate features, we then perform a visual inspection where each feature was classified into one of four categories, listed as follows:

1. **Resolved Systems** - 92
2. **Single-Line Systems** - 688
3. **Other Doublets** - 102
4. **Low Signal-to-Noise** - 867

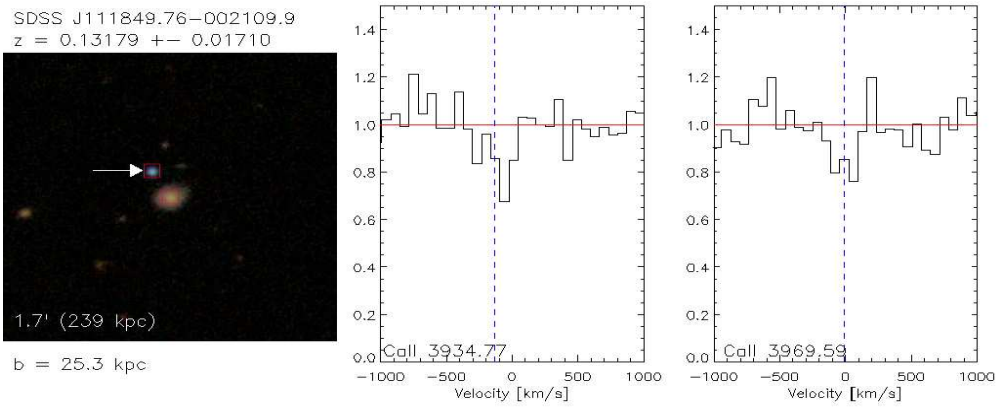

(a)

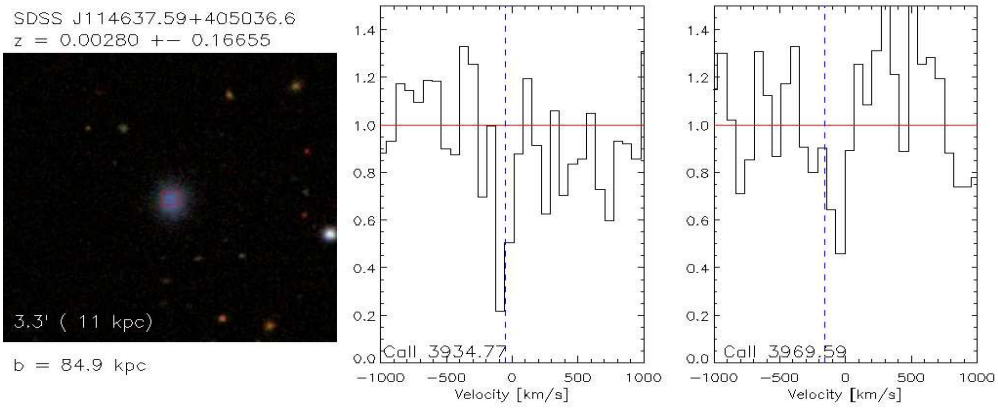

(b)

Figure 3.3 A subset of Ca II Absorbers: The image is centered on the galaxy position. The quasar, if visible, is marked with a white arrow. All objects with an SDSS spectrum are marked with a red square. The galaxy name and redshift are displayed at the top. In the lower left is the image scale. Below that is the impact parameter between the quasar and galaxy. The absorption lines detected are shown on the right. The y-axis shows the normalized flux. The middle panel displays the strong line at 3934.77Å, with the weaker line at 3969.59Å on the right. Each panel is centered in velocity space on the galaxy redshift. The dashed blue line marks the velocity offset of the line from the host galaxy. The red line marks the normalized continuum.

We consider only those systems visually categorized as a 'resolved' system, thus claiming among the parent sample for Ca II systems, 92 detections, and 1657 questionable candidates. The main reasons why a doublet was rejected during visual inspection include: (a)

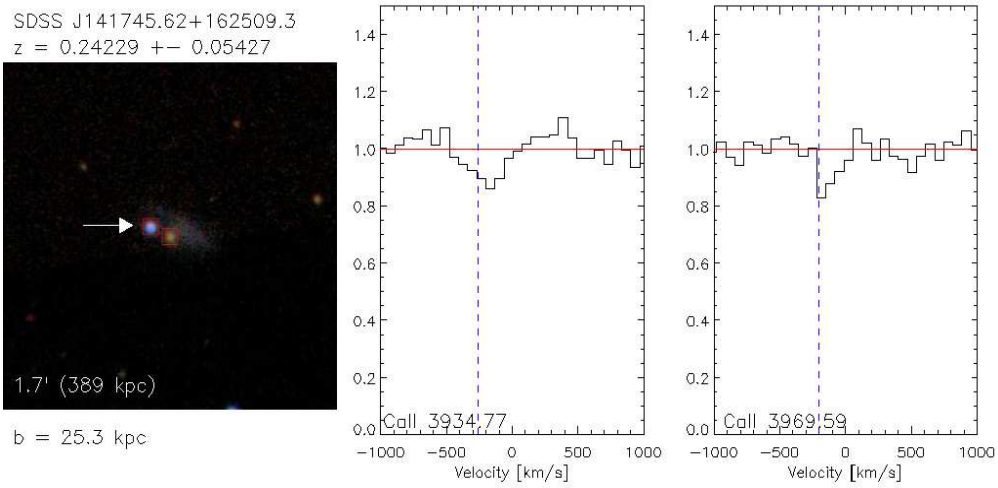

(c)

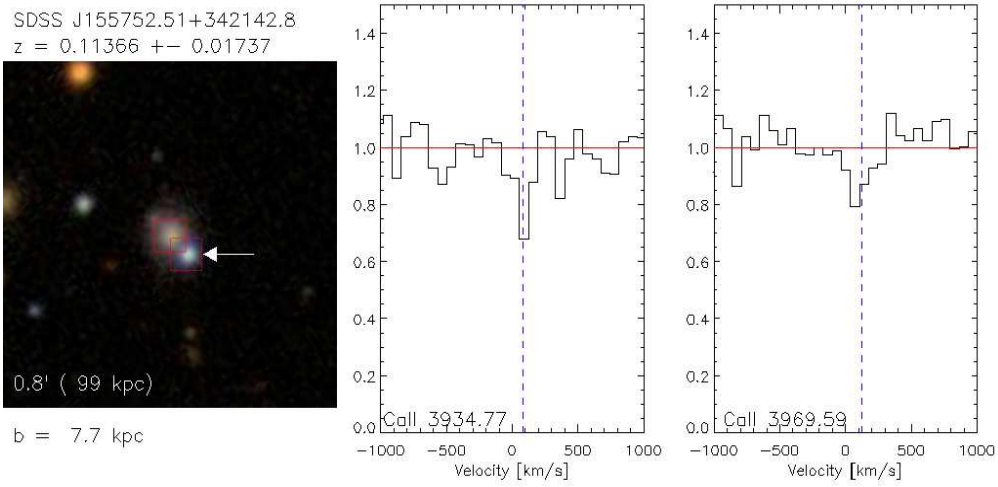

(d)

Figure 3.3 cont'd

possibility of confusion with an interloping non-Ca II system, (b) a pixel pattern in the doublet region which looked inconsistent with the profile of a real doublet, and (c) the doublet region has low signal-to-noise. Each galaxy/quasar pair in Table 3.1 is marked with an A, Q, or N indicating a Ca II absorber or questionable candidate, or non-detection. For the 92 detections, the line finder yields a mean line significance level of the Ca II K line of (μ,σ)=(2.9±0.1,0.6±0.1). The Ca II absorber catalog consists of 92 detections involving pairs of individual galaxy and quasar spectra. These 92 detections result from 13 unique galaxy spectra and 61 unique quasar spectra. Listed in Table 3.2 are the individual Ca II

Table 3.2 Individual Ca II Absorbers

Galaxy	z_{sdss}	QSO Count	Notes
SDSS J091338.99+193707.4	0.00143±0.00001	1	
SDSS J102703.86+283721.9	0.00020±0.00016	7	inconsistent spectrum, not a part of NGC 3245A
SDSS J111849.76-002109.9	0.13179±0.00016	1	see also Zych et al. (2007)
SDSS J113420.50-033525.4	0.00008±0.00007	12	inconsistent spectrum
SDSS J114637.59+405036.6	0.00280±0.00002	1	
SDSS J121323.27+295518.4	0.00042±0.00001	1	KUG 1210+301B
SDSS J121344.76+363802.4	0.00045±0.00018	1	in NGC 4190
SDSS J121633.70+130153.6	0.00006±0.00007	21	VCC 200 (dE2)
SDSS J122843.30+114518.1	0.00054±0.00007	1	VCC 1125 (S0(9))
SDSS J122844.91+124835.1	0.00004±0.00033	41	VCC 1129 (dE3)
SDSS J123745.22+070618.3	0.00011±0.00032	3	VCC 1726 (SdmIV)
SDSS J141745.62+162509.3	0.24229±0.00015	1	
SDSS J155752.51+342142.8	0.11366±0.00006	1	

Note. — Inconsistent spectrum refers to an inconsistency between the reported SDSS redshift with the galaxy spectrum.

absorber galaxies, with the number of quasars found associated with each particular galaxy, along with any notes regarding that particular galaxy. Table 3.2 highlights the fact that a low-redshift galaxy may have a large search radius such that many quasar sightlines are intersected, producing a large number of non-unique spectral pairs. With more than one of these galaxies, it is therefore also possible to have one quasar be considered in multiple pairs with different galaxies. These facts combine to produce the numbers of unique galaxy and quasar spectra above. For example, the galaxy SDSS J21633.70+130153.6 had 21 quasars identified within 100 kpc which exhibited Ca II absorption located within ±500 km s^{-1} of the galaxy redshift. This system would then account for 1 out of 13 unique galaxy spectra, 21 out of 61 unique quasar spectra, and 21 out of 92 Ca II detections. Also see the last paragraph of Section 2.3.

3.2.2 Na I Doublet Sample

The second line list contained Na I systems. The automated line finder identified 109,223 candidate features out of the 95,651 Na I pairs. As with the Ca II sample, some of the

Table 3.3 Individual Na I Absorbers

Galaxy	z_{sdss}	QSO Count	Notes
SDSS J102703.86+283721.9	0.00020±0.00016	1	inconsistent spectrum, not in NGC 3245A
SDSS J111849.76-002109.9	0.13179±0.00016	1	
SDSS J113420.50-033525.4	0.00008±0.00007	2	inconsistent spectrum
SDSS J114313.05+193646.9	0.02085±0.00009	1	in Abell 1367
SDSS J114318.07+193401.3	0.02262±0.00015	1	in Abell 1367
SDSS J114336.98+193616.7	0.02201±0.00019	1	in Abell 1367
SDSS J115115.25+485331.0	0.02565±0.00011	1	
SDSS J122037.63+283803.3	0.02764±0.00011	1	
SDSS J122844.91+124835.1	0.00004±0.00033	1	VCC 1129 (dE3)
SDSS J124006.10+613609.5	0.00026±0.00017	1	in NGC 4605
SDSS J140613.22+153035.5	0.06040±0.00018	1	
SDSS J142009.64+132626.7	0.14152±0.00020	1	
SDSS J150400.94+240437.1	0.06894±0.00010	1	in group
SDSS J150403.17+240559.8	0.06997±0.00019	1	in group
SDSS J151145.63+071510.6	0.04393±0.00019	1	

detected features were duplicates. Out of the 109,223 candidate features, 10,482 consisted of these duplicates. The remaining 98,741 features break down as follows:

- **No Detections** - 68750
- **Outside Pixel** - 1808
- **Line Not Significant** - 21898
- **Large Velocity Difference** - 1780
- **Weak Line Not Detected** - 3319
- **Not Good Doublet** - 7
- **Good Doublet** - 1179

Some of the Na I doublets are resolved and some are blended. For partially blended doublets, occasionally the line finder failed to distinguish both components of the doublet, instead treating the entire doublet as the Na I D2 line. It then attempted to find a 'false'

Table 3.4 Individual Na I & Ca II Absorbers

Galaxy	z_{sdss}	QSO Count	Notes
SDSS J111849.76-002109.9	0.13179±0.00016	1	
SDSS J155752.51+342142.8	0.11366±0.00006	1	

weaker component for Na I. This led us to treat the Na I candidates differently from the Ca II candidates. We required that the line finder identify the 'Na I D2 line' of the doublet only. This criteria selected those candidates with flags 'Good Doublet', 'Not Good Doublet', and 'Weak Line Not Detected' as candidate absorbers (4505 systems), with the remaining 94236 features classified as non-detections. We then visually inspected the absorbers and categorized them into one of eleven groups, listed as follows:

1. **Resolved Systems** - 471
2. **Blended Systems** - 112
3. **Symmetrical Single Line** - 81
4. **Other Doublets** - 400
5. **Bad Continuum** - 202
6. **Wrong Doublet Ratio** - 77
7. **Low Signal-to-Noise** - 1764
8. **Emission Lines** - 67
9. **Unknown** - 74
10. **Single-Line Systems** - 1257

Post visual inspection, we only adopt those systems classified as 'Resolved' or 'Blended'. We are left with 583 detections, and 3922 questionable candidates. We typically rejected as questionable candidates lines showing profile shapes that appear inconsistent with a blended physical doublet, as well as Na I systems that had (a) the possibility of an interloping non-Na I system, and (b) systems with low signal-to-noise within the doublet region. Many of the candidate systems were found at very low velocities, i.e., close to the rest-frame wavelength of Na I, and thus were affected by incomplete Na I sky-line subtraction in SDSS. This turned out to be a severe problem. To minimize contamination from incorrect sky subtraction, we excluded from the sample all candidate lines that fell between 5888.0 Å and 5901.0 Å. This reduced the number of Na I detections down to 16 systems. For the 16 detections, the line finder yields a mean line significance level of 2.8±0.9. These 16 detections result from 15 unique galaxy spectra and 12 unique quasar spectra. Listed in Table 3.3 are the individual Na I absorber galaxies, with the same columns as in Table 3.2.

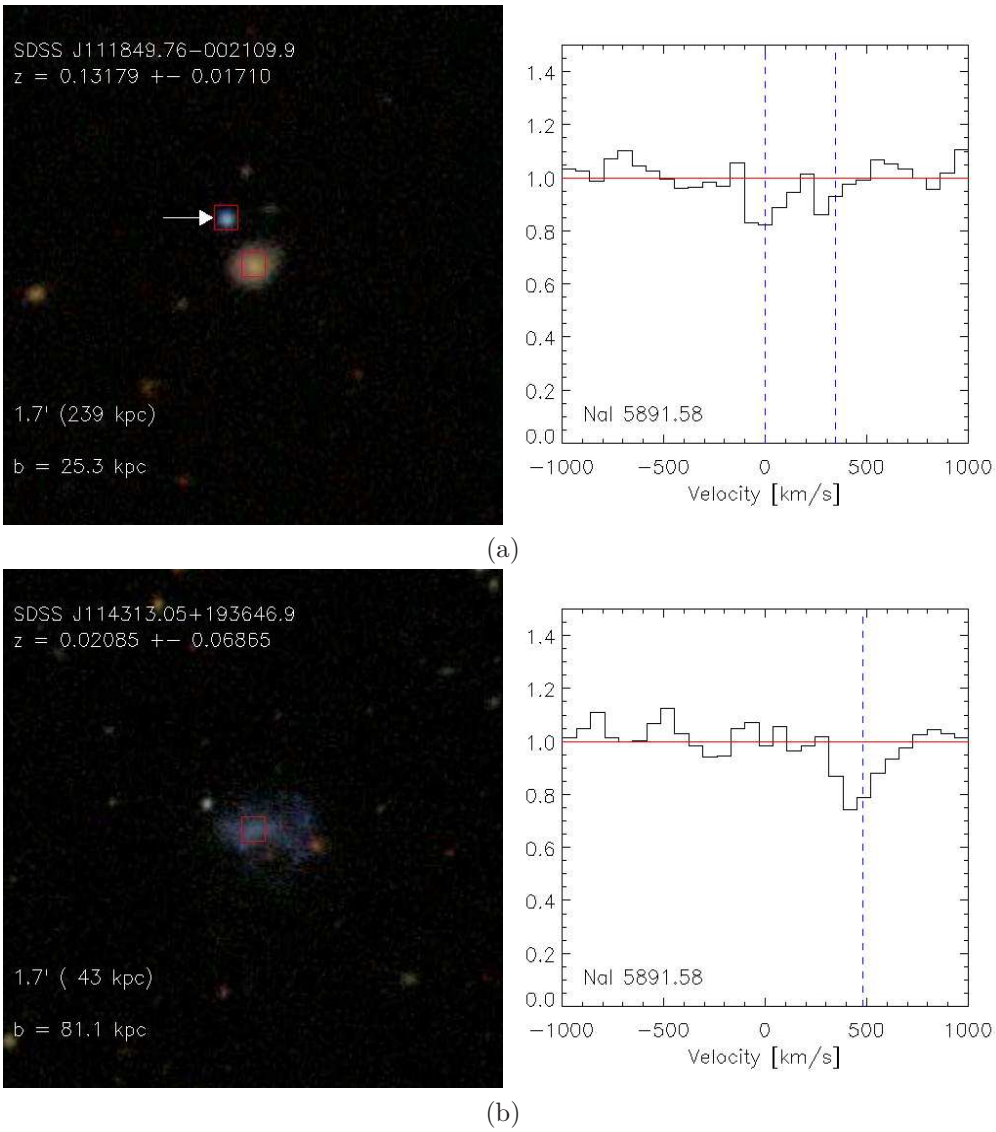

Figure 3.4 A subset of Na I Absorbers: The image marks are the same as in Figure 3.3. If visible, the quasar is marked with a white arrow. The absorption line is shown in the right panel, centered on the expected position of the 5891.58 Å line from the galaxy redshift. The y-axis shows the normalized flux. The dashed blue line represents the velocity offset of the line from the expected position, or in the case of a blend, the offset as determined across the whole profile.

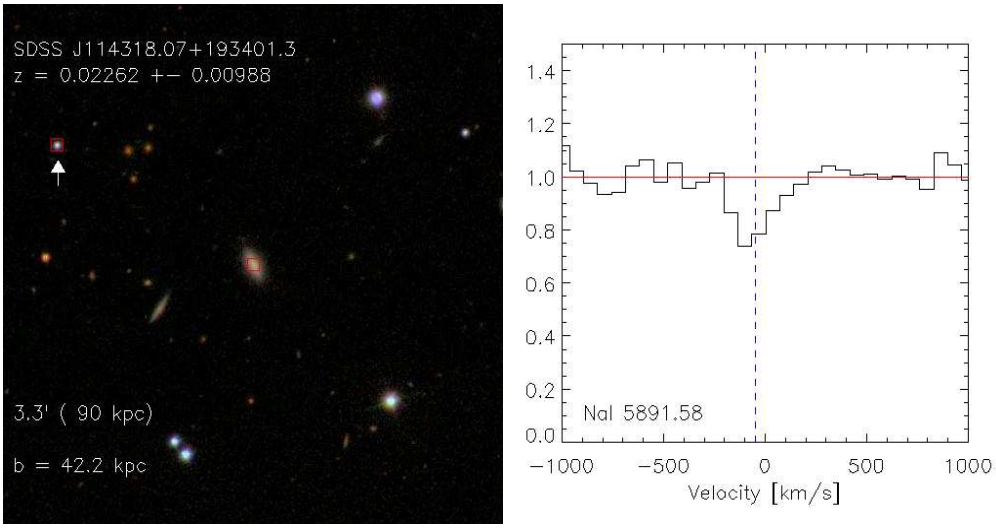

(c)

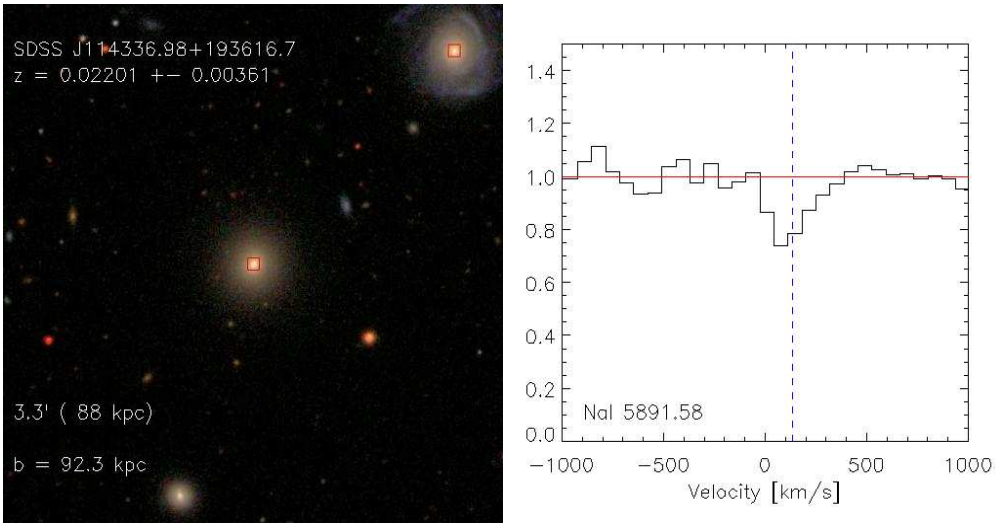

(d)

Figure 3.4 cont'd

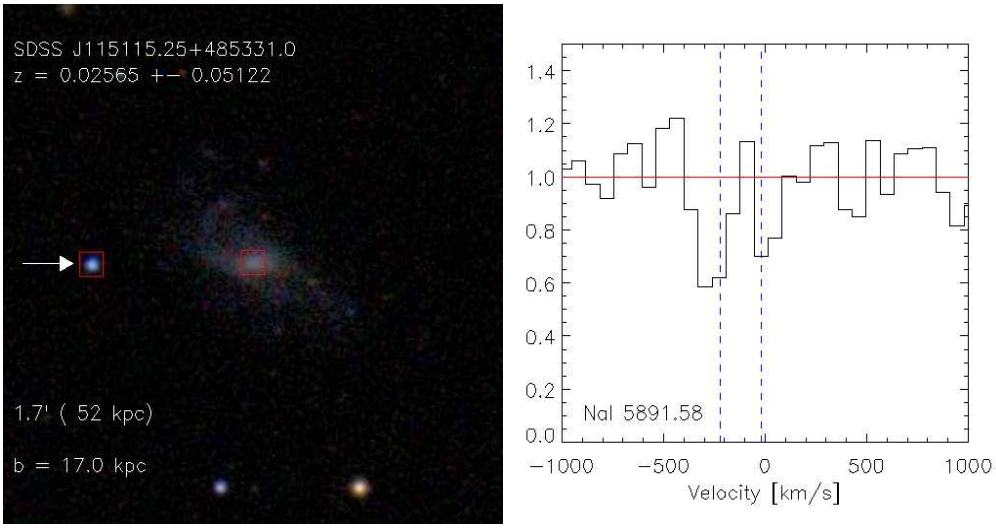

(e)

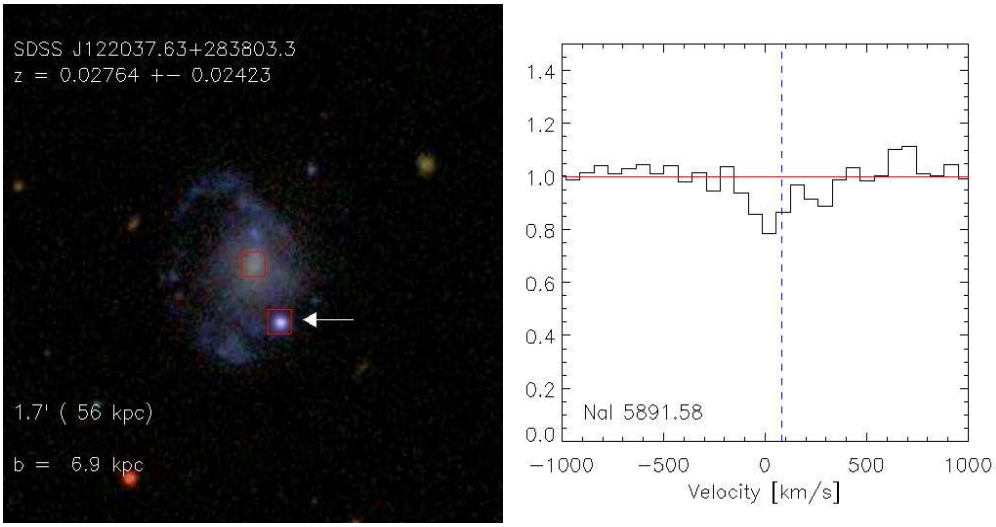

(f)

Figure 3.4 cont'd

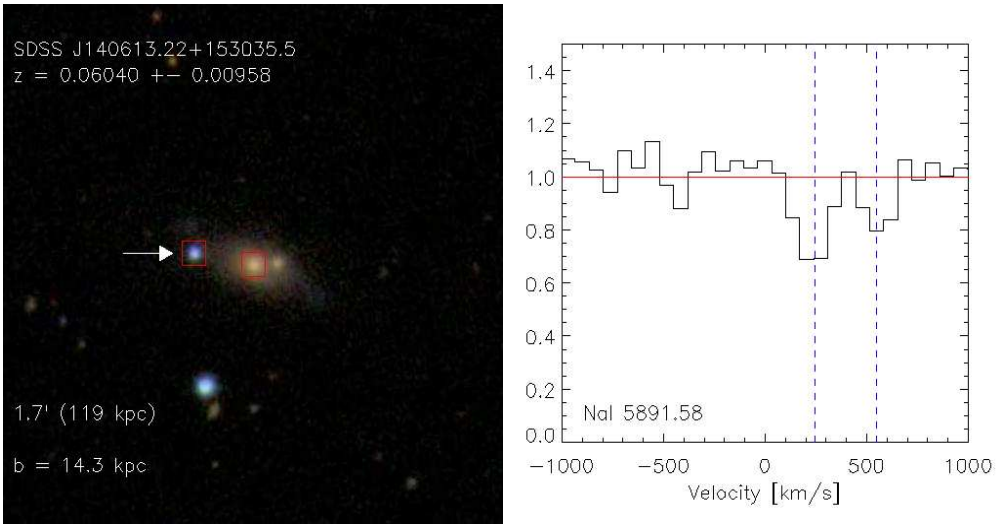

(g)

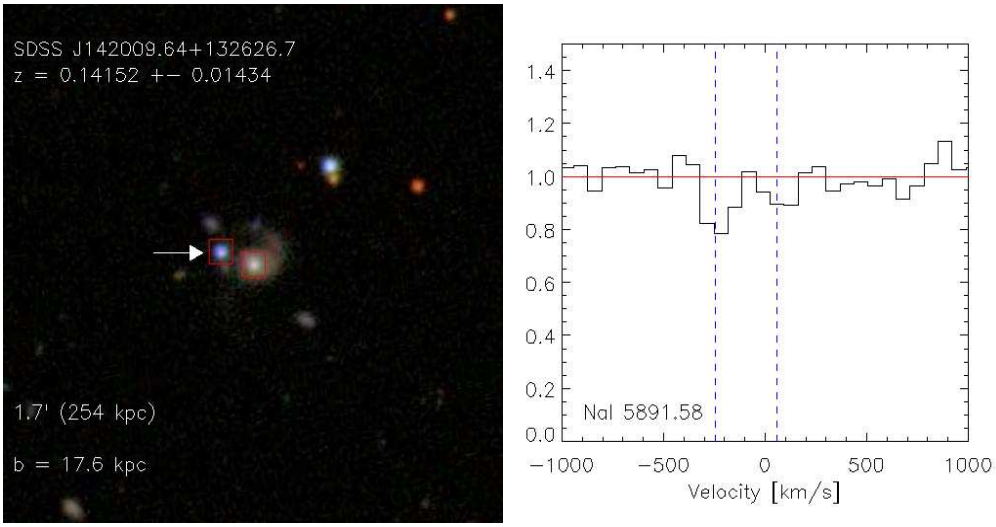

(h)

Figure 3.4 cont'd

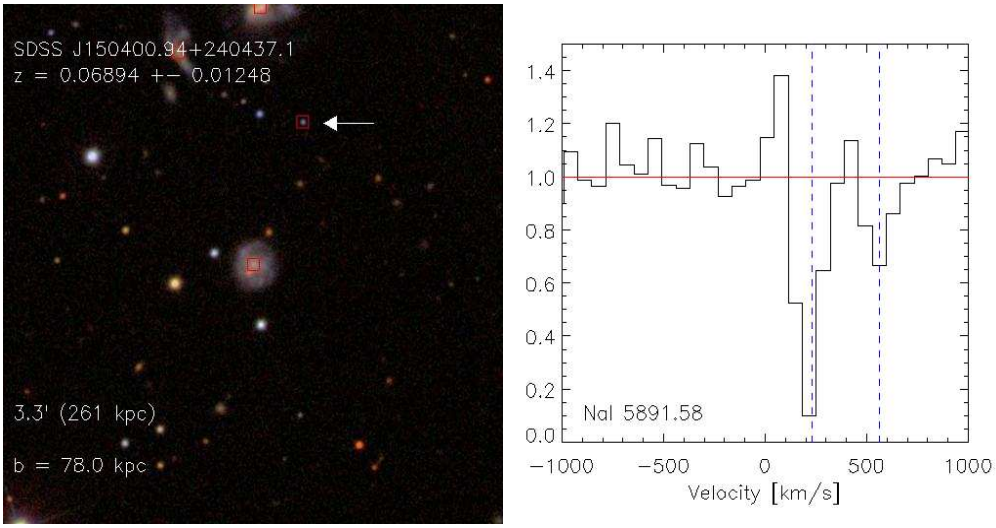

(i)

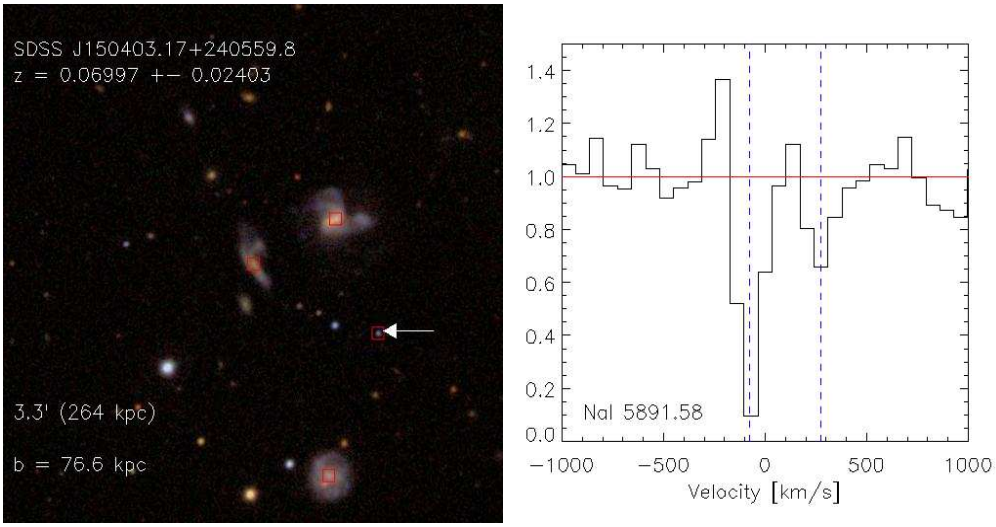

(j)

Figure 3.4 cont'd

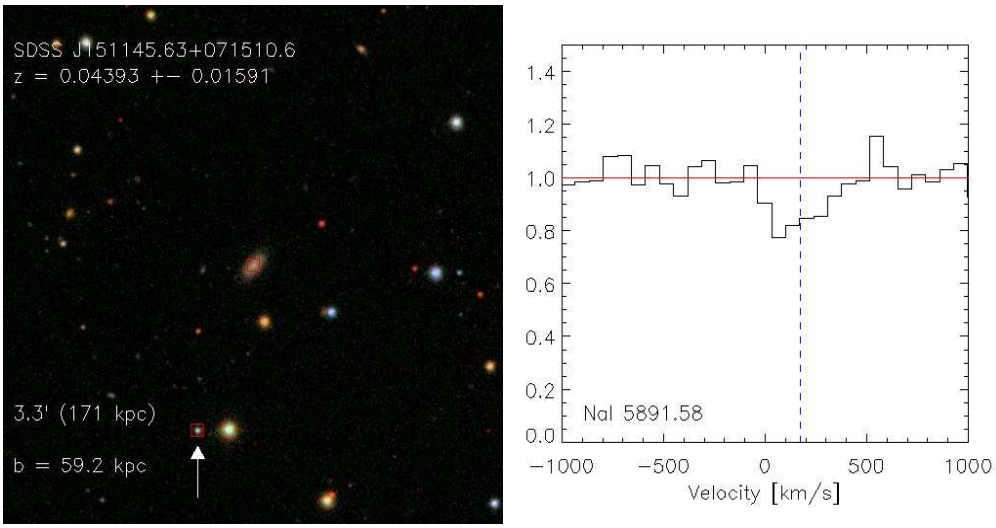

(k)

Figure 3.4 cont'd

3.2.3 Ca II K and Na I D2 Sample

We generated a third list in which both the Ca II K line and the Na I D2 line are detected by the line finder. In this list we use the Ca II K line as the "confirmation" line for the Na I D2 line, and vice versa. This required that we impose a limit on their allowable velocity separation. We adopted a limit of 3 pixels, or 210 km s^{-1}. The visual inspection of this list, after applying the same sky subtraction processing as in the Na I sample, yielded 2 detections. The line finder gives a mean line significance level for the Na I lines of 2.8, and 2.3 for the Ca II K lines. These two detections result from two unique galaxy and quasar spectra. Listed in Table 3.4 are the individual absorber galaxies.

In all tables and figures, 'Na I' refers to those absorbers in the Na I Doublet Sample. 'Ca II' refers to those absorbers in the Ca II Doublet Sample. 'Both' refers to absorbers that have at least the Ca II K line and the Na I D2 line detected. These absorbers are listed in the 'Ca II K and Na I D2 Sample' and may also be listed in either the Ca II or Na I Doublet Sample.

3.2.4 Absorber Catalog

The absorber catalog represents a merger of the above three final line lists of detections, consisting of 92 Ca II detections and 16 Na I detections, of which 2 are common to both samples. There may well be additional Ca II and Na I systems among the questionable candidates. We investigated this possibility by stacking the spectra of questionable candidates using various cuts, and the doublets do become detectable in some of the stacks. Further analysis on the stacked spectra is detailed in Chapter 4. The confirmation of questionable candidates on an individual basis requires future spectroscopy with a higher signal-to-noise ratio and spectral resolution.

As the line finder would occasionally mistake a Na I blend for the Na I D2 line of the doublet, it would measure an equivalent width across the entire line profile, as opposed to just the Na I D2 component. Due to this, we decided to remeasure the equivalent widths manually, to ensure each line has a proper value. To be consistent, we remeasured all the lines within the absorber sample. We measured the rest equivalent width (rEW), rest equivalent

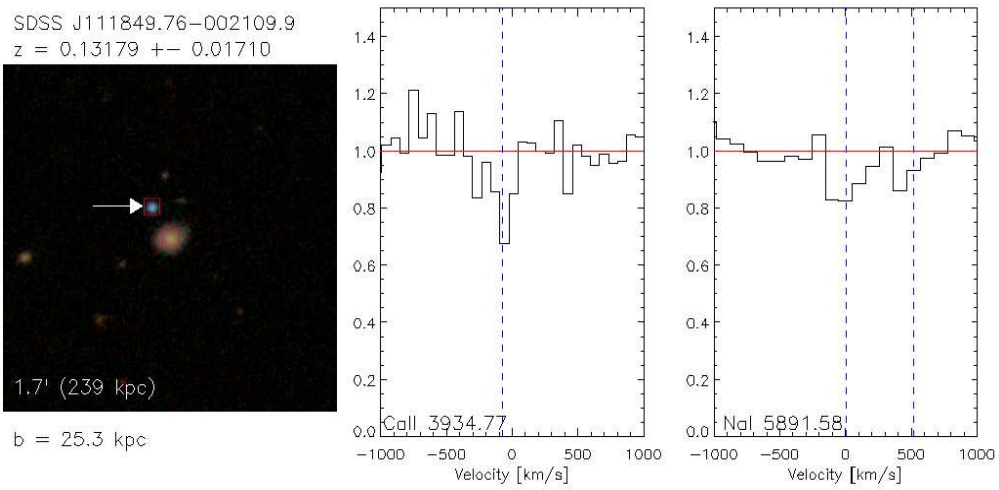

(a)

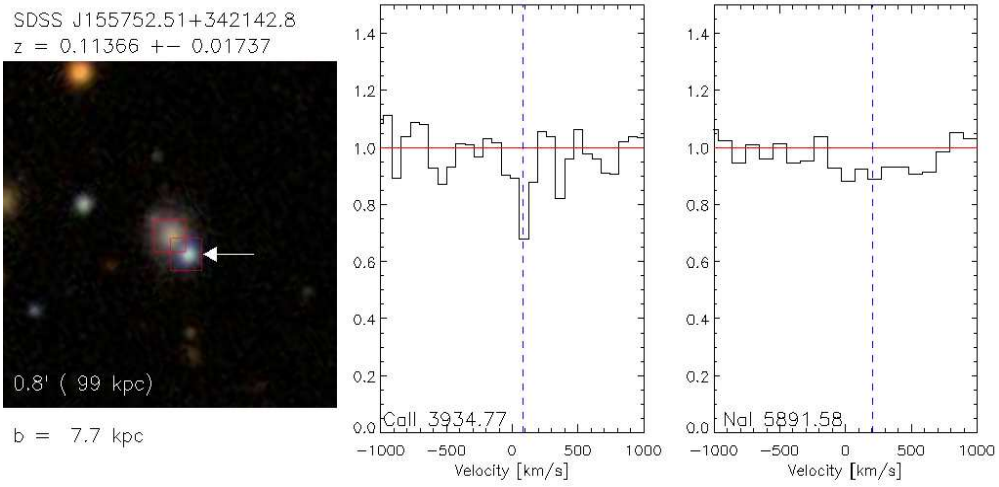

(b)

Figure 3.5 Absorbers with Ca II and Na I strong lines. The figure displays the same format as in Figure 3.3.

width error, central wavelength, and central wavelength error, of the lines. The equivalent widths were computed from a direct summation of the flux pixels within the line region. The line equivalent width error is the total error of the sum in quadrature of the pixel equivalent width errors. The central wavelength of a line is the equivalent-width weighted mean of the pixels' wavelengths; its errors is the uncertainty of the mean.

Table 3.5 is our absorber catalog. The columns of the catalog are: (1) galaxy IAU designation, (2) galaxy redshift, (3&4) galaxy Galactic coordinates, (5) quasar spectrum IAU

designation, (6) quasar redshift, (7&8) quasar Galactic coordinates, (9) impact parameter, (10) the ratio of impact parameter to r-band Petrosian radius, and (11) an identifier for which absorber list it belongs to.

Table 3.6 is a list of the measured line parameters for each absorber. The columns are (1) galaxy IAU designation, (2) SDSS redshift, (3) the catalog the absorber belongs to, (4) the absorption line Local Standard of Rest (LSR) velocity along the sightline to the quasar. For Line 1 in the doublet, we list (5) the rest equivalent width (rEW) of the line, (6) the significance of the line (rEW/σ_{rEW}), (7) the heliocentric redshift of the line, and (8) the velocity offset of the line from that of the expected position. For Line 2, we list (9) the rest equivalent width (rEW) of the line, (10) the heliocentric redshift of the line, and (11) the velocity offset of the line from that of the expected position. For blended Na I features, Line 1 reports the blended values, while Line 2 is blank.

In Figures 3.3-3.5, we show a few examples of absorbers from the 'Ca II', 'Na I', and 'Both' samples, ordered by IAU galaxy name. All absorbers shown were selected using the LSR velocity cutoff (see Section 4.2). Each figure displays an image centered on the galaxy, with the image size given in the lower left. The galaxy name, redshift and impact parameter to the quasar are also displayed. The quasar is marked with a white arrow in all images. All objects with spectroscopy are indicated with a red square. To the right of each image are the Ca II or Na I doublet lines, centered in velocity space on the redshift of the galaxy. The dashed line indicates the velocity offset of the absorber from the galaxy position.

Table 3.5 Total Absorber Sample: Position Information

Galaxy	z_{SDSS}	l [°]	b [°]	QSO	z_{QSO}	l [°]	b [°]	b [kpc]	b/r_{Petro}	Ion
(1)	(2)	(3)	(4)	(5)	(6)	(7)	(8)	(9)	(10)	(11)
SDSS J091338.99+193707.4	0.00143±0.04196	209	40	SDSS J091511.03+201248.3	1.23900	209	40	74.13	245.1	CaII
SDSS J102703.86+283721.9	0.00020±0.08822	202	58	SDSS J100417.96+282444.1	0.32820	201	53	75.87	411.5	CaII
				SDSS J100927.44+273215.7	1.51230	203	54	61.12	331.6	CaII
				SDSS J101353.43+244916.4	1.63430	208	55	72.86	395.2	CaII
				SDSS J101956.59+274401.7	1.92500	203	57	27.34	148.3	CaII
				SDSS J104111.97+282805.0	0.21100	203	61	47.11	255.6	CaII
				SDSS J104221.97+282013.3	1.68590	203	61	51.15	277.5	NaI
				SDSS J104224.85+231001.7	1.23720	213	61	97.85	530.8	CaII
				SDSS J105124.28+320044.5	0.44600	195	64	94.74	513.9	CaII
SDSS J111849.76-002109.9	0.13179±0.01710	260	55	SDSS J111850.13-002100.7	1.02560	260	55	25.25	2.2	NaI
				SDSS J111850.13-002100.7	1.02560	260	55	25.25	2.2	CaII
				SDSS J111850.13-002100.7	1.02560	260	55	25.25	2.2	Both
SDSS J113420.50-033525.4	0.00008±0.01645	269	54	SDSS J104102.43+023242.8	1.95870	246	50	83.38	9958.3	NaI
				SDSS J110156.34+073525.2	1.51360	245	58	78.45	9369.3	CaII
				SDSS J110557.87+045728.3	0.90850	250	56	63.14	7541.0	CaII
				SDSS J111012.07+011327.8	0.09500	256	55	43.89	5241.4	CaII
				SDSS J111507.65+023757.5	0.56650	256	56	44.69	5337.7	CaII
				SDSS J111816.94+074558.2	1.73500	250	61	68.47	8178.1	CaII

Note. — Ion refers to which line list the absorber belongs to. Absorbers listed as Na I have the Na I doublet detected. Absorbers listed as Ca II have the Ca II doublet detected. Absorbers listed as Both have at least both the Ca II K and Na I D2 lines detected. The full table is provided in Appendix D.

3.2.5 Differences between the DR5/6 and DR7 Absorber Samples

If one compares our final absorber lists from DR5/6 and DR7, one would find that many of our absorbers from the DR5/6 list do not appear in our absorber sample from DR7. The absence of the absorbers can be due to a variety of reasons, ranging from the the different procedures and criteria we used to select the samples to the change in flux calibration between SDSS DR5/6 and DR7, to our more stringent visual inspection on the DR7 absorber sample. Here we outline all of the DR5/6 absorbers, and discuss whether or not they appear in the final DR7 absorber sample.

Ca II Absorbers

- **SDSS J021249.59+003448.7** This absorber was found by the automated line finder and classified as a 'Good Doublet' but it did not survive our visual classification in DR7. It was placed in the 'Low Signal-to-Noise' category.
- **SDSS J030337.58+010638.7** This galaxy-quasar pair did not meet the impact parameter criterion of b$\leq$100 kpc. The impact parameter for this pair is 0.92$'$ while the scale of 100 kpc at the redshift of the galaxy is 0.62$'$.
- **SDSS J092301.03+075105.1** This absorber was flagged as 'Weak Line Not Detected'. Since in the DR7 dataset we only considered candidates with the 'Good Doublet' flag set, this absorber was not selected into the final sample.
- **SDSS J104949.75+325903.1** This absorber was flagged as 'Weak Line Not Detected'. Since in the DR7 dataset we only considered candidates with the 'Good Doublet' flag set, this absorber was not selected into the final sample.
- **SDSS J104955.07+325926.9** This absorber was flagged as 'Weak Line Not Detected'. Since in the DR7 dataset we only considered candidates with the 'Good Doublet' flag set, this absorber was not selected into the final sample.
- **SDSS J114720.19+522918.6** This absorber was found by the automated line finder and classified as a 'Good Doublet' but it did not survive our visual classification in DR7. It was placed in the 'Single-Line Systems' category.
- **SDSS J122037.63+283803.2** This absorber was found but it no longer met the $\geq$2 significance threshold. The significance of the feature in the DR5/6 spectrum was mea-

sured as 2.01 while the significance of the feature in the DR7 spectrum was 1.3. This difference can be attributed to the changes in the flux calibration between the two SDSS data releases.

- **SDSS J155752.51+342142.7** This absorber made it into the final list of 13 unique DR7 Ca II absorbers (see Table 3.2).
- **SDSS J163150.46+141124.6** This absorber was found by the automated line finder but it did not survive visual classification. It was placed in the 'Single-Line Systems' category.
- **SDSS J165819.50+623821.3** This absorber was found by the automated line finder but it did not survive visual classification. It was placed in the 'Low Signal-to-Noise' category.
- **SDSS J211701.26-002633.7** This absorber was found by the automated line finder but it did not survive visual classification. It was placed in the 'Single-Line Systems' category.
- **SDSS J214053.72+003111.7** The galaxy in this pair was not classified as a SciencePrimary and thus was not in our parent DR7 galaxy sample.
- **SDSS J231648.38+005948.8** This absorber was found by the automated line finder but it did not survive visual classification. It was placed in the 'Single-Line Systems' category.

Na I Absorbers

- **SDSS J015617.64+010249.2** This galaxy did not have the SciencePrimary flag set and thus was not in our DR7 galaxy sample. This galaxy however is a child object under the SDSS galaxy J015616.95+010302.9. The parent galaxy - quasar pair is in the DR7 parent sample and a candidate feature was found by the line finder but did not survive our visual inspection in DR7. This absorber was placed in the 'Low Signal-to-Noise' category.
- **SDSS J104323.72+404848.9** The absorber was excluded from the DR7 absorber sample when the Ly-α cut was applied.

- **SDSS J115115.25+485331.0** This absorber was found by the automated line finder, survived visual inspection, and thus made it into the final list of 16 unique DR7 Na I absorbers (see Table 3.3).
- **SDSS J122037.63+283803.2** This absorber was found by the automated line finder, survived visual inspection, and thus made it into the final list of 16 unique DR7 Na I absorbers (see Table 3.3).
- **SDSS J142009.64+132626.7** This absorber was found by the automated line finder, survived visual inspection, and thus made it into the final list of 16 unique DR7 Na I absorbers (see Table 3.3).
- **SDSS J155752.51+342142.7** This absorber was found by the automated line finder but it did not survive our visual classification in DR7. It was placed in the 'Low Signal-to-Noise' category.
- **SDSS J163150.46+141124.6** This absorber was found by the automated line finder but it did not survive our visual classification in DR7. It was placed in the 'Other Doublet' category.
- **SDSS J163317.74+352001.5** The background object in this case is classified in SDSS as a galaxy and not a quasar. With the DR5/6 sample, we considered galaxy-galaxy projections as well as galaxy-quasar projections, thus this pair was a viable pair. When the DR7 sample was constructed, we considered solely galaxy-quasar projections so this pair was not included.
- **SDSS J165819.50+623821.3** This absorber was found by the line finder but it no longer met the $\geq$2 significance threshold. The significance of the feature in the DR5/6 spectrum was measured as 2.36 while the significance of the feature in the DR7 spectrum was 1.53. This difference can be attributed to the changes in the flux calibration between the two SDSS data releases.

Table 3.6 Total Absorber Sample: Line Measurements

Galaxy	z_{SDSS}	Ion	v_{LSR} [km s^{-1}]	rEW_1 [Å]	rEW_1/σ_{rEW_1}	z_{line1}	Δv_1 [km s^{-1}]	rEW_2 [Å]	z_{line2}	Δv_2 [km s^{-1}]	(1
(1)	(2)	(3)	(4)	(5)	(6)	(7)	(8)	(9)	(10)	(11)	
SDSS J091338.99+193707.4	0.00143±0.04196	CaII	-32.2	0.30± 0.15	1.97	-0.00009±0.00047	-455.6± 139.9	0.29± 0.13	-0.00008±0.00047	-453.1± 140.1	
SDSS J102703.86+283721.9	0.00020±0.08822	CaII	-64.8	0.25± 0.09	2.66	-0.00021±0.00051	-123.8± 160.1	0.21± 0.12	-0.00059±0.00055	-237.8± 172.4	
		CaII	-79.9	0.44± 0.12	3.50	-0.00026±0.00038	-139.0± 125.5	0.18± 0.12	-0.00015±0.00059	-104.8± 183.1	
		CaII	-30.6	0.39± 0.10	3.81	-0.00009±0.00041	-89.4± 131.3	0.32± 0.10	-0.00024±0.00044	-132.7± 141.8	
		CaII	-53.5	0.31± 0.12	2.60	-0.00017±0.00046	-113.1± 145.5	0.23± 0.13	0.00015±0.00053	-15.8± 165.6	
		CaII	-19.8	0.34± 0.10	3.35	-0.00007±0.00044	-80.7± 140.7	0.29± 0.10	-0.00016±0.00047	-109.8± 149.8	
		NaI	-216.9	0.81± 0.37	2.16	-0.00072±0.00019	-277.8± 75.2	0.59± 0.28	-0.00046±0.00022	-199.1± 82.8	
		CaII	-38.6	0.30± 0.15	1.93	-0.00013±0.00047	-98.7± 148.8	0.23± 0.14	0.00001±0.00052	-56.8± 165.0	
		CaII	-77.9	0.32± 0.14	2.26	-0.00026±0.00045	-139.9± 143.9	0.36± 0.15	-0.00064±0.00042	-251.6± 135.5	
SDSS J111849.76-002109.9	0.13179±0.01710	NaI	39538.5	0.68± 0.27	2.51	0.13180±0.00019	2.3± 75.7	0.31± 0.27	0.13187±0.00029	22.1± 98.7	
		CaII	39400.1	0.73± 0.32	2.32	0.13134±0.00028	-136.1± 96.7	0.62± 0.28	0.13176±0.00030	-10.6± 102.5	
		Both$_{NaI}$	39544.4	0.70± 0.24	2.89	0.13182±0.00019	8.2± 75.1	0.31± 0.27	0.13187±0.00029	22.1± 98.7	
		Both$_{CaII}$	39544.4	0.60± 0.23	2.58	0.13154±0.00031	-76.7± 104.8	0.63± 0.25	0.13175±0.00030	-14.3± 101.9	
SDSS J113420.50-033525.4	0.00008±0.01645	NaI	-190.8	1.30± 1.16	1.11	-0.00062±0.00015	-209.7± 49.4	0.82± 0.77	-0.00024±0.00019	-94.0± 59.8	
		CaII	-81.5	0.51± 0.28	1.78	-0.00027±0.00036	-102.4± 109.0	0.37± 0.23	-0.00008±0.00042	-46.0± 126.5	
		CaII	33.6	0.33± 0.09	3.59	0.00012±0.00044	12.8± 134.8	0.23± 0.10	0.00019±0.00053	34.0± 160.2	
		CaII	34.5	0.32± 0.12	2.73	0.00012±0.00045	14.0± 136.9	0.23± 0.11	-0.00019±0.00052	-78.6± 157.7	
		CaII	-21.8	0.49± 0.18	2.72	-0.00007±0.00036	-42.8± 111.2	0.59± 0.18	-0.00011±0.00033	-55.5± 100.6	
		CaII	-24.8	0.22± 0.08	2.59	-0.00008±0.00055	-46.7± 165.5	0.10± 0.09	-0.00010±0.00081	-52.8± 243.8	

Note. — If the Na I doublet is blended, the values listed for line 1 are measurements based on the blend while the values for line 2 are marked with '-'. The full table is provided in Appendix D.

3.3 ABSORBER ANALYSIS

This absorber catalog consists of 108 pairs of galaxy-quasar spectra with either the Ca II or Na I doublet detected, or both. The absorbers can be broadly classified into Galactic or extra-galactic systems. The selection of these systems may vary depending on the science one wishes to explore through follow-up observations.

3.3.1 Selection from Equivalent Width Significance

Figure 3.6 shows the significance of the equivalent width measurements as a function of the rest equivalent width of the strong line in a doublet (Ca II K or Na I D2). The 3σ limit, or 99% confidence limit, is indicated as a red horizontal line in the figure. We find 43 systems with the significance of either Ca II K or Na I D2 line > 3.0, 53 systems with a significance between 2-3, and 12 systems with a significance <2.0. While we set the line finder to only accept lines with a significance > 2, manually remeasuring the equivalent widths and errors has, in some instances, resulted in different significances than what the line finder reported. This is due to having slightly different boundaries defining the line edges during the direct summation of the equivalent widths in each pixel.

In the Milky Way, Ca II and Na I equivalent widths have measured values less than what has been observed in external galaxies. Ca II K equivalent widths have been measured in the range of 0.08-0.8 Å, with the median equivalent width around 0.18 Å (Bowen, David V. et al., 1991). Welsh et al. (2009a) searched Milky Way sightlines (within 400 pc of the Sun) and found Ca II K equivalent widths <0.3 Å, and Na I D2 equivalent widths <0.5 Å. Bowen, David V. et al. (1991) showed that the larger equivalent widths seen in external galaxies can be recovered from the smaller values seen in the Milky Way when taking into account contributions from multiple, unresolved components, as well as projection effects through a highly extended, inclined disc. He showed that the equivalent widths seen in the Milky Way would be roughly doubled when viewed from outside our Galaxy.

Equivalent widths, seen in nearby external galaxies, of Ca II and Na I range from 0.4-1.0 Å for the Ca II K line (Womble et al., 1990; Womble, 1993; Womble et al., 1992;

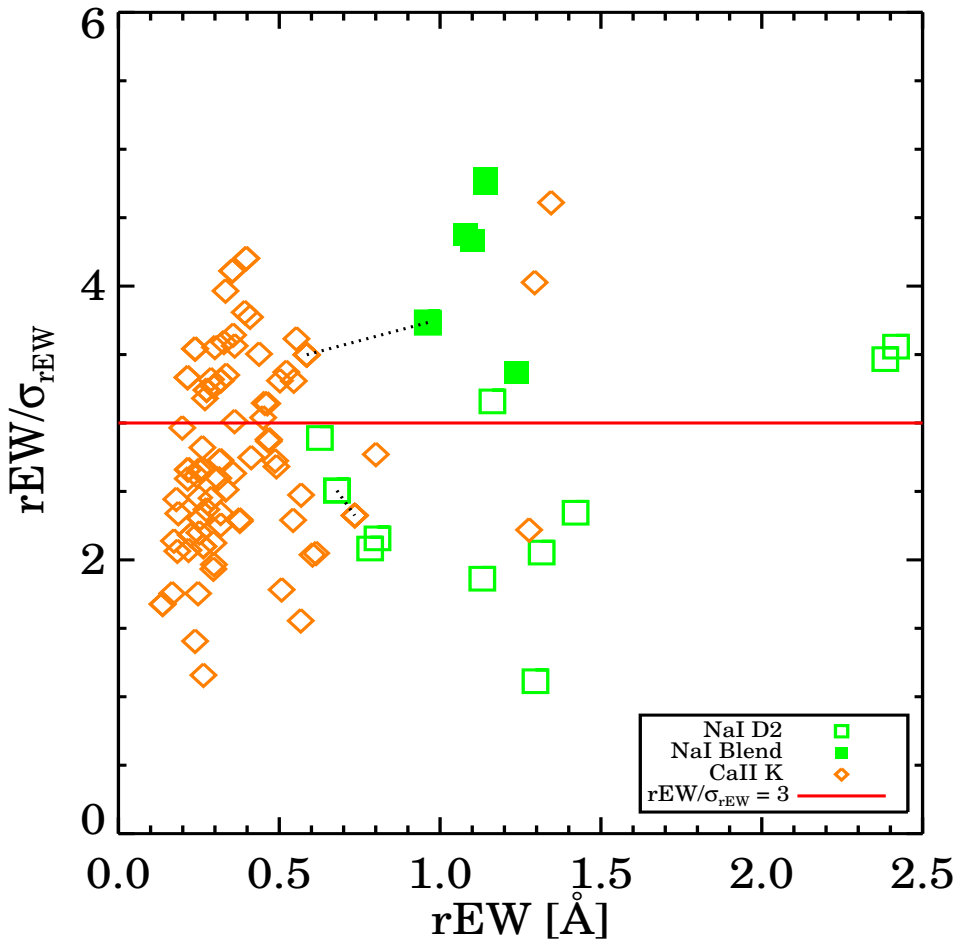

Figure 3.6 Plot of the significance (rEW/σ_{rEW}) of the Ca II K or Na I D2 lines vs the rest equivalent width, for the list of absorbers. Open green squares refer to the Na I D2 line. Filled green squares refer to blended (D2+D1) Na I systems. Open orange diamonds refer to the Ca II K line. Symbols connected by a dotted line indicate absorbers with both Na I and Ca II detected.

Zych et al., 2007; Boksenberg & Sargent, 1978; Boksenberg et al., 1980; Blades, J. C. et al., 1981; Bergeron et al., 1987; Bowen, David V. et al., 1991) and between ∼0.2-1.8 Å for the Na I D2 line (Junkkarinen & Barlow, 1994; Womble et al., 1990), or ∼2.2 Å for blended Na I systems (Kunth, D. & Bergeron, J., 1984).

There is overall agreement between our rEW values and those typically seen in the Milky Way and in nearby external galaxies. As seen in Figure 3.6, we find that the Ca II absorbers and the Na I absorbers naturally divide, with the Ca II absorbers located primarily at rEWs $\lesssim$ 0.5 Å and the Na I absorbers primarily occupying the region with rEW $\gtrsim$ 0.5 Å. This division is possibly due to a bias between the Ca II and Na I samples, where the Ca II systems include greater contributions from Galactic sightlines. While both samples should include contributions from Galactic and extragalactic sightlines, the cut we placed on the Na I sample to remove regions contaminated by incomplete Na I sky subtraction, and hence, low velocity systems, may have effectively removed Galactic contributors. Since this cut was not placed on the Ca II sample, it becomes biased towards Galactic absorbers. With this in mind, our Ca II subset could be a mix of Galactic and extragalactic absorbers, weighted more towards Galactic contributions. There are 49 Ca II systems with rEW>0.3 Å, that could be extragalactic in origin. Our Na I subset can also be a mix of Galactic and extragalactic systems, weighted more towards extragalactic systems. All of our Na I systems have a rEW>0.5 Å, and thus could be considered extragalactic, based on their strength. There are 2 Na I systems that are resolved and have unusually high rEWs for what has been seen previously, but we have checked for interloping absorption systems and none could be identified.

Figure 3.7 shows the rEW of our absorbers as a function of SDSS galaxy redshift. We again see the split in rEW between the Ca II and Na I absorbers, as well as a separation in redshift. Given the possible velocity overlap between Virgo Cluster galaxies and High-Velocity Clouds (see Section 4.2), if we consider the redshift region $\geq$0.01[2], we find that the minimum rEW seen in the resulting absorbers is 0.5 Å.

While this cannot rule out extragalactic absorbers having rEW values below ∼0.5 Å, this is consistent with rEW values seen in extragalactic absorbers so far. The large cluster of

[2]This redshift marks the estimate of Virgo's outer boundary (Binggeli et al., 1993).

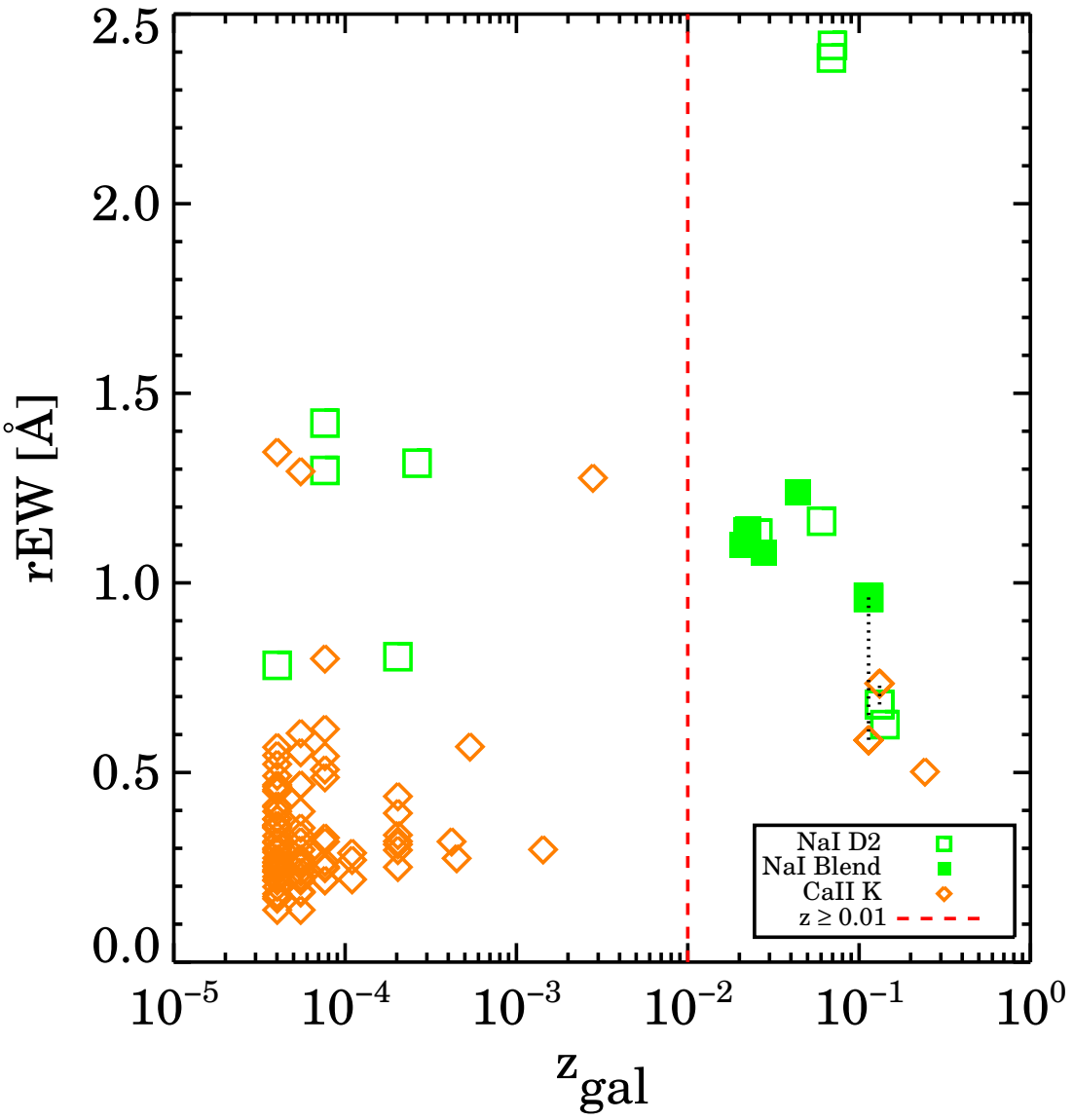

Figure 3.7 Plot of absorber rest equivalent width vs SDSS galaxy redshift, for the list of absorbers. Symbols are the same as in Figure 3.6. The dashed vertical line separates absorbers with z≥0.01. This redshift separator was chosen as a guide to separate absorbers due to Galactic sightlines and Virgo cluster galaxies from 'true' extragalactic systems, based on the outer boundary to the Virgo cluster (Binggeli et al., 1993).

Ca II systems with rEW $\lesssim 0.5$ Å at low redshifts also points to a domination by contributions from Galactic sightlines.

Examples of systems with rEW/$\sigma_{rEW} > 3.0$. are shown in Figures 3.3c, d for Ca II, and Figures 3.4e, f, g, k, n for Na I.

3.3.2 Selection from LSR Velocity

The absorber catalog contains a large number of low-redshift systems. Since we allowed velocity deviations of up to ±500 km s^{-1} from the galaxies' redshifts, it is possible that some of our detections overlap with Ca II and Na I absorbers in the Milky Way Galaxy or with absorbers in the Local Group, or with absorbers in the Virgo Cluster. One method of distinguishing Galactic absorbers from extragalactic ones is through an exploration of the v_{LSR}-galactic longitude-galactic latitude parameter space.

Wakker, B. P. & van Woerden, H. (1991) and Ben Bekhti et al. (2008) have mapped out Galactic High-Velocity Cloud (HVC) Complexes around the Milky Way. Figure 2b and 2e of Wakker, B. P. & van Woerden, H. (1991) show v_{LSR} vs l and b, respectively, of HVC's around the Milky Way. The HVCs are not uniform across the sky. They predominantly lie within two distinct regions. One region of HVCs, with -500<v_{LSR}<-90 km s^{-1}, is located below the galactic plane ($b < 0°$) and at $l < 180°$. Another group of HVCs predominantly lies in the region $l < 180°$, $b > 0°$, with LSR velocities between 90-345 km s^{-1}. The region of space between v_{LSR}±90 km s^{-1} is primarily located within the Galactic disk. As most of the HVCs lie at v_{LSR}<345 km s^{-1}, a cut above this limit will select out systems free from HVC contamination. Below this cutoff, one must place tighter constraints on galactic l and b, or obtain higher-resolution data to disentangle likely contributions by Galactic gas to any absorber candidates.

In Figures 3.8 and 3.9, we show the LSR velocity of the Ca II K or Na I D2 absorbers as a function of Galactic longitude and latitude along the sightline towards the quasar. Also plotted are lines indicating the $|v_{LSR}| > 345$ km s^{-1} cutoffs. Most of our absorbers lie within the range that is easily confused with Galactic HVCs. We find that the majority of Ca II systems (also the ones located at small rEWs in Figure 3.6) lie in the space v_{LSR}±100 km s^{-1},

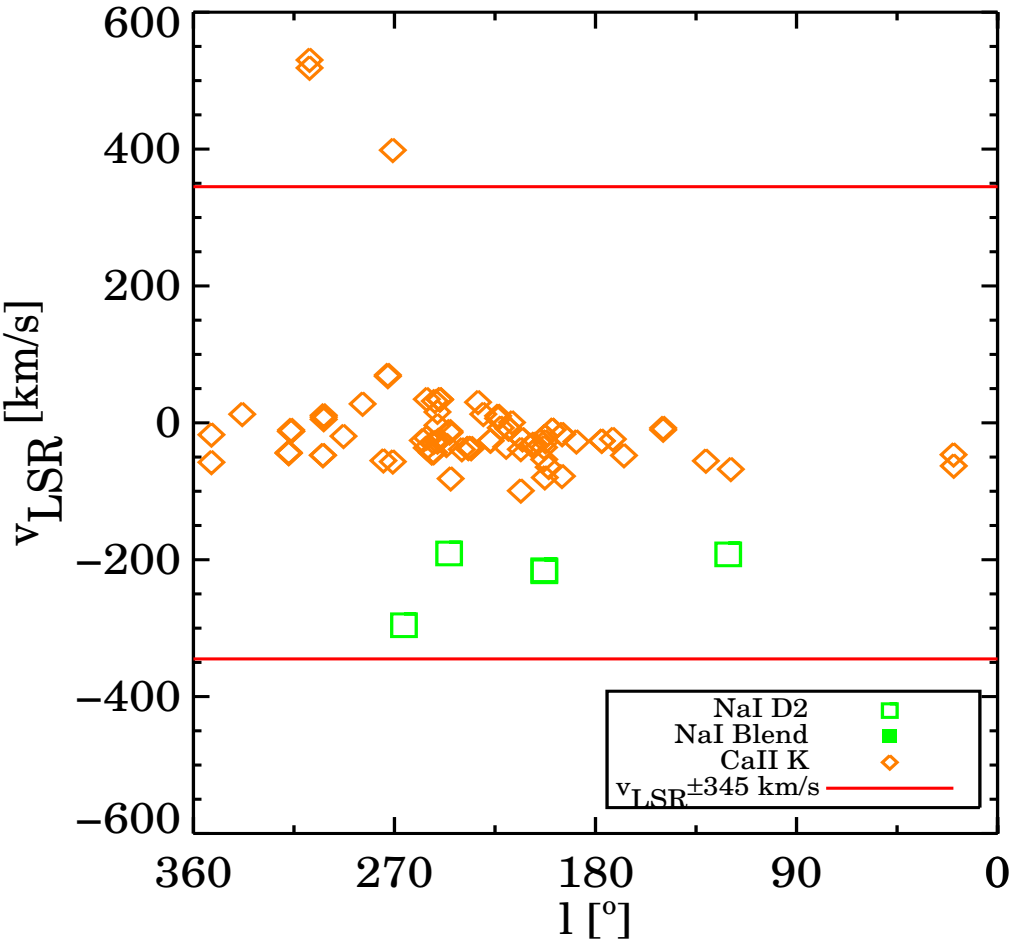

Figure 3.8 Plot of the LSR velocity of the Ca II K or Na I D2 line (or Na I doublet, if blended) against the Galactic latitude along the quasar sightline, for the list of absorbers. The two solid lines at ±345 km s^{-1} indicate the velocity cutoff separating Galactic High-Velocity Cloud complexes from extragalactic absorbers Wakker, B. P. & van Woerden, H. (1991). There are several pairs with $v_{LSR} > 600$ km s^{-1} not shown on the plot.

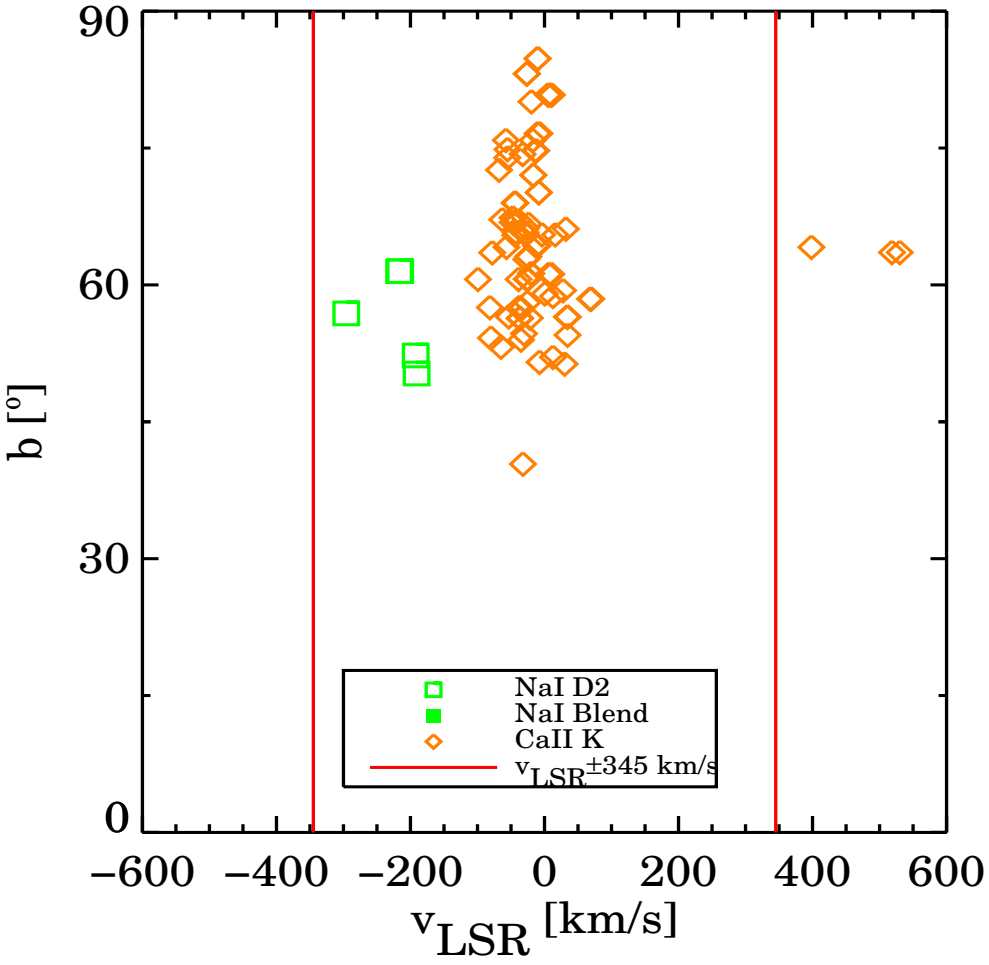

Figure 3.9 Plot of the Galactic latitude against the LSR velocity of the Ca II K or Na I D2 line (or Na I doublet, if blended) along the quasar sightline, for the list of absorbers. The two solid lines at ±345 km s^{-1} indicate the velocity cutoff separating Galactic High-Velocity Cloud complexes from extragalactic absorbers Wakker, B. P. & van Woerden, H. (1991). There are several pairs with $v_{LSR} > 600$ km s^{-1} not shown on the plot.

and thus are most likely sightlines through the Galactic disk. There are 4 Na I systems around v_{LSR}∼-200 km s^{-1} spread over 180° in Galactic longitude but are primarily concentrated around b∼55°. These systems lie in an l, b space empty of HVCs. There are also 3 Ca II systems located above the velocity cutoff for HVCs at ∼315°. Although these 7 systems lie in regions void of HVCs, there are a few Virgo cluster galaxies in our sample whose sightlines, due to our ±500 km s^{-1} window on absorber line position, can scatter out to these LSR velocities. These sightlines may then be either associated with the Virgo Cluster, the Galactic disk, or HVCs. At v_{LSR}>600 km s^{-1}, there are 11 Na I systems and 3 Ca II systems. In general, we find the stronger Ca II and Na I equivalent width systems located at large LSR velocities, as expected if these systems were truly extragalactic in nature. All the absorbers displayed in Figures 3.3-3.5 depict examples of systems with $|v_{LSR}|\geq$345 km s^{-1}.

3.3.3 Selection from Impact Parameter

As an alternative to selecting on LSR velocity, one can select absorbers based on their impact parameter. Figure 3.10 shows the distribution of absorbers in impact parameter vs b/r_{Petro} ratio. The striping seen at low Petrosian radii is due to the large search radius (in angular scale) for extremely low redshift galaxies. Each stripe corresponds to multiple quasar sightlines being associated with one galaxy. As with the prior two selection criteria, we also find a natural division between the Ca II and Na I systems. Most of the Ca II systems seen at low Petrosian radii are due to the large search area around low-redshift galaxies picking up Galactic sightlines.

DLAs are an absorber class of immense interest due to their large column densities and the fact that they trace the bulk of the neutral Hydrogen content in the Universe. Rao et al. (2003) studied the properties of low-redshift DLA galaxies (0.05<z<1.0) and found them out to an impact parameter of 38 kpc, with a mean value of 12 kpc (converted to our cosmology). Rao et al. (2011) recently identified a set of host galaxies within in the redshift range 0.1-1.0 exhibiting DLA, sub-DLA, and Lyman Limit (LL) absorption. They found a median impact parameter of 17.4 kpc for the DLAs increasing to 36.4 kpc for the LL systems, with the full range extending out to 100 kpc. Considering a mean impact parameter of 12 kpc, there are

3 systems in our sample found at small impact parameters that would be of interest. For an impact parameter of 38 kpc, covering the entire range of DLA detections, there are 17 sightlines [9 galaxies] in our sample that are within the range where DLAs have been found.

From HI maps of the Milky Way, as well as many nearby galaxies, we know the neutral Hydrogen extent of a galaxy can extend many times past the optical radius of the galaxy. Cayatte et al. (1994) and Broeils, A. H. & Rhee, M.-H. (1997) have shown that neutral Hydrogen can extend to at least twice the optical radius for spirals, and as much as 4-5x in dwarf galaxies (Swaters et al., 2002; de Blok, W. J. G. et al., 1996). It may be useful then to select systems based on the ratio of the impact parameter to the optical radius of the galaxy. Here we use the r-band Petrosian radius as a proxy for the radius of the galaxy. In some cases the Petrosian radius may miss extended light from the galaxy (Stoughton et al., 2002), so this radius can be thought of as a lower limit to the optical radius of the galaxy. With this sample, we find 7 sightlines that lie within 5x the Petrosian radius, 3 of which lie within the optical disk of the galaxy ($b/r_{\rm Petro}$<1)).

For extragalactic systems, the median impact parameter seen for Ca II and Na I is ∼15 kpc, and ∼14 kpc, respectively (Womble et al., 1990; Womble, 1993; Womble et al., 1992; Zych et al., 2007; Boksenberg & Sargent, 1978; Boksenberg et al., 1980; Bergeron et al., 1987; Bowen, David V. et al., 1991; Blades, J. C. et al., 1981; Junkkarinen & Barlow, 1994). Considering this region of parameter space in Figure 3.10, we find that our Ca II and Na I absorbers are located within Petrosian radii ∼10 kpc, the median value seen in the SDSS Spec-Photo sample we draw from. These systems then are most likely extragalactic. Examples of systems with b/r_{Petro}<5 are shown in Figures 3.3a, c, d, for Ca II and Figures 3.4a, e, f, g, h for Na I.

3.3.4 Notes on Individual Absorbers

Here we provide a few notes on individual absorbers from our absorber list.

- **SDSS J102703.86+283721.9**

  This galaxy has a SDSS redshift of 0.00020±0.00016, classified manually with high confidence, and has an *SDSS zwarning* of 'Absorption lines inconsistent'. The galaxy is

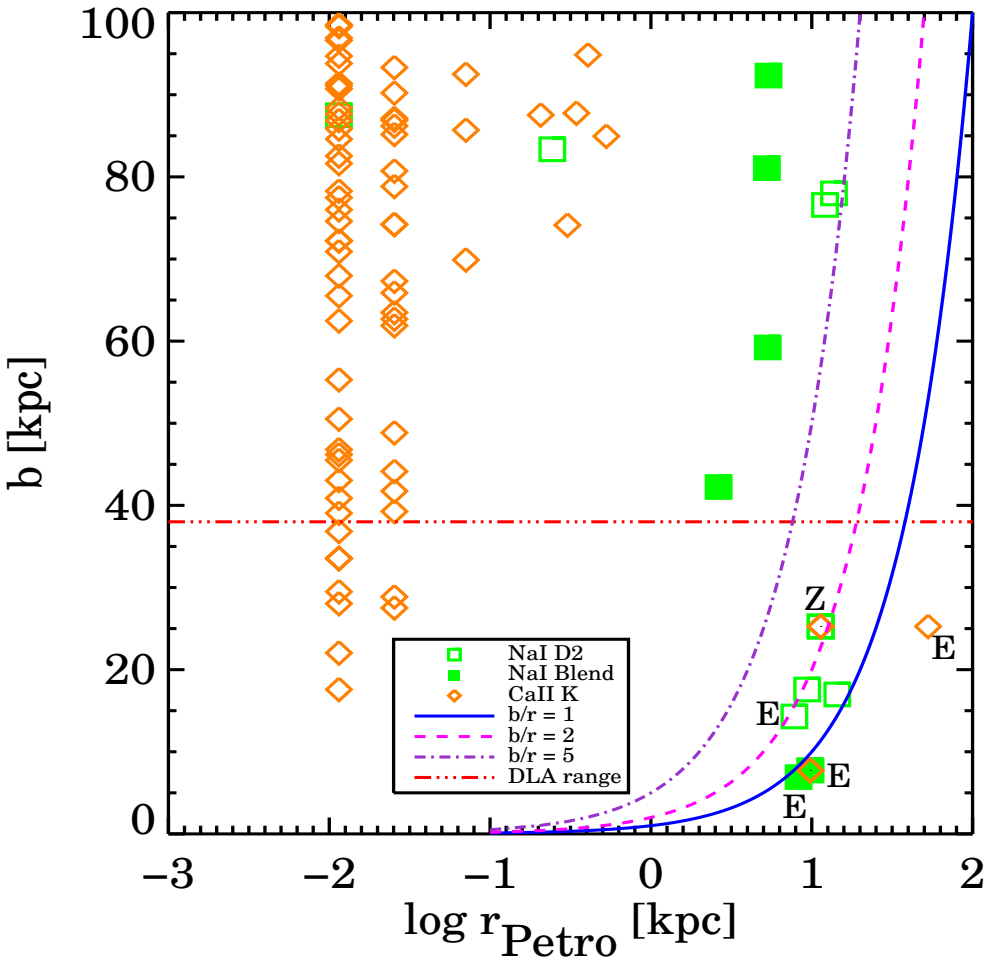

Figure 3.10 Plot of quasar impact parameter versus SDSS r-band Petrosian radius, for the list of absorbers. The line at 38 kpc represents the impact parameter out to which low-z DLAs have been found by Rao et al. (2003). The three curved lines indicate the ratio of the impact parameter to the r-band Petrosian radius (1, 2, and 5, respectively). The vertical striping apparent in the data at low Petrosian radii is a result of multiple QSO sightlines being found within the 100 kpc search radius of a low redshift galaxy. The absorbers marked with 'E' and 'Z' represent the four extragalactic absorbers, and the Zych absorber, discussed in Section 3.4.

projected against NGC 3245A, which has a redshift of 0.00441±0.000008. Within the 100 kpc search radius, seven quasar sightlines were identified with Ca II absorption, and one sightline with Na I absorption. However, the uncertainty of this galaxy's redshift may have resulted in erroneous matches and calls into question the apparent association of this galaxy with these sightlines. We exclude this galaxy from Figures 3.10 and 3.11.

- **SDSS J113420.50-033525.4**

  This galaxy has a SDSS redshift of 0.00008±0.00007, at high confidence. Twelve quasars sightlines were identified with Ca II absorption and four sightlines with Na I absorption. Upon viewing the spectrum for this galaxy, there appear to be several absorption lines indicating a stellar spectrum that corroborates the reported SDSS redshift. Light from a star may have entered the fiber when the spectrum was taken. This galaxy is also identified in the 2dFGRS as N171Z241, with a reported redshift of 0.1151±0.0003. The spectrum for N171Z241 visually does not agree with the spectrum from SDSS. Although the sightlines discovered through this association are real detections of Na I or Ca II, this discrepancy in the galaxy redshift leaves some doubt as to the associations between this galaxy with these quasar sightlines. We exclude this galaxy from Figures 3.10 and 3.11.

- **SDSS J114313.05+193646.9**

  The galaxy lies at a redshift of 0.02085±0.00009. SDSS J114323.71+193448.0, the quasar, is located 81 kpc from the galaxy position. This galaxy is in the cluster Abell 1367 (as indicated in NED[3]), along with SDSS J114318.07+193401.3 and SDSS J114336.98+193616.7, listed below. As these three galaxies intersect the same sightline to the quasar, it is unknown which galaxy is responsible for the absorbing gas, or if the gas is intracluster material.

- **SDSS J114318.07+193401.3**

  The galaxy lies at a redshift of 0.02262±0.00015, and is located 42 kpc from the quasar. This galaxy is in the cluster Abell 1367.

- **SDSS J114336.98+193616.7**

  The galaxy lies at a redshift of 0.02201±0.00019, and is located 92 kpc from the quasar.

[3]NASA Extragalactic Database

This galaxy is in the cluster Abell 1367.

- **SDSS J150400.94+240437.1**

  This galaxy lies at a redshift of 0.06894±0.00010. The quasar, SDSS J150359.48+240532.8, is located 78 kpc from the galaxy position. This galaxy is possibly in a group with SDSS J150403.17+240559.8, listed below. The two galaxies intersect the same sightline to the quasar SDSS J150359.48+240532.8, so it is unclear which galaxy is responsible for the absorber, or whether the absorption is coming from intragroup material.

- **SDSS J150403.17+240559.8**

  The galaxy lies at a redshift of 0.06997±0.00019, and is located 77 kpc from the quasar. This galaxy is in a group with SDSS J150400.94+240437.1.

3.4 CHARACTERISTICS OF EXTRAGALACTIC ABSORBER GALAXIES

In the previous section we described various ways to differentiate Galactic absorbers from extragalactic ones. While the absorbers in the Galactic disk or in HVCs are interesting in and of themselves, our original purpose was to identify Ca II and Na I systems due to, as well as residing close to, nearby external galaxies.

3.4.1 Emission-Selected Systems

There are four absorption systems that satisfy the following three conditions: $b/r_{\rm Petro} < 5$, $|v_{LSR}| \geq 345$ km s^{-1}, and rEW$/\sigma_{rEW} \geq 3$. There are two systems detected in Ca II, one of which was also detected in Na I, and two detected in Na I. These systems are SDSS J141745.62+162509.3 (Figure 3.3c), SDSS J155752.51+342142.8 (Figures 3.3d and 3.5b), SDSS J122037.63+283803.3 (Figure 3.4f), and SDSS J140613.22+153035.5 (Figure 3.4g). These four systems have a $\langle g-r \rangle$ of (μ,σ)=(0.6,0.2) and a $\langle M_r \rangle$ of (μ,σ)=(-20.1,1.8). Adopting an $^{0.1}r$-band L^* of -21.28 (Blanton et al., 2003c), we find that the $\langle L^*_{r^{0.1}} \rangle$ is (μ,σ)=(0.8,0.4) $L_\odot$. All colors and magnitudes were calculated using Kcorrect v4.2 (Blanton & Roweis, 2007). The mean impact parameter of the 4 systems is (μ,σ)=(13.6,9.8) kpc, while the

$\langle b/r_{\rm Petro} \rangle$ ratio is (μ,σ)=(1.0,0.6).

Figure 3.11 shows the rest-frame $g-r$ color versus the SDSS absolute r-band magnitude, band-shifted to $z = 0.1$. As one galaxy may have multiple quasar sightlines associated with it, we only plot the 22 unique galaxies. The two galaxies with uncertain redshifts have been excluded from the plot. Adopting a red/blue color separation from Yan et al. (2006), we find 2 red galaxies and 20 blue galaxies. In both the red and blue samples we find a mix of galaxies with Ca II and Na I sightlines. Our four extragalactic Ca II and Na I systems lie below the color separation line, and would be classified as blue, $\sim$0.1-1.0L_r^* galaxies.

3.4.2 Comparison with Absorption-Selected Systems

Zych et al. (2007) selected Ca II systems from the SDSS using the more traditional approach of identifying the absorption line in the quasar spectrum first, with follow-up imaging to locate the associated host galaxy. They identified 5 Ca II absorption systems in this manner and found them primarily located in blue, $\sim$L*, star-forming galaxies with the Ca II located at small impact parameters (11.6$\pm$8.4 kpc)[4]. Of the 5 pairs reported by Zych et al. (2007), one is found in our sample, the galaxy SDSS J111849.76-002109.9 (Figures 3.3a and 3.4a). The Ca II equivalent width we measure for SDSS J111849.76-002109.9 is consistent with that reported in Zych et al. (2007). We detect Na I from this galaxy as well. This galaxy, along with one additional Na I system, is included in our list of extragalactic absorbers if we relax the condition on absorption line significance. Of the other 4 galaxies in Zych's sample, one galaxy was detected within the fiber of the quasar and the other 3 do not have spectroscopy in SDSS, and thus are not in our sample of DR7 galaxies.

It is interesting to note that there is a general agreement in the overall galaxy properties between our emission-selected absorbers and their absorption-selected absorbers. Both methods returned blue, $\sim$L* galaxies.

[4]Mean value calculated using data from their Table 5

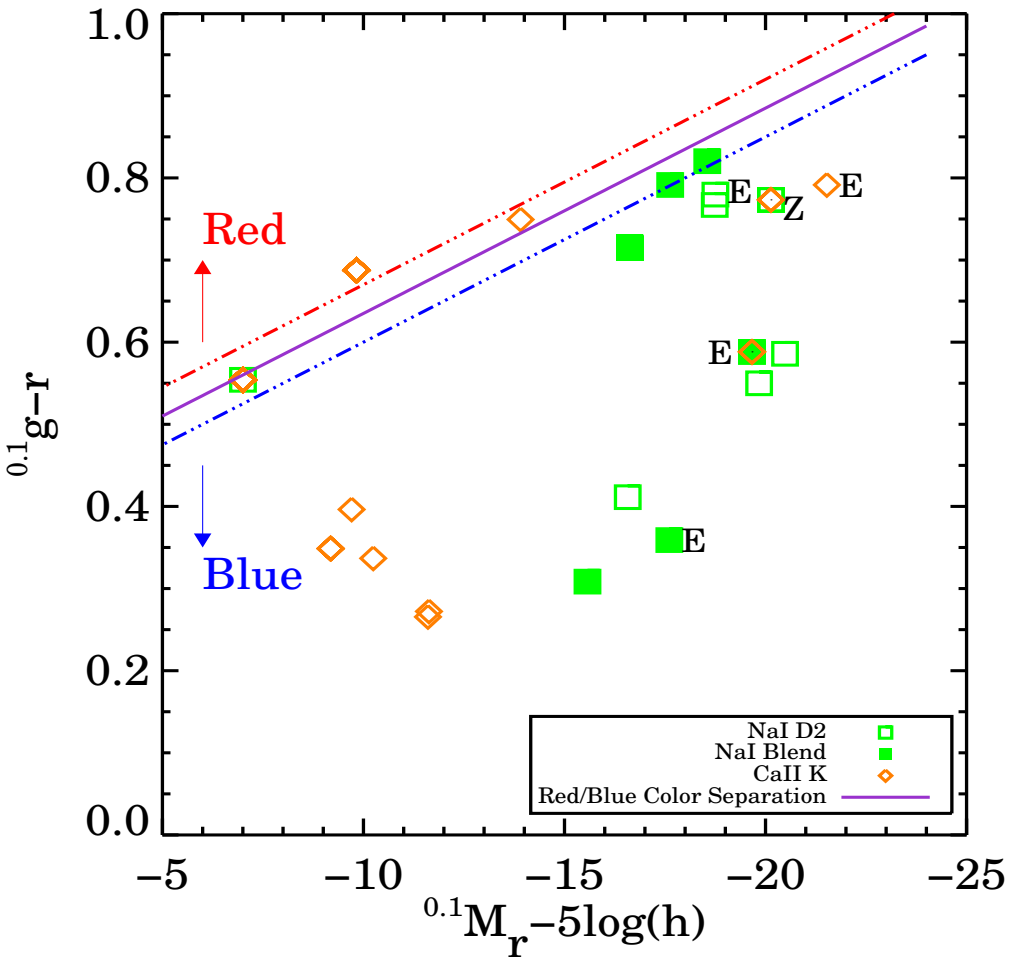

Figure 3.11 Plot of galaxy $g-r$ color versus galaxy SDSS r-band absolute magnitude, for the list of absorbers. The purple line corresponds to the average of the red/blue galaxy cutoffs from Yan et al. (2006). Applying the cut divides our sample into 5 red galaxies and 19 blue galaxies. Galaxies between the red and blue regions are ambiguous in their classification. The absorbers marked with 'E' and 'Z' represent the 4 extragalactic absorbers and the Zych absorber, discussed in Section 3.4. All absolute magnitudes were calculated using distances derived from heliocentric redshifts, with the exception of the four Virgo cluster galaxies. For those galaxies, distances were derived from redshifts corrected for the Local Group infall towards Virgo, taken from HyperLeda (Paturel et al., 2003).

3.5 SUMMARY

We have searched the SDSS DR7 for low-redshift galaxy-quasar pairs, where the quasar is projected within 100 kpc of the galaxy, and found 97,489 galaxy/quasar pairs from a sample of 105,783 spectroscopic quasars and 798,948 spectroscopic galaxies. From this list of pairs, we searched for Ca II and Na I absorbers, using an automated process followed by visual inspection, and found 108 absorption line systems, 92 of which are Ca II, 16 of which are Na I, along with ∼5600 questionable candidate features. Within our sample of 108 absorbers, we find many sightlines that coincide with sightlines through the Galactic disk or through High-Velocity Cloud complexes in our halo.

Our goal was to identify Ca II and Na I systems that lie within or near known low-redshift galaxies. To this end, we placed constraints on the absorber line significance (rEW/σ_{rEW} $\geq$3), on the LSR velocity ($|v_{LSR}|\geq$345 km s^{-1}), and on the ratio of impact parameter to r-band Petrosian radius ($b/r_{\rm Petro} < 5$). We find 4 bonafide extragalactic galaxies with Ca II and/or Na I absorption detected along sightlines to background quasars. One is detected in Ca II only, two are detected in Na I only, and one is detected in both Ca II and Na I. These absorption systems arise in blue, ∼0.1-1.0L_r^* galaxies. With the absorbers' impact parameters within the range seen for low-redshift DLAs, these systems would be good candidates for follow-up HI 21 cm or UV observations to determine neutral Hydrogen column densities.

The work in Chapter 4 consists of a statistical exploration of different galaxy properties for the Ca II and Na I absorbers and non-absorbing systems via stacking techniques. Another area of future work will be to compare the emission line properties of the absorbing galaxies in our sample with those from the absorption-selected samples.

4.0 SPECTRAL STACKING AND HOST GALAXY ANALYSES

In this chapter we continue our analysis of the DR7 sample of Ca II and Na I absorbers. We focus various comparisons between the DR7 absorber samples with the non-absorber samples. In Section 4.1, we describe the motivation for the stacking analysis. In Section 4.2, we detail the creation of the sample subset with which we perform the analysis. One question regarding the sample construction is the number of contaminants within the absorber sample. Section 4.3 addresses this concern. In it, we describe the results of a series of Monte Carlo realizations used to ascertain the expected number of false positives in the absorber sample described in Section 4.2 from the sample of non-absorbers. From these results we select a subset of absorbers with a very low false positive contamination, a significance at least 3σ. In Section 4.4, we analyze the sample and, in Section 4.5, we discuss the results of the analysis.

4.1 INTRODUCTION

In section 3.2, we outlined the creation of the general sample of Ca II and Na I absorber galaxy-quasar pairs from the SDSS DR7 and subsequent visual classification of individual systems. In section 3.3 we discussed the visually identified absorber systems within the context of identifying probable sightlines through Milky Way High-Velocity Clouds, the Virgo Cluster, or external galaxies. For the few visually identified absorbers around external galaxies, we briefly describe some of their galaxy properties and compare them to another small sample from Zych et al. (2007). Although the visual identification of individual systems allows for a more satisfying sample, the process usually results in a low number of systems, making any statistical analysis of the sample rather difficult. With such low numbers, it

becomes hard to quantify the relationship between absorber environment and galaxy as well as differences between absorber and non-absorber galaxies. The low numbers of systems identified through visual inspection can be attributed to the low S/N ratios seen in the SDSS spectra. The typical S/N ratios achieved in our quasar spectra are ∼8 near rest-frame Ca II and ∼11 near rest-frame Na I. This makes high significance detections of these absorption lines difficult within individual systems as the spectra are quite noisy. One solution is to stack the spectra. This allows us to reach much higher S/N ratios and produce a cleaner spectrum with which to detect absorption and examine trends between absorber and galaxy properties. Spectral stacking also allows us to include many more visually uncertain absorption-line systems identified by the line-finder. This improves our sample numbers making statistical analysis between the absorber and non-absorber galaxy samples possible.

4.2 SAMPLE CONSTRUCTION

For the purposes of constructing a large enough sample allowing statistical analyses, we have performed the following steps to create such a sample:

1. Recall that in Section 3.2, we noted that the automated line finder identified 1749 Ca II systems satisfying the following criteria: 1.) the significance of the Ca II K line must be ≥ 2.0, 2.) a minimum velocity separation of $\Delta v \sim 500$ km s^{-1}, 3.) the significance of the Ca II H line must be ≥ 1.0, and 4.) conditional checks ensuring the doublet ratio was physically consistent as well as the location of the Ca II H line was in the expected location. The other 106,379 features were considered to be Ca II non-absorbers. As for the Na I systems, 4505 systems were identified satisfying the criteria: 1.) the significance of the Na I D2 line ≥ 2.0, and 2.) a minimum velocity separation of $\Delta v \sim 500$ km s^{-1}. The other 94,236 systems were considered to be Na I non-absorbers. We also removed from the absorber samples those systems visually classified as an interloping doublet system.
2. We then removed spectra with regions of corrupted flux and/or flux errors. This reduced the absorber samples to 1744 Ca II systems, and 4470 Na I systems. For spectra that had bad pixels within the fitting region, we interpolated over those regions and replaced

the flux and error values using values from the surrounding continuum. We also applied this processing to the sample of non-absorbers, after placing the following redshift cut.

3. We then placed a redshift cut on the entire sample, requiring $z_{gal} \geq 0.01$, in order to sufficiently remove contributions from Galactic sightlines or sightlines through Virgo Cluster galaxies. This redshift cut, marking Virgo's outer boundary (Binggeli et al., 1993), was chosen due to the possible velocity overlap between Virgo Cluster galaxies and High-Velocity Clouds (see Section 4.2). This reduced the samples to:
   - Ca II Absorbers - 95
   - Ca II Non-Absorbers - 12545
   - Na I Absorbers - 321
   - Na I Non-Absorbers - 11520

   The above list represents the final samples used in all further analyses depicted in this chapter.

4.3 ROBUSTNESS OF THE AUTOMATED LINE FINDER ALGORITHM

One issue that can affect any interpretation of the absorber/non-absorber analysis is the number of false positives produced by the line finding algorithm, i.e. the number of true non-absorbers that have been falsely classified by the line finder as an absorber or a detection. If the number of contaminants to the absorber sample is large, then any analysis using that sample will be biased. To ascertain the false positive rate, or the expected number of false positives, we implement a Monte Carlo realization on a 'null' spectrum, one with zero signal and Gaussian distributed random noise based on typical SDSS errors, with an additional error component representing errors on the continuum placement. From this 'null' spectrum, we generate a new simulated spectrum by, on a per pixel basis, randomly generating a new flux value, f_i, drawn from a Gaussian distribution with $\mu = f_i^o$ and $\sigma = \sigma_i^o$, where f_i^o and σ_i^o are the original flux and error values from the spectrum, at that pixel. We then run the automated line finder, look for any absorption feature satisfying the original criteria, i.e., the significance threshold for the strong line in the doublet, the velocity separation, and the

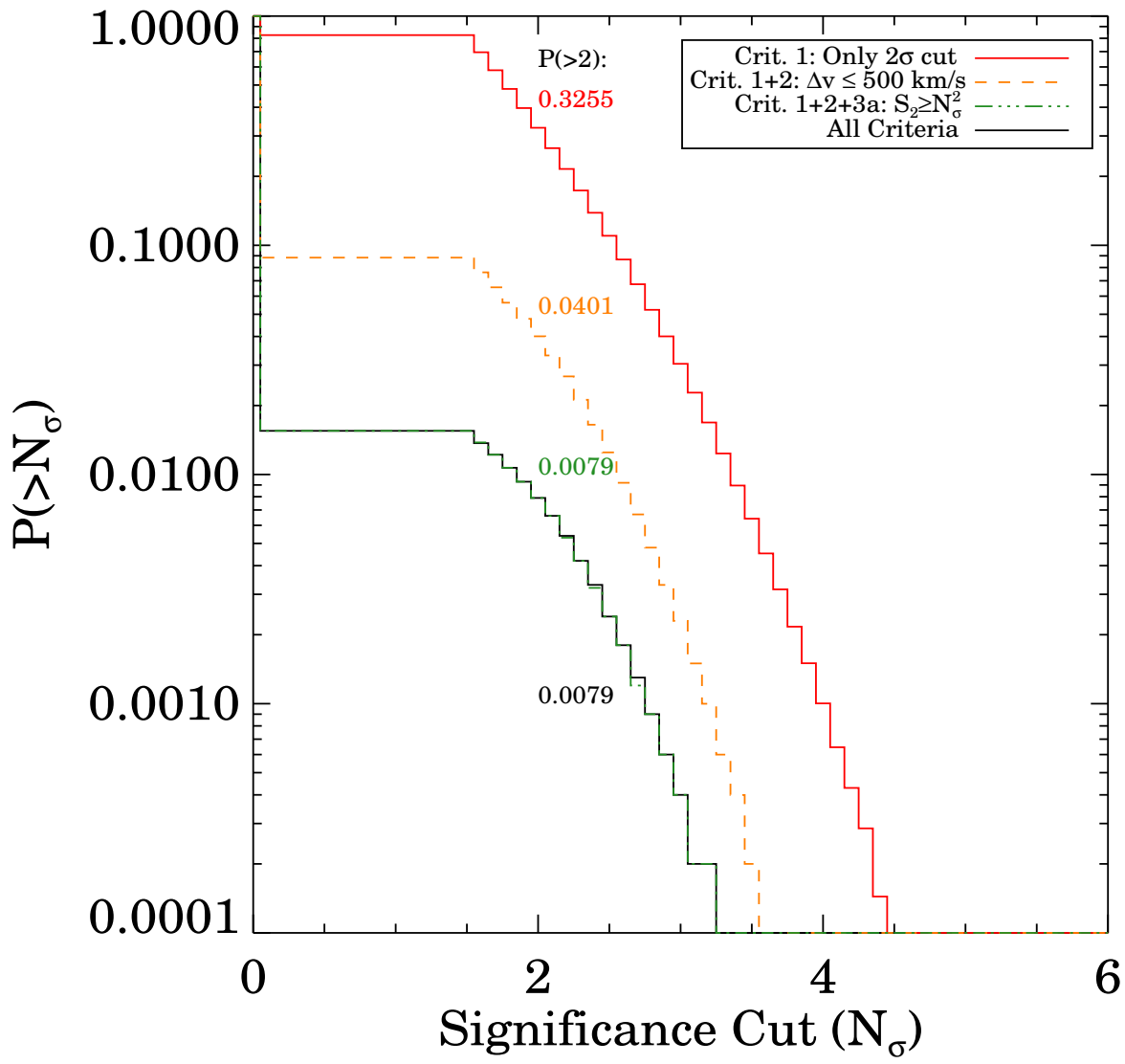

Figure 4.1 Monte Carlo Realization results for a null spectrum, looking for a Ca II doublet. Each curve represents the probability of detection above a given N_σ, as a function of N_σ. The solid black curve is the probability estimate given our original search criteria. The probability of being detected at or above 2σ is 0.0079. The solid red curve shows the probability considering only our first criterion, the significance of the Ca II K line. Moving downwards, each curve folds in an additional criteria until we reach the solid black curve.

significance threshold and doublet ratio checks on the weaker line in the doublet. Recall the significance of an absorption feature i is calculated as

$$S_i = \frac{EW_i}{\sigma_{EW_i}} \tag{4.1}$$

where EW and σ_{EW} are the equivalent width and error as measured directly from the pixel spectrum. The line finder checks that $S_i \geq N_\sigma$, where N_σ is our chosen significance threshold. When we refer to a 2σ detection, we mean where $N_\sigma = 2.0$ and $S_i \geq 2.0$, for the Ca II K line, for example. To study the behavior of the expected number of systems with N_σ, we lowered the initial significance threshold on the strong line from 2σ to 1.5σ. If a candidate feature was detected, we record the measured line significance, while if the feature failed any of the criteria, a zero is recorded for the significance. We do this 10,000 times to retrieve a distribution of line significances (for the strong line) for that spectrum. From that distribution, we compute the probability of being detected at a given significance threshold, N_σ, as a function of N_σ. To account for variability in the resulting probability distribution, we repeat the entire realization process 20,000 times and take the mean of the resulting probability distributions to produce the final curves seen in Figures 4.1 and 4.2.

Figure 4.1 shows the results of the Monte Carlo realizations for the 'null' spectrum. The solid black curve represents the probability of detection given all our original search criteria. The other colored lines represent the probability using only certain criteria. The solid red line (top) marks the probability of detection considering only our first criterion, namely that the strong line of the doublet exceeds the N_σ threshold. Each additional curve represents the probability when each of our additional criteria are folded into the realizations. The dashed orange curve folds in the second criterion, i.e. the velocity separation from the expected galaxy position. The dash-dotted green curve then adds in the significance threshold criterion on the weaker Ca II H line. The solid black curve includes the criterion of the consistency checks between the Ca II K and H lines. As expected, the inclusion of additional cuts reduces the probability of a false positive. The probability of a false positive being detected at or above the 2σ level, given all of our line criteria, is 0.0078. Considering all 12545 Ca II non-absorbers in our sample, the expected number of false positives detected at or above the 2σ level is 99.

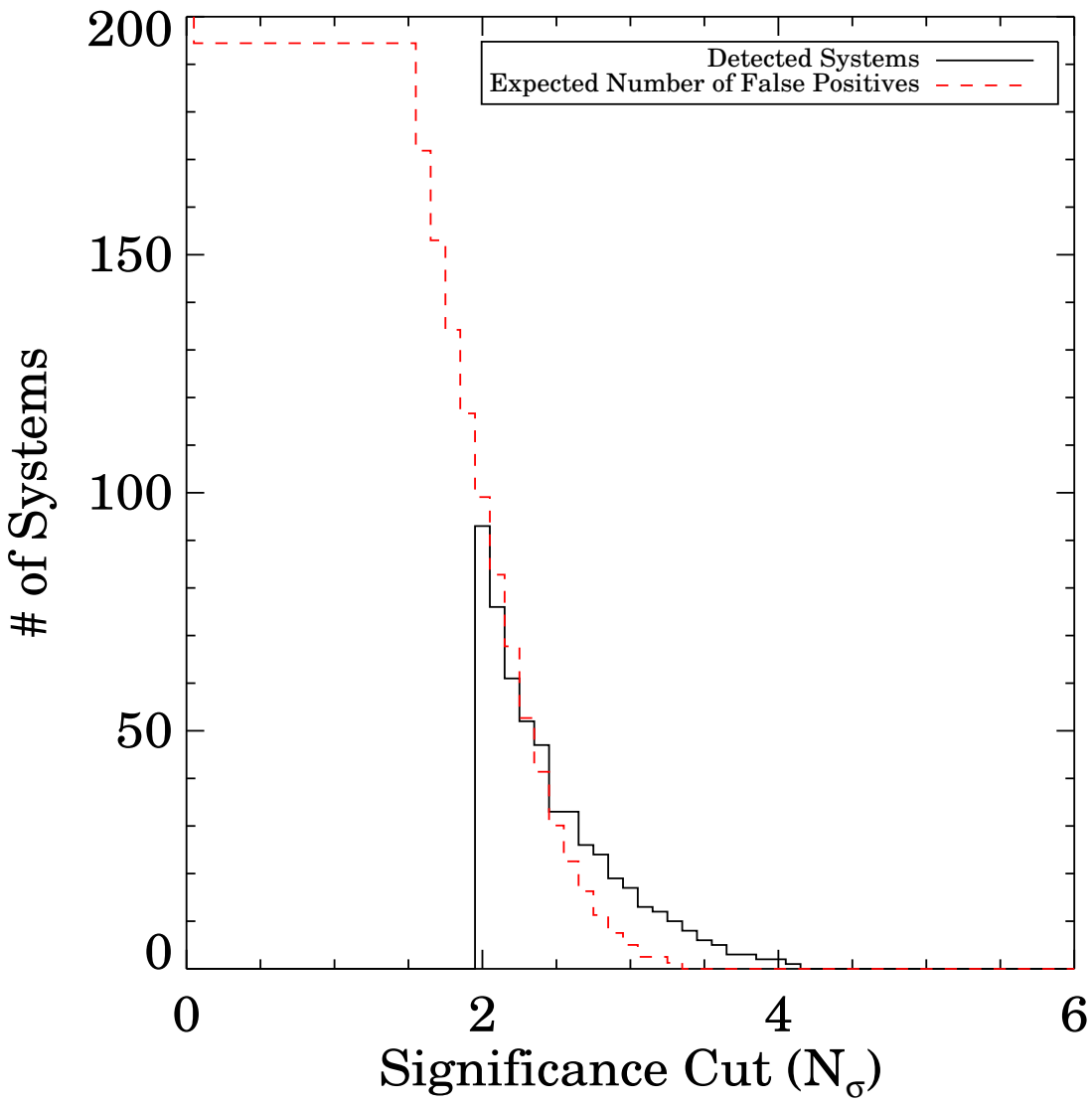

Figure 4.2 The number of systems above a given significance cut as a function of significance cut. The solid black line shows the number of detected Ca II systems by the automated line finder. There are 95 Ca II systems detected at or above 2σ, while we have 19 systems detected at or above the 3σ level. The dashed red line shows the expected of number of false positives for a given N_σ threshold. At the 2σ level and above, $\sim$100 false positives are expected, while only 5 false positives are expected at or above the 3σ level.

From the Monte Carlo realizations of the 'null' spectrum, we found the expected number of false positives to be around 99 systems. Figure 4.2 compares the number of detected Ca II absorbers by the automated line finder with the expected number of false positives at a given N_σ threshold. Considering our original 2σ threshold, we have 95 identified Ca II absorbers and there are 99 expected false positives. Therefore, at the 2σ level, we are unable to rule out the possibility that any of the 95 absorbers are actually false detections. However, considering systems detected at or above 3σ, we find the expected number of false positives to be only 5 systems, while we detect 19 systems with a line significance greater than or equal to 3σ. It becomes clear from Figure 4.2 that, given the typical spectral resolution and S/N ratio for SDSS spectra, absorption doublets detected at 2σ are quite unreliable. At the 2.5σ level, there is a crossover point where the expected number of false positives drops below the total number of detections, and you could begin to pick out reliable absorption systems. However, to ensure a large sample of reliable absorption doublets with a low false positive rate, one should choose at least 3σ as the significance threshold.

4.4 ANALYSIS OF 3σ ABSORBER SYSTEMS

Given the results of the Monte Carlo realizations from the previous section, we have decided to select out only those absorption systems where the strong line in the doublet was detected at or above a significance of 3. With this subset we will redo some of the analysis in this chapter and compare the results. For the Ca II absorber subset, there are 19 systems out of the 95 where the Ca II K line was detected at or above 3σ and 36 systems from the Na I absorber subset detected at or above 3σ.

4.4.1 Spectral Stacking Analysis

Stacking is a widely used technique (Nestor et al., 2003; Pieri et al., 2010; Dobos et al., 2011) to combine multiple low signal-to-noise spectra into one spectrum with a much higher signal-to-noise. The general steps are as follows. Prior to stacking, we first fit all quasar spectra with

a b-spline to perform a local continuum fit around the absorption line regions of interest. With each b-spline fit, we mask out a ∼20 Å region centered at the expected absorber line location and linearly interpolate across the region. Twenty breakpoints were used in the fitting. After fitting, we then shift each spectrum to the rest-frame of the absorber galaxy. Due to the varying dispersion from short to long wavelengths in the SDSS spectrum, we rebin the wavelengths to a constant dispersion of 0.1 Å/pixel for the absorber spectra. For computational reasons, we rebin the non-absorber spectra to a constant dispersion of 0.5 Å/pixel. Once all the spectra are on the same wavelength scale, we interpolate the fluxes and errors over the new wavelength range. Finally we stack each absorber and non-absorber group. To produce the stacked spectrum, for each pixel bin across all spectra, we first reject pixels that deviate from the median flux value by 5σ. We then stack the remaining pixels using an inverse-variance weighted mean. The error on the stacked flux in a given pixel was computed as $1/\sqrt{\sum_{i=1}^{N} 1/\sigma_i^2}$.

Figure 4.3a shows the stack of all 19 Ca II absorbers. The mean S/N ratio in the stack is 47. The Ca II doublet is present in the stack. We measure the equivalent width by a weighted direct-summation across the line profile. We also fit a Gaussian profile to the doublet to get velocity widths. The K line has an equivalent width of 1.46±0.03 Å and v_{FWHM} = 725±17 km s^{-1}. The H line has an equivalent width of 0.84±0.03 Å and v_{FWHM} = 746±28 km s^{-1}. The doublet is partially saturated, with a doublet ratio ∼1.7. The mean 3σ equivalent width upper limit per resolution element (resel) in the continuum is 0.018 Å. Figure 4.3b shows the wavelength region around rest-frame Na I for the Ca II absorbers. We find a weak blended Na I signal with an EW of 0.16±0.02 Å and a v_{FWHM} = 294±38 km s^{-1}. The mean S/N ratio in the continuum is 60, and the mean 3σ EW upper limit per resel is 0.023 Å. As expected, the mean S/N at longer wavelengths (red end) is generally higher than at shorter wavelengths (blue end).

Figure 4.4b shows the stack of 36 Na I absorbers. The mean S/N ratio is 88. We detect a blended Na I absorption feature with an EW = 1.86±0.03 Å and a v_{FWHM}=813±11 km s^{-1}. The mean 3σ EW upper limit per resel in the continuum is 0.017 Å. Figure 4.4a shows the Ca II rest-frame wavelength region for the Na I absorbers. The mean S/N ratio in the stack is 51. We detect no Ca II absorption features in the stack. The mean 3σ EW upper limit

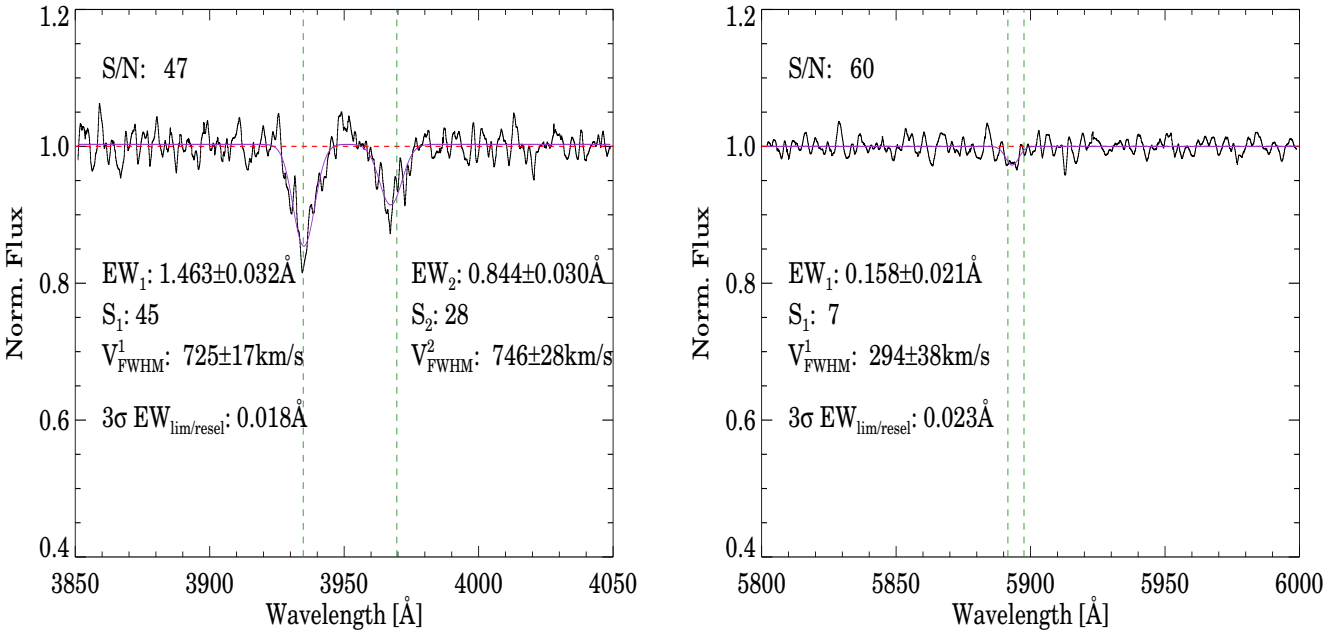

(a) Ca II

(b) Na I

Figure 4.3 The stack of all 19 Ca II absorbers. 4.3a shows a stack around the Ca II rest wavelength region. 4.3b shows a stack around the Na I rest wavelength region. For all stacked plots, the two dashed green vertical lines indicate the rest-frame position of the absorber lines, the dashed red line shows the continuum, and the solid purple line shows our fit to the absorption. 1 denotes measurements of the either the Ca II K line or the Na I D blend, 2 denotes measurements for the Ca II H line, where S_1 and S_2 are the significances of lines 1 and 2, respectively.

per resel is 0.016 Å.

To test how robust the stacks are to any outlying spectra that may be contributing to the stack, we randomly select and stack 70% of the absorbers in a set. The resulting stacks do not show any appreciable difference from the stacks generated using the entire set of spectra, as depicted in Figures 4.3 and 4.4. We perform the same robustness tests on the stack of the non-absorbers.

Figure 4.5a shows the stack of the 12545 Ca II non-absorbers. The mean S/N ratio of the continuum is 1056. As a reminder, the non-absorber sample should include absorbers

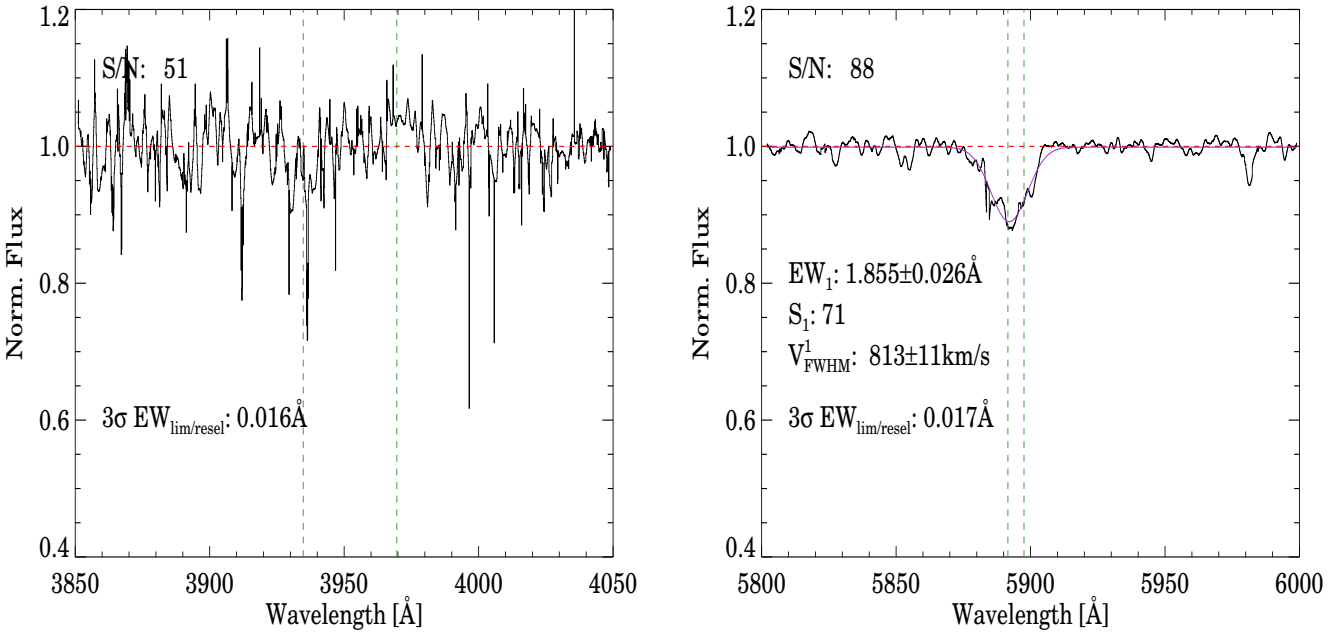

(a) Ca II

(b) Na I

Figure 4.4 The stack of all 36 Na I absorbers. 4.4a shows a stack around the Ca II rest wavelength region. 4.4b shows a stack around the Na I rest wavelength region.

that did not meet our required criteria, i.e. with line significance <2.0. We detect no Ca II features in the stacked spectrum. The mean 3σ EW upper limit per resel is 0.019 Å. Figure 4.5b shows the Na I rest-frame wavelength region of the Ca II non-absorbers. The mean S/N ratio here is 1473. In contrast with the Ca II wavelength region, we detect a weak, blended, Na I absorption line. The line has an EW of 0.101±0.040 Å, with v_{FWHM} = 930±32 km s^{-1}.

Figure 4.6b shows the stack of the 11520 Na I non-absorbers. As with the Ca II non-absorbers, this stack includes absorbers with line significance <2.0. We again detect a weak, blended, Na I absorption line in the stack of non-absorbers. The mean S/N ratio is 1416. The Na I line has an EW of 0.035±0.028 Å, and a v_{FWHM} of 917±67 km s^{-1}. We do not detect any weak Ca II features in the Ca II rest-frame wavelength region. The mean 3σ EW upper limit per resel is 0.017 Å.

Comparing Figures 4.4a and 4.6a with the other stacks shows the Ca II wavelength region

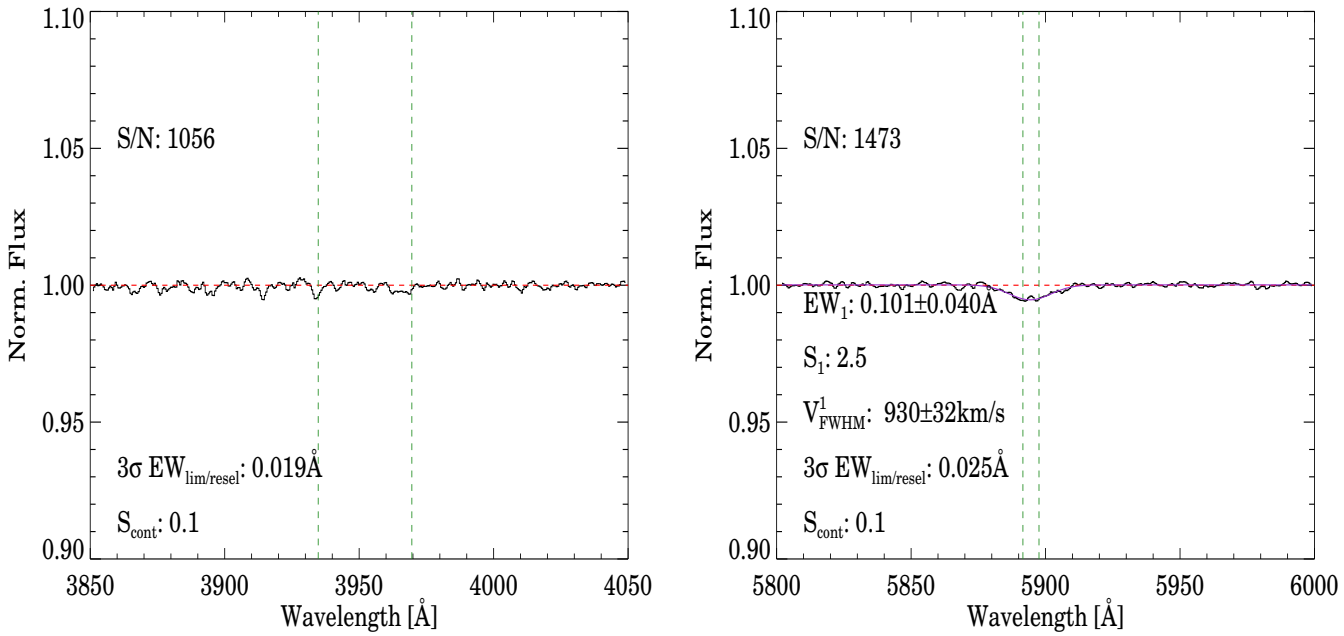

(a) Ca II

(b) Na I

Figure 4.5 The stack of all 12545 Ca II non-absorbers. 4.5a shows a stack around the Ca II rest wavelength region. 4.5b shows a stack around the Na I rest wavelength region.

of the Na I absorbers and non-absorbers to be visibly noisier. This is due to the inclusion of Ca II Ly-α forest contamination in the set of Na I spectra. Recall that in Section 3.1, two parent samples were constructed based on the rejection of Ly-α forest contaminants in the Ca II or Na I absorption regions, respectively. Those systems rejected from the Ca II parent sample are not necessarily rejected from the Na I parent sample. Thus when the Ca II region of the Na I systems is examined, the region is noisier. The exclusion of these systems from the Na I stacks produces a cleaner stack, however the presence of any Ca II signal remains absent.

Of note is the lack of Ca II present in the stacked spectra of the non-absorbers, both of the Ca II non-absorbers, as well as in the Ca II region of the Na I non-absorbers (see Figures 4.5a and 4.6a). Given that the non-absorber sample should contain many weak absorption systems that did not pass our search criteria, their presence should appear upon stacking the non-absorber set. And this is indeed seen with the Na I non-absorber stacks.

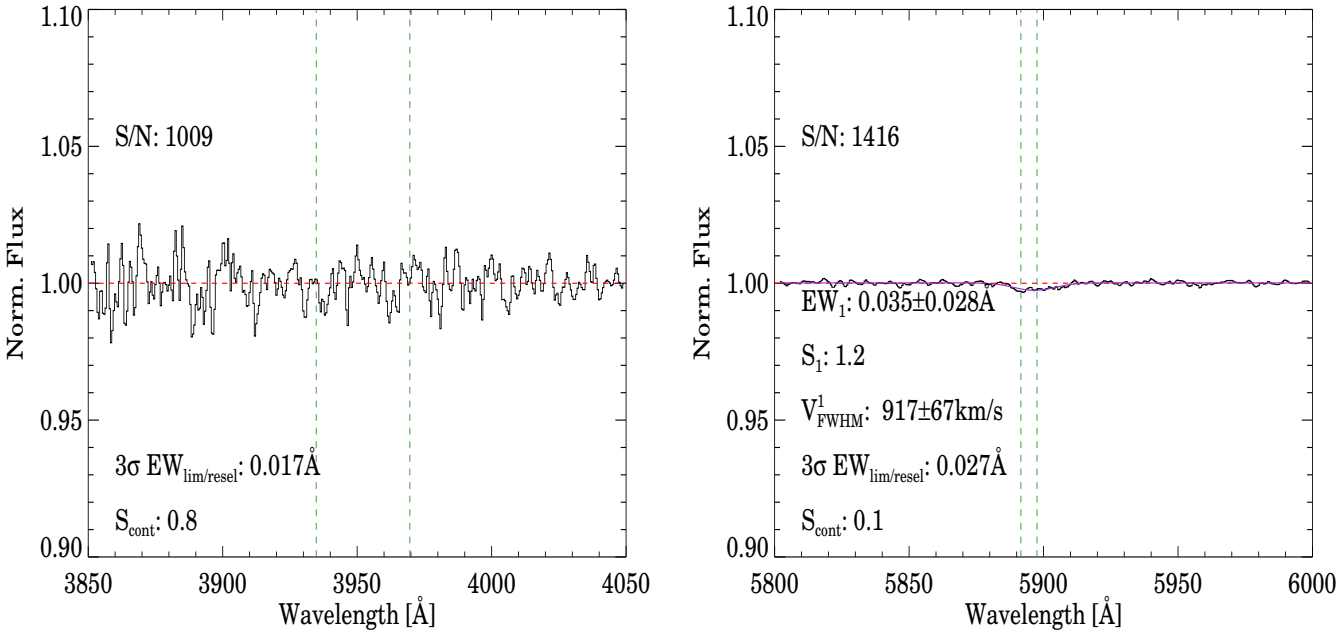

(a) Ca II

(b) Na I

Figure 4.6 The stack of all 11520 Na I non-absorbers. 4.6a shows a stack around the Ca II rest wavelength region. 4.6b shows a stack around the Na I rest wavelength region.

Several possible scenarios may explain the lack of a Ca II signal, as follows:

1. **Poor B-Spline Fitting in the Absorber Region**

   Since the b-spline continuum fitting linearly interpolates across the absorber region, it may be possible that it over- or under- estimates the actual continuum in the absorber region. Stacking many such systems then might wipe out any small Ca II absorption signal that is present in the data. However this effect should be taken into account by including the errors on the continuum. If such a problem does exist, it should apply to both the Ca II and Na I absorbers, although with the higher signal-to-noise at redder wavelengths, a small Na I signal might still be visible.

2. **Low Signal-to-Noise**

   Another possibility is that the weak Ca II signal is below the detection threshold in this region, and the lower signal-to-noise ratio in the blue wavelength region of the SDSS spectra prevents the signal from being detected. The mean 3σ limiting equivalent

width threshold per resolution element as measured from the stacks, for the Ca II non-absorbers, is 0.019 Å. The weak dip seen in Figure 4.5a at 3934.77 is measured to have rEW=0.014±0.019, lower than the detection threshold. If the Ca II region had the same signal-to-noise as the Na I region, the detection threshold would be ∼0.010 Å and the line would have been detected at a significance of 1.4.

3. **Spurious Spectra in the Stack**

   The stacks may include spectra with spurious features at the Ca II rest wavelength that effectively wipe out the weak Ca II signal. Since the stacks are inverse-variance weighted, brighter quasars contribute more to the stack. If these systems have odd features in the spectra then they would dominate this region. By randomly selecting a subset of the spectra and re-stacking, we can test how much affect spurious spectra have on the stack. Repeating this many times, we find that variations occur in the signal at the expected location, in both regions of both non-absorber samples. The weak Na I signal seen in Figures 4.5b and 4.6b sometimes appears weaker and sometimes stronger. In the Ca II regions of the non-absorbers, while most runs produce a similar result as shown, some stacks do appear to present a weak Ca II K line, but not the Ca II H line. So perhaps the weaker Ca II systems are present in the spectra, but whose presence is reduced due to more weight being given to spectra with either no Ca II signal or a spurious feature.

4. **Differing Physical Conditions**

   Due to the nature of the ionization energies of Ca II and Na I, these species may exist within different physical conditions in the ISM. Na I primarily exists in the dense, cold, neutral gas phase while Ca II exists in the diffuse, warmer, neutral and partially ionized phase of the ISM. Ca II is also heavily depleted onto dust. Thus if the sightline probes a highly dusty environment, Ca II may be removed from the gas phase and absent in the spectrum. The CNM of the ISM should have larger amounts of dust compared to other phases of the ISM, where shock-heating may destroy dust grains. Sightlines predominantly probing the CNM then might detect Na I with a lack of Ca II. However, a physical origin for the lack of Ca II and the presence of Na I in the non-absorber stacks seems unlikely. This would require that we have somehow selected sightlines, which are randomly distributed across the SDSS footprint, through galaxy environments that only

probe specific physical conditions. Since brighter quasars contribute more weight to the stack, if many of those sightlines have no Ca II, or are highly dusty such that Ca II is depleted, then the weak Ca II signal might be damped out.

4.4.2 Galaxy Classifications

In this section, we wish to look for and explore connections between absorber environment and galaxy, as well as differences between absorbing and non-absorbing galaxies. One particular interest is whether or not morphology is a factor in absorber properties. To explore the morphological dependence, we divide the samples using three different classifications. We divide the samples up based on the r-band concentration index of the galaxy, the *fracdev* parameter, and into a red and blue galaxy sample. Table 4.1 shows the results of the classification schemes. Concentration index is defined as petroR90/petroR50, the ratio of the Petrosian radii containing 90% and 50% of the galaxy flux, respectively. Concentration index is known to correlate with galaxy morphology (Strateva et al., 2001; Shimasaku et al., 2001), where elliptical galaxies have large concentration indices and disk galaxies have smaller concentrations. We adopt $C_r \geq 2.6$ to separate ellipticals from disks. For the Ca II absorbers, we find that 74% are classified as disk galaxies, and 26% as ellipticals. The Na I absorbers also breakdown similarly, with about 10% more systems classified as ellipticals, compared to the Ca II absorbers.

For all galaxies in the SDSS, a composite surface brightness profile is fit to the galaxy, using a linear combination of exponential and de Vaucouleurs profiles. The *fracdev* parameter is the fraction representing the weight to the de Vaucouleurs component. A value of 1 is a pure de Vaucouleurs profile, representative of elliptical galaxies, while 0 is a pure exponential disk, representative of spirals. We divide the sample at fracdev$\geq$0.8 into ellipticals, with fracdev$<$0.8 as disk galaxies, following Padilla & Strauss (2008) and Chen et al. (2010). For the Ca II absorbers, we find that 79% are classified as disks and 21% as ellipticals, a result similar to the division based on concentration index. The Na I absorbers again divide similarly, with a slightly higher percentage classified as ellipticals.

Finally, we divide the samples into a Red and Blue sample, based on galaxy color. It is

Table 4.1 Ca II and Na I Galaxy Classifications based on r-band concentration index, fracdev (the weight of the de Vaucouleurs component to the surface brightness profile fit, and a color cut based on the g-r, M_r parameter space from Yan et al. (2006).

		Absorbers (16)		Non-Absorbers (12545)	
Ca II	C_r	≥2.6	<2.6	≥2.6	<2.6
		5 (26%)	14 (74%)	4584 (37%)	7960 (63%)
	FracDeV	≥0.8	<0.8	>0.8	≤0.8
		4 (21%)	15 (79%)	3342 (27%)	9203 (73%)
	Color	Red	Blue	Red	Blue
		4 (21%)	15 (79%)	1420 (11%)	11125 (89%)
		Absorbers (36)		Non-Absorbers (11520)	
Na I	C_r	≥2.6	<2.6	≥2.6	<2.6
		13 (36%)	23 (64%)	4216 (37%)	7304 (63%)
	FracDeV	≥0.8	<0.8	>0.8	≤0.8
		12 (33%)	24 (67%)	3088 (27%)	8432 (73%)
	Color	Red	Blue	Red	Blue
		2 (6%)	34 (94%)	1286 (11%)	10234 (89%)

well known that in the parameter space of g-r color, and M_r, galaxies generally separate into a bimodal distribution, consisting of a red sequence and a blue cloud (Strateva et al., 2001; Blanton et al., 2003b; Hogg et al., 2002; Baldry et al., 2004). We adopt the color-magnitude relation of Yan et al. (2006) to separate our sample into red and blue galaxies. We find that for both the Ca II and Na I absorber samples, there is a preponderance of blue galaxies, about ∼80-90% of the overall sample. The non-absorber samples separate out in a similar manner, being dominated by blue galaxies. The low percentage of red galaxies within the sample is due to the physical search radius adopted for the DR7 sample.

Recalling our DR5/6 absorber sample consisting of galaxy-quasar pairs separated by $b/r_{\rm Petro}\leq 2.0$, and using the same color criterion, we found roughly 50% red and blue galaxies

(see Section 2.5.1 and Figure 2.7). Using an angular search radius, a higher percentage of red galaxies was selected compared with the DR7 sample which used a physical search radius, as the angular search radius covers a larger search area at higher z. With a physical search radius, we are selecting many more galaxies with fainter magnitudes and bluer colors. Considering the DR7 Ca II sample, out of 12564 total systems, 147 are at $b/r_{\rm Petro} \leq 2.0$. Of these systems, only 40% are classified as red galaxies. These results make sense considering the magnitude-limited survey of SDSS. Since we make no corrections for Malmquist bias, higher redshift systems are made up of Luminous Red Galaxies (LRGs). These are precisely the systems cut out when using a physical kpc scale matching, while fainter galaxies at low redshift aren't rejected, as is the case with an angular matching routine.

All further analysis will be done on the full sample, as well as each of the morphological subsets.

4.4.3 Correlations of Absorption Properties with Absorber Host Galaxy Properties

In this section we examine trends between absorption properties and host galaxy properties.

- **Spearman Rank Correlation Tests**

  Due to the unresolved nature of the absorption features, the only absorber properties we have access to are the rest-frame equivalent width and the velocity offset from the galaxy. We perform a Spearman's rank correlation test between the rEW and Δv, and the various galaxy properties listed in Tables 4.2 and 4.3. For each galaxy property, we list the Spearman correlation coefficient ρ, the p-value for the correlation, and the significance of the correlation. Correlations whose significances are $\geq 3.0\sigma$ are marked with a checkmark in the table. For the Ca II systems, rEW refers to the equivalent width of the Ca II K line as measured by the line finder. Since the line finder had difficulty separating out the Na I D2 and D1 lines, rEW here could either refer to the D2 line or a blend of the D2 and D1 lines. Without visual examination and measurement, we cannot differentiate between the two.

  For Na I absorbers, we find a strong positive correlation at strong significance between the

Table 4.2 Spearman's Rank Correlation Coefficient between Ca II K line rEW, and velocity offset Δv and various galaxy properties. We test correlations between $g-r$, $u-r$ and $r-i$ galaxy colors, r-band absolute magnitude, r-band luminosity, impact parameter in kpc, the ratio of the impact parameter to the r-band Petrosian radius of the galaxy, r-band concentration index, *fracdev* parameter (i.e. the fraction depicting the kind of profile fit to the galaxy where 0 is a pure exponential disk and 1 is a pure deVaucouleur profile), galaxy inclination i, galaxy redshift, r-band galaxy half-light radius, color excess along the quasar sightline, the axis ratio b/a, the azimuthal angle Θ (i.e. the projected angle between the quasar and galaxy major axis), g-band QSO magnitude, rest-frame line equivalent width rEW, and velocity offset Δv between the absorber and galaxy.

	rEW				Δv			
Property Name	ρ	p-value	N_σ	✓	rho	p-value	N_σ	✓
$g-r$	-0.361	0.129	1.53		-0.0325	0.895	0.13	
$u-r$	-0.389	0.100	1.65		-0.110	0.655	0.45	
$r-i$	-0.171	0.484	0.73		0.0974	0.692	0.40	
M_r	0.301	0.210	1.28		-0.0781	0.751	0.32	
L_r^*	-0.301	0.210	1.28		0.0781	0.751	0.32	
b [kpc]	0.0465	0.850	0.20		-0.499	0.0295	2.18	
$b/r_{\rm Petro}$	0.162	0.507	0.69		-0.485	0.0352	2.11	
C_r	-0.285	0.237	1.21		-0.319	0.184	1.33	
$fracdev$	-0.510	0.0257	2.16		0.00625	0.980	0.03	
i	-0.0676	0.783	0.29		-0.0904	0.713	0.37	
z	-0.164	0.502	0.70		0.312	0.194	1.30	
R_{50}^r	-0.0570	0.817	0.24		-0.203	0.405	0.83	
$E(B-V)_{QSO}$	0.312	0.194	1.32		0.513	0.0246	2.25	
b/a	0.0290	0.906	0.12		0.0957	0.697	0.39	
Θ	0.0184	0.940	0.08		0.0237	0.923	0.10	
g_{QSO}	0.718	0.000534	3.05		-0.0755	0.759	0.31	
rEW	1.00	–	–		-0.0614	0.803	0.25	
Δv	-0.0614	0.803	0.26		1.00	–	–	

quasar g-magnitude and rEW (see Figure 4.7). This is as expected given the Malmquist bias that affects our galaxy and quasar samples. Only the stronger rEW systems are detectable above the limiting rEW for fainter quasars. This effect results in the lower envelope to the points seen in Figure 4.7. Brighter quasars should be able to probe both strong and faint rEW sightlines. The apparent lack of strong rEW systems seen along sightlines toward bright QSOs is mainly a result of the poor S/N ratio for faint quasars. Due to a worse signal-to-noise ratio in faint quasar spectra, the measured error on the equivalent width is larger than for systems at the bright end, resulting in up-scattering occurring more frequently compared to systems at the bright end. This effect artificially inflates the observed correlation and produces the gap seen for strong equivalent systems in bright quasars. Also contributing is the Eddington bias. The Eddington bias is a statistical bias affecting surveys that results in an overestimate of the number of objects in a bin when you have two neighboring disparately sized bins. Due to statistical fluctuations in the measurement error, objects from the larger bin scatter more easily into the smaller bin than vice versa, thus producing an overestimate in the number counts in that bin. In our case, there are many more weaker equivalent width systems than stronger ones. Thus more weaker systems will scatter into the high equivalent width bins. The Eddington bias may be responsible for the outlying points seen at rEW$\sim$4-6 Å.

We find no other correlations between the Ca II K or Na I rEW and any other galaxy properties at the 3.0σ level or higher. Considering the velocity offset, Δv, we find no significant correlations above 3.0σ with any of the galaxy properties, for either the Ca II or Na I absorbers. Tables E1 and E2 in Appendix E show the Spearman correlation coefficients for the Ca II and Na I absorbers for the various morphological subsets. We find no new correlations between rEW or Δv and any galaxy property, for both the Ca II and Na I absorbers. The correlation results for the subsets of systems classified as 'Red' galaxies or 'Elliptical' based on C_r or $fracdev$ are unreliable due to small number statistics in those subsets (see Table 4.1).

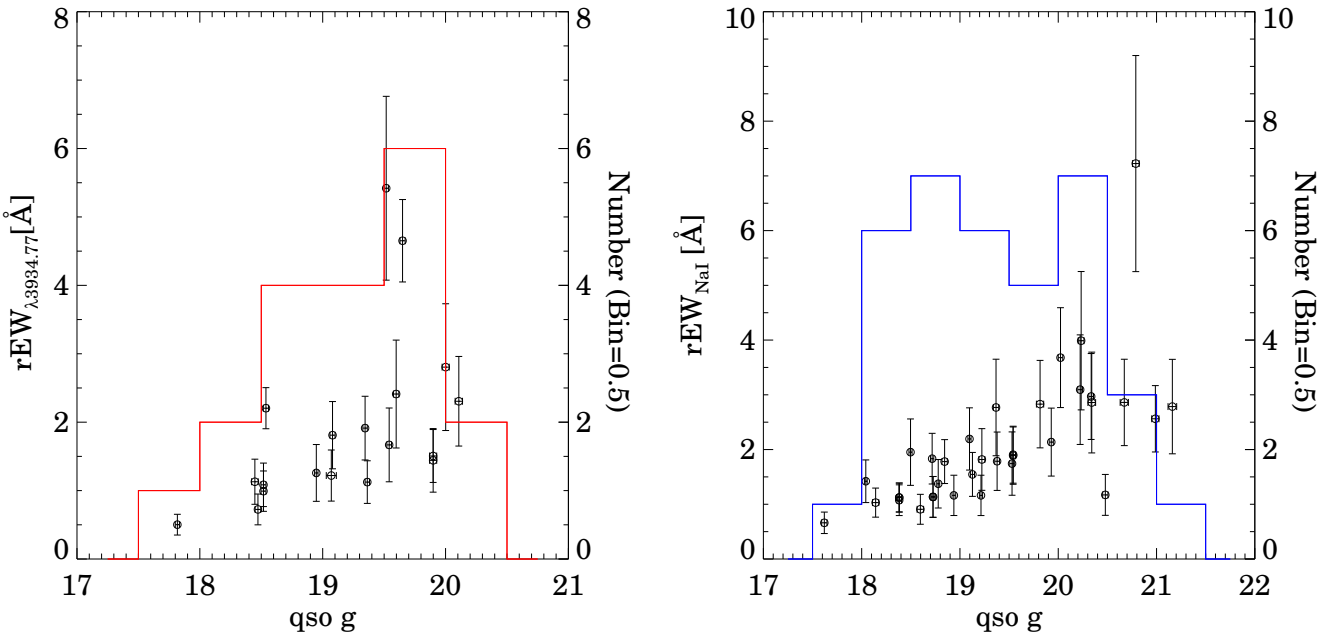

(a) Ca II Absorbers

(b) Na I Absorbers

Figure 4.7 rEW versus QSO g magnitude for a.) the Ca II absorbers and b.) the Na I absorbers. The distributions in QSO g magnitude are overlayed in each plot.

4.4.4 Host Galaxy Comparisons Between the Absorbers and the Non-Absorbers

In this section, we explore statistical differences in galaxy properties between the Ca II and Na I absorber and non-absorber samples. To do so, we perform two statistical tests, the Kolmogorov-Smirnov (K-S) test, and the Mann-Whitney U test. Both tests are non-parametric tests that do not depend on binning and are fairly robust to small sample sizes. The K-S test is sensitive to any type of difference between the two distributions, while the U test is particularly sensitive to differences in the means of the two distributions. The K-S test however, works best for continuous distributions. For robustness, on every sample comparison, we perform 10000 realizations of each test and record the median p-value. Since we perform two statistical tests on sixteen different parameters, to determine whether or not two samples are statistically different at some significance, we apply the Bonferroni correction. This correction says that if we wish to test for a difference between two parameters at a significance of α, we compute $\beta = \alpha/\mathrm{n}$, where n is the total number of

Table 4.3 Spearman's Rank Correlation Coefficient between the NaI rEW, and velocity offset Δv, and various galaxy properties. The galaxy properties are the same as in Table 4.2.

	rEW				Δv			
Property Name	ρ	p-value	N_σ	✓	ρ	p-value	N_σ	✓
g-r	0.140	0.416	0.81		0.0327	0.850	0.19	
u-r	0.184	0.282	1.08		0.0386	0.823	0.22	
r-i	0.169	0.324	0.99		-0.0481	0.780	0.28	
M_r	0.00721	0.967	0.04		0.124	0.471	0.72	
L_r^*	-0.00721	0.967	0.04		-0.124	0.471	0.72	
b [kpc]	0.262	0.122	1.55		0.116	0.499	0.68	
b/r_{Petro}	0.112	0.514	0.65		0.145	0.397	0.85	
C_r	0.0121	0.944	0.07		-0.0481	0.780	0.28	
fracdev	-0.0567	0.743	0.33		0.0115	0.947	0.07	
i	0.412	0.0126	2.50		0.0520	0.763	0.30	
z	0.139	0.418	0.81		-0.142	0.408	0.83	
R_{50}^r	-0.120	0.485	0.70		-0.0337	0.845	0.19	
$E(B\text{-}V)_{QSO}$	0.155	0.367	0.90		-0.180	0.294	1.05	
b/a	-0.386	0.0199	2.33		-0.0723	0.675	0.42	
Θ	0.101	0.557	0.59		-0.101	0.556	0.59	
g_{QSO}	0.793	8.05E-09	5.42	✓	0.00438	0.980	0.03	
rEW	1.00	–	–		0.205	0.230	1.20	
Δv	0.205	0.230	1.20		1.00	–	–	

tests performed. If any of the individual tests produces a result of β, then the two samples are said to be statistically different at α. For our purposes, we test for differences at the 3.0σ level. With sixteen parameters and two tests, $n = 32$. If either the KS or U test returns a p-value $\leq$8.4e-5, or a significance $\geq 3.9\sigma$, then the two samples are different at 3.0σ for a given property.

Tables 4.4 and 4.5 shows the results between the Ca II and Na I absorber and non-absorber galaxy samples, respectively, for the same galaxy properties used in the correlation testing in Section 4.4.3.

For the Ca II systems, we find no significant differences at the 3σ level between the absorbers and non-absorbers for any of the galaxy properties we test. While there are no significant results, we show the distribution in $b/r_{\rm Petro}$ ratio in Figure 4.8c as this parameter has the smallest p-value resulting from the statistical tests. The median $b/r_{\rm Petro}$ ratio for the Ca II absorbers is 7. Relative to the galaxy size, the Ca II absorbers are predominantly found within seven times the galaxy radii compared to the non-absorbers. We also show the distribution in impact parameter in Figure 4.8a. The median impact parameter of the Ca II absorbers is 54 kpc, with a covering fraction of $\sim$5% within 10 kpc of the galaxy. The covering fraction is an estimate of the fraction of absorbing gas to the total number of sightlines probed, and is representative of the amount of clumpiness of an absorbing medium, assuming uniformly distributed gas within a spherical halo. Above 10 kpc, the covering fraction of Ca II absorbers drops off significantly to $<$1%. Upon dividing the sample into morphological subsets, seen in Table F1 in Appendix F, we find no statistical differences between the Ca II absorbers and the non-absorbers.

With the Na I systems, we also find no significant differences between the absorbers and non-absorbers at the 3σ level. Although the Na I absorbers show no significance differences with the non-absorbers, we show the impact parameter and $b/r_{\rm Petro}$ distributions for comparison with the Ca II absorbers in Figures 4.8b and 4.8d. As with the Ca II absorbers, there is a larger fraction of Na I absorbers below 10 kpc, with a covering fraction of 5%. It quickly drops to $<$1% above 10 kpc and remains roughly constant out to 100 kpc. When the Na I absorbers are divided based on galaxy color or shape, as with the Ca II absorbers, we find no statistical differences between the absorbers and non-absorbers. Note that the

Table 4.4 Results of the K-S and Mann-Whitney U tests between Ca II absorbing and non-absorbing galaxies. For each test, we give the p-value and the corresponding level of significance. Applying the Bonferroni correction, if either test returns a p-value $\leq$8.4e-5, then the two samples, for a given property, are statistically different at the 3.0σ level. If that condition is met, then the last column is marked with a checkmark for that property.

	K-S		U		✓
Property Name	p-value	N_σ	p-value	N_σ	
$g-r$	0.254	1.14	0.227	1.21	
$u-r$	0.212	1.25	0.208	1.26	
$r-i$	0.280	1.08	0.234	1.19	
M_r	0.222	1.22	0.163	1.40	
L_r^*	0.218	1.23	0.166	1.39	
b [kpc]	0.0263	2.22	0.0161	2.41	
$b/r_{\rm Petro}$	0.000413	3.53	0.000255	3.66	
C_r	0.0768	1.77	0.0347	2.11	
$fracdev$	0.0356	2.10	0.171	1.37	
i	0.253	1.14	0.200	1.28	
z	0.0496	1.96	0.147	1.45	
R_{50}^r	0.0322	2.14	0.0881	1.71	
$E(B-V)_{QSO}$	0.103	1.63	0.135	1.49	
b/a	0.321	0.993	0.190	1.31	
Θ	0.137	1.49	0.142	1.47	
g_{QSO}	0.296	1.05	0.258	1.13	

Table 4.5 Results of the K-S and Mann-Whitney U tests between Na I absorbing and non-absorbing galaxies.

	K-S		U		✓
Property Name	p-value	N_σ	p-value	N_σ	
$g-r$	0.138	1.48	0.244	1.17	
$u-r$	0.187	1.32	0.243	1.17	
$r-i$	0.204	1.27	0.230	1.20	
M_r	0.261	1.12	0.272	1.10	
L_r^*	0.264	1.12	0.264	1.12	
b [kpc]	0.221	1.22	0.214	1.24	
$b/r_{\rm Petro}$	0.283	1.07	0.258	1.13	
C_r	0.149	1.44	0.159	1.41	
$fracdev$	0.0501	1.96	0.231	1.20	
i	0.144	1.46	0.0928	1.68	
z	0.239	1.18	0.270	1.10	
R_{50}^r	0.230	1.20	0.208	1.26	
$E(B-V)_{QSO}$	0.000756	3.37	0.0121	2.51	
b/a	0.153	1.43	0.108	1.61	
Θ	0.234	1.19	0.146	1.46	
g_{QSO}	0.185	1.33	0.226	1.21	

K-S test for the 'Red' sample of Na I absorbers failed due to low number statistics in that subset.

4.5 DISCUSSION AND RESULTS

In Section 4.4.3 we explored correlations between the absorber properties of rest equivalent width and velocity offset from the galaxy position with various galaxy properties. In Section 4.4.4, we tested for statistical differences between the absorber and non-absorber galaxies. Here we discuss those results in the context of what is known about Ca II and Na I absorbers from the literature.

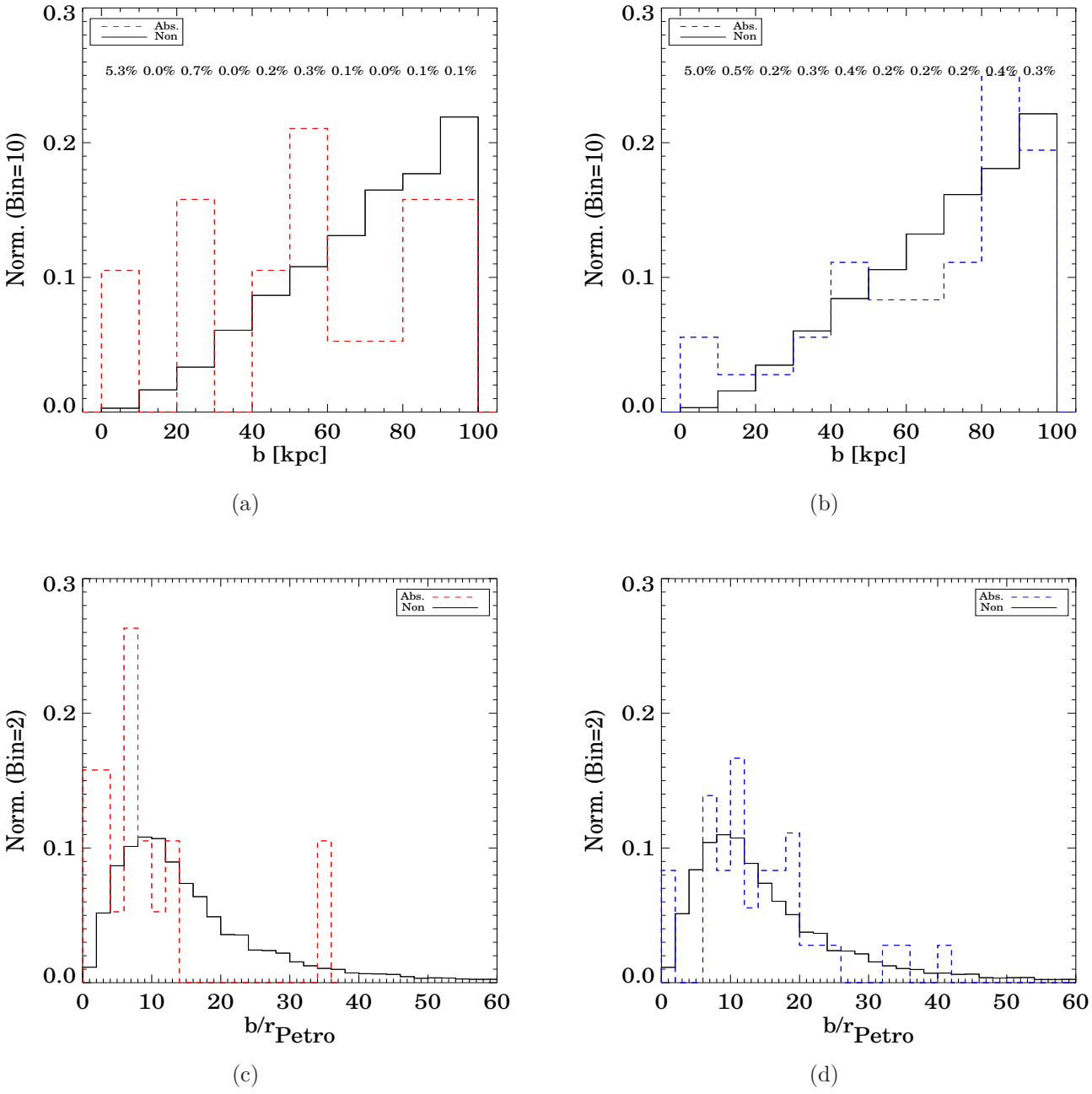

Figure 4.8 Normalized distributions for the Ca II and Na I absorbers vs non-absorbers. The top panels show the impact parameter distributions for the Ca II and Na I absorbers. The bottom panels show the distributions in $b/r_{\rm Petro}$, the ratio between impact parameter and the r-band galaxy Petrosian radius. In panels a.) and b.), the percentages present the covering fraction of the absorbers within each impact parameter bin. For both the Ca II and Na I absorbers, the covering fraction is 5% below 10 kpc and then dramatically drops off at >10 kpc and remains roughly constant out to 100 kpc.

4.5.1 Covering Fraction and Absorber Cross Section

Given the ongoing interest in understanding the baryon distribution within galaxy halos (Mo & Mao, 2002; White & Rees, 1978), quasar absorption lines can be used as a unique probe of halo gas cross-sections in order to understand halo sizes and the gas distribution inside halos. The absorber cross-section and covering fraction are two such quantities to aid our understanding. Absorber gas cross-sections are generally understood in terms of absorber size or impact parameter and a Holmberg-scaling law with luminosity (Steidel et al., 1994; Steidel, 1995) along with the covering fraction of absorbing gas, which is representative of the amount of clumpiness of an absorbing medium, assuming uniformly distributed gas within a spherical halo.

In Figures 4.9a and 4.9b we plot the impact parameter of the Ca II and Na I samples against the r-band luminosity in units of L_r^*. The non-absorbers for each sample are indicated as black points, while the absorbers are colored symbols. We color-code the absorbers based on the significance of the Ca II K line rEW and Na I D rEW lines, with circles, and squares denoting significances greater than 3, and 4, respectively. For both samples, we find absorbers out to 100 kpc, the edge of our search radius, and spanning a wide range of galaxy luminosities, dominated by sub-L^* galaxies. The Ca II absorbers have a median impact parameter of 55 kpc, and a median luminosity of 0.17 L_r^*, with a range from 0.009-3 L_r^*. The Na I absorbers have a median impact parameter of 77 kpc, and a median luminosity of 0.11 L_r^*, spanning 0.001 - 2 L_r^*. For both samples, we find lines detected at 3 and 4σ non localized in any particular area of b-L parameter space. As the Ca II and Na I absorbers extend out to our maximum search radius of 100 kpc, this places a lower bound on the absorber cross section.

In Figure 4.9c and 4.9d we again plot the distribution of impact parameter but now in galaxy luminosity bins of $\leq$0.01 L_r^*, 0.01$<L_r^* \leq$0.1, 0.1$<L_r^* \leq$1 L_r^*, and $L_r^*>$1.0. As with the previous impact parameter distributions, we note the approximate covering fraction in each impact parameter bin. While we are dominated by low numbers statistics in each bin, the covering fraction does increase within low impact parameter bins (<10 kpc) for more luminous galaxies, with the majority of absorbers between 0.1-1 L_r^*. Galaxies in this lumi-

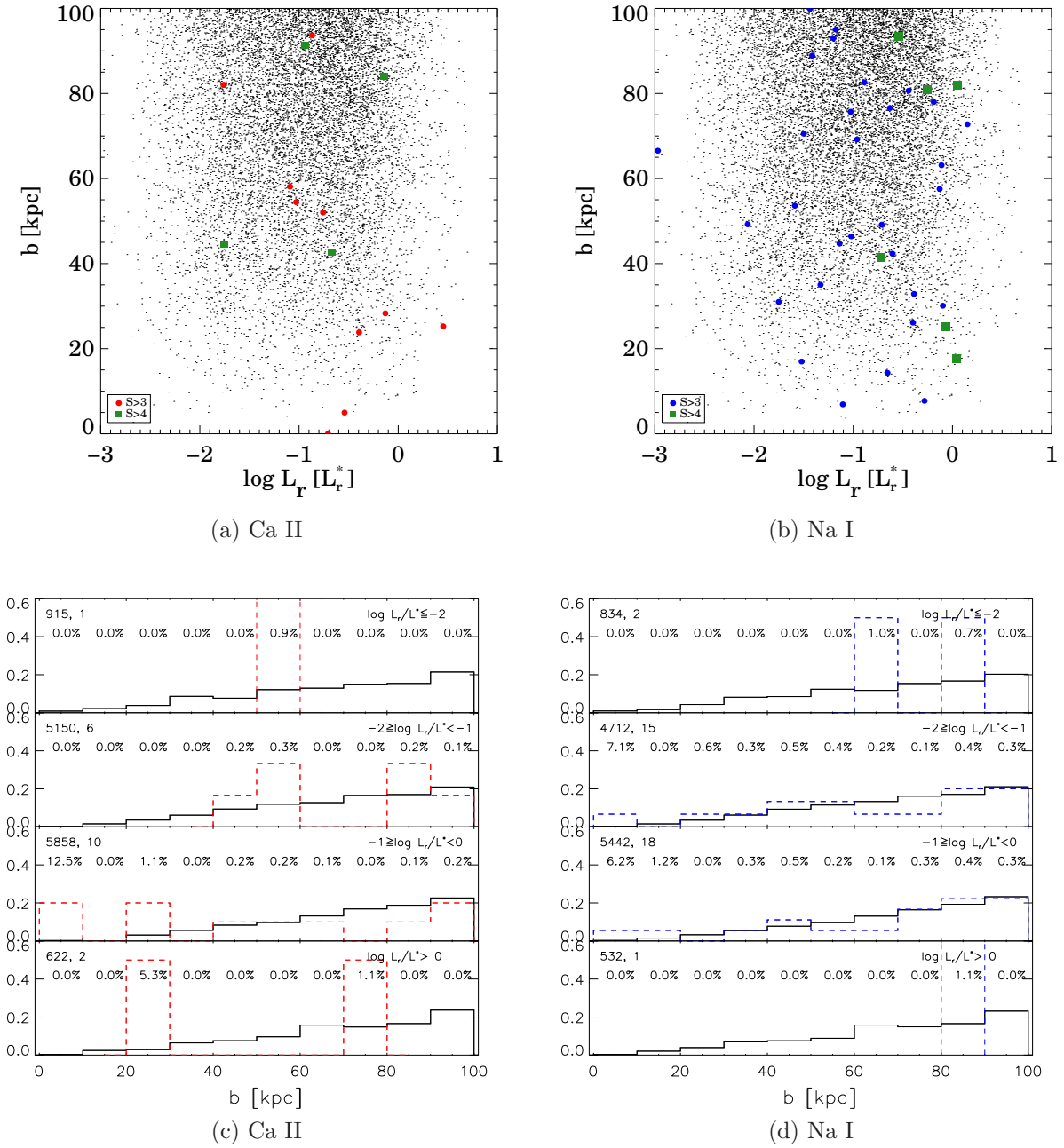

(a) Ca II (b) Na I

(c) Ca II (d) Na I

Figure 4.9 Top Row: Impact Parameter distribution as a function of galaxy luminosity in units of L_r^*, for the (a) Ca II absorbers and (b) Na I absorbers. The respective non-absorbers are the black points, while the absorbers are given as filled symbols. In each plot, the absorbers are shown with line significances S>3,4, respectively as circles, and squares. Bottom Row: Impact parameter distribution binned by galaxy luminosity. Percentages list the covering fraction of absorbers in each impact parameter bin. The numbers in the top left indicate the number of non-absorbers, absorbers, respectively, within each luminosity bin.

nosity range tend to have more absorbers located closer in than their fainter counterparts, although low numbers combined with SDSS selection effects may skew the low luminosity bin. Within the inner 10 kpc, the covering fraction of Ca II absorbers has increased to 12.5% for 0.1-1.0 L_r^* galaxies, again falling off to nearly 0% beyond 10 kpc. The covering fraction of Na I absorbers has increased slightly to 6-7% for 0.01-1.0 L_r^* galaxies, before dramatically falling off.

4.5.2 Outflow/Inflow versus Disk or Halo Gas

Using galaxy inclination and relational parameters between the quasar and galaxy such as impact parameter, and the azimuthal angle, Θ, the relative location of the absorbing gas to the galaxy can be ascertained, with regards to predominantly halo, disk, or from an outflow or inflow. Here the azimuthal angle is the relative angle between the quasar sightline and the galaxy major axis, where $\Theta \sim 0^o$ denotes that the quasar is aligned along the galaxy's major axis, or with the disk of the galaxy, and $\Theta \sim 90^o$ denotes alignment along the galaxy minor axis. Quasars preferentially aligned with the minor axis would indicate an absorber cross-section dominated by galactic outflows as they are the only mechanism by which material is produced along the minor axis. Stewart et al. (2011) showed that other scenarios such as gaseous disk, or in-falling material are preferentially aligned with the major axis.

If the absorber strength is dominated by disk gas, then a correlation should exist with galaxy inclination, as path lengths through edge-on galaxies probe more of the disk as compared to galaxies with lower inclinations. If instead there is a strong outflow component then the absorber strength should exhibit the opposite correlation with galaxy inclination. Heckman et al. (2000) found, for a sample of star-forming galaxies, a higher probability of probing outflowing gas when viewing galaxies with inclinations $<60^o$, owing to the fact that one is now looking down the galaxy minor axis, along the outflow sightline.

Mg II absorbers are a well studied class of absorbers, consisting of a 'weak' (rEW<0.3 Å) and 'strong' (rEW>0.3 Å) class. The strong Mg II absorbers are thought to originate from the outflows of star-forming galaxies. Bouche et al. (2011) recently looked at a population of 10 strong Mg II absorbers and found a strong bimodal distribution in azimuthal angle

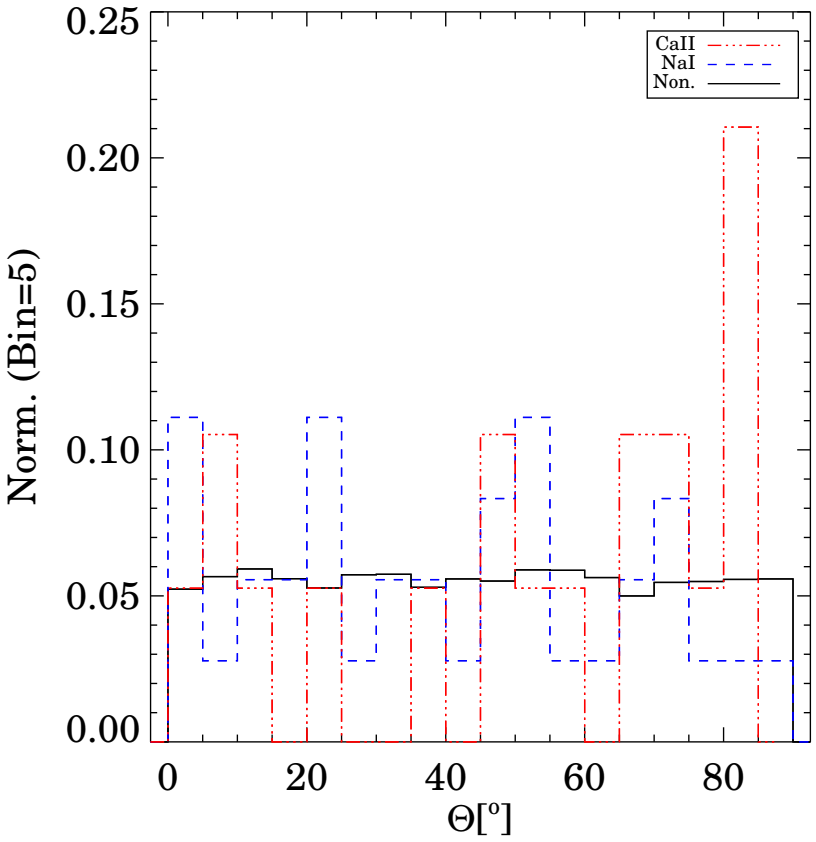

Figure 4.10 Normalized Distribution of the azimuthal angle, i.e. the relative angle between the quasar sightline and the galaxy major axis, for the Ca II (red dot-dash)and Na I (blue dash) absorbers. For both absorber samples, the distribution is relatively uniform across all angles. The solid line shows the distribution of Ca II non-absorbers.

that samples extremely low and high angles, suggesting that both extended gaseous disks and outflows are responsible. Kacprzak et al. (2011) found an additional positive inclination correlation with the Mg II absorber strength, in addition to the known anti-correlation between Mg II rEW and impact parameter. Both of these correlations suggest a non-spherical distribution of Mg II halo gas.

For each galaxy-quasar pair, we compute the azimuthal angle of the quasar sightline to the galaxy major axis using the SDSS images. We adopt the the r-band Isophotal position angle as the position angle to the galaxy major axis. Figure 4.10 shows the distribution of

azimuthal angles. Even with the small sample sizes, the distributions in azimuthal angle are fairly uniform for both the Ca II and Na I absorbers. We also find a lack of significant correlation with absorber strength and azimuthal angle, as well as no differences between the distribution for the absorbers and non-absorbers. The uniformity of the distributions and lack of correlations remain if we instead use the r-band Exponential or de Vaucouleurs position angles for the galaxies instead of the Isophotal position angles. We also saw from Tables 4.2 and 4.3 that there are no correlations of absorber strength or velocity offset from the galaxy with galaxy inclination, azimuthal angle, and position angle of the quasar (not shown).

Figure 4.11 shows the azimuthal angle as a function of galaxy inclination, with symbols binned in $b/r_{\rm Petro}$ and color coded by the absorber velocity offset from the galaxy. The absorbing clouds are uniformly distributed in Θ and i, and no correlations are obvious with either the velocity offset or $b/r_{\rm Petro}$. Given the lack of correlations (see Tables 4.2 and 4.3) as well as the uniformity in the distribution of azimuthal angle, we conclude that with both the Ca II and Na I absorbers, there is no preferred alignment along either the galaxy's major or minor axis, and is independent of both the galaxy inclination and impact parameter. This would indicate that the Ca II and Na I absorbers, in contrast with Mg II absorbers, are spherically distributed within galaxy halos, and there is no strong indication of either a pure disk or outflow signal, although it cannot be ruled out that they do not contribute to the absorber production.

4.5.3 Results for Ca II

Studies of Ca II absorber systems have grown in the past few years to the point where we now have divided them into strong and weak systems based on the EW values. Weak Ca II systems have rEW<0.2 Å while Ca II systems with rEW>0.2 Å are considered to be strong systems. With an average rEW of 1.08 Å, and a minimum detected rEW of 0.3 Å, all of our Ca II absorbers are classified as strong absorption line systems.

Zych et al. (2007) examined 5 strong (>0.5 Å) Ca II absorbers around galaxies from the SDSS, with impact parameters of 5-24 kpc. They found the galaxies to be massive $\sim$L*

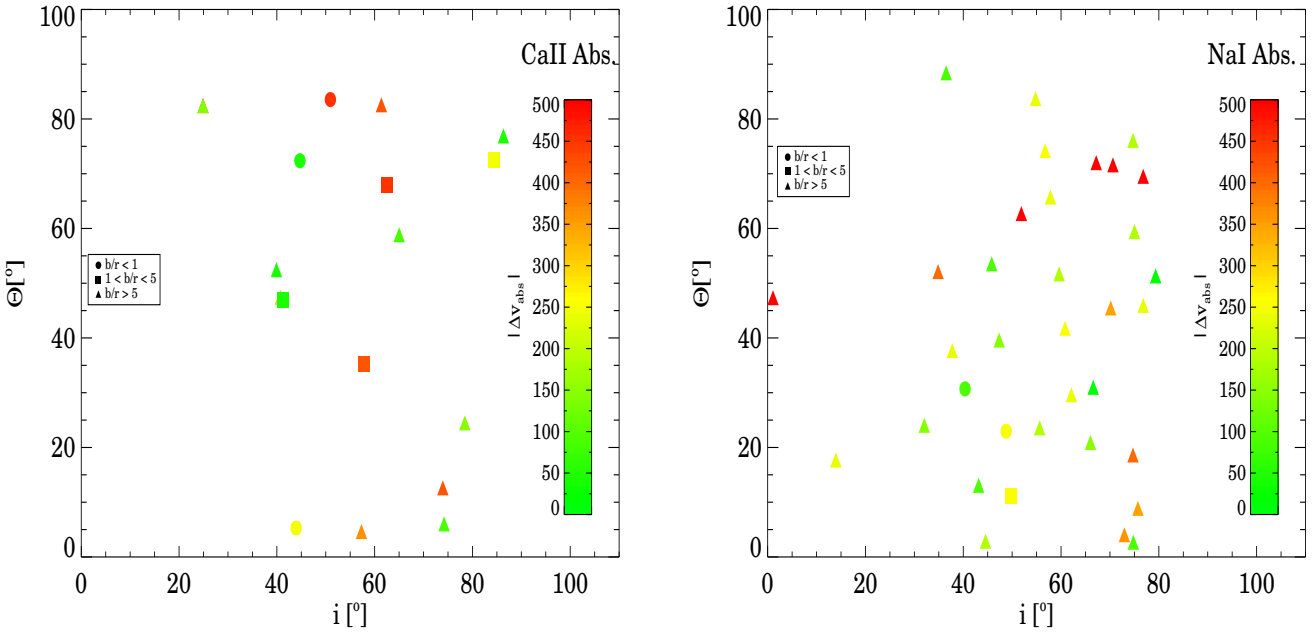

(a) Ca II

(b) Na I

Figure 4.11 Azimuthal angle vs galaxy inclination for a) Ca II absorbers and b) Na I absorbers. We divide the sample into three bins based on $b/r_{\rm Petro}$: $b/r_{\rm Petro}\leq 1$ (circles), $1< b/r_{\rm Petro} \leq 5$ (squares), and $b/r_{\rm Petro}>5$ (triangles). The symbols are color coded by the absolute value of the absorber velocity offset from the galaxy. There are no correlations seen between all four parameters, suggesting the absorbing gas is uniformly spherically distributed within galaxy halos.

spirals (ranging from 0.7-1.8 L^*_B), with large metallicities and star-formation rates. When we select absorbers with b<24 kpc (3 systems), we find galaxies ranging from 0.2-0.4 L^*_r in luminosity, with a median impact parameter of ∼5 kpc, and a median $b/r_{\rm Petro}$ of 0.7. We found Ca II absorbers to lie close in to the host galaxies, in good agreement with the strong EW absorbers found by Zych et al. (2007), however our galaxies tend to be sub-L^* galaxies.

Nestor et al. (2008); Wild & Hewett (2005b); Wild et al. (2006a); Zych et al. (2009) found that $z \sim 1$ strong Ca II absorption line systems are dusty, having on average $E(B-V) > 0.1$. These dusty absorbers are a subset of the DLA population, existing in high column density systems. The average E(B-V) of our Ca II sample is 0.09 but ranges from -0.14 to 0.5. For

the Ca II absorbers at $b < 24$ kpc, the mean E(B-V) is >0.1. Thus, we are at least consistent with the picture that Ca II absorbers are on average dustier than other absorber classes. Estimates of the extinction from the galaxy would help confirm the dusty environment for our Ca II sightlines.

Hewett & Wild (2007) imaged a sample of Ca II absorption line systems at z∼1 and found an excess of luminous $\sim L_K^*$ galaxies within 50 kpc compared with the field, although these galaxies have not been verified with spectroscopy. The average impact parameter of their sample was 24 kpc. They found that a scaling law of $L_K^{0.7}$ modeled their distribution of Ca II absorbers well. They conclude that Ca II absorbers are predominantly located in large gaseous structures far from the host galaxy, again inside regions of high column density.

With no correlations seen with azimuthal angle, impact parameter, or galaxy inclination, we find no evidence of an outflow origin for strong Ca II gas. The uniformity of the distribution in azimuthal angle suggests a spherical distribution of Ca II within the galaxy halo, although an outflow origin cannot be ruled out as a contributor.

Richter et al. (2011) studied at a sample of weak (<0.2 Å) EW Ca II absorption line systems and found that half of their systems are detectable within lower HI columns of >17.4 cm^{-2}, suggesting that the weak Ca II absorbers, or some fraction of them, exist in High Velocity Clouds (HVCs). As all our absorbers would be considered strong Ca II systems, they should primarily exist in high column density regions. While getting high column density gas to survive far from the galaxy is difficult, it is not unheard of. Filaments of high HI column density gas have been found around M81 (Yun et al., 1994) and NGC 5291 (Boquien et al., 2007) due to interactions with neighboring systems. While the volume filling factor of HVCs is low (∼10-20% in the Milky Way), many tidal interactions and mergers with smaller galaxies would act to redistribute the gas more uniformly within a spherical halo, producing a much larger filling factor.

Richter et al. (2011) also perform some simple disk+halo modeling and, considering all galaxies with L>0.05 L^*, find a characteristic scale length for HVCs of 55 kpc and a covering fraction of 33%. HVCs have been seen out to 50 kpc which is not inconsistent with the range of spatial extent seen in Ca II absorbers. The estimated covering fraction of HVCs from Ben Bekhti et al. (2008) is 0.25, based on the detections and non-detections of Ca II

through various sightlines through the Milky Way. The covering fraction we estimate for Ca II from the overall impact parameter distribution is 5% within the inner 10 kpc and is much lower at larger radii. Considering galaxies >0.1 L_r^*, the covering fraction increases to 12.5% within 10 kpc. Thus, our values of the covering fraction, at least for brighter galaxies, are not inconsistent with those seen from HVCs in the Milky Way.

It remains difficult to explain the larger impact parameters seen of absorbers around faint galaxies, as seen in Figure 4.9a. One explanation could be the that the Ca II absorbing gas is actually due to dwarf galaxies closer in separation to the quasar sightline yet still associated with the identified galaxy. If this is the case, the points would drop to lower b in the figure, possibly allowing for a better constraint on the absorber cross-section. Dwarf galaxy associations with our identified galaxies might highlight the picture of tidal or galaxy group interactions redistributing gas around galaxies. At least two such strong Ca II absorbers have been found to belong in groups (Cherinka et al., 2009).

Taken all together, perhaps we are probing Ca II absorbing gas in the halo that is the vestigial remnants of past processes. Outflows driven by past episodes of star-formation, tidal interactions with nearby systems, the capture and/or production of Intermediate- and High- Velocity clouds may all contribute to the production, and/or redistribution, of Ca II into galaxy halos.

4.5.4 Results for Na I

The known literature on interstellar Na I D in external galaxies is still quite sparse. Studies of interstellar Na I D lines in star-forming disk galaxies point to an origin inside galaxy outflows. Both Heckman et al. (2000) and Chen et al. (2010) looked at interstellar Na I D lines in the inner 3-12 kpc of galaxies, and found the majority to be entrained inside galactic outflows from galaxies more heavily viewed face-on, with highly blue-shifted velocity offsets from the galaxy systemic velocity, and very few red-shifted components. Chen et al. (2010) found a distinct disk-like component of Na I in edge-on galaxies, lying at the systemic galaxy velocity, as well as a separate heavily blue-shifted outflow component, with Na I EWs ranging from 0.2-2 Å. The strength of the Na I absorption seen in both the disk and outflow components is

heavily correlated with galaxy extinction. With its low ionization energy, Na I can only exist in high column density regions heavily shielded from UV ionizing radiation by dust. The larger dust levels allow Na I to survive far out into the galaxy halo in gas with much lower column density. The Na I EWs seen in outflows also depend heavily on the star formation surface density, as it is the primary driver of the galaxy outflow.

Our mainly null results from the correlation testing and statistical tests for Na I absorbers is an interesting result regarding the nature of Na I absorbing galaxies in our sample. We find no significant differences in the galaxy populations. As with the Ca II absorbers, the lack of correlations seen with impact parameter, galaxy inclination, and azimuthal angle suggest a spherical distribution for the Na I.

The range of impact parameters seen in the literature from individual Na I systems is 11-14 kpc. We find Na I systems out to 100 kpc with a median impact parameter of 77 kpc. From Figure 4.8b, we estimate the covering fraction of Na I within 10 kpc to be 5%, and falling off to less than 1% above 10 kpc out to 100 kpc. This is, in principle, in agreement with what Chen et al. (2010) measured for the covering fractions of interstellar Na I from star-forming disk galaxies. Probing only the inner regions of galaxies, they found a covering fraction of ∼4-12% for the outflow component of Na I, with a slightly higher covering fraction of ∼15% for Na I in the disk. Our Na I systems within 10 kpc (2 systems) all have $b/r_{\rm Petro}<1$, and inclinations between from 40-50^o. The median rEW is 1.0±0.3 Å. Figure 4.9b showed that Na I systems below 10 kpc are $\gtrsim$ 0.1 L_r^* galaxies. Thus, within 10 kpc, we may be probing primarily Na I in the gaseous disks of luminous galaxies.

Figure 4.9d showed that the covering fraction of Na I within the inner 10 kpc increased slightly to 6% for >0.1 L* galaxies. If >0.1L* galaxies have a higher star-formation surface density, then more material will be driven out of the gaseous disk. With a median E(B-V) of 0.15 for galaxies <10 kpc, they are dustier along the sightline compared to the overall sample (E(B-V)∼0.12). With both more raw material being removed from the disk as well as more dust-shielding, more Na I should be able to survive, thus increasing the covering fraction.

4.6 CONCLUSION

We have performed a spectral stacking analysis of 19 Ca II absorbers and 36 Na I absorbers, and their respective non-absorber samples, for $z > 0.01$. We find a strong Ca II and Na I presence in the stack at a combined S/N of ∼47 for Ca II and ∼60 for Na I. Upon stacking the non-absorbers we find a weak Na I signal, as expected given the presence of low significance absorbers we reject during our search criteria. However we do not find a weak Ca II signal in the stack of the Ca II non-absorbers. This may be due in part to the different S/N's in the different regions of the SDSS spectra, an effect due to weighting the stack by quasar brightness, or it might reflect physical conditions in the interstellar medium itself.

Using the Spearman rank correlation coefficient, we tested for correlations between the rEW of the absorption line and the absorber line velocity offset Δv with a suite of galaxy properties. We looked for correlations at the 3.0σ level or higher. With both the Ca II and Na I absorbers we found only a correlation between rEW and the quasar g magnitude, as expected due to the sample selection effects. Upon division of the absorbers into various morphological subsets, we found no new correlations with either the Ca II or the Na I absorbers.

We also performed a K-S and Mann-Whitney U test to look for any statistical differences between the absorber and non-absorber galaxies. We found no strong differences in galaxy properties between the Ca II or Na I absorber and their respective non-absorber samples. Upon division into morphological subsets, the differences in the $b/r_{\rm Petro}$ ratio seen for the Ca II systems remained for disk galaxies. No new differences arose for either the Ca II or the Na I absorbers.

We estimated the covering fraction of both the Ca II and Na I absorbers at 5% within the inner 10 kpc, respectively, from the overall impact parameter distribution. Above 10 kpc, the covering fraction dropped to less than 1%. Upon division by galaxy luminosity, the covering fraction of Ca II absorbers within 10 kpc increased to 12.5% for 0.1-1.0 L_r^* galaxies. The covering fraction of the Na I absorbers only slightly increased for galaxies in the same luminosity range.

Some information on whether gas originates in the disk, halo, or from an outflow can be

gained through examination of the impact parameter, galaxy inclination, and the azimuthal angle, defined as the relative angle between the quasar and galaxy major axis. We find no correlations between any of these parameters, along with no correlations with the rEW. A bimodal distribution in azimuthal peaked at low and high degrees point to a distinct disk or outflow origin of the gas. We find a uniform distribution in azimuthal angle with both the Ca II and Na I absorbers, suggesting a uniformly distributed spherical symmetric gas configuration.

For our Ca II absorbing galaxies selected at b<24 kpc, there is good agreement with what has been found in the literature so far with galaxy properties at both low and high redshifts, namely that these galaxies are luminous star-forming galaxies with high dust and metal content. Our sample consists primarily of strong (rEW>0.2 Å) Ca II absorbers. Such systems should exist in high column density gas and may be a subset of the DLA population. Ca II has been seen in the lower HI column density High Velocity Clouds in the Milky Way and in low redshift quasar absorption-line systems. We cannot rule out an outflow origin to the Ca II however the uniformity in azimuth angle points may point to vestigial remnants of past star-forming or tidally interacting periods where high columned gas is stripped and redistributed within a galaxy halo. This combined with Intermediate and High Velocity Clouds may be the source of Ca II.

The lack of trends seen for the Na I absorbers is an interesting result. It might suggest a ubiquitous nature for the absorber class, with dense neutral clouds existing far out in galaxies halos, around galaxies with a wide range in luminosities. Our results generally agree with the picture that interstellar Na I is transported into halos through galaxy outflows, entrained in high column density, dusty gas clouds. With the uniformity in azimuthal angle, Na I might be also be redistributed within halos through merger processes over time.

5.0 FOLLOW-UP AND FUTURE WORK

This chapter outlines follow-up work that has been performed and briefly touches upon possible future work as well as outlining some prospects for ongoing and future surveys. Section 5.1 describes HI 21 cm emission-line observations of two galaxies from the sample of SDSS DR5/6 galaxy-quasar pairs. These results are presented in Cherinka et al. (2009). Section 5.2 discusses several areas of future work that can be carried out with our sample of galaxy-quasar pairs, including cross-correlating with radio catalogs such as FIRST and UV catalogs like GALEX. We also briefly touch upon the ability of ongoing and future surveys such as BOSS, LSST, and BIG BOSS for detecting galaxy-quasar pairs and Ca II and Na I absorption-line systems.

5.1 HI EMISSION OBSERVATIONS OF MRK1456 AND SDSS 2100

5.1.1 Introduction

Damped Lyman Alpha (DLA) absorbers are the primary reservoir of cool, neutral gas in the Universe and the ability to detect them easily over a wide range of redshifts makes them an important tracer of the evolution of gas in galaxies or protogalaxies over cosmic time. DLA systems are identified at redshifts $0<z<6$ in the spectra of QSOs (e.g. Wolfe et al., 2005). Identified from the strong n=1 to n=2 absorption line of HI, the detection of these absorption-selected objects depends primarily on the brightness of the background QSO rather than on emission from stars or gas in a galaxy. It is noteworthy that the column density of $N_{\rm HI} > 10^{20.3}$ atoms cm^{-2}, that defines a DLA (Wolfe et al., 1986), is similar

to the threshold column density required for the onset of star formation in the local Universe (Kennicutt, 1998). DLAs, then, should be associated with present-day visible galaxies (Wolfe et al., 1986; Prochaska & Wolfe, 1997; Boissier et al., 2003). However, difficulty still remains in connecting observations of high-redshift DLAs with those of low-redshift DLAs, as well as connecting galaxy-evolution simulations with DLA observations. Simulations at low redshift by Okoshi & Nagashima (2005) and Nagamine et al. (2007) indicate that the DLA incidence is dominated by more compact, faint galaxies with a narrow impact parameter distribution (<3 kpc), rather than by large disk galaxies. Observationally, low redshift DLA systems have been shown to consist of galaxies spanning a wide range of luminosities, surface brightnesses, impact parameters, and morphologies (Le Brun et al., 1997; Chen & Lanzetta, 2003; Rao et al., 2003; Rao et al., 2011). At higher redshifts, the associated host galaxy to the DLA has proven difficult to identify due to the high brightness contrast between the quasar and the absorbing galaxy. Another issue in the identification of the host galaxy at high redshift is the fact that one can no longer detect faint galaxies that may be intercepting the sightline, the result of which might cause a misidentification of the host galaxy, especially in high density regions like groups. This may contribute to the larger impact parameters being measured for high redshift systems. Christensen et al. (2007) identified candidate hosts to high-redshift (2<z<4) DLAs through IFU observations of the Lyα-emission line. While they have a small sample size, they find an average impact parameter of 16 kpc, and suggest that the distribution of HI clouds for DLAs extends far beyond the optical sizes of dwarfs. Simulations by Gardner et al. (2001) resulted in larger impact parameters (10-15 kpc) for 2<z<4.

Selecting systems by identifying damped Lyman-α absorption provides only a pencil-beam examination of the gas content of DLA host galaxies, missing the full gas content that can be probed. An alternative then, to searching for gas through Lyman-alpha absorption, is to use the 21 cm emission line, which probes the global gas content in galaxies, to look for systems that are likely to show damped Lyman-α profiles if there were a background source. The HI hyperfine structure line at 21 cm is very weak, and its detection is currently limited to low redshifts. HI 21 cm observations probe the cold, neutral Hydrogen gas in a galaxy and come in two forms, 21 cm absorption and 21 cm emission. Twenty-one cm absorption,

like other absorption-line probes, provides a pencil-beam look at the HI content of a galaxy. It requires a background radio-loud point source and allows for a direct determination of N_{HI}. Twenty-one cm line emission is a probe of the gas contained within the beam of the telescope, smoothed according to the spatial resolution of the telescope. The resulting HI emission spectrum reveals the global HI content of the galaxy and allows for determination of the HI mass while maps show the distribution and cross-sections of HI gas associated with a galaxy. Estimates of the gas column density within the beam can be obtained by the ratio of the HI flux to the area covered. A probe of emission might reveal an average HI column above $10^{20.3}$ cm^{-2}, however this is over a much larger area than that probed by absorption, therefore there is no guarantee that a QSO probe will reveal a DLA at every position within the emission beam. Emission-line probes above $10^{20.3}$ cm^{-2} only say that somewhere they generally exceed the DLA limit. Ryan-Weber et al. (2003) showed that HI-emission selected galaxies generally show more cross-section at higher column densities than they do at lower column densities and most exhibit column densities that are above the DLA limit. The HI-emission-selected galaxies are consistent with the hypothesis that the local galaxy population can explain the properties of the local DLAs. Rosenberg & Schneider (2003), and Ryan-Weber et al. (2003) studied the expected properties of the z=0 DLA population using blind 21 cm emission surveys, and found that, while a large fraction of HI-selected galaxies are dwarf or low surface brightness galaxies, there is no need for an optically invisible population of galaxies to explain the HI population or to contribute significantly to the DLA cross section.

There are presently only a small number of (sub) DLAs or DLA candidates known at low-redshift and an even smaller number that have HI measured in emission. It should be noted that a DLA (and sub-DLA) system is classically defined as a system with an observed $N_{\rm HI} > 10^{20.3}$ atoms cm^{-2} ($10^{19.0}$ cm^{-2} $< N_{HI} < 10^{20.3}$ cm^{-2}) measured via the Ly-α absorption line. The term "candidate DLA" is used to describe all galaxies that have $N_{\rm HI} > 10^{20.3}$ atoms cm^{-2} measured through other means, or those with no N_{HI} measurement but meet the criteria of various metal-DLA relationships (e.g. Mg II,Ca II,Na I). Zwaan et al. (2005) compared the properties of 20 low-redshift (z<1) DLA/sub-DLA galaxies with a sample of local, optically selected galaxies studied in HI 21 cm. Only 2 of the 20 DLAs,

SBS 1543+593 and NGC 4203, have measured HI 21 cm emission. One other DLA, the absorber towards the QSO OI 363, and two sub-DLAs, the absorbers towards the QSOs PKS 0439-433 and PG 1216+069, have been searched for 21 cm emission. We use the HI observations of these objects, along with the ones reported here, to further investigate the properties of DLAs at z=0 and expand on the number of DLAs or candidates known at low-z with HI 21 cm emission measurements.

Table 5.1 lists the HI and optical properties of the known/candidate DLAs. A summary of the HI 21 cm observations of these five known/candidate DLAs is as follows. The z=0.009 dwarf galaxy SBS 1543+593 has an HI column density of log N_{HI}=20.41 (Bowen et al., 2005) as measured by the Lyman α line, while Chengalur & Kanekar (2002) find a column density of log N_{HI} = 20.69 from the 21 cm emission mapped at the position of the QSO. The z=0.004 S0 galaxy NGC 4203 was first mapped at 21 cm before the presence of the background QSO Ton 1480 was revealed by X-ray observations. The HI absorption in the X-ray spectrum of Ton 1480 suggests a sufficiently high column density (log N_{HI} = 20.34) to make this system a candidate DLA. Another known DLA, the z=0.0912 absorber towards B 0738+313 (OI 363), has been searched for 21 cm emission but was undetected (Lane et al., 2000). Two sub-DLA's have also been searched for 21 cm emission. The z=0.101 absorber towards PKS 0439-433 was thought to be a candidate DLA system based on its X-ray spectrum but measurement of the Lyman α line (Chen et al., 2005) revealed a column density (log $N_{HI} = 19.85 \pm 0.04$) just below the limit for DLAs and it was undetected in 21 cm emission (Kanekar et al., 2001). Briggs & Barnes (2006) report a weak 21 cm emission detection along the line of sight towards the QSO PG 1216+069, which is consistent with the velocity of the z=0.0063 sub-DLA absorber.

In this section we present the 21 cm emission detection of Mrk 1456 with the Green Bank Telescope (GBT) and of SDSS J211701.26-002633.7 with the Arecibo telescope[1]. Section 5.1.2 describes the sample selection, observations, data reductions and analysis. In section 5.1.3, we discuss the HI properties of our sample and compare them to HI-detected DLAs and HI-selected galaxies. We adopt a cosmology of H_o=71 km s^{-1} Mpc^{-1}, Ω_m=0.27, Ω_Λ=0.73

[1]The Arecibo Observatory is part of the National Astronomy and Ionosphere Center, which is operated by Cornell University under a cooperative agreement with the National Science Foundation.

Table 5.1 Optical and HI properties of Known/Candidate DLA Galaxies

Property	SBS 1543+593	NGC 4203	'Galaxy'	"Jet" [a]	"Arm"	–
type[b]	Sdm	SO	Sab	LSB	LSB	–
z	0.009±0.001	0.0036±0.00001	0.101±0.001	0.09118±0.00001	0.09118±0.00001	0.00632±0.00002
D_L[Mpc]	38.3±4.3	15.25±0.4	460.0±4.6	412.46±0.04	412.46±0.04	26.84±0.08
QSO	HS 1543+5921	Ton 1408	PKS 0439-433	OI 363	OI 363	PG 1216+069
z_{QSO}	0.807±0.002	0.6156±0.0002	0.593±0.003	0.631±0.002	0.631±0.002	0.3313±0.0003
b["]	2.4	126	3.9	<2	<2	<30
b[kpc]	0.4	9.2	7.2	<3.4	<3.4	<3.9
r["][c]	4.8	105	3.7	4	4	–
r[kpc][c]	0.9	7.7	6.8	6.7	6.7	–
axis ratio b/a	0.777	0.880	0.556	–	–	–
i[d][°]	40	29	58	–	–	–
$M_B^{k,f,i}$[e]	-16.1±0.2	-19.65±0.01	-20.96±0.08	-14.72[f]	-15.12[f]	–
$L_B[10^{10}L_\odot]$	0.04±0.01	0.96±0.02	3.2±0.2	0.01	0.02	–
L_B^*	0.01	0.32	1.06±0.07	0.0001	0.0002	–
$SFR[M_\odot yr^{-1}]$[g]	0.006	0.16	–	–	–	–
$W_{50}[kms^{-1}]$	75	243	–	–	–	–
$M_{HI}[10^9 M_\odot]$	1.3±0.1	1.3	<(2.15-3.02)	<3	<3	(0.006-0.017)
M_{HI}^*	0.21	0.21	<0.34-0.48	<0.48	<0.48	(0.001-0.002)
$M_{dyn}[10^{11}M_\odot]$	0.07	1.2	–	–	–	–
$\frac{M_{HI}}{L_B}$	3.6±0.9	0.14±0.01	<(0.06-0.09)	<30	<20	–
$\frac{M_{HI}}{M_{dyn}}$	0.19	0.01	–	–	–	–
$logN_{HI}[cm^{-2}]$[h]	20.42±0.04	20.34	19.85±0.10	21.18±0.06	21.18±0.06	19.32±0.03
Refs[i]	1,2,3,4	5,6	7,8,9,10	11,12,13	11,12,13	14,15,16

[a] Cherinka,König,& Schulte-Ladbeck attempted detection of Hα of the "jet" with the GMOS-N IFU , but none was found, 2005, unpublished

[b] morphological classification

[c] radius estimates for: SBS 1543 & NGC 4203 - from diameter of 25th B-band isophote; PKS 0439-433 galaxy - radius towards QSO,measured from V band image; OI 363 - using K band estimate 8"

[d] SBS 1543 - HI incl. measured from rotation curve; NGC 4203 - HI inclination of inner disk; PKS 0439-433 galaxy - optical incl. from K-band

[e] absolute B-band magnitude: superscripts k, f, and i denote the magnitude is k-corrected, foreground extinction corrected, and internal extinction corrected via Tully et al. (1998), respectively

[f] K-band magnitudes, not internal extinction corrected, converted to luminosity using Loveday (2000) solar value

[g] SBS 1543 SFR - total H_α star-formation rate from Schulte-Ladbeck et al. (2004); NGC 4203 SFR - FIR star-formation rate calculated with 60 and 100 μm flux densities available from the Infrared Astronomical Satellite (IRAS) along with equations from Helou et al. (1988) and Hopkins et al. (2003)

[h] N_{HI} source: SBS 1543 - Ly-α line; NGC 4203 - X-ray absorption; PKS 0439-433 galaxy - Ly-α line; Jet and Arm near OI 363 - Ly-α line; Unknown galaxy with PG 1216+069 - HI 21cm emission

[i] 1-Bowen et al. (2001b); 2-Rosenberg et al. (2006); 3-Schulte-Ladbeck et al. (2004); 4-Chengalur & Kanekar (2002); 5-Miller et al. (1999); 6-van Driel et al. (1988a); 7-Kanekar et al. (2001); 8-Petitjean et al. (1996); 9-Chen & Lanzetta (2003); 10-Chen et al. (2005); 11-Lane et al. (2000); 12-Turnshek et al. (2001); 13-Rao & Turnshek (1998); 14-Briggs & Barnes (2006); 15-Tripp et al. (2005); 16-Kanekar & Chengalur (2005)

throughout this section (Hinshaw et al., 2009).

5.1.2 Observations and Data Analysis

5.1.2.1 Sample Selection and Optical Data We have selected two galaxies drawn from the SDSS DR5/6 sample of galaxy-quasar pairs. Recall that this sample consists of 154 galaxy-quasar pairs with the quasar projected within twice the Petrosian radius of the galaxy (see Sections 2.2 and 2.4). Mrk 1456 and SDSS J211701.26-002633.7 (SDSS J2117 for brevity) were selected from this set because the background QSOs are within the stellar disks of the galaxy. Mrk 1456 has an impact parameter, b=4.9 kpc, compared with the galaxy's r-band Petrosian radius, r=7.1 kpc. For SDSS J2117, b=5.7 kpc while r=7.5 kpc. These values are both less than the median impact parameters for DLA hosts (b<8.0 kpc) as found by Zwaan et al. (2005). The SDSS redshifts reported for Mrk 1456, Mrk 1457, and SDSS J2117 throughout this section are optical emission line redshifts.

Mrk 1456 and SDSS J2117 were chosen for follow-up HI observations because they are strong DLA candidates that are within the redshift limits of HI 21 cm observations. The beam of our HI observations also included Mrk 1457 so we present the data for this galaxy as well.

Direct measurement of the damped Lyman-α line in low-z systems requires UV spectroscopy from space, which has not been carried out on the two QSOs in this study. However, the small QSO impact parameters, and the strength of the Ca II doublets ($\lambda\lambda$3934,3969) in both Mrk 1456 and SDSS J2117 indicate that they are likely to be DLAs. Wild & Hewett (2005b) and Wild et al. (2006a) have estimated that ∼20-30% of systems with a rest EW (λ3934) $\geq 0.5\mathring{A}$ are DLAs and those with EW$\geq 0.68\mathring{A}$ are highly likely to be a subset of the DLA population. Nestor et al. (2008) note that while strong Ca II absorbers are likely to be DLAs, not all DLAs will have strong Ca II EWs. König et al. (2006) reported a Ca II K EW of $1.24\pm0.15\mathring{A}$ for Mrk 1456, well above the threshold for DLA candidates. For SDSS J2117, we measure a rest Ca II K EW of $1.1\pm0.2\mathring{A}$, also above threshold. The Ca II EW measurements for both Mrk 1456 and SDSS J2117 were made by fitting Gaussians to the lines using a local fit to the continuum.

König et al. (2006) reported on Mrk 1456 as a typical, L^*, giant spiral galaxy with a spectrum of an Sc type disk galaxy. For SDSS J2117, comparison of its spectrum with the templates of Kennicutt (1992) and using the inverse concentration index and u-r color (Park & Choi, 2005; Shimasaku et al., 2001) suggests that it is an Sb type spiral galaxy. A morphological examination of the optical image for SDSS J2117 shows it is a late-type disk galaxy. Mrk 1457 is classified as a Seyfert 2 galaxy in NED[2] and lies 2.3'(2.2 kpc) south of Mrk 1456.

The inclinations, i, of each galaxy were computed using the minor-to-major axis ratio in the r band measured from an exponential fit to the profile, measured out to a radius of three times the effective radius. This gives 45°, 25°, and 52°, for the inclinations of Mrk 1456, Mrk 1457, and SDSS J2117 respectively.

We use the SDSS g and r photometry to calculate the galaxies' absolute magnitudes and luminosities and then transform to Johnson-Morgan-Cousins B using the Smith et al. (2002) transformation laws. The absolute B-band magnitudes reported here were converted to the AB zeropoint system, corrected for galactic extinction (Schlegel et al., 1998), and k-corrected. In order to make a consistent comparison of Mrk 1456 and SDSS J2117 to objects published in the literature, we use k-corrections from Poggianti (1997). With the galaxy inclinations given above, and the HI velocity widths listed in Table 5.3, we correct for internal extinction using the method of Tully et al. (1998). All magnitudes and luminosities are listed in Table 5.2. Assuming $M_B^* = -20.9$ (Marinoni et al., 1999), Mrk 1456 and SDSS J2117 are $\sim 0.5 L_B^*$ galaxies, and Mrk 1457 is a $1.4 L_B^*$ galaxy.

Following the prescription of Hopkins et al. (2003), we derive star-formation rates (SFR) for our objects and for those literature objects for which the data were available or could be calculated (see Table 5.2). The star-formation rates for Mrk 1456, and SDSS J2117 are global Petrosian u-band SFRs corrected for internal extinction using the Balmer-line ratio and a Calzetti obscuration curve (Calzetti et al., 2000). For Mrk 1456 we adopt the Balmer-line ratio from König et al. (2006). For SDSS J2117, we measure a Balmer-line ratio of 7.2 using the Hα flux, corrected for absorption via Hopkins et al. (2003), and the Hβ flux, with the absorption and emission components of the line deblended with two Gaussians. The u-band

[2]NASA Extragalactic Database

Table 5.2 Optical Properties of Mrk 1456 and SDSS J2117

Property	Mrk 1456	SDSS J2117
Type	Sc	Sb
z	0.04757±0.00008	0.05792±0.00009
D_L[Mpc]	208.5±0.3	255.8±0.4
QSO	SDSS J114719.89+522923.1	SDSS J211701.31-0026.38.8
z_{QSO}	1.99	1.14
b["]	5.3	5.1
b[kpc]	4.9	5.7
r["]	7.7	6.7
r[kpc]	7.1	7.5
axis ratio b/a	0.724	0.638
i[°]	45	52
$M_r^{k,f}$	-20.58±0.01	-20.14±0.01
$M_u^{k,f}$	-19.14±0.02	-18.55±0.04
$SFR_u[M_\odot yr^{-1}]$	3.1±0.2	5.6±1.2
$M_B^{k,f,i}$	-20.40±0.09[a]	-20.07±0.09
$L_B[10^{10}L_\odot]$[b]	1.92±0.16	1.41±0.12
L_B^*	0.63±0.05	0.46±0.04
REW(CaII)	1.24±0.15	1.1±0.2
$H\alpha$ [10^{-16}ergs cm^{-2} s^{-1}]	65.65±0.3	20.3±0.2
$L_{H\alpha}$ [10^{40}ergs s^{-1}][c]	8.64±1.69	13.8±0.2
$N_{HI}d$ [10^{22} cm^{-2}][d]	1.8	3.0
$H\beta$ [10^{-16}ergs cm^{-2} s^{-1}]	15.15±0.2	2.8±0.2
$[NII]\lambda6550$ [10^{-16}ergs cm^{-2} s^{-1}]	6.8±0.2	2.09±0.14
$[NII]\lambda6585$ [10^{-16}ergs cm^{-2} s^{-1}]	19.40±0.3	5.29±0.15
$[OII]\lambda3727$ [10^{-16}ergs cm^{-2} s^{-1}]	35.25±0.2	9.3±0.8
$[OIII]\lambda5008$ [10^{-16}ergs cm^{-2} s^{-1}]	9.33±0.1	2.1±0.2
12+log(O/H)[O3N2][e]	8.6±0.1±0.14	8.58±0.02±0.14
12+log(O/H)[N2][e]	8.5±0.2±0.18	8.56±0.01±0.18
12+log(O/H)[R23][e]	8.7±0.2±0.10	8.10±0.11±0.10

[a] this magnitude differs from the value (-21.0±0.02) of König et al. (2006) in that we use Poggianti's kcorrection code and an internal extinction correction based on inclination and HI velocity width, while they use Blanton's kcorrection code (v3.2) Blanton & Roweis (2007) and correct for internal extinction using the Balmer-line ratio and the method of Cardelli et al. (1989)

[b] using colors from Holmberg et al. (2006) and converting to AB zeropoint with Frei & Gunn (1994)

[c] dereddened luminosity

[d] nuclear HI column density derived from $SFR_{H\alpha}$

[e] the two errors listed are our measured error and the systematic error in the calibration for each of the three techniques used, respectively

absolute magnitudes and star-formation rates are given in Table 5.2. We derive 3.1±0.2 and 5.6±1.2 $M_{\odot}\mathrm{yr}^{-1}$ for Mrk 1456 and SDSS J2117, respectively, both in good agreement with the average SFRs for late-type spirals (Kennicutt, 1983, 1998).

Table 5.2 lists several emission-line measured, and derived, properties for Mrk 1456 and SDSS J2117. For Mrk 1456, we adopt the values from König et al. (2006) for emission-line fluxes and derived abundances. For SDSS J2117, emission-line fluxes were measured by fitting Gaussians to the OIII, $H\beta$, NII, and $H\alpha$ emission-lines, while oxygen abundances were measured using the strong-line indices of $\frac{OIII[\lambda5007]/H\beta}{NII[\lambda6583]/H\beta}$ (O3N2), $\frac{NII[\lambda6583]}{H\alpha}$ (N2) (Pettini & Pagel, 2004) and R23 (Kobulnicky et al., 1999; McGaugh, 1991). We find that the O3N2 and N2 derived abundances are in good agreement with each other. Assuming a solar abundance of 8.74±0.08 from Holweger (2001), SDSS J2117 has a metallicity near the solar value.

5.1.2.2 Green Bank Telescope Observations and Reduction The observations of Mrk 1456 were made on 2006 August 27 with the Green Bank Telescope, a 100-m diameter single dish telescope with a FWHM beamwidth of 12.4′/f(GHz). The L-band Gregorian receiver was used, which covers a frequency range of 1.15-1.73 GHz, giving a FWHM beamwidth of 9′ with two linear polarizations. The gain on the L-band receiver is 2 K/Jy. The back-end used was the GBT Spectrometer in the narrow bandwidth, high resolution mode. The spectrometer was set for a 12.5 MHz bandwidth, with 1 spectral window. 9-level sampling was employed to increase sensitivity and to improve the ability to excise Radio Frequency Interference (RFI). The raw spectral resolution was 0.38146 kHz over 32768 channels. We obtained 42 on/off pairs each with a 5 minute integration time resulting in a total integration time of 7 hours, including both signal and reference observations.

To reduce the data we (1) removed any Radio Frequency Interference (RFI) identified by eye in individual scans, (2) subtracted off a baseline, and (3) averaged the two polarizations to achieve the final spectrum. RFI usually presents itself as sharp spikes in the data. Each of the 84 scans was investigated, by eye, for any such spikes and, if found, the bad data were removed. During the RFI removal, two other problems were discovered in the data, including "Bad Lag". "Bad Lag" refers to the incorrect scaling of the raw lags by the spectrometer

(O'Neil, K. 2006)[3]. Each record, 2.5 seconds of data, where this "Bad Lag" occurred was removed from the scan. In addition, when the power spectrum of the data was analyzed, we found a sharp peak at a frequency corresponding to a standing wave on the antenna. The standing wave arises from light that is reflected back and forth between the reflector and the panel gaps on the telescope (Fisher et al., 2003). Due to these standing waves, fourteen scans (140 minutes), were removed from the 1st polarization and eight scans (80 minutes) were removed from the 2nd polarization. Once the bad data were removed, a 3rd, 5th, or 7th order polynomial was fit to each scan and subtracted. After the subtraction of the baseline, each scan was then Hanning smoothed and then further smoothed with a 500 channel (45 km s^{-1}) boxcar filter. After smoothing the data, a weighted average of all of the scans in both polarizations was computed. Each scan is assigned a weight based on its antenna temperature, exposure time, and frequency resolution. Since an entire scan gets a single weight, the channels in a scan that were flagged for RFI removal have an incorrect weighting value. Because data in the flagged channels are removed but not down-weighted, they still contribute some noise to the average spectrum. However, the number of flagged channels for RFI removal in each scan is small enough that it does not cause any noticeable effects in the final averaging. The final spectrum is shown in Figure 5.1.

5.1.2.3 Arecibo Observations and Reduction The data for SDSS J2117 were taken with the 305 m diameter Arecibo telescope on 2006 October 27 on the L-band wide receiver and the interim 50 MHz correlator. The correlator was configured for 9-level sampling in 2 linear polarizations with four boards. Two of the boards were centered on the 1420.4058 MHz line of neutral hydrogen while the other two boards were centered on the 1667.359 and 1720.530 MHz OH lines. Radio frequency interference was too strong at these higher frequencies to make use of the OH observations. For the HI observations, the center frequency was set to 1338.147 MHz, the expected emission frequency of the galaxy. One board was set up with a 25 MHz bandwidth while the other was set-up with a 6.25 MHz bandwidth. In both cases there were 2048 lags per board resulting in velocity resolutions of 2.9 and 0.7 km s^{-1} respectively, before Hanning smoothing.

[3]http://wiki.gb.nrao.edu/bin/view/Software/ModificationRequest15C306

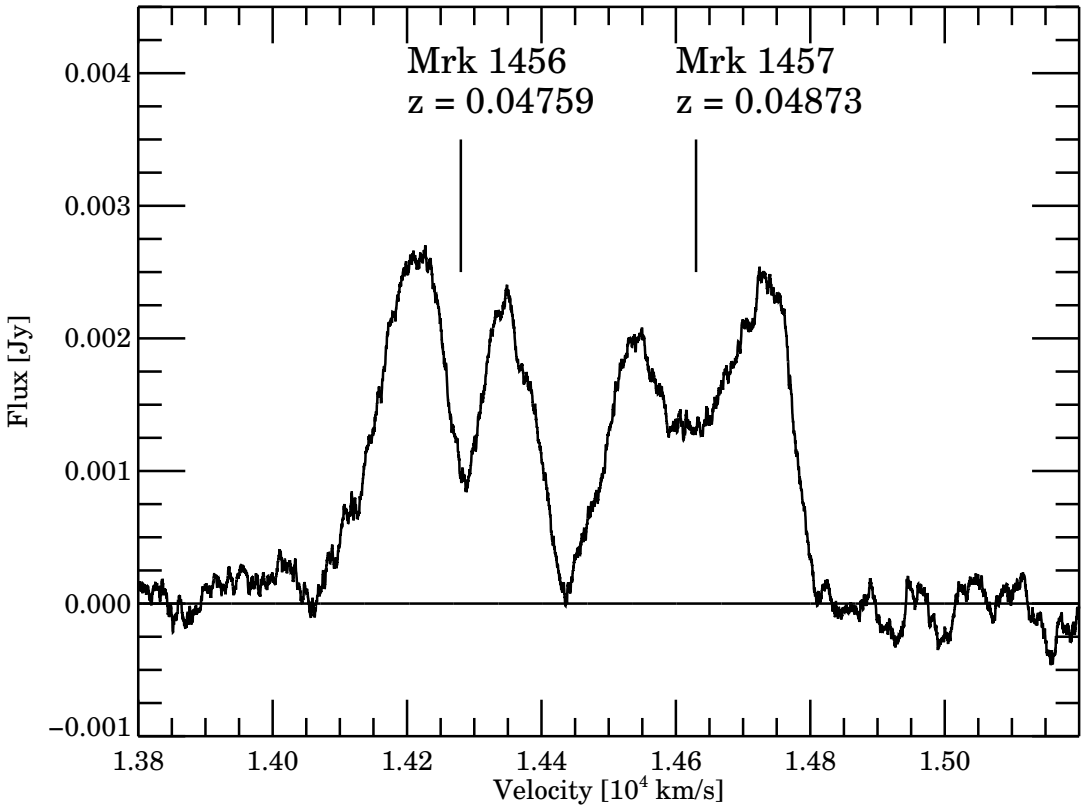

Figure 5.1 HI 21 cm spectrum from GBT showing Mrk 1456 and Mrk 1457

Prior to the beginning of observations a test scan was taken on a blank sky position that showed emission from the 1350/1330 MHz FAA radar. Because of this emission, the radar blanker was used during the observations which reduces the effective integration times by approximately a factor of 1/1.188. The observations of the source consist of 4 on/off observations of 5 minutes each. Each resulting on/off pair was combined, Hanning smoothed and a baseline was fit to the result and subtracted. The eight spectra – 4 on/off pairs with 2 polarizations each – were then averaged and an additional second order polynomial was subtracted from the resulting spectrum. An additional boxcar smoothing of 25 channels or 18.1 km s^{-1} was applied to the spectrum. The final spectrum is shown in Figure 5.2.

5.1.2.4 Analysis Two signals were detected in the GBT observations of Mrk 1456 (see Figure 1). Both signals show the typical double-horned profile as expected from an in-

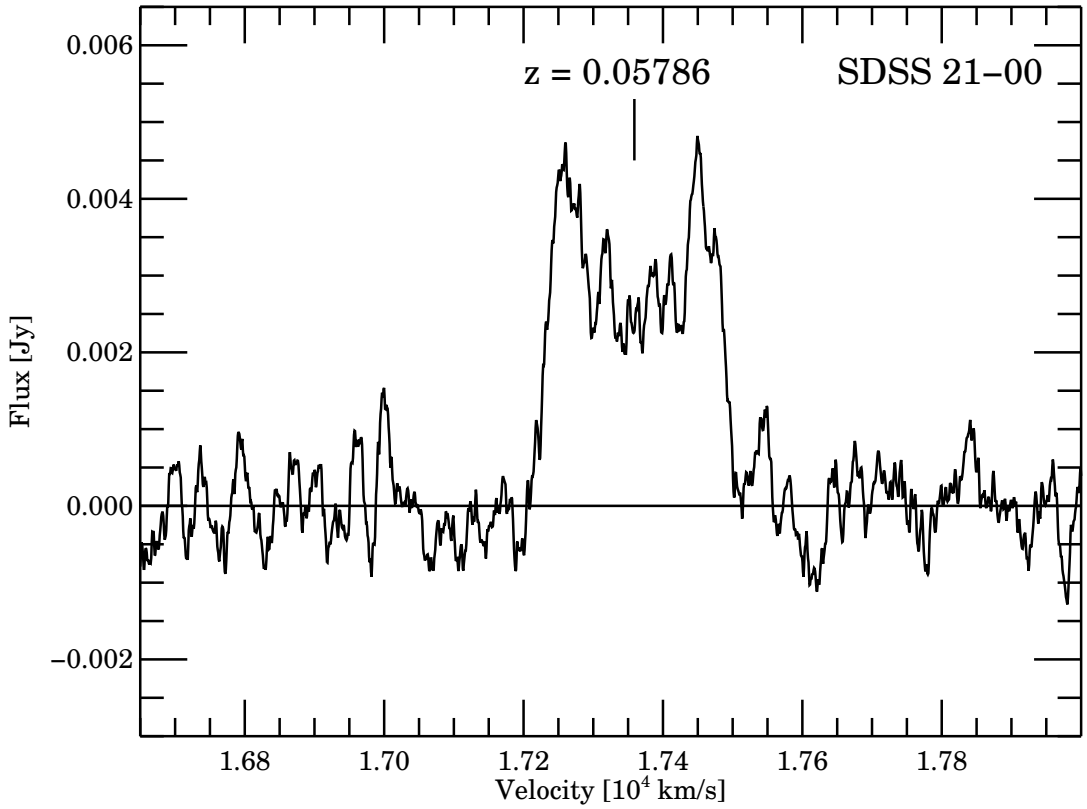

Figure 5.2 HI 21 cm spectrum from Arecibo showing SDSS J211701.26-002633.7

clined disk galaxy. One signal is located at the frequency 1.35587±0.00003 GHz, and corresponds to a redshift of 0.04759±0.00002, which matches the SDSS redshift of Mrk 1456 (0.04757±0.00008) within the errors. The second signal, located at frequency 1.3544±0.0001 GHz, corresponds to a redshift of 0.04873±0.00008, which matches the position and redshift of Mrk 1457 (SDSS redshift 0.04857±0.00009). Mrk 1457 is located about 2.3' south of Mrk 1456. Given the beamwidth of 9', we note that two other members, Mrk 1458 and SDSS J114711.09+522653.4, located at frequencies of 1.35517 GHz (14442 km s^{-1}) and 1.35574 GHz (14310 km s^{-1}) respectively, are also within the beam. Examination of the spectrum in Figure 1 shows that Mrk 1458 falls in the gap between Mrk 1456 and Mrk 1457, where the HI flux falls to zero. SDSS J114711.09+522653.4 falls in the middle of the signal of Mrk 1456. As there is no way to disentangle the two signals, there may be some contribution of HI from SDSS J114711.09+522653.4. However, SDSS J114711.09+522653.4 is an E/S0

galaxy that is 2.8' from Mrk 1456 (the beam center), so we expect the contribution to the HI flux to be small. The regular shape of the spectrum also indicates that this is the case.

GBTIDL is an interactive package for data reduction and analysis of spectral line data taken with the GBT. The task *Gmeasure* in GBTIDL was used to measure the integrated flux, $S(v)dv$, in K·(km s^{-1}), the velocity width W, and systematic velocity of the galaxy profile. The rms noise in the data was taken as the error in the flux. The results of the analysis are shown in Table 5.3.

HI mass was determined from the data using (Verschuur et al., 1974)

$$\frac{M_{HI}}{M_{\odot}} = 2.4 \times 10^5 D^2 \int S(v)dv \tag{5.1}$$

where D is the luminosity distance in Mpc (see Table 5.2), and $S(v)dv$ is the flux integrated over the line in Jy·(km s^{-1})[4]. We include flux and distance errors on the HI mass measurement in Table 5.3.

We estimate the dynamical mass from

$$M_{dyn} = \frac{v_{rot}^2 * r_{HI}}{G} \tag{5.2}$$

where $r_{HI} = 1.5 * r_{opt}$ (Broeils, A. H. & Rhee, M.-H., 1997), r_{opt} is the SDSS r-band Petrosian radius, and v_{rot} is the rotational velocity, estimated by $v_{rot} = \frac{W_{50}}{2 * sin(i)}$, where i here is the optical inclination of the galaxy.

In addition to these basic HI properties of the galaxies, we calculate the HI gas mass fraction, defined as $f_{gas} = M_{HI}/M_{dyn}$, and the gas richness, $M_{HI}/L_B[\mathrm{L}_{\odot}]$. These values are also given in Table 5.3. All HI parameters were calculated using the HI line width at 50% of the peak.

[4] $S(v)dv$ is converted from K·(km s^{-1}) to Jy·(km s^{-1}) before M_{HI} is computed

Table 5.3 HI properties of Mrk 1456, SDSS J2117, and Mrk 1457

Galaxy	Sdv	W_{50}	W_{20}	v_{sys}	M_{HI}	M^*_{HI}	M_{dyn}	$\frac{M_{HI}}{L_B}$	$\frac{M_{dyn}}{L_B}$	$\frac{M_{HI}}{M_{dyn}}$
	$[K \cdot (km\,s^{-1}]$	$[km\,s^{-1}]$	$[km\,s^{-1}]$	$[km\,s^{-1}]$	$[10^9 M_\odot]$		$[10^{11} M_\odot]$			
Mrk 1456	1.0808±0.0016	271.3	322.53	14262.1	5.64±0.002	0.89	0.9±0.4	0.30±0.02	4.8±0.6	0.062±0.006
SDSS J2117	–	255.6	281.8	17357.7	13.6±0.3	2.03	0.69±0.15	1.2±0.1	6.1±0.9	0.20±0.03
Mrk 1457	1.0953±0.0012	294.1	344.94	14631.1	5.97±0.02	0.94	2.1±0.7	0.14±0.01	5.0±0.4	0.029±0.002

[1]measurements made using Gmeasure mode 2, which takes 20% or 50% of the highest peak, and all properties calculated using the W_{50} velocity width

5.1.3 Discussion

5.1.3.1 HI properties of Mrk 1456, SDSS J211701.26-002633.7, and Mrk 1457

We find that both Mrk 1456 and SDSS J2117 have typical HI properties, ie. HI mass, gas richness, gas mass fraction, for galaxies with their given morphological types (Roberts & Haynes, 1994; Salpeter & Hoffman, 1996; Broeils, A. H. & Rhee, M.-H., 1997). Mrk 1457, when compared to other Seyferts, lies at the high end of the normal range of HI masses ([0.2-9.0]x$10^9 M_\odot$) and appears to have an unusually large gas-mass fraction relative to the average f_{gas} of 0.009±0.002 for Seyferts (Haan et al., 2008).

Using the value of $M^*_{HI} = 6.3\times10^9$ $M_\odot$ from Zwaan et al. (2005), Mrk 1456 and Mrk 1457 are slightly sub-M^*_{HI} galaxies, while SDSS J2117 is twice an M^*_{HI} galaxy. Mrk 1456 and SDSS J2117 are representative of average Sb-Sc spiral galaxies with a fair amount of HI gas remaining, while having typcial SFR rates of most spirals, indicative of an on-going SFR process and conversion of their neutral gas reservoir into stars.

5.1.3.2 Comparison with HI-detected DLAs In the following, we discuss HI observations of known/candidate DLAs and sub-DLAs, namely, SBS 1543+593, NGC 4203, and the absorbers towards OI 363, PKS 0439-433, and PG 1216+069. The data are collected in Table 5.1. All values listed have been recalculated using the cosmology adopted in this section, and all magnitudes listed are Johnson-Morgan-Cousins B-band magnitudes converted to the AB zeropoint system, except the magnitude of the OI 363 absorber which is a K-band magnitude.

Presently, only one bonafide DLA has been successfully detected in HI 21 cm emission (Bowen et al., 2001b). SBS 1543+593, a z=0.009 dwarf spiral (Schulte-Ladbeck et al., 2004) is a quasar absorption line galaxy, first found through study of its emission lines (Martel & Osterbrock, 1994; Reimers & Hagen, 1998). SBS 1543+593 is a low surface brightness system that has been extensively studied in emission and absorption (Rosenberg et al., 2006; Bowen et al., 2001a; Bowen et al., 2005; Schulte-Ladbeck et al., 2005). It has HI properties consistent with other dwarf spirals (Roberts & Haynes, 1994; de Blok, W. J. G. et al., 1996; Broeils, A. H. & Rhee, M.-H., 1997) including a low HI mass, a large M_{HI}/L_B, and a

small gas mass fraction.

NGC 4203 was mapped in 21 cm (van Driel et al., 1988b; Burstein & Krumm, 1981) and exhibits a typical HI mass and f_{gas} for the average S0, but an atypically large gas richness (Roberts & Haynes, 1994). The absorbers toward the QSOs OI 363 and PKS 0439-433 were not detected in 21 cm emission (Lane et al., 2000; Kanekar et al., 2001) but have 3σ upper limits to the HI mass. For the OI 363 absorber, it was not optically detected with the exception of two regions of patchy structure near the QSO OI 363, referred to as the "jet" and the "arm" (Turnshek et al., 2001). Although no optical counterpart has been found in conjunction with the z=0.0063 absorber towards PG 1216+069, a weak 21 cm emission signal was found at 3σ significance within 30" (3.8 kpc) of the QSO (Briggs & Barnes, 2006).

Figure 5.3 provides a comparison of several of the galaxy properties listed in Tables 5.1 and 5.2. For the morphological type, we assign a value to each type ranging from 0-E to 6-Irr, with intermediates taking half-integer values, ie. 2.5-Sab. For the z=0.101 galaxy associated with PKS 0439-433, Kanekar et al. (2001) report two upper limits to the HI mass, listed in Table 5.1 and in Figure 5.3, we plot the larger value for the upper limit to the HI mass and M_{HI}/L_B. The absorbers associated with OI 363 and PG 1216+069 are not included as no host galaxy has, as of yet, been clearly identified with the absorbing system. Five objects do not carry statistical weight, but are used to just highlight some broad trends and consistencies.

The morphologies of the DLAs/candidates in Fig. 5.3 consist of one dwarf, one S0 galaxy, and three giant late-type spirals. This diversity in galaxy types naturally accounts for some spread in the derived HI and optical properties shown in Fig. 5.3. With regards to their optical properties, SDSS J2117 and Mrk 1456 fall right in the middle of the distribution of L^*, and M_{HI}/L_B^* values in the given sample. They do, however, exhibit one noteworthy property: they have the highest HI masses of the sample. Our observations of Mrk 1456 and SDSS J2117 have added two candidate DLA galaxies with morphologies and luminosities of giant late-type spirals. Thus they are most directly comparable to the galaxy toward PKS 0439-433, also a late-type giant spiral. The PKS galaxy is an Sab class sub-DLA with an HI column just below the DLA limit, and an impact parameter that is just outside its stellar disk. Given that HI column densities are higher at lower radii and in later morphological subtypes, we

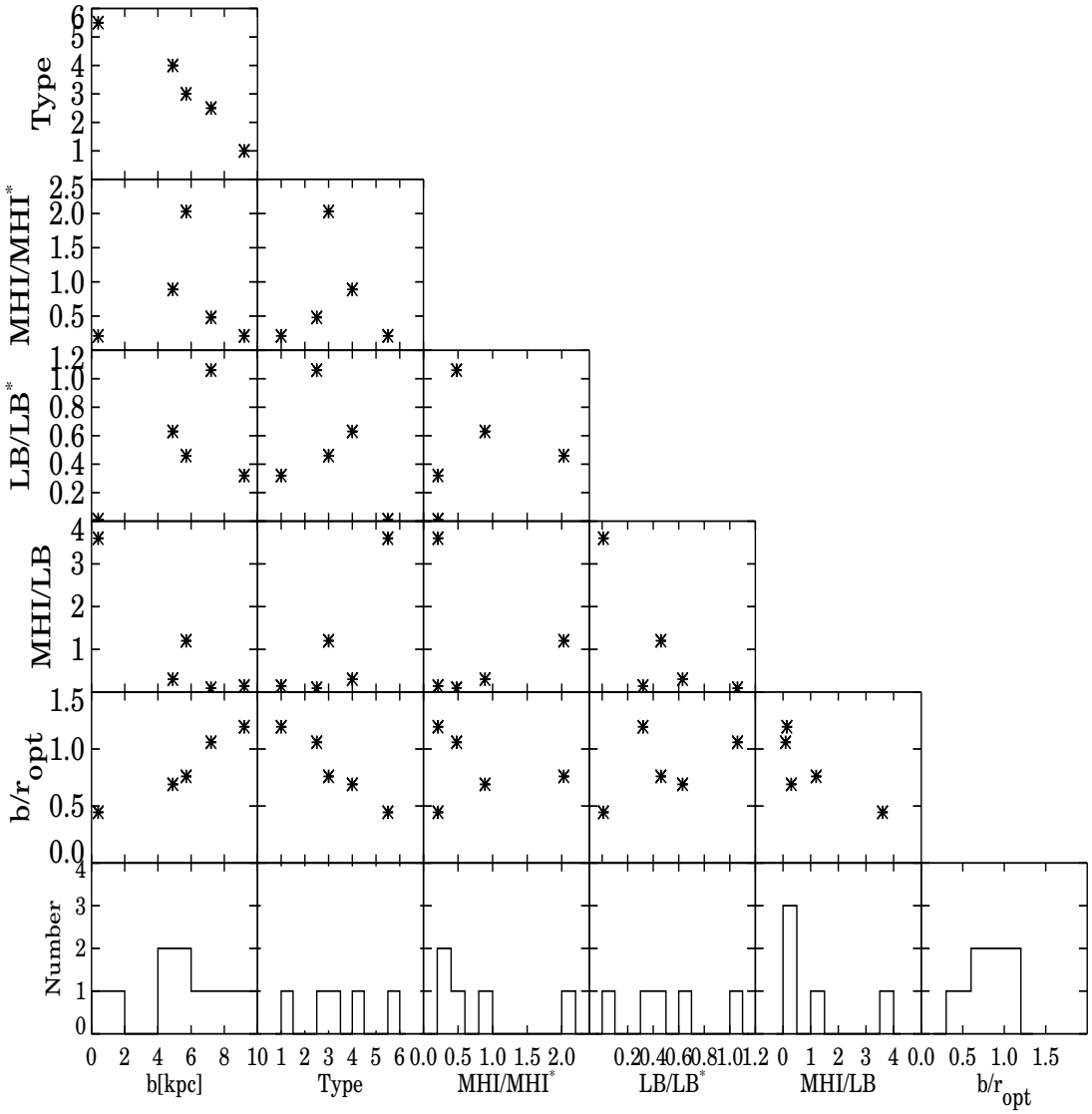

Figure 5.3 Histograms and plots of impact parameter, morphological type, M_{HI}, L_B, M_{HI}/L_B, and ratio of impact parameter to optical radius of the HI DLA sample. The morphological type is represented with numbers from 0-6 for types E-Irr, respectively. M_{HI} is in units of M^*_{HI} and L_B is in units of L^*_B. The absorbers associated with OI 363 and PG 1216+069 are omitted from the diagram.

expect that future observations on the QSO sightlines of Mrk 1456 and SDSS J2117 might reveal HI column densities larger than the DLA limit, as both are later subtypes than the

Table 5.4 Properties of the Mrk 1456 & 'SDSS J2117' Galaxy Group

Group	COM [hh:mm:ss, dd:mm:ss]	COM v_{rad} [km s^{-1}]	W [km s^{-1}]	M_{vir} [$10^{13} M_{\odot}$]	No. of Members	R_{vir} [Mpc]
Mrk 1456	11:47:23.76, +52:27:32.40	14390.04	172.275	0.7352	4	0.3551
SDSS J211701.26-002633.7	21:17:18.96, -00:21:14.40	17339.520	70.697	0.3911	7	1.1219

[1]table lists overall group properties from (Merchán & Zandivarez, 2005):
columns are group coordinates, group systematic velocity, group velocity width, virial mass, # of members, and virial radius

PKS galaxy and both have sightlines to their QSOs that lie inside their stellar disks. The properties of Mrk 1456 and SDSS J2117 agree within the distributions of expected optical properties of z=0 DLAs.

Rosenberg et al. (2006) found that SBS 1543+593 is in a small galaxy group with three other companions, a disk galaxy and two dwarfs, all of which are of low luminosity. All three companions are gas rich systems, with low HI mass ($< 10^9 M_{\odot}$), and average gas content for disk and late-type dwarf galaxies (see Rosenberg et al., 2006, Table 2). This group, and other small groups like it, are likely to be fairly common and important in the contribution to the DLA population. Furthermore, if young, gas-rich galaxy groups are more prevalent at higher redshifts, then these systems might be important to the DLA cross-section. From a search using the NASA/IPAC extragalactic database (NED), none of the other DLAs that have been observed in 21 cm have associated groups, but faint dwarfs could have been missed.

Merchán & Zandivarez (2005) completed a sample of galaxy groups in the DR3 of the Sloan Digital Sky Survey (SDSS). Mrk 1456 is in one such group, with four other members. Mrk 1457 is one such member. All other galaxies in the group are contained within the beam of the GBT, centered on Mrk 1456, but Mrk 1457 was the only other member to be detected in HI 21 cm emission. Merchán & Zandivarez (2005) also show that SDSS J2117 is in a group, consisting of seven other members. Table 5.4 lists a few global properties of the group, ie. the group coordinates, group systematic velocity, group velocity width, virial mass and radius of the group, as calculated by Merchán & Zandivarez (2005) and Table 5.5 lists each group's members and their properties. As both galaxies are situated in groups, the question

of misidentification of the DLA host galaxy becomes an issue. Traditionally, identifying DLA hosts has proven difficult since either no obvious galaxy is visible or identifying the correct host in a group is difficult as the galaxy giving rise to the line may not be the brightest or closest galaxy to the QSO. This is not an issue with Mrk 1456 or SDSS J2117. For both systems, the QSO lies within the stellar disk of the galaxy, and in both groups, the closest companion outside the named galaxy here lies more than 120 kpc from the QSO.

Without HI observations of the galaxies in these groups, it is hard to determine the richness of the group and the environment these galaxies live in. We use u-r color and morphological type as a rough indicator of the gas content of the other galaxies in these groups. The reliability, however, of using optical properties as a predictor of gas content is uncertain as HI-selected galaxies differ more in their optical properties than optically-selected ones, the exception being the most blue galaxies, as they have retained most of their primordial gas. Figure 5.4 shows how galaxies of different morphologies segregate in color and concentration. We plot the galaxies from Park & Choi (2005) overlaid with the Mrk 1456 group (black circles) and the SDSS J2117 group (black diamonds). The galaxies in the Mrk 1456 group, with the exception of Mrk 1456, fall in the region of the diagram occupied by early types. The galaxies in the SDSS J2117 galaxy group, on the other hand, are predominantly Sb-Sc morphological types with only two E/S0 galaxies. Kannappan (2004) showed that there is a relationship between u-r color and gas richness. Galaxies with u-r < 1.5 are gas-rich, $1.5 <$ u-r < 2.5 are intermediate in gas richness, and those with u-r $>$ 2.5 are generally gas-poor. The u-r colors of the galaxies in the two galaxy groups are listed in Table 5.5. These results indicate that both the Mrk 1456 and SDSS J2117 galaxy groups are intermediate in their gas-richness.

The total HI mass of all 4 galaxies detected in the SBS 1543+593 galaxy group adds up to $<3\times10^9 M_\odot$. With two of four galaxies detected in the Mrk 1456 group, its HI content is already much larger, $\sim12\times10^9 M_\odot$. The single galaxy detected in the SDSS J2117 galaxy group has an HI mass of $\approx14\times10^9 M_\odot$, much larger than the entire SBS 1543+593 galaxy group.

5.1.3.3 Comparison with HI-detected galaxies

West (2005) used SDSS to identify

Table 5.5 Properties of Groups Members

Mrk 1456 Galaxy Group								
Members	Ra	Dec	v_{sys}	z	b	b^a_{COM}	Type	u-r
	[hh:mm:ss]	[dd:mm:ss]	[km s^{-1}]		[']	[']		
Mrk 1456	11:47:20.20	+52:29:18.60	14261±24	0.04757±0.00008	—	1.9	Sc	1.47
Mrk 1457	11:47:21.61	+52:26:58.31	14562±28	0.04857±0.00009	2.3	0.7	Sy2	1.94
Mrk 1458	11:47:41.67	+52:26:55.88	14431±27	0.04814±0.00009	4.0	2.8	Sa	2.29
SDSS J114711.09+522653.4	11:47:11.10	+52:26:53.40	14308±46	0.0477±0.0002	2.8	2.0	E/S0	2.57
SDSS J211701.26-002633.7 Galaxy Group								
Members	Ra	Dec	v_{sys}	z	b	b^a_{COM}		
	[hh:mm::ss]	[dd:mm:ss]	[km s^{-1}]		[']	[']		
SDSS J211701.26-002633.7	21:17:01.27	-00:26:33.80	17363±27	0.05792±0.00009	–	6.9	Sbc	1.69
SDSS J211716.84-002715.6	21:17:16.85	-00:27:15.60	17423±28	0.05812±0.00009	4.0	6.0	Sbc	1.83
SDSS J211715.44-002435.5	21:17:15.44	-00:24:35.50	17310±40	0.0577±0.0001	4.1	3.5	E/S0	2.60
SDSS J211709.94-003028.3	21:17:09.94	-00:30:28.30	17365±17	0.05792±0.00006	4.5	9.5	Sc	1.41
SDSS J211723.72-001845.9	21:17:23.72	-00:18:45.90	17391±16	0.05801±0.00005	9.6	2.7	Sbc	1.97
SDSS J211731.47-001246.9	21:17:31.47	-00:12:46.90	17308±46	0.0577±0.0002	15.7	9.0	S0	2.70
SDSS J211733.50-000805.0	21:17:33.50	-00:08:05.00	17217±19	0.05743±0.00007	20.2	13.7	Sc	2.09

[a]distance from Center of Mass of the group

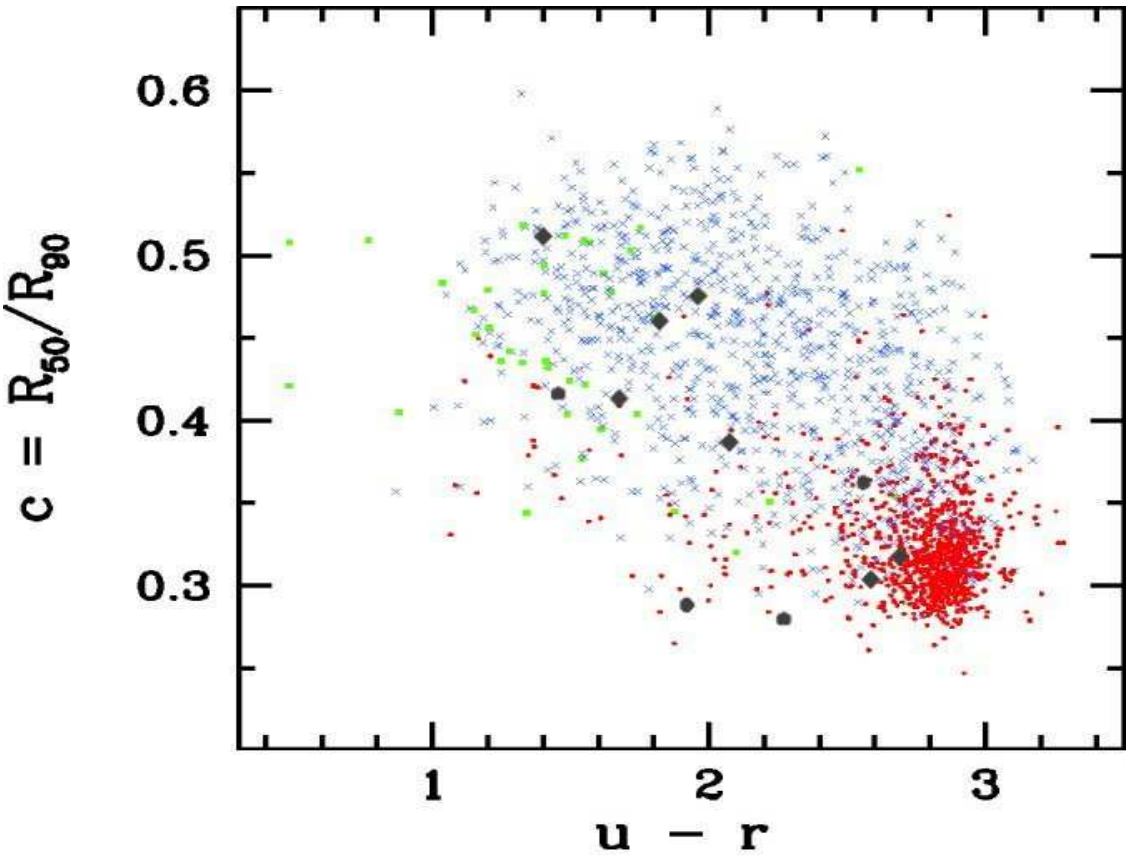

Figure 5.4 Galaxy concentration index versus optical color. The red circles show early type galaxies, green squares show intermediate types, and blue crosses show late types from Park & Choi (2005). The black dots are the Mrk 1456 galaxy group members and the black diamonds are the SDSS J2117 group memebers. Most members from the Mrk 1456 group tend to be early-types, while most from the SDSS J2117 group tend to be late-types, suggesting the latter group is overall more gas-rich than the former.

optical counterparts of HI-selected galaxies from HIPASS and found that HI-selection yields a high fraction of late-type galaxies. For HI-selected spirals, West et al. (2009) give the following median properties: $M_{HI}/L_B = 0.5$, $M_{HI} = M^*_{HI}$, and $L_B = 0.6\ L^*_B$. Our Ca II absorbing galaxies appear to have properties that are comparable to those of HI-selected galaxies.

Rosenberg & Schneider (2003) and Ryan-Weber et al. (2003) also looked at HI-selected galaxies, and focused more specifically on the question of how these contribute to the DLA

cross-section. Rosenberg & Schneider (2003) find a tight correlation between the expected DLA cross-section and the HI mass. Their equation 3 predicts the following DLA cross-sections for Mrk 1456 and SDSS J2117: 853.7 kpc^2 and 2058.4 kpc^2. Using these sizes to estimate the average column density for the galaxies, we find for Mrk 1456, $N_{HI} = 8.23 \times 10^{20} cm^{-2}$, and for SDSS J2117, $N_{HI} = 8.25 \times 10^{20} cm^{-2}$. Rosenberg & Salzer (in prep.) looked at the predicted optical properties for z=0 DLAs from an HI-selected sample and find that the most common morphological type is spiral (45%) and that 50% of the DLAs should have an $M_{HI}/L_B > 0.77$ (2 of the 6 galaxies from the Rosenberg & Salzer (in prep.) sample are from this sample). Ryan-Weber et al. (2003) also find that gas-rich, late-type spirals contribute most to the DLA cross-section.

Figure 5.5 shows the HI mass contribution to dN/dz, the number of expected systems per unit redshift, for z∼0, for a sample of HI-selected galaxies with an HI column larger than the DLA limit from the Arecibo Dual-Beam Survey (ADBS, see Rosenberg & Schneider (2003) for details). The figure shows that 50% of the cross-sectional area is from galaxies with HI masses between 2.9×10^8 and 3.5×10^9. The red-hatched histogram overlayed on top is the HI mass distribution of the objects listed in Tables 1 and 2, with the exception of the OI 363 absorber. The right hand axis lists the values for this histogram, N, the number of galaxies. One might expect the HI mass distribution of DLAs in general to follow the same HI mass distribution of HI-selected galaxies expected to be DLAs. It should be noted that the two galaxy/QSO pairs we add here were not selected using the traditional selection method for quasar absorption line systems, ie. through UV absorption lines. Thus, they introduce some bias in the HI mass distribution as they are giant spirals optically-selected from SDSS with quasars projected within their stellar disks. However, even with this caveat and low statistics, it appears the HI mass distribution of the (candidate) DLAs mimics the distribution of HI-selected galaxies expected to be DLAs.

Zwaan et al. (2005) looked at an optically-selected sample of the local galaxy population (z∼0), mapped in 21 cm emission, in order to connect them to the low-redshift (z<1) DLA population and calculated expected probability distribution functions of different properties for the low-redshift DLAs. They find that, for expected DLA systems, most will be late-type, with a median impact parameter of 8.0 $\mathrm{kpc}^{+10.8}_{-5.3}$, median log M_{HI} of $9.3^{+0.5}_{-0.7}$, and median

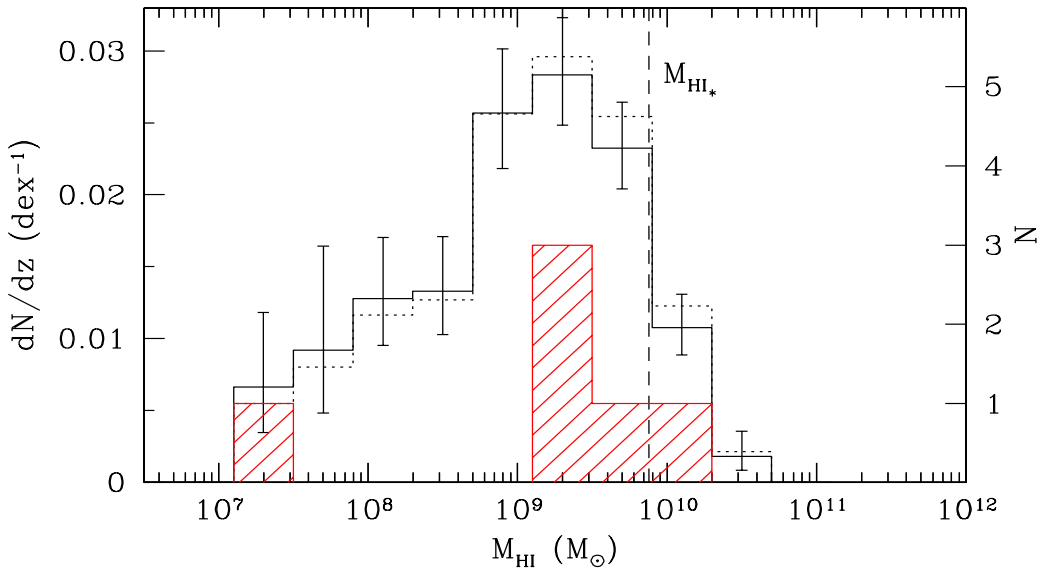

Figure 5.5 dN/dz as a function of HI mass. The open solid and dashed histograms show the distribution for a HI-selected sample of galaxies, representative of z=0 DLAs, from Rosenberg & Schneider (2003). The red hatched histrogram shows the HI masses for the DLA systems listed in Tables 1 and 3. The right-hand axis shows the number of galaxies. The dashed line indicates M^*_{HI}.

M_B=-17.98$^{+2.7}_{-2.0}$. Mrk 1456 and SDSS J2117 are indeed late-types within the range for the expected impact parameter and have values for HI mass and absolute magnitude that lie close to the expected values, on the high end.

5.1.4 Conclusion

We report on the HI 21 cm emission observations of two galaxies, Mrk 1456 and SDSS J211701.26-002633.7. Both are average disk galaxies and candidate DLAs, based on the strengths of their Ca II K EW's and their low impact parameters to the QSO. In terms of their HI properties, both galaxies have typical HI properties for their morphological types with $M_{HI} \sim M^*_{HI}$, average gas richness, and gas mass fractions that are representative of disk galaxies.

These data add to the total number of strong candidate DLAs with HI observations, in the local Universe. Compared with other HI-detected DLAs, Mrk 1456 and SDSS J2117 are similar in most respects, with comparatively higher HI masses. When compared to the expected properties of z=0 DLAs from HI-detected galaxies, we find that Mrk 1456 and SDSS J2117 fall within range of the expected HI mass distribution, median impact parameter, and absolute magnitudes for local DLAs. We also find that both Mrk 1456 and SDSS J2117 reside in groups, adding two DLAs in gas-rich groups to the known population. This may indicate a common phenomenon with regards to the environment of DLAs.

In spite of many years of observational effort, associated galaxies have only been identified in a very small fraction of known DLA systems. Therefore, the nature of the evolving DLA galaxy population has continued to be under investigation, both observationally and theoretically. Historically, two very different scenarios were developed to explain what kind of galaxies produce DLAs. In the explanation put forth by Wolfe et al. (1986), DLAs are associated with massive spiral galaxies. In the model proposed by Haehnelt et al. (1998), DLAs instead arise in low-mass dwarf galaxies.

The numerical and semi-analytical galaxy formation simulations presented over the last decade have modified our view of DLAs. Current models suggest that the median properties of DLA galaxies and their range evolve as a function of cosmic time. In this scenario, dwarfs make up most of the DLA cross-section at high redshifts, with massive disk galaxies contributing more as the Universe evolves. Johansson & Efstathiou (2006) find that higher mass systems make an increasing contribution to the DLA population as redshift decreases. Specifically, Johansson & Efstathiou (2006) predict a median DLA Hydrogen mass of $M_{HI} =$

$2\times 10^9 M_\odot$ at z=0; in good agreement with the results for HI-selected galaxies (Zwaan et al., 2005), and what we find here (cf. Fig. 4). Thus, although Mrk 1456 and SDSS J2117 are case studies of bright QSOs seen through the disks of nearby spiral galaxies, we do not conclude that they support the original Wolfe et al. (1986) picture. Rather, we interpret our results to be compatible with the current theoretical models, as galaxies contributing to the fraction of disk galaxies that make up the DLA cross-section at low redshift. We conclude that our result further strengthens the picture that the local galaxy population, in its variety of gas rich galaxy types that randomly intercept QSO sightlines, can explain the properties of the low-redshift DLAs.

5.2 FUTURE WORK

5.2.1 Future Work on the SDSS pairs

5.2.1.1 Radio Observations: HI 21 cm Emission Zwaan et al. (2005) predict that large disk galaxies should contribute to the DLA population at low redshift, however this observation has yet to occur. Why DLAs have not been seen in disk galaxies at low z is not well understood. With the current (small) batch of low z candidate DLA galaxies with detected HI, this question has yet to be satisfactorily answered. Current radio telescopes have the sensitivity to observe the HI 21 cm line in emission only in galaxies out to $z \sim 0.2$. Out of the 97468 galaxy-quasar pairs, there about ∼15000 individual galaxies with $z < 0.2$. With many more potential systems, HI 21 cm emission-line observations of these systems would allow us to begin to systematically address whether or not large disk galaxies should, and by how much, contribute to the DLA population. Although the HI column density is not directly measurable through 21 cm emission, the likelihood of being a DLA can be inferred using the HI mass estimate (see Section 5.1). Even if 1% of the above systems are detected in emission, 150 systems would greatly enhance the sparsity of candidate DLAs detected in HI at low redshifts.

5.2.1.2 Radio Observations: HI 21 cm Absorption

One area of future work is again with the HI 21 cm line. While HI 21 cm emission-line studies are currently constrained to low redshifts ($z < 0.2$), HI absorption-line studies can be used to study the cold, neutral gas in galaxy environments at all redshifts. HI absorption is also a line-of-sight analysis as opposed to a global HI profile seen in HI emission single-dish observations. Observations of the HI 21 cm line in absorption allows one to probe the ISM and/or nearby environment of external galaxies. By cross-correlating our catalog of 154 galaxy-quasar pairs from SDSS DR5/6 with the FIRST radio survey, we have identified 11 radio-loud quasars. From this sample we obtained HI 21 cm observations of six of these 11, looking for HI 21 cm in absorption from the associated galaxy. Observations were taken in October 2010 using the 100-meter single-dish radio telescope in Green Bank, West Virginia. Data reduction and analysis of the observations are forthcoming. We have also cross-correlated our catalog of 97,468 DR7 galaxy-quasar pairs with FIRST and identified 4505 radio-loud quasars with a mean separation between SDSS and FIRST source positions of $0.4''$.

5.2.1.3 UV Observations: Damped Ly-α line

As discussed in Section 5.1, DLAs are the strongest neutral Hydrogen absorbers known, and make up most of the neutral Hydrogen content of the Universe. The galaxies responsible for DLAs are still not well understood. While estimates of the HI column density from HI 21 cm studies are a good proxy for the DLAs, by definition the HI column density comes from the Lyman-α line of Hydrogen, located in the UV part of the spectrum, at 1216 Å. GALEX is a space telescope tasked with surveying the sky in the ultra-violet, which released their data in public releases much like the SDSS. By cross-correlating our galaxy-quasar catalog with GALEX UV bright sources, we can identify possible DLA absorber candidates that would be easily observable with a UV instrument. We have cross-correlated our catalog of 97,468 DR7 galaxy-quasar pairs with the GALEX DR6 and identified 133,401 matches within a $5''$ radius, with 74,089 matches consisting of only the closest SDSS-GALEX matches. The rest are multiple GALEX sources matched with given SDSS objects. Several observing proposals for the Hubble Space Telescope were submitted (but unsuccessful) to observe a subset of the galaxy-quasar pairs with the COS instrument in an attempt to observe the DLA line of the galaxy in each pair. UV follow-up observations

are an important avenue to explore in furthering our understanding of the DLA-HI galaxy connection.

5.2.2 Potential of Future Surveys Yielding Pairs

Before the SDSS, absorption-line studies were mainly done without any knowledge of the host galaxy causing the absorption. When host galaxies were identified, this was often on a case-by-case basis. With such large numbers of observed objects, the SDSS was the first survey to really allow for a more statistical approach in astronomy. The data used in this thesis was culled from the SDSS, and in particular the spectroscopic subset of galaxies. While several hundred thousand galaxies have spectra taken, it pales in comparison to the number of photometric galaxies surveyed by Sloan, which is at least 3 orders of magnitude larger.

5.2.2.1 SDSS Photometric Sample The SDSS DR7 photometric sky coverage is about 12000 sq. deg down to $r \sim 22$, which allows for the detection of $\sim$100 times fainter galaxies than in the spectroscopic survey. With about 15000 galaxies and 100 quasars per sq. deg, an order of magnitude estimate of the number of galaxy-quasar pairs separated by $1'$, detected over the entire SDSS sky coverage, is 20 million pairs, a sample roughly 200 times larger than that analyzed here.

5.2.2.2 BOSS With the release of DR7, SDSS Phases I and II have been completed. SDSS has now moved on to Phase III, which consists of 4 surveys running through 2014, with each survey focusing on a particular science goal. One such survey is the Baryon Oscillation Spectroscopic Survey (BOSS). BOSS will map the large-scale structure of luminous red galaxies (LRGs) and quasars at intermediate redshifts to study the scale of baryon acoustic oscillations imprinted onto galaxy structure in the early Universe. BOSS will effectively measure redshifts to $\sim$1.7 million galaxies out to $z = 0.7$ and 160,000 quasars at $z = 2-3$. An order-of-magnitude estimate gives $\sim$21,000 spectroscopic galaxy-quasar pairs separated by $1'$, over $\sim$15,000 sq.deg. of the sky. While the spectroscopy itself is not a huge improvement from the previous SDSS data releases, there is about a factor of two improvement over

the number of spectroscopic pairs compared with the DR7 spectroscopic sample, with an emphasis on LRGs as opposed to the Main Galaxy Sample of the SDSS DR7.

5.2.2.3 LSST The Large Synoptic Survey Telescope (LSST) is an upcoming survey that will scan the entire sky every 3 nights, down to $r \sim 26.5$, about another factor of 100 fainter than the SDSS photometric survey. LSST should be able to identify ∼300 million galaxy-quasar pairs at $1'$ over the 20,000 sq. deg sky coverage.

5.2.2.4 BIG BOSS BIG BOSS is a planned instrument upgrade to the Mayall 4-m telescope at KPNO , with the goal of looking for Baryon Acoustic Oscillations. To do so, it will acquire spectra for approximately 20 million galaxies in the redshift range 0.2-1.7 and ∼630,000 of quasars between redshifts 2.2 and 3.5, over ∼14,000 sq. deg of the sky. BIG BOSS should find about 1 million galaxy-quasars pairs separated by $1'$, all with spectra at a resolution of 3000-4800. With spectral coverage from 3400-10600 Å, Ca II and Na I should be detectable out to redshifts of 1.5 and 0.7, respectively. The total spectroscopic exposure time for quasars will be 83 minutes. This gives 3σ limiting equivalent width thresholds for Ca II and Na I around 0.23 Å, and 0.16 Å, a factor of 2 and 3 better than SDSS, respectively. This will allow for an unprecedented number of Ca II and Na I absorption lines to be detected in a large number of galaxy-quasar pairs at intermediate redshifts. With a focus on LRGs, we will be able to study the environments of older systems at intermediate redshifts, complementing our understanding of Ca II and Na I absorption around more active environments today.

APPENDIX A

SQL SELECTION CODE

- **Initial Quasar Galaxy Matching**

```
declare @qid bigint, @a float, @b float
declare cur1 cursor for select q.objid, q.ra, q.dec from mydb..qsoquery1_dr5 as q;

open cur1

fetch next from cur1 into @qid, @a, @b
while @@fetch_status=0
begin
insert into mydb..qsogalmatch(quasar_id, qsora, qsodec, galaxy_id) select @qid, @a, @b, p.objid
from photoobjall as p, dbo.fgetnearbyobjeq(@a,@b,1) as n where p.type=3 and p.objid=n.objid
fetch next from cur1 into @qid, @a,@b
end

close cur1
deallocate cur1
```

- **First Cut - Redshift Cut**

```
select q.quasar_id, s.z, s.zerr, s.specclass, q.galaxy_id, s1.z as galz, s1.zerr as galzerr, s1.specclass
as galspecclass
```

from mydb.qsogalmatch as q join dr6.specobjall as s on q.quasar_id=s.bestobjid join dr6.specobjall as s1 on q.galaxy_id=s1.bestobjid

where (s.z > s1.z and ((s.z-s1.z) > sqrt(power(s.zerr,2) + power(s1.zerr,2))))

- **Second Cut - 2×Petrosian radius Cut**

  select f.quasar_id, p1.ra, p1.dec, f.z, f.zerr, f.specclass, f.galaxy_id, p.ra as galra, p.dec as galdec, f.galz, f.galzerr, f.galspecclass, p.petrorad_r, p.petroraderr_r,

  dbo.fdistancearcmineq(p.ra,p.dec,p1.ra,p1.dec)*60 as b,

  dbo.fdistancearcmineq(p.ra,p.dec,p1.ra,p1.dec)*60/p.petrorad_r as ratio

  from mydb.final_dr6testzcut1nolimits as f left outer join photoobjall as p on f.galaxy_id = p.objid left outer join photoobjall as p1 on f.quasar_id = p1.objid

  where (dbo.fdistancearcmineq(p.ra,p.dec,p1.ra,p1.dec)*60 ≥ 2*p.petrorad_r and

  dbo.fdistancearcmineq(p.ra,p.dec,p1.ra,p1.dec)*60 != 0)

  order by p.ra

APPENDIX B

SDSS DR5/6 SUPPLEMENTARY TABLES

Table B1: List of the 154 Galaxy/Quasar Pairs from the DR5/6 Sample. Included for each pair are the redshifts, the impact parameter between the galaxy and quasar, the r-band Petrosian radius of the galaxy, and the b/r_{Petro} ratio.

Galaxy	z_{gal}	Quasar	z_{QSO}	b ["]	b [kpc]	r_{Petro} ["]	r_{Petro} [kpc]	b/r_{Petro}
SDSS J000508.89+002610.6	0.08451±0.00015	SDSS J000508.85+002608.3	0.6680±0.0021	2.39	3.74	3.66 ±0.14	5.7 ±0.2	0.65± 0.03
SDSS J000512.73+000805.3	0.26340±0.00015	SDSS J000512.18+000802.9	1.1210±0.0012	8.53	34.37	5.47 ±0.35	22.1±1.4	1.56± 0.10
SDSS J001233.41+010014.2	0.08543±0.00009	SDSS J001233.34+010010.3	1.2132±0.0010	3.99	6.32	3.58 ±0.26	5.7 ±0.4	1.11± 0.08
SDSS J003339.85-005522.3	0.21242±0.00010	SDSS J003340.21-005525.5	0.9378±0.0018	6.28	21.54	7.76 ±7.65	26.6±26.2	0.8 ± 0.8
SDSS J004316.15+001035.6	0.14352±0.00017	SDSS J004316.50+001045.1	0.5799±0.0006	10.93	27.27	6.51 ±0.19	16.2±0.5	1.68± 0.05
SDSS J004515.67-011317.8	0.10551±7.38242	SDSS J004515.44-011317.7	1.5942±0.0025	3.45	6.59	9.14 ±0.41	17.5±0.8	0.38± 0.02
SDSS J004604.12+000710.8	0.05745±0.00011	SDSS J004603.29+000729.5	2.5557±0.0018	22.52	24.77	18.02 ±-999	19.8±-999	1.25± -999
SDSS J005244.07-005946.7	0.43247±0.00019	SDSS J005243.92-005954.0	0.6590±0.0002	7.58	42.47	4.31 ±0.57	24.1±3.2	1.8 ± 0.2
SDSS J005850.38+151236.1	0.19803±0.00024	SDSS J005850.70+151227.1	1.3187±0.0016	10.03	32.55	9.27 ±0.69	30.1±2.2	1.08± 0.08
SDSS J015617.64+010249.2	0.07809±0.00017	SDSS J015618.22+010204.2	0.7132±0.0022	45.86	66.94	23.91 ±2.41	35.0±3.5	1.91± 0.19
SDSS J015620.56+010239.0	0.08264±0.00017	SDSS J015618.22+010204.2	0.7132±0.0022	49.44	75.98	6.84 ±0.30	10.5±0.5	7.2 ± 0.3
SDSS J020105.02-002049.6	0.07791±0.00008	SDSS J020105.80-002055.8	1.1106±0.0021	13.24	19.28	6.91 ±0.51	10.1±0.7	1.92± 0.14
SDSS J020328.90+004222.7	0.33954±0.00019	SDSS J020328.34+004222.2	2.1729±0.0014	8.37	40.31	4.39 ±0.47	21.1±2.3	1.9 ± 0.2
SDSS J020838.88+000742.5	0.06722±0.00017	SDSS J020838.40+000737.5	1.6187±0.0023	8.74	11.13	13.11 ±0.21	16.7±0.4	0.67± 0.02
SDSS J020915.27-000047.9	0.06849±0.00003	SDSS J020915.92-000031.0	1.9503±0.0046	19.57	25.33	68.31 ±-999	88.4±-999	0.29± -999
SDSS J021249.59+003448.7	0.16379±0.00023	SDSS J021249.47+003448.6	1.2133±0.0014	1.79	4.91	2.74 ±0.19	7.6 ±0.5	0.66± 0.05
SDSS J021511.59+010005.5	0.12236±0.00018	SDSS J021511.44+005957.6	1.1372±0.0019	8.22	17.89	4.46 ±0.30	9.7 ±0.7	1.84± 0.13
SDSS J021734.23-002637.2	0.04069±0.00015	SDSS J021734.63-002641.9	1.5574±0.0023	7.55	5.91	4.89 ±0.19	3.9 ±0.1	1.54± 0.06
SDSS J022606.84-001655.9	0.40700±0.00100	SDSS J022607.16-001704.0	0.9376±0.0056	9.41	50.84	7.36 ±-999	39.8±-999	1.28± -999
SDSS J023818.88-003030.5	0.03724±0.00009	SDSS J023819.26-003029.3	2.6050±0.0011	5.92	4.32	7.01 ±0.27	5.1 ±0.2	0.84± 0.03
SDSS J024240.70-000047.9	0.00379±0.00001	SDSS J024304.68+000005.4	1.9948±0.0056	363.61	28.13	41.96 ±2.23	3.2 ±0.2	8.7 ± 0.5
SDSS J024243.18-002159.6	0.36981±0.00013	SDSS J024242.51-002212.9	1.9085±0.0017	16.67	84.85	27.92 ±-999	142.±-999	0.51± -999
SDSS J024329.07+003833.7	0.02796±0.00009	SDSS J024328.86+003831.2	2.7532±0.0009	4.02	2.23	6.84 ±0.36	3.8 ±0.2	0.59± 0.03
SDSS J024421.09+004031.3	0.00932±0.00011	SDSS J024420.36+004029.2	2.2179±0.0015	11.17	2.11	34.88 ±2.75	6.6 ±0.5	0.32± 0.03
SDSS J024824.63+010109.1	0.19508±0.00010	SDSS J024824.53+010102.1	1.6192±0.0016	7.21	23.11	3.76 ±0.17	12.1±0.5	1.92± 0.09
SDSS J024830.67-005024.9	0.27091±0.00021	SDSS J024831.08-005025.7	0.8838±0.0016	6.18	25.45	4.26 ±0.52	17.5±2.2	1.45± 0.18
SDSS J025942.67+000141.2	0.04324±0.00023	SDSS J025942.42+000138.1	2.2043±0.0012	4.82	4.06	7.39 ±0.15	6.2 ±0.1	0.65± 0.01

Continued on next page ...

Table B1 – continued

Galaxy	z_{gal}	Quasar	z_{QSO}	b ["]	b [kpc]	r_{Petro} ["]	r_{Petro} [kpc]	b/r_{Petro}
SDSS J030337.58+010638.7	0.15595±0.00016	SDSS J030340.01+010557.1	3.4701±0.0007	55.28	147.7	27.92 ±-999	74.6±-999	1.98± -999
SDSS J030434.14-004701.8	0.17324±0.00012	SDSS J030434.15-004705.5	0.4549±0.0014	3.74	10.91	3.55 ±0.26	10.3±0.8	1.05± 0.08
SDSS J030436.88+004722.2	0.24081±0.00015	SDSS J030437.21+004729.1	2.4166±0.0049	8.52	32.16	7.97 ±0.49	30.1±1.9	1.07± 0.07
SDSS J031236.13+002607.2	0.15673±0.00011	SDSS J031236.20+002603.1	0.4025±0.0009	4.25	11.42	3.21 ±0.36	8.6 ±0.10	1.33± 0.15
SDSS J031257.55-001923.8	0.20834±0.00012	SDSS J031257.10-001927.8	3.3326±0.0012	7.78	26.27	4.47 ±0.11	15.1±0.7	1.74± 0.08
SDSS J032231.78+000647.5	0.34464±0.00025	SDSS J032231.37+000649.6	0.7016±0.0001	6.45	31.35	4.99 ±0.52	24.2±2.5	1.29± 0.14
SDSS J032634.26-011314.4	0.08497±0.00010	SDSS J032634.30-011322.9	2.2346±0.0020	8.43	13.28	4.91 ±0.55	7.9 ±0.9	1.69± 0.19
SDSS J032758.83+001652.0	0.03702±0.00011	SDSS J032759.51+001713.1	2.0617±0.0015	23.31	16.98	27.92 ±-999	20.3±-999	0.84± -999
SDSS J032803.11+002055.1	0.02363±0.00013	SDSS J032801.70+002100.1	0.3220±0.0011	21.63	10.18	11.31 ±-999	5.3 ±-999	1.91± -999
SDSS J033915.91+003304.8	0.14044±0.00014	SDSS J033915.54+003305.9	1.8374±0.0016	5.73	14.04	3.79 ±0.17	9.3 ±0.4	1.51± 0.07
SDSS J034058.04+003253.1	0.13896±0.00018	SDSS J034058.43+003246.4	3.7616±0.0020	8.92	21.65	5.24 ±0.48	12.7±1.2	1.70± 0.16
SDSS J035749.12-061112.3	0.23865±0.00017	SDSS J035749.11-061121.9	2.0054±0.0016	9.57	35.87	5.12 ±3.13	19.2±11.7	1.9 ± 1.14
SDSS J074927.57+175431.6	0.07305±0.00014	SDSS J074928.05+175434.1	0.5233±0.0014	7.41	10.18	4.66 ±0.18	6.4 ±0.3	1.59± 0.06
SDSS J075010.54+304106.3	0.01477±0.00028	SDSS J075010.17+304032.3	1.8921±0.0018	34.25	10.18	22.91 ±0.41	6.8 ±0.1	1.49± 0.03
SDSS J075622.91+421347.2	0.41812±0.00016	SDSS J075623.03+421352.1	2.0885±0.0007	5.02	27.51	3.33 ±1.47	18.3±8.1	1.5 ± 0.7
SDSS J075828.11+374711.8	0.04083±0.00023	SDSS J075825.87+374628.9	1.4999±0.0017	50.45	40.11	45.76 ±0.83	36.5±0.7	1.10± 0.01
SDSS J075829.06+132404.4	0.16557±0.00016	SDSS J075830.78+132341.9	0.2509±0.0001	33.65	94.51	18.02 ±-999	50.6±-999	1.87± -999
SDSS J081653.19+495324.6	0.07231±0.00015	SDSS J081651.85+495334.8	0.1592±0.0014	16.41	22.45	8.83 ±1.11	12.0±1.6	1.9 ± 0.3
SDSS J082412.95+205946.7	0.47102±0.00022	SDSS J082414.91+210006.2	0.7737±0.0018	33.64	198.0	18.02 ±-999	106.±-999	1.87± -999
SDSS J084113.62+285929.1	0.07824±0.00021	SDSS J084113.02+285927.0	1.1488±0.0015	8.13	11.89	6.64 ±0.19	9.7 ±0.3	1.22± 0.04
SDSS J084408.90+333056.5	0.02571±0.00010	SDSS J084409.98+333033.5	3.1839±0.0007	26.67	13.62	20.81 ±4.69	10.7±2.4	1.3 ± 0.3
SDSS J084957.48+510842.3	0.07343±0.00007	SDSS J084957.97+510829.0	0.5835±0.0015	14.01	19.46	10.01 ±0.99	13.9±1.4	1.31± 0.14
SDSS J085442.10+305757.3	0.19562±0.00011	SDSS J085441.73+305754.7	0.1970±0.0012	5.47	17.57	7.21 ±0.88	23.2±2.8	0.76± 0.09
SDSS J090638.43+172221.9	0.12911±0.00021	SDSS J090638.18+172223.4	2.7898±0.0033	3.86	8.80	4.63 ±0.46	10.6±1.1	0.83± 0.08
SDSS J090817.21+052001.7	0.15241±0.00019	SDSS J090816.77+052011.9	0.3441±0.0012	12.15	31.87	7.42 ±0.81	19.5±2.1	1.64± 0.18
SDSS J091557.78+292626.4	0.12206±0.00015	SDSS J091557.29+292618.3	0.5286±0.0014	10.21	22.36	6.41 ±0.23	13.9±0.5	1.61± 0.06
SDSS J091737.67+081347.5	0.07955±0.00018	SDSS J091738.31+081338.7	1.5695±0.0023	12.98	19.27	10.87 ±0.57	16.1±0.8	1.19± 0.06
SDSS J092301.03+075105.1	0.10388±0.00015	SDSS J092300.67+075108.2	1.2980±0.0024	6.21	11.71	6.16 ±0.36	11.6±0.7	1.01± 0.06
SDSS J093211.10+094121.3	0.07598±0.00018	SDSS J093210.96+094116.5	0.0984±0.0010	5.19	7.39	3.84 ±0.31	5.5 ±0.4	1.35± 0.11
SDSS J093641.06+101415.8	0.06001±0.00131	SDSS J093641.77+101424.5	0.9846±0.0016	13.69	15.68	11.17 ±2.83	12.8±3.2	1.2 ± 0.3
SDSS J095641.81+111144.7	0.04157±0.00010	SDSS J095641.68+111130.5	0.7028±0.0016	14.32	11.61	12.23 ±0.14	9.9 ±0.1	1.17± 0.01
SDSS J101552.22+025158.1	0.11734±0.00017	SDSS J101551.80+025201.2	1.8746±0.0014	7.07	14.84	8.87 ±0.36	18.6±0.8	0.71± 0.03
SDSS J103610.02+503218.3	0.04693±0.00016	SDSS J103611.19+503212.8	0.1552±0.0001	12.38	11.26	12.46 ±2.69	11.3±2.4	1.0 ± 0.2

Continued on next page ...

Table B1 – continued

Galaxy	z_{gal}	Quasar	z_{QSO}	b ["]	b [kpc]	r_{Petro} ["]	r_{Petro} [kpc]	b/r_{Petro}
SDSS J103731.74+020816.0	0.11182±0.00014	SDSS J103731.48+020818.3	1.8019±0.0018	4.58	9.21	4.18 ±0.32	8.4 ±0.6	1.09± 0.08
SDSS J103906.41+541956.5	0.06353±0.00016	SDSS J103905.79+542017.8	0.2374±6.8028	22.03	26.6	11.93 ±0.50	14.4±0.6	1.85± 0.08
SDSS J104323.72+404848.9	0.07482±0.00015	SDSS J104325.56+404849.4	4.9324±0.0006	20.79	29.19	11.01 ±0.15	15.6±0.2	1.87± 0.03
SDSS J104329.52+394114.6	0.02351±0.00018	SDSS J104331.07+394044.5	0.1986±8.7878	35.01	16.31	13.71 ±0.76	6.4 ±0.4	2.55± 0.14
SDSS J104533.61+074610.7	0.11102±0.00018	SDSS J104532.99+074559.7	1.0480±0.0021	14.36	28.71	8.65 ±5.52	17.3±11.0	1.7 ± 1.1
SDSS J104922.55+575622.2	0.07551±0.00008	SDSS J104922.07+575631.4	2.9779±0.0009	10.03	14.21	5.14 ±0.20	7.3 ±0.3	1.95± 0.08
SDSS J104949.75+325903.1	0.00541±0.00008	SDSS J104947.40+330026.2	1.0834±0.0019	88.19	9.72	46.55 ±3.46	5.1 ±0.4	1.89± 0.14
SDSS J104955.07+325926.9	0.00572±0.00010	SDSS J104947.40+330026.2	1.0834±0.0019	113.26	13.18	37.89 ±2.37	4.4 ±0.3	2.99± 0.19
SDSS J111025.10+032138.7	0.03001±0.00019	SDSS J111023.85+032136.1	0.9657±0.0010	18.91	11.25	12.83 ±0.26	7.6 ±0.2	1.47± 0.03
SDSS J111508.71+420732.1	0.08213±0.00015	SDSS J111508.34+420728.0	1.6238±0.0011	5.86	8.96	7.62 ±0.74	11.6±1.1	0.77± 0.08
SDSS J112020.74+340546.5	0.03502±0.00019	SDSS J112020.12+340555.3	0.7696±0.0001	11.74	8.08	13.56 ±0.68	9.3 ±0.5	0.87± 0.04
SDSS J112023.20+574429.5	0.00697±0.00013	SDSS J112029.33+574400.5	1.2521±0.0015	56.91	8.07	31.89 ±-999	4.5 ±-999	1.79± -999
SDSS J112206.56+355837.5	0.41853±0.00026	SDSS J112206.71+355833.2	1.7227±0.0020	4.70	25.84	4.49 ±0.95	24.7±5.2	1.1 ± 0.2
SDSS J112512.47+450400.5	0.04525±0.00009	SDSS J112513.25+450346.3	2.3707±0.0186	16.45	14.45	11.77 ±1.01	10.3±0.10	1.31± 0.13
SDSS J113731.00+060748.6	0.49994±0.00031	SDSS J113730.85+060750.9	0.6396±0.0010	3.28	19.99	7.73 ±0.79	47.1±4.8	0.42± 0.04
SDSS J113756.82+005338.4	0.09347±0.00016	SDSS J113757.09+005343.6	1.4571±0.0020	6.54	11.24	5.26 ±0.07	9.0 ±0.1	1.24± 0.02
SDSS J113933.18+261322.5	0.10504±0.00013	SDSS J113933.12+261319.9	0.7202±0.0013	2.70	5.15	3.29 ±0.16	6.3 ±0.3	0.82± 0.04
SDSS J113955.50+132802.0	0.01193±0.00028	SDSS J113955.97+132713.3	1.9939±0.0092	49.15	11.84	25.02 ±-999	6.0 ±-999	1.96± -999
SDSS J114002.72+444806.1	0.06895±0.00015	SDSS J114003.05+444750.7	0.9220±0.0009	15.71	20.58	8.00 ±0.23	10.4±0.3	1.97± 0.06
SDSS J114720.19+522918.6	0.04757±0.00008	SDSS J114719.89+522923.1	1.9883±0.0007	5.33	4.91	7.19 ±0.19	6.6 ±0.2	0.74± 0.01
SDSS J114910.11+084156.2	0.08341±0.00016	SDSS J114911.04+084209.9	1.7633±0.0025	19.36	30.01	13.92 ±0.12	21.6±0.2	1.39± 0.01
SDSS J115115.25+485331.0	0.02564±0.00011	SDSS J115118.58+485331.1	1.0718±0.0019	32.86	16.74	27.92 ±-999	14.2±-999	1.18± -999
SDSS J115507.52+572229.2	0.29095±0.00015	SDSS J115507.95+572228.2	0.2926±0.0012	3.65	15.81	3.50 ±0.25	15.2±1.1	1.04± 0.07
SDSS J115840.67+625423.7	0.25958±0.00015	SDSS J115839.90+625428.0	0.5925±0.0000	6.77	27.01	7.32 ±4.11	29.2±16.4	0.9 ± 0.5
SDSS J121006.28+574425.0	0.06267±0.00004	SDSS J121007.05+574423.5	0.2996±0.0010	6.32	7.54	4.73 ±0.46	5.6 ±0.6	1.33± 0.13
SDSS J121353.59+131022.2	0.00819±0.00010	SDSS J121350.33+131057.8	0.9588±0.0015	59.42	9.87	37.67 ±1.99	6.3 ±0.3	1.58± 0.08
SDSS J121428.17+272159.2	0.10239±0.00005	SDSS J121428.35+272153.4	1.1744±0.0013	6.27	11.67	4.84 ±0.88	9.0 ±1.6	1.2 ± 0.2
SDSS J121802.58+325630.8	0.17611±0.00016	SDSS J121802.01+325632.4	0.6915±0.0013	7.34	21.68	4.54 ±0.08	13.4±0.2	1.62± 0.03
SDSS J122037.63+283803.2	0.02762±0.00011	SDSS J122037.23+283752.0	2.2041±0.0023	12.46	6.82	17.31 ±0.23	9.5 ±0.1	0.72± 0.01
SDSS J122054.17+081637.1	0.07189±0.00018	SDSS J122055.27+081638.3	0.6433±0.0013	16.30	22.06	8.910 ±0.16	12.2±0.2	1.81± 0.03
SDSS J122754.83+080525.4	0.00207±0.00008	SDSS J122752.60+080526.6	1.6213±0.0022	33.03	1.31	19.11 ±0.28	0.8 ±0.0	1.73± 0.03
SDSS J122847.72+370606.9	0.13833±0.00016	SDSS J122847.42+370612.0	1.5168±0.0014	6.110	14.98	3.71 ±0.05	8.10±0.1	1.67± 0.02
SDSS J123006.25+030151.3	0.07933±0.00018	SDSS J123005.84+030204.2	1.6050±0.0023	14.24	21.08	7.17 ±0.15	10.6±0.2	1.99± 0.04

Continued on next page ...

Table B1 – continued

Galaxy	z_{gal}	Quasar	z_{QSO}	b ["]	b [kpc]	r_{Petro} ["]	r_{Petro} [kpc]	b/r_{Petro}
SDSS J123636.73+141333.1	0.00341±0.00060	SDSS J123637.35+141316.2	1.6013±0.0026	19.18	1.33	13.98 ±0.39	0.10±0.0	1.37± 0.04
SDSS J124207.85+323240.5	0.00217±0.00010	SDSS J124225.23+322752.9	0.8441±0.0015	361.95	16.05	169.71±0.03	7.5 ±0.0	2.13± 0.01
SDSS J124207.85+323240.5	0.00217±0.00010	SDSS J124301.34+322902.8	1.0523±0.0018	710.72	31.52	323.11±0.03	14.3±0.0	2.11± 0.01
SDSS J124643.22-004237.2	0.08211±0.00015	SDSS J124644.39-004247.2	1.0588±0.0014	20.19	30.85	11.87 ±0.47	18.1±0.7	1.70± 0.07
SDSS J125700.31+010143.3	0.00930±0.00027	SDSS J125703.67+010132.0	0.9590±0.0016	51.58	9.72	39.18 ±-999	7.4 ±-999	1.32± -999
SDSS J130149.58+033955.2	0.18257±0.00017	SDSS J130149.45+033947.6	1.2234±0.0019	7.79	23.68	4.44 ±0.13	13.5±0.4	1.76± 0.05
SDSS J130351.28+141652.5	0.29843±0.00017	SDSS J130351.25+141650.3	1.1847±0.0014	2.26	9.94	3.04 ±0.19	13.4±0.9	0.74± 0.05
SDSS J131058.62+010842.5	0.03569±0.00009	SDSS J131058.13+010822.2	1.3887±0.0026	21.61	15.14	11.82 ±0.24	8.3 ±0.2	1.83± 0.04
SDSS J131529.74+472958.7	0.00086±0.00001	SDSS J131531.57+473054.6	1.7217±0.0022	58.89	1.04	67.53 ±3.34	1.2 ±0.1	0.87± 0.04
SDSS J131733.12+363033.0	0.07281±0.00016	SDSS J131732.75+363059.6	0.4653±0.0002	26.94	36.81	22.97 ±8.39	31.5±11.5	1.2 ± 0.4
SDSS J131739.09+534600.7	0.07854±0.00015	SDSS J131738.53+534547.5	0.1214±0.0011	14.01	20.69	7.27 ±0.23	10.7±0.3	1.94± 0.06
SDSS J131821.87+555046.4	0.07991±0.00004	SDSS J131820.92+555031.0	0.2118±0.0009	17.37	25.89	11.31 ±-999	16.9±-999	1.54± -999
SDSS J133036.42+040506.2	0.17265±0.00017	SDSS J133036.90+040502.7	1.0743±0.0013	7.96	23.14	6.72 ±0.41	19.5±1.4	1.18± 0.09
SDSS J133734.31+610159.3	0.04163±0.00015	SDSS J133734.53+610227.3	1.2117±0.0018	28.13	22.84	12.27 ±0.42	9.10±0.3	2.29± 0.08
SDSS J134353.45+575429.4	0.09283±0.00016	SDSS J134357.62+575442.4	0.9325±0.0013	35.68	60.89	18.02 ±-999	30.7±-999	1.98± -999
SDSS J134843.94+451931.4	0.26955±0.00018	SDSS J134842.87+451928.4	1.8808±0.0022	11.70	47.98	7.22 ±0.35	29.6±1.4	1.62± 0.08
SDSS J140625.97+250923.3	0.40042±0.00022	SDSS J140626.60+250921.0	0.8668±0.0015	8.84	47.21	4.53 ±0.83	24.2±4.5	2.0 ± 0.4
SDSS J140813.76+535300.5	0.04154±0.00021	SDSS J140812.10+535303.2	0.1164±0.0001	14.98	12.13	17.66 ±0.47	14.3±0.4	0.85± 0.02
SDSS J141801.61+414939.4	0.10262±0.00022	SDSS J141802.79+414935.2	1.0416±0.0020	13.81	25.77	12.32 ±0.53	22.1±0.10	1.12± 0.05
SDSS J142009.64+132626.7	0.14152±0.00019	SDSS J142010.10+132629.1	1.5691±0.0024	7.06	17.39	3.76 ±0.16	9.3 ±0.4	1.88± 0.08
SDSS J142032.11+604321.3	0.16831±0.00015	SDSS J142033.31+604315.1	1.0723±0.0021	10.79	30.72	5.59 ±0.08	15.9±0.2	1.93± 0.03
SDSS J142437.43+453506.8	0.13383±0.00023	SDSS J142438.02+453454.0	0.5193±0.0014	14.15	33.27	8.210 ±0.22	19.5±0.5	1.71± 0.05
SDSS J143313.55+551225.5	0.04283±0.00010	SDSS J143312.27+551231.3	1.1326±0.0013	12.39	10.33	12.52 ±0.11	10.4±0.1	0.99± 0.01
SDSS J144322.25+010553.2	0.03808±0.00009	SDSS J144323.27+010550.8	1.1726±0.0016	15.41	11.49	9.42 ±0.25	7.0 ±0.2	1.64± 0.04
SDSS J145018.25+340538.1	0.08907±0.00019	SDSS J145017.66+340557.0	3.1118±0.0218	20.19	33.11	10.91 ±0.09	17.9±0.1	1.85± 0.02
SDSS J150430.52+430410.0	0.05030±0.00017	SDSS J150431.90+430421.1	1.7675±0.0093	18.81	18.26	11.21 ±0.41	10.1±0.4	1.66± 0.06
SDSS J150842.48+332801.0	0.18988±0.00017	SDSS J150842.19+332802.6	0.8777±0.0019	3.88	12.19	5.08 ±0.52	15.1±1.6	0.76± 0.08
SDSS J151603.95+430936.5	0.01829±0.00011	SDSS J151601.51+430931.4	2.6299±0.0013	27.21	9.97	21.35 ±0.31	7.8 ±0.1	1.27± 0.02
SDSS J151830.96+391606.6	0.19760±0.00016	SDSS J151831.39+391608.3	1.6822±0.0019	5.27	17.06	6.23 ±0.24	20.2±0.8	0.85± 0.03
SDSS J152429.70+303224.1	0.06262±0.00016	SDSS J152428.67+303237.5	0.2743±0.0013	18.92	22.55	10.21 ±0.13	12.2±0.2	1.85± 0.02
SDSS J155613.73+344629.8	0.07309±0.00015	SDSS J155614.96+344630.3	1.8181±0.0021	15.21	20.9	9.710 ±2.34	13.5±3.2	1.6 ± 0.4
SDSS J155752.51+342142.7	0.11367±0.00006	SDSS J155752.31+342140.0	1.2655±0.0013	3.75	7.65	4.75 ±0.23	9.7 ±0.5	0.79± 0.04
SDSS J160345.47+264922.2	0.36594±0.00282	SDSS J160345.98+264923.6	0.4680±0.0019	7.02	35.47	3.54 ±0.47	17.9±2.4	2.0 ± 0.3

Continued on next page ...

Table B1 – continued

Galaxy	z_{gal}	Quasar	z_{QSO}	b ["]	b [kpc]	r_{Petro} ["]	r_{Petro} [kpc]	b/r_{Petro}
SDSS J160502.48+234008.5	0.02987±0.00010	SDSS J160501.66+234028.1	2.4748±0.0013	22.62	13.36	14.98 ±0.77	8.8 ±0.5	1.51± 0.08
SDSS J160652.11+072103.4	0.22354±0.00014	SDSS J160652.26+072109.5	2.4845±0.0015	6.46	23.05	3.65 ±0.13	13.0±0.5	1.77± 0.07
SDSS J160817.07+165018.8	0.14326±0.00015	SDSS J160817.44+165024.0	1.8024±0.0019	7.48	18.61	4.02 ±0.42	10.0±1.0	1.86± 0.19
SDSS J160925.63+240516.8	0.27721±0.00316	SDSS J160925.54+240517.9	0.4127±0.0055	1.62	6.79	4.11 ±2.57	17.2±10.8	0.4 ± 0.2
SDSS J161116.37+242942.1	0.03255±0.00010	SDSS J161116.77+242916.1	1.5325±0.0022	26.54	17.02	25.85 ±-999	16.6±-999	1.03± -999
SDSS J161432.46+301534.3	0.13087±0.00015	SDSS J161432.30+301541.0	2.0607±0.0018	6.98	16.09	4.14 ±0.01	9.6 ±0.2	1.68± 0.03
SDSS J163150.46+141124.6	0.13102±0.00016	SDSS J163150.47+141131.0	1.9530±0.0016	6.39	14.76	5.14 ±0.32	11.9±0.7	1.24± 0.08
SDSS J163317.74+352001.5	0.03454±0.00015	SDSS J163317.75+352018.4	0.2312±0.0011	16.93	11.50	1.02 ±0.81	0.7 ±0.5	16.6± 13.2
SDSS J165006.38+215448.4	0.19324±0.00015	SDSS J165006.23+215451.8	0.1947±0.0011	4.04	12.86	3.83 ±0.19	12.2±0.6	1.06± 0.05
SDSS J165339.11+230944.2	0.33672±0.00019	SDSS J165339.43+230948.3	0.9876±0.0015	6.09	29.15	4.16 ±0.31	19.9±1.9	1.46± 0.14
SDSS J165534.12+370034.3	0.11237±0.00014	SDSS J165533.72+370036.2	1.5848±0.0016	5.17	10.44	3.07 ±0.06	6.2 ±0.1	1.69± 0.03
SDSS J165819.50+623821.3	0.28042±0.00018	SDSS J165819.52+623823.1	0.7033±0.0013	1.79	7.56	3.69 ±0.16	15.6±0.7	0.49± 0.02
SDSS J170330.32+240330.8	0.03083±0.00015	SDSS J170331.83+240339.8	0.9582±0.0016	22.52	13.71	12.01 ±2.76	7.3 ±1.7	1.9 ± 0.4
SDSS J203623.47-043707.4	0.02075±0.00018	SDSS J203624.65-043610.5	0.4574±0.0013	59.64	24.74	33.40 ±1.69	13.9±0.7	1.79± 0.09
SDSS J211701.26-002633.7	0.05792±0.00009	SDSS J211701.31-002638.8	1.1368±0.0039	5.11	5.66	6.75 ±0.18	7.5 ±0.2	0.76± 0.02
SDSS J212626.95+003915.7	0.28913±0.00018	SDSS J212628.04+003911.9	1.7776±0.0015	16.77	72.21	18.02 ±-999	77.7±-999	0.93± -999
SDSS J213108.37-001236.2	0.05855±0.00007	SDSS J213107.44-001229.0	0.7450±0.0012	15.66	17.53	8.83 ±0.31	9.9 ±0.3	1.77± 0.06
SDSS J214053.72+003111.7	0.10851±0.00009	SDSS J214053.58+003108.4	2.8870±0.0013	3.91	7.66	2.77 ±0.13	5.4 ±0.3	1.41± 0.07
SDSS J215418.70+002119.4	0.06714±0.00010	SDSS J215418.48+002054.0	1.2734±0.0015	25.51	32.54	14.27 ±0.48	18.1±0.6	1.79± 0.06
SDSS J215732.60-001226.7	0.10813±0.00019	SDSS J215734.01-001223.6	0.8634±0.0044	21.44	41.89	15.05 ±2.06	29.4±4.0	1.42± 0.2
SDSS J215732.70-001224.3	0.10837±0.00018	SDSS J215734.01-001223.6	0.8634±0.0044	19.66	38.49	13.95 ±1.94	27.3±3.8	1.41± 0.2
SDSS J221216.89+003243.9	0.02971±0.00011	SDSS J221217.27+003227.0	2.2541±0.0021	17.88	10.51	3.66 ±-999	2.2 ±-999	4.88± -999
SDSS J223643.14-011054.1	0.08791±0.00016	SDSS J223642.77-011059.7	2.2598±0.0012	7.83	12.73	3.94 ±1.41	6.4 ±2.3	2.0 ± 0.7
SDSS J224823.20-000934.9	0.05418±0.00013	SDSS J224822.92-000948.8	2.1323±0.0023	14.53	15.13	7.60 ±0.23	7.9 ±0.2	1.91± 0.06
SDSS J231648.38+005948.8	0.06895±0.00016	SDSS J231649.42+005940.7	2.0770±0.0015	17.68	23.03	15.34 ±0.42	19.1±0.5	1.15± 0.03
SDSS J233724.00+002330.0	0.00931±0.00026	SDSS J233722.01+002238.9	1.3771±0.0019	59.13	11.15	43.31 ±-999	8.2 ±-999	1.37± -999
SDSS J234020.41+005602.1	0.35517±0.00016	SDSS J234020.86+005559.7	0.6071±0.0016	7.07	35.06	5.16 ±0.43	25.6±2.1	1.37± 0.11
SDSS J234139.32+003641.8	0.17658±0.00009	SDSS J234139.92+003644.2	1.0257±0.0016	9.26	27.42	5.15 ±0.17	15.2±0.5	1.80± 0.06

Table B2: List of the galaxy optical properties in the final sample of 154 galaxy/quasar pairs generated from the DR5/6. Each galaxy lists the redshift, g and r-band Sloan apparent magnitudes, B-band absolute magnitude, the B-band luminosity in units of L^*, our spectroscopic and morphological classification, and the assigned color based on the cut of Yan et al. (2006).

Galaxy	z_{gal}	g[a]	r[a]	M_B	L_B $[L^*]$	SpecType	MorphType	Color
SDSS J000508.89+002610.6	0.08451±0.00015	18.237± 0.012	17.122± 0.007	-18.77± 0.05	0.14± 0.01	0.5	0.5	Red
SDSS J000512.73+000805.3	0.26340±0.00015	19.225± 0.026	17.819± 0.012	-21.41± 0.13	1.59± 0.19	2.0	0.5	Red
SDSS J001233.41+010014.2	0.08543±0.00009	19.629± 0.034	18.979± 0.022	-17.65± 0.08	0.05± 0.00	4.0	3.0	Blue
SDSS J003339.85-005522.3	0.21242±0.00010	19.354± 0.036	18.730± 0.025	-20.49± 0.09	0.69± 0.06	4.0	4.0	Blue
SDSS J004316.15+001035.6	0.14352±0.00017	17.840± 0.009	16.744± 0.006	-20.73± 0.04	0.86± 0.04	0.5	0.5	Red
SDSS J004515.67-011317.8	0.10551±7.38242	17.616± 0.015	17.335± 0.013	-20.42± 0.05	0.64± 0.03	4.0	4.0	Blue
SDSS J004604.12+000710.8	0.05745±0.00011	17.369± 0.010	17.040± 0.012	-19.12± 0.05	0.19± 0.01	4.0	5.0	Blue
SDSS J005244.07-005946.7	0.43247±0.00019	20.551± 0.064	18.752± 0.017	-21.96± 0.12	2.64± 0.30	1.5	0.5	Red
SDSS J005850.38+151236.1	0.19803±0.00024	20.053± 0.067	18.318± 0.022	-19.42± 0.13	0.26± 0.03	0.0	0.5	Red
SDSS J015617.64+010249.2	0.07809±0.00017	16.191± 0.009	15.362± 0.006	-20.73± 0.04	0.86± 0.04	0.0	0.5	Blue
SDSS J015620.56+010239.0	0.08264±0.00017	16.445± 0.004	15.548± 0.003	-20.60± 0.04	0.76± 0.03	0.0	0.5	Red
SDSS J020105.02-002049.6	0.07791±0.00008	18.902± 0.025	18.561± 0.024	-18.33± 0.07	0.09± 0.01	4.5	4.5	Blue
SDSS J020328.90+004222.7	0.33954±0.00019	20.936± 0.067	19.124± 0.021	-20.66± 0.13	0.80± 0.01	1.5	0.5	Red
SDSS J020838.88+000742.5	0.06722±0.00017	15.758± 0.004	14.930± 0.003	-20.80± 0.04	0.91± 0.03	2.0	2.5	Red
SDSS J020915.27-000047.9	0.06849±0.00003	19.986± 0.052	19.527± 0.051	-16.85± 0.11	0.02± 0.00	4.5	3.5	Blue
SDSS J021249.59+003448.7	0.16379±0.00023	19.492± 0.019	18.414± 0.011	-19.49± 0.06	0.27± 0.02	2.0	0.5	Red
SDSS J021511.59+010005.5	0.12236±0.00018	17.352± 0.006	16.361± 0.004	-20.77± 0.04	0.89± 0.03	2.0	0.5	Red
SDSS J021734.23-002637.2	0.04069±0.00015	18.319± 0.012	17.594± 0.009	-17.06± 0.05	0.03± 0.00	0.5	2.0	Red
SDSS J022606.84-001655.9	0.40700±0.00100	20.865± 0.075	19.497± 0.030	-21.12± 0.15	1.22± 0.17	-1.5	3.0	Blue
SDSS J023818.88-003030.5	0.03724±0.00009	17.855± 0.011	17.559± 0.014	-17.68± 0.05	0.05± 0.00	5.5	6.0	Blue
SDSS J024240.70-000047.9	0.00379±0.00001	9.950 ± 0.005	9.407 ± 0.007	-20.13± 0.04	0.49± 0.02	-1.5	3.0	Red

Continued on next page ...

Table B2 – continued

Galaxy	z_{gal}	g[a]	r[a]	M_B	L_B $[L^*]$	SpecType	MorphType	Color
SDSS J024243.18-002159.6	0.36981±0.00013	20.765± 0.083	19.856± 0.051	-20.77± 0.17	0.89± 0.14	4.0	5.0	Blue
SDSS J024329.07+003833.7	0.02796±0.00009	18.008± 0.012	17.893± 0.015	-16.97± 0.05	0.03± 0.00	5.5	5.5	Blue
SDSS J024421.09+004031.3	0.00932±0.00011	15.256± 0.004	14.907± 0.005	-17.21± 0.05	0.03± 0.00	5.5	6.0	Blue
SDSS J024824.63+010109.1	0.19508±0.00010	19.488± 0.026	18.836± 0.011	-20.11± 0.07	0.48± 0.03	3.0	3.0	Blue
SDSS J024830.67-005024.9	0.27091±0.00021	20.213± 0.059	19.299± 0.032	-20.47± 0.17	0.67± 0.10	3.0	0.5	Blue
SDSS J025942.67+000141.2	0.04324±0.00023	17.513± 0.001	17.159± 0.001	-18.31± 0.05	0.09± 0.00	4.0	3.5	Blue
SDSS J030337.58+010638.7	0.15595±0.00016	19.220± 0.054	19.966± 0.085	-20.39± 0.12	0.63± 0.07	0.5	1.5	Red
SDSS J030434.14-004701.8	0.17324±0.00012	18.903± 0.018	17.881± 0.010	-20.30± 0.06	0.58± 0.03	0.5	0.5	Red
SDSS J030436.88+004722.2	0.24081±0.00015	19.024± 0.032	17.901± 0.016	-21.19± 0.09	1.31± 0.11	2.0	1.5	Red
SDSS J031236.13+002607.2	0.15673±0.00011	20.185± 0.031	19.439± 0.026	-18.73± 0.01	0.14± 0.01	3.0	2.5	Blue
SDSS J031257.55-001923.8	0.20834±0.00012	19.194± 0.025	18.451± 0.016	-20.56± 0.07	0.73± 0.05	3.0	3.5	Blue
SDSS J032231.78+000647.5	0.34464±0.00025	19.753± 0.054	18.022± 0.017	-21.94± 0.16	2.61± 0.31	1.0	0.5	Red
SDSS J032634.26-011314.4	0.08497±0.00010	19.030± 0.034	18.546± 0.023	-18.30± 0.08	0.09± 0.01	4.0	2.5	Blue
SDSS J032758.83+001652.0	0.03702±0.00011	19.072± 0.067	18.191± 0.043	-16.00± 0.13	0.01± 0.00	6.0	6.0	Red
SDSS J032803.11+002055.1	0.02363±0.00013	18.828± 0.031	18.528± 0.039	-15.65± 0.08	0.01± 0.00	6.0	6.0	Blue
SDSS J033915.91+003304.8	0.14044±0.00014	18.974± 0.011	17.972± 0.011	-19.59± 0.06	0.21± 0.02	2.0	2.0	Red
SDSS J034058.04+003253.1	0.13896±0.00018	18.408± 0.014	17.367± 0.008	-20.01± 0.05	0.48± 0.02	0.5	0.5	Red
SDSS J035749.12-061112.3	0.23865±0.00017	19.921± 0.047	18.767± 0.022	-20.31± 0.11	0.58± 0.06	0.5	1.5	Red
SDSS J074927.57+175431.6	0.07305±0.00014	17.327± 0.005	16.517± 0.004	-19.45± 0.04	0.26± 0.01	0.5	0.5	Red
SDSS J075010.54+304106.3	0.01477±0.00028	16.475± 0.008	16.165± 0.015	-16.97± 0.08	0.03± 0.00	4.5	3.0	Blue
SDSS J075622.91+421347.2	0.41812±0.00016	20.903± 0.065	19.250± 0.022	-21.40± 0.14	1.59± 0.20	0.5	0.5	Red
SDSS J075828.11+374711.8	0.04083±0.00023	13.778± 0.002	12.933± 0.002	-21.51± 0.04	1.76± 0.06	1.5	0.5	Red
SDSS J075829.06+132404.4	0.16557±0.00016	17.948± 0.010	16.941± 0.007	-21.07± 0.05	1.17± 0.05	2.0	1.5	Blue
SDSS J081653.19+495324.6	0.07231±0.00015	17.291± 0.007	16.536± 0.005	-19.48± 0.04	0.27± 0.01	2.0	2.5	Blue
SDSS J082412.95+205946.7	0.47102±0.00022	20.913± 0.122	19.283± 0.037	-21.96± 0.25	2.65± 0.60	1.5	0.5	Blue
SDSS J084113.62+285929.1	0.07824±0.00021	18.270± 0.015	17.730± 0.011	-18.83± 0.05	0.15± 0.01	2.5	3.5	Blue
SDSS J084408.90+333056.5	0.02571±0.00010	14.915± 0.003	14.113± 0.002	-19.21± 0.04	0.23± 0.01	2.0	3.0	Red
SDSS J084957.48+510842.3	0.07343±0.00007	16.348± 0.006	15.941± 0.005	-20.70± 0.04	0.83± 0.03	4.0	4.0	Blue

Continued on next page ...

Table B2 – continued

Galaxy	z_{gal}	g[a]	r[a]	M_B	L_B $[L^*]$	SpecType	MorphType	Color
SDSS J085442.10+305757.3	0.19562±0.00011	18.719± 0.018	17.695± 0.009	-20.84± 0.06	0.95± 0.05	3.0	1.5	Blue
SDSS J090638.43+172221.9	0.12911±0.00021	18.681± 0.013	17.724± 0.008	-19.61± 0.05	0.30± 0.01	3.0	1.5	Red
SDSS J090817.21+052001.7	0.15241±0.00019	18.084± 0.011	16.983± 0.007	-20.69± 0.05	0.82± 0.04	0.5	0.5	Red
SDSS J091557.78+292626.4	0.12206±0.00015	17.920± 0.012	17.163± 0.009	-20.28± 0.05	0.56± 0.03	3.0	2.5	Blue
SDSS J091737.67+081347.5	0.07955±0.00018	16.204± 0.004	15.302± 0.003	-20.74± 0.04	0.87± 0.03	0.5	0.5	Red
SDSS J092301.03+075105.1	0.10388±0.00015	17.412± 0.007	16.293± 0.005	-20.18± 0.04	0.52± 0.02	2.0	0.5	Red
SDSS J093211.10+094121.3	0.07598±0.00018	17.581± 0.006	16.652± 0.004	-19.23± 0.04	0.21± 0.01	0.0	0.5	Red
SDSS J093641.06+101415.8	0.06001±0.00131	15.898± 0.003	15.136± 0.003	-20.46± 0.09	0.67± 0.05	-1.0	3.0	Blue
SDSS J095641.81+111144.7	0.04157±0.00010	15.697± 0.004	14.963± 0.003	-19.76± 0.04	0.35± 0.01	2.0	2.5	Blue
SDSS J101552.22+025158.1	0.11734±0.00017	17.824± 0.011	16.899± 0.007	-20.20± 0.05	0.53± 0.02	1.0	1.5	Red
SDSS J103610.02+503218.3	0.04693±0.00016	17.432± 0.006	16.459± 0.005	-18.14± 0.04	0.08± 0.00	2.0	2.5	Red
SDSS J103731.74+020816.0	0.11182±0.00014	17.821± 0.008	16.887± 0.005	-20.07± 0.04	0.46± 0.02	1.0	1.5	Red
SDSS J103906.41+541956.5	0.06353±0.00016	15.852± 0.004	15.106± 0.003	-20.61± 0.04	0.76± 0.03	2.0	2.5	Blue
SDSS J104323.72+404848.9	0.07482±0.00015	16.726± 0.007	16.215± 0.005	-20.31± 0.04	0.58± 0.02	2.5	3.5	Blue
SDSS J104329.52+394114.6	0.02351±0.00018	14.341± 0.002	13.503± 0.002	-19.67± 0.04	0.32± 0.01	2.0	2.0	Red
SDSS J104533.61+074610.7	0.11102±0.00018	18.407± 0.015	17.504± 0.009	-19.46± 0.05	0.27± 0.01	2.5	2.0	Red
SDSS J104922.55+575622.2	0.07551±0.00008	17.803± 0.006	17.405± 0.006	-19.34± 0.04	0.24± 0.01	4.0	4.5	Blue
SDSS J104949.75+325903.1	0.00541±0.00008	13.547± 0.002	13.189± 0.002	-17.79± 0.03	0.06± 0.00	-1.5	4.5	Blue
SDSS J104955.07+325926.9	0.00572±0.00010	12.805± 0.002	12.507± 0.002	-18.62± 0.07	0.12± 0.01	-1.5	6.0	Blue
SDSS J111025.10+032138.7	0.03001±0.00019	16.396± 0.005	15.939± 0.005	-18.53± 0.04	0.11± 0.00	2.5	4.0	Blue
SDSS J111508.71+420732.1	0.08213±0.00015	16.845± 0.005	15.804± 0.004	-20.12± 0.04	0.49± 0.02	2.0	1.5	Red
SDSS J112020.74+340546.5	0.03502±0.00019	14.821± 0.002	14.075± 0.002	-20.17± 0.04	0.51± 0.02	0.5	2.5	Red
SDSS J112023.20+574429.5	0.00697±0.00013	16.619± 0.001	16.201± 0.013	-15.12± 0.08	0.00± 0.00	-1.5	5.5	Blue
SDSS J112206.56+355837.5	0.41853±0.00026	20.971± 0.070	19.392± 0.027	-21.45± 0.32	1.65± 0.49	2.0	0.5	Red
SDSS J112512.47+450400.5	0.04525±0.00009	17.136± 0.008	16.458± 0.005	-18.55± 0.05	0.12± 0.00	3.5	3.0	Blue
SDSS J113731.00+060748.6	0.49994±0.00031	21.642± 0.241	19.002± 0.035	-21.61± 0.46	1.92± 0.81	1.0	0.5	Red
SDSS J113756.82+005338.4	0.09347±0.00016	17.484± 0.006	16.564± 0.004	-19.90± 0.04	0.31± 0.01	0.0	0.5	Red
SDSS J113933.18+261322.5	0.10504±0.00013	18.329± 0.001	17.521± 0.007	-19.46± 0.05	0.26± 0.01	2.0	1.5	Red

Continued on next page ...

Table B2 – continued

Galaxy	z_{gal}	g[a]	r[a]	M_B	L_B $[L^*]$	SpecType	MorphType	Color
SDSS J113955.50+132802.0	0.01193±0.00028	15.762± 0.005	15.309± 0.004	-17.01± 0.09	0.03± 0.00	4.5	5.5	Blue
SDSS J114002.72+444806.1	0.06895±0.00015	17.261± 0.007	16.773± 0.007	-19.56± 0.04	0.29± 0.01	3.0	3.5	Blue
SDSS J114720.19+522918.6	0.04757±0.00008	16.234± 0.003	15.894± 0.003	-19.82± 0.04	0.37± 0.01	4.0	4.0	Blue
SDSS J114910.11+084156.2	0.08341±0.00016	16.937± 0.005	16.017± 0.004	-20.12± 0.04	0.49± 0.02	2.0	2.5	Red
SDSS J115115.25+485331.0	0.02564±0.00011	17.295± 0.011	16.920± 0.030	-17.37± 0.05	0.04± 0.00	4.0	4.5	Blue
SDSS J115507.52+572229.2	0.29095±0.00015	20.517± 0.046	19.229± 0.023	-20.59± 0.36	0.75± 0.25	2.0	0.5	Red
SDSS J115840.67+625423.7	0.25958±0.00015	19.579± 0.042	18.418± 0.023	-20.92± 0.01	1.02± 0.09	2.0	0.5	Blue
SDSS J121006.28+574425.0	0.06267±0.00004	17.766± 0.006	16.917± 0.005	-18.61± 0.04	0.12± 0.00	4.0	2.0	Red
SDSS J121353.59+131022.2	0.00819±0.00010	12.938± 0.002	12.231± 0.002	-18.76± 0.05	0.14± 0.01	4.0	3.5	Red
SDSS J121428.17+272159.2	0.10239±0.00005	18.021± 0.008	17.539± 0.007	-19.80± 0.04	0.36± 0.01	4.0	4.0	Blue
SDSS J121802.58+325630.8	0.17611±0.00016	18.639± 0.011	17.874± 0.008	-20.61± 0.05	0.77± 0.04	3.0	3.5	Blue
SDSS J122037.63+283803.2	0.02762±0.00011	16.398± 0.006	16.073± 0.007	-18.44± 0.04	0.10± 0.00	4.0	4.5	Blue
SDSS J122054.17+081637.1	0.07189±0.00018	16.357± 0.004	15.433± 0.003	-20.31± 0.04	0.58± 0.02	1.0	0.5	Red
SDSS J122754.83+080525.4	0.00207±0.00008	14.902± 0.003	14.282± 0.002	-13.95± 0.13	0.00± 0.00	0.0	0.5	Red
SDSS J122847.72+370606.9	0.13833±0.00016	18.634± 0.009	17.823± 0.007	-19.89± 0.05	0.31± 0.02	2.0	2.5	Blue
SDSS J123006.25+030151.3	0.07933±0.00018	16.527± 0.005	15.642± 0.003	-20.42± 0.04	0.64± 0.02	0.5	0.5	Red
SDSS J123636.73+141333.1	0.00341±0.00060	17.032± 0.010	16.461± 0.011	-12.91± 0.59	0.00± 0.00	-1.5	0.0	Red
SDSS J124207.85+323240.5	0.00217±0.00010	19.224± 0.011	17.753± 0.009	-9.09 ± 0.16	1.8±9 2.83	-1.5	5.0	Red
SDSS J124207.85+323240.5	0.00217±0.00010	19.224± 0.011	17.753± 0.009	-9.09 ± 0.16	1.8±9 2.83	-1.5	5.0	Red
SDSS J124643.22-004237.2	0.08211±0.00015	16.205± 0.004	15.383± 0.003	-20.88± 0.04	0.98± 0.03	2.0	2.0	Blue
SDSS J125700.31+010143.3	0.00930±0.00027	16.162± 0.006	15.757± 0.007	-16.17± 0.11	0.01± 0.00	-1.5	5.5	Blue
SDSS J130149.58+033955.2	0.18257±0.00017	18.530± 0.013	17.374± 0.008	-20.81± 0.05	0.92± 0.04	2.0	1.5	Red
SDSS J130351.28+141652.5	0.29843±0.00017	20.889± 0.076	18.828± 0.019	-20.04± 0.22	0.45± 0.09	2.0	1.5	Red
SDSS J131058.62+010842.5	0.03569±0.00009	15.492± 0.003	14.828± 0.003	-19.68± 0.04	0.33± 0.01	2.5	3.0	Blue
SDSS J131529.74+472958.7	0.00086±0.00001	15.034± 0.004	14.754± 0.004	-12.22± 0.05	0.00± 1.69	-1.5	6.0	Blue
SDSS J131733.12+363033.0	0.07281±0.00016	17.909± 0.007	17.043± 0.005	-18.83± 0.04	0.15± 0.01	0.5	0.5	Red
SDSS J131739.09+534600.7	0.07854±0.00015	16.958± 0.005	16.329± 0.004	-20.11± 0.04	0.48± 0.02	3.0	3.0	Blue
SDSS J131821.87+555046.4	0.07991±0.00004	18.618± 0.016	18.264± 0.017	-18.64± 0.06	0.12± 0.01	5.5	6.0	Blue

Continued on next page ...

Table B2 – continued

Galaxy	z_{gal}	g[a]	r[a]	M_B	L_B $[L^*]$	SpecType	MorphType	Color
SDSS J133036.42+040506.2	0.17265±0.00017	18.441± 0.013	17.311± 0.008	-20.72± 0.05	0.85± 0.04	2.0	0.5	Red
SDSS J133734.31+610159.3	0.04163±0.00015	17.631± 0.007	16.883± 0.005	-17.77± 0.04	0.06± 0.00	0.5	2.5	Red
SDSS J134353.45+575429.4	0.09283±0.00016	18.344± 0.013	17.332± 0.009	-18.98± 0.05	0.17± 0.01	2.0	2.0	Red
SDSS J134843.94+451931.4	0.26955±0.00018	19.035± 0.020	17.572± 0.009	-21.65± 0.06	2.00± 0.12	0.5	0.5	Red
SDSS J140625.97+250923.3	0.40042±0.00022	21.622± 0.091	19.844± 0.035	-21.27± 0.25	1.41± 0.33	2.0	0.5	Red
SDSS J140813.76+535300.5	0.04154±0.00021	15.026± 0.002	14.206± 0.002	-20.33± 0.04	0.59± 0.02	0.0	0.5	Red
SDSS J141801.61+414939.4	0.10262±0.00022	16.543± 0.004	15.663± 0.003	-21.11± 0.04	1.22± 0.04	2.0	2.5	Blue
SDSS J142009.64+132626.7	0.14152±0.00019	17.531± 0.006	16.968± 0.005	-21.16± 0.04	1.28± 0.05	1.5	3.5	Blue
SDSS J142032.11+604321.3	0.16831±0.00015	18.587± 0.015	17.701± 0.009	-20.53± 0.06	0.71± 0.04	2.5	2.5	Blue
SDSS J142437.43+453506.8	0.13383±0.00023	18.592± 0.014	18.007± 0.013	-19.93± 0.05	0.41± 0.02	3.0	4.5	Blue
SDSS J143313.55+551225.5	0.04283±0.00010	17.634± 0.015	17.220± 0.015	-18.15± 0.05	0.08± 0.00	3.5	6.0	Blue
SDSS J144322.25+010553.2	0.03808±0.00009	15.741± 0.004	14.984± 0.003	-19.45± 0.04	0.26± 0.01	2.0	1.5	Red
SDSS J145018.25+340538.1	0.08907±0.00019	16.193± 0.004	15.232± 0.003	-21.03± 0.04	1.12± 0.04	0.5	0.5	Red
SDSS J150430.52+430410.0	0.05030±0.00017	15.244± 0.002	14.421± 0.002	-20.58± 0.04	0.75± 0.03	2.0	2.5	Red
SDSS J150842.48+332801.0	0.18988±0.00017	19.889± 0.029	18.255± 0.010	-19.44± 0.07	0.26± 0.02	0.5	0.5	Red
SDSS J151603.95+430936.5	0.01829±0.00011	15.701± 0.003	15.303± 0.003	-18.16± 0.04	0.08± 0.00	4.0	5.0	Blue
SDSS J151830.96+391606.6	0.19760±0.00016	18.501± 0.015	17.481± 0.008	-21.09± 0.06	1.19± 0.06	2.5	1.5	Blue
SDSS J152429.70+303224.1	0.06262±0.00016	17.273± 0.007	16.736± 0.007	-19.28± 0.04	0.23± 0.01	4.0	3.5	Blue
SDSS J155613.73+344629.8	0.07309±0.00015	16.452± 0.004	15.531± 0.003	-20.27± 0.04	0.56± 0.02	0.5	1.5	Red
SDSS J155752.51+342142.7	0.11367±0.00006	17.823± 0.008	17.252± 0.006	-20.25± 0.04	0.55± 0.02	4.0	3.5	Blue
SDSS J160345.47+264922.2	0.36594±0.00282	21.748± 0.120	20.064± 0.041	-20.11± 0.25	0.52± 0.12	6.0	0.5	Red
SDSS J160502.48+234008.5	0.02987±0.00010	15.493± 0.003	14.883± 0.003	-19.28± 0.04	0.23± 0.01	4.0	4.0	Blue
SDSS J160652.11+072103.4	0.22354±0.00014	18.991± 0.014	17.778± 0.008	-21.03± 0.06	1.13± 0.06	2.0	1.5	Red
SDSS J160817.07+165018.8	0.14326±0.00015	18.611± 0.012	17.588± 0.008	-19.98± 0.05	0.43± 0.02	1.5	1.5	Red
SDSS J160925.63+240516.8	0.27721±0.00316	20.965± 0.051	19.942± 0.028	-19.85± 0.17	0.38± 0.06	3.0	0.5	Blue
SDSS J161116.37+242942.1	0.03255±0.00010	16.812± 0.008	16.243± 0.007	-18.17± 0.04	0.08± 0.00	3.5	3.5	Blue
SDSS J161432.46+301534.3	0.13087±0.00015	17.861± 0.007	16.873± 0.005	-20.47± 0.04	0.67± 0.03	0.5	0.5	Red
SDSS J163150.46+141124.6	0.13102±0.00016	18.009± 0.010	17.088± 0.007	-20.33± 0.05	0.59± 0.03	2.5	1.5	Red

Continued on next page ...

Table B2 – continued

Galaxy	z_{gal}	g[a]	r[a]	M_B	L_B $[L^*]$	SpecType	MorphType	Color
SDSS J163317.74+352001.5	0.03454±0.00015	18.499± 0.001	17.588± 0.007	-16.43± 0.05	0.02± 0.00	2.0	2.0	Red
SDSS J165006.38+215448.4	0.19324±0.00015	18.785± 0.014	17.568± 0.008	-20.77± 0.05	0.88± 0.04	2.0	0.5	Red
SDSS J165339.11+230944.2	0.33672±0.00019	20.343± 0.051	18.674± 0.018	-21.38± 0.33	1.56± 0.47	0.5	0.5	Red
SDSS J165534.12+370034.3	0.11237±0.00014	18.453± 0.009	17.497± 0.006	-19.44± 0.04	0.26± 0.01	0.5	1.5	Red
SDSS J165819.50+623821.3	0.28042±0.00018	19.226± 0.019	18.193± 0.012	-21.56± 0.07	1.84± 0.12	3.5	3.5	Blue
SDSS J170330.32+240330.8	0.03083±0.00015	17.103± 0.007	16.247± 0.005	-17.54± 0.04	0.05± 0.00	1.5	2.5	Red
SDSS J203623.47-043707.4	0.02075±0.00018	13.500± 0.002	12.719± 0.002	-20.24± 0.04	0.54± 0.02	2.0	3.0	Red
SDSS J211701.26-002633.7	0.05792±0.00009	17.164± 0.006	16.775± 0.007	-19.30± 0.04	0.23± 0.01	3.0	3.5	Blue
SDSS J212626.95+003915.7	0.28913±0.00018	19.722± 0.031	18.038± 0.014	-21.23± 0.09	1.35± 0.11	2.0	1.5	Red
SDSS J213108.37-001236.2	0.05855±0.00007	17.034± 0.006	16.658± 0.006	-19.46± 0.04	0.27± 0.01	4.0	3.5	Blue
SDSS J214053.72+003111.7	0.10851±0.00009	18.998± 0.014	18.659± 0.014	-19.03± 0.05	0.18± 0.01	4.0	5.5	Blue
SDSS J215418.70+002119.4	0.06714±0.00010	15.054± 0.003	14.444± 0.003	-21.64± 0.04	1.97± 0.07	5.5	3.0	Blue
SDSS J215732.60-001226.7	0.10813±0.00019	18.518± 0.035	16.689± 0.011	-18.84± 0.08	0.15± 0.01	0.0	0.5	Red
SDSS J215732.70-001224.3	0.10837±0.00018	16.624± 0.005	15.716± 0.004	-21.17± 0.04	1.28± 0.05	0.0	0.5	Red
SDSS J221216.89+003243.9	0.02971±0.00011	17.876± 0.014	17.387± 0.013	-16.95± 0.05	0.03± 0.00	6.0	6.0	Blue
SDSS J223643.14-011054.1	0.08791±0.00016	18.010± 0.001	16.957± 0.006	-19.13± 0.05	0.11± 0.01	1.5	1.5	Red
SDSS J224823.20-000934.9	0.05418±0.00013	17.852± 0.013	17.461± 0.015	-18.49± 0.05	0.11± 0.01	4.0	6.0	Blue
SDSS J231648.38+005948.8	0.06895±0.00016	15.874± 0.004	15.173± 0.003	-20.82± 0.04	0.93± 0.03	2.0	3.5	Blue
SDSS J233724.00+002330.0	0.00931±0.00026	15.397± 0.009	14.960± 0.024	-16.78± 0.11	0.02± 0.00	-1.5	5.5	Red
SDSS J234020.41+005602.1	0.35517±0.00016	19.784± 0.041	18.038± 0.013	-22.21± 0.37	3.63± 1.24	0.5	0.5	Red
SDSS J234139.32+003641.8	0.17658±0.00009	18.015± 0.012	17.296± 0.009	-21.27± 0.05	1.41± 0.07	4.0	3.0	Blue

[a]Galactic dereddened magnitude

APPENDIX C

FITS HEADER FOR SDSS DR7 PARENT SAMPLE

COMMENT Parent Sample of 97468 galaxy/quasar pairs from SDSS DR7

GNAME = SDSS IAU galaxy name

ZGAL = SDSS galaxy redshift

ZERR = error on SDSS galaxy redshift

QNAME = SDSS IAU quasar name

ZQSO = SDSS quasar redshift, err on zqso 0.004; see Schneider DR7 QSO cat

PHYSSCALE = angular size in arcmin of 100 kpc radius at galaxy redshift

BARC = galaxy-quasar impact parameter in arcmin

BKPC = galaxy-quasar impact parameter in kpc using Ho=70,Om=0.3,Ol=0.7

INCA = flag to exclude Lyaforest contams for CaII

INNA = flag to exclude Lyaforest contams for NaI

CAFLAG = flag indicating absorber group for CaII

NAFLAG = flag indicating absorber group for NaI

*** FLAGS ARE AS FOLLOW ***

A - absorber candidate

Q - questionable candidate

N - non-detection

S - removed for bad sky subtraction

D - interloping doublet

- - not in parent sample

CAVC = flag indicating the visual classification for CaII

NAVC = flag indicating the visual classification for NaI

*** VISUAL CLASSIFICATION FLAGS ARE AS FOLLOWS ***

CAII

1 - Resolved Doublet

2 - Single-Line System

3 - Interloping Doublet System

4 - Low Signal-to-Noise

NAI

1 - Resolved Doublet

2 - Blended Doublet

3 - Symmetrical Single-Line

4 - Interloping Doublet System

5 - Bad Continuum

6 - Wrong Doublet Ratio

7 - Low Signal-to-Noise

8 - NaI Emission Lines

9 - Unknown

10 - Single-Line System

END

APPENDIX D

SDSS DR7 SUPPLEMENTARY TABLES

Table D1: Total Absorber Sample: Position Information

Galaxy	z_{abs}	l [°]	b [°]	QSO	z_{QSO}	l [°]	b [°]	b [kpc]	b/r_{Petro}	Ion
SDSS J091338.99+193707.4	0.00143±0.00001	209	40	SDSS J091511.03+201248.3	1.23900	209	40	74.13	245.1	CaII
SDSS J102703.86+283721.9	0.00020±0.00016	202	58	SDSS J100417.96+282444.1	0.32820	201	53	75.87	411.5	CaII
				SDSS J100927.44+273215.7	1.51230	203	54	61.12	331.6	CaII
				SDSS J101353.43+244916.4	1.63430	208	55	72.86	395.2	CaII
				SDSS J101956.59+274401.7	1.92500	203	57	27.34	148.3	CaII
				SDSS J104111.97+282805.0	0.21100	203	61	47.11	255.6	CaII
				SDSS J104221.97+282013.3	1.68590	203	61	51.15	277.5	NaI
				SDSS J104224.85+231001.7	1.23720	213	61	97.85	530.8	CaII
				SDSS J105124.28+320044.5	0.44600	195	64	94.74	513.9	CaII
SDSS J111849.76-002109.9	0.13179±0.00016	260	55	SDSS J111850.13-002100.7	1.02560	260	55	25.25	2.2	NaI
				SDSS J111850.13-002100.7	1.02560	260	55	25.25	2.2	CaII
				SDSS J111850.13-002100.7	1.02560	260	55	25.25	2.2	Both
SDSS J113420.50-033525.4	0.00008±0.00007	269	54	SDSS J104102.43+023242.8	1.95870	246	50	83.38	9958.3	NaI
				SDSS J110156.34+073525.2	1.51360	245	58	78.45	9369.3	CaII
				SDSS J110557.87+045728.3	0.90850	250	56	63.14	7541.0	CaII
				SDSS J111012.07+011327.8	0.09500	256	55	43.89	5241.4	CaII
				SDSS J111507.65+023757.5	0.56650	256	56	44.69	5337.7	CaII
				SDSS J111816.94+074558.2	1.73500	250	61	68.47	8178.1	CaII
				SDSS J112224.15+031802.6	0.47450	257	58	42.70	5099.5	CaII
				SDSS J113330.30+105223.3	0.51010	251	66	82.25	9823.4	CaII
				SDSS J113416.80-001902.3	0.35580	266	57	18.61	2222.8	NaI

Continued on next page ...

Table D1 – continued

Galaxy	z_{abs}	l [°]	b [°]	QSO	z_{QSO}	l [°]	b [°]	b [kpc]	b/r_{Petro}	Ion
				SDSS J113615.14+103430.8	0.52280	252	66	80.59	9625.5	CaII
				SDSS J113625.42+100523.2	0.55230	253	65	77.84	9297.1	CaII
				SDSS J113642.26+105825.8	1.68990	252	66	82.88	9898.8	CaII
				SDSS J115052.29-005016.4	0.80870	273	58	28.22	3370.0	CaII
				SDSS J121353.44-020720.9	1.18540	284	59	56.77	6779.7	CaII
SDSS J114313.05+193646.9	0.02085±0.00009	235	73	SDSS J114323.71+193448.0	3.35690	235	73	81.07	15.4	NaI
SDSS J114318.07+193401.3	0.02262±0.00015	235	73	SDSS J114323.71+193448.0	3.35690	235	73	42.24	16.0	NaI
SDSS J114336.98+193616.7	0.02201±0.00019	235	73	SDSS J114323.71+193448.0	3.35690	235	73	92.34	17.1	NaI
SDSS J114637.59+405036.6	0.00280±0.00002	163	71	SDSS J114535.66+402906.0	1.71270	164	71	84.95	160.8	CaII
SDSS J115115.25+485331.0	0.02565±0.00011	147	65	SDSS J115118.59+485331.1	1.07160	147	65	16.98	1.2	NaI
SDSS J121323.27+295518.4	0.00042±0.00001	192	81	SDSS J122525.89+305920.2	0.77990	177	83	87.54	423.7	CaII
SDSS J121344.76+363802.4	0.00045±0.00018	161	78	SDSS J122035.10+385316.4	0.37560	150	77	87.76	255.0	CaII
SDSS J121633.70+130153.6	0.00006±0.00007	271	74	SDSS J104730.54+101728.9	0.14430	237	56	90.22	3550.0	CaII
				SDSS J105007.75+113228.6	0.13350	236	58	86.90	3419.4	CaII
				SDSS J105126.34+183952.4	0.24380	224	61	87.13	3428.3	CaII
				SDSS J105210.02+165543.7	1.33690	227	61	85.17	3351.4	CaII
				SDSS J105237.24+240627.3	0.39700	213	63	93.32	3671.9	CaII
				SDSS J110557.87+045728.3	0.90850	250	56	78.84	3102.1	CaII
				SDSS J112457.67+232436.0	1.86580	219	70	65.87	2591.9	CaII
				SDSS J113109.48+311405.4	0.29020	195	72	86.19	3391.6	CaII

Continued on next page ...

Table D1 – continued

Galaxy	z_{abs}	l [°]	b [°]	QSO	z_{QSO}	l [°]	b [°]	b [kpc]	b/r_{Petro}	Ion
				SDSS J113330.30+105223.3	0.51010	251	66	44.14	1737.0	CaII
				SDSS J113615.14+103430.8	0.52280	252	66	41.74	1642.6	CaII
				SDSS J115052.29-005016.4	0.80870	273	58	62.68	2466.4	CaII
				SDSS J115652.89+174554.0	0.52210	247	74	27.52	1082.7	CaII
				SDSS J115712.46+181739.8	0.31610	245	75	28.86	1135.6	CaII
				SDSS J122525.89+305920.2	0.77990	177	83	74.23	2920.7	CaII
				SDSS J122830.85+281411.7	0.09990	199	85	63.49	2498.1	CaII
				SDSS J125001.48+042839.8	1.46170	302	67	48.84	1921.6	CaII
				SDSS J125036.22+175705.6	0.35240	302	81	39.27	1545.0	CaII
				SDSS J130029.01+004637.2	1.86530	308	64	67.30	2648.1	CaII
				SDSS J131204.70+064107.5	0.24190	317	69	61.88	2434.9	CaII
				SDSS J131426.49+020115.6	0.30660	316	64	74.19	2919.3	CaII
				SDSS J133602.01+172513.0	0.55190	352	76	80.72	3176.2	CaII
SDSS J122037.63+283803.3	0.02764±0.00011	199	83	SDSS J122037.22+283752.0	2.20420	199	83	6.92	0.8	NaI
SDSS J122843.30+114518.1	0.00054±0.00007	283	74	SDSS J122226.47+133418.8	1.52630	275	75	94.86	233.7	CaII
SDSS J122844.91+124835.1	0.00004±0.00033	281	75	SDSS J101318.69+152502.2	1.60370	222	52	98.53	8573.8	CaII
				SDSS J102016.96+174314.3	1.48880	220	54	93.81	8162.7	CaII
				SDSS J102325.40+274638.9	0.32890	203	57	98.31	8554.1	CaII
				SDSS J102421.69+112143.8	1.17010	230	52	91.10	7926.7	CaII
				SDSS J102450.91+094346.3	0.89400	233	51	91.37	7950.3	CaII
				SDSS J103818.46+204906.0	1.80890	217	59	82.55	7182.9	CaII
				SDSS J104111.97+282805.0	0.21100	203	61	88.38	7689.9	CaII
				SDSS J104221.97+282013.3	1.68590	203	61	87.51	7614.9	NaI
				SDSS J104224.85+231001.7	1.23720	213	61	81.63	7102.5	CaII
				SDSS J104730.54+101728.9	0.14430	237	56	74.60	6491.2	CaII

Continued on next page ...

Table D1 – continued

Galaxy	z_{abs}	l [°]	b [°]	QSO	z_{QSO}	l [°]	b [°]	b [kpc]	b/r_{Petro}	Ion
				SDSS J104810.76+284042.5	0.98930	202	63	84.61	7361.9	CaII
				SDSS J105007.75+113228.6	0.13350	236	58	72.24	6285.4	CaII
				SDSS J105126.34+183952.4	0.24380	224	61	72.20	6281.9	CaII
				SDSS J105210.02+165543.7	1.33690	227	61	70.90	6169.6	CaII
				SDSS J105237.24+240627.3	0.39700	213	63	76.00	6613.0	CaII
				SDSS J110539.81+342534.6	0.50900	189	66	85.85	7469.8	CaII
				SDSS J110557.87+045728.3	0.90850	250	56	65.53	5701.9	CaII
				SDSS J111507.65+023757.5	0.56650	256	56	62.47	5435.4	CaII
				SDSS J111830.28+402554.0	0.15450	172	67	94.71	8241.3	CaII
				SDSS J112439.18+420145.0	0.22500	167	67	96.92	8433.5	CaII
				SDSS J112457.67+232436.0	1.86580	219	70	55.30	4811.8	CaII
				SDSS J112653.64+151413.8	1.41180	240	67	45.49	3958.6	CaII
				SDSS J113109.48+311405.4	0.29020	195	72	67.96	5913.7	CaII
				SDSS J113330.30+105223.3	0.51010	251	66	40.88	3557.1	CaII
				SDSS J113615.14+103430.8	0.52280	252	66	39.05	3398.1	CaII
				SDSS J115712.46+181739.8	0.31610	245	75	28.05	2440.3	CaII
				SDSS J115731.02+044102.4	1.87270	271	64	33.54	2918.4	CaII
				SDSS J115731.02+044102.4	1.87270	271	64	33.54	2918.4	CaII
				SDSS J122035.10+385316.4	0.37560	150	77	78.27	6810.7	CaII
				SDSS J122830.85+281411.7	0.09990	199	85	46.19	4019.3	CaII
				SDSS J123953.24+430046.1	1.39730	131	74	90.72	7894.0	CaII
				SDSS J124410.82+172104.5	1.28160	293	80	17.59	1530.2	CaII
				SDSS J125001.48+042839.8	1.46170	302	67	29.49	2566.3	CaII
				SDSS J125036.22+175705.6	0.35240	302	81	22.04	1917.5	CaII
				SDSS J125719.55+442935.4	0.30030	119	73	96.62	8407.0	CaII
				SDSS J130029.01+004637.2	1.86530	308	64	43.04	3745.0	CaII
				SDSS J131204.70+064107.5	0.24190	317	69	36.84	3205.4	CaII
				SDSS J131426.49+020115.6	0.30660	316	64	46.80	4072.3	CaII

Continued on next page . . .

Table D1 – continued

Galaxy	z_{abs}	l [°]	b [°]	QSO	z_{QSO}	l [°]	b [°]	b [kpc]	b/r_{Petro}	Ion
				SDSS J133602.01+172513.0	0.55190	352	76	50.52	4395.8	CaII
				SDSS J140104.87+004332.6	0.66530	338	59	77.46	6740.5	CaII
				SDSS J142613.32+195524.6	0.21330	20	67	86.88	7559.8	CaII
				SDSS J142725.04+194952.2	0.11090	20	67	87.67	7628.0	CaII
SDSS J123745.22+070618.3	0.00011±0.00032	293	70	SDSS J125036.22+175705.6	0.35240	302	81	92.51	1307.1	CaII
				SDSS J131204.70+064107.5	0.24190	317	69	69.89	987.6	CaII
				SDSS J131426.49+020115.6	0.30660	316	64	85.70	1211.0	CaII
SDSS J124006.10+613609.5	0.00026±0.00017	125	55	SDSS J130458.48+644804.3	1.71930	121	52	83.36	342.1	NaI
SDSS J140613.22+153035.5	0.06040±0.00018	3	69	SDSS J140614.06+153037.6	2.45410	3	69	14.30	1.8	NaI
SDSS J141745.62+162509.3	0.24229±0.00015	9	67	SDSS J141746.03+162512.2	1.71690	9	67	25.26	0.5	CaII
SDSS J142009.64+132626.7	0.14152±0.00020	4	65	SDSS J142010.10+132629.1	1.56980	4	65	17.58	1.9	NaI
SDSS J150400.94+240437.1	0.06894±0.00010	35	60	SDSS J150359.48+240532.8	3.03420	35	60	77.99	5.7	NaI
SDSS J150403.17+240559.8	0.06997±0.00019	35	60	SDSS J150359.48+240532.8	3.03420	35	60	76.58	6.3	NaI
SDSS J151145.63+071510.6	0.04393±0.00019	9	51	SDSS J151147.16+071406.0	3.46870	9	51	59.23	11.1	NaI
SDSS J155752.51+342142.8	0.11366±0.00006	55	50	SDSS J155752.31+342140.0	1.26520	55	50	7.74	0.8	CaII
				SDSS J155752.31+342140.0	1.26520	55	50	7.74	0.8	Both

Table D2: Total Absorber Sample: Line Measurements

Galaxy	z_{abs}	Ion	v_{LSR} [km s^{-1}]	rEW_1 Å	rEW_1/σ_{rEW_1}	z_{line1}	Δv_1 [km s^{-1}]	rEW_2 Å	z_{line2}	Δv_2 [km s^{-1}]
SDSS J091338.99+193707.4	0.00143±0.00001	CaII	-32.2	0.30± 0.15	1.97	-0.00009±0.00047	-455.6± 139.9	0.29± 0.13	-0.00008±0.00047	-453.1± 140.1
SDSS J102703.86+283721.9	0.00020±0.00016	CaII	-64.8	0.25± 0.09	2.66	-0.00021±0.00051	-123.8± 160.1	0.21± 0.12	-0.00059±0.00055	-237.8± 172.4
		CaII	-79.9	0.44± 0.12	3.50	-0.00026±0.00038	-139.0± 125.5	0.18± 0.12	-0.00015±0.00059	-104.8± 183.1
		CaII	-30.6	0.39± 0.10	3.81	-0.00009±0.00041	-89.4± 131.3	0.32± 0.10	-0.00024±0.00044	-132.7± 141.8
		CaII	-53.5	0.31± 0.12	2.60	-0.00017±0.00046	-113.1± 145.5	0.23± 0.13	0.00015±0.00053	-15.8± 165.6
		CaII	-19.8	0.34± 0.10	3.35	-0.00007±0.00044	-80.7± 140.7	0.29± 0.10	-0.00016±0.00047	-109.8± 149.8
		NaI	-216.9	0.81± 0.37	2.16	-0.00072±0.00019	-277.8± 75.2	0.59± 0.28	-0.00046±0.00022	-199.1± 82.8
		CaII	-38.6	0.30± 0.15	1.93	-0.00013±0.00047	-98.7± 148.8	0.23± 0.14	0.00001±0.00052	-56.8± 165.0
		CaII	-77.9	0.32± 0.14	2.26	-0.00026±0.00045	-139.9± 143.9	0.36± 0.15	-0.00064±0.00042	-251.6± 135.5
SDSS J111849.76-002109.9	0.13179±0.00016	NaI	39538.5	0.68± 0.27	2.51	0.13180±0.00019	2.3± 75.7	0.31± 0.27	0.13187±0.00029	22.1± 98.7
		CaII	39400.1	0.73± 0.32	2.32	0.13134±0.00028	-136.1± 96.7	0.62± 0.28	0.13176±0.00030	-10.6± 102.5
		Both_{NaI}	39544.4	0.70± 0.24	2.89	0.13182±0.00019	8.2± 75.1	0.31± 0.27	0.13187±0.00029	22.1± 98.7
		Both_{CaII}	39544.4	0.60± 0.23	2.58	0.13154±0.00031	-76.7± 104.8	0.63± 0.25	0.13175±0.00030	-14.3± 101.9
SDSS J113420.50-033525.4	0.00008±0.00007	NaI	-190.8	1.30± 1.16	1.11	-0.00062±0.00015	-209.7± 49.4	0.82± 0.77	-0.00024±0.00019	-94.0± 59.8
		CaII	-81.5	0.51± 0.28	1.78	-0.00027±0.00036	-102.4± 109.0	0.37± 0.23	-0.00008±0.00042	-46.0± 126.5
		CaII	33.6	0.33± 0.09	3.59	0.00012±0.00044	12.8± 134.8	0.23± 0.10	0.00019±0.00053	34.0± 160.2
		CaII	34.5	0.32± 0.12	2.73	0.00012±0.00045	14.0± 136.9	0.23± 0.11	-0.00019±0.00052	-78.6± 157.7
		CaII	-21.8	0.49± 0.18	2.72	-0.00007±0.00036	-42.8± 111.2	0.59± 0.18	-0.00011±0.00033	-55.5± 100.6
		CaII	-24.8	0.22± 0.08	2.59	-0.00008±0.00055	-46.7± 165.5	0.10± 0.09	-0.00010±0.00081	-52.8± 243.8
		CaII	-25.7	0.25± 0.14	1.75	-0.00008±0.00051	-47.3± 154.6	0.26± 0.14	-0.00023±0.00049	-91.3± 150.0
		CaII	-27.6	0.22± 0.08	2.66	-0.00009±0.00055	-50.9± 165.5	0.18± 0.08	-0.00010±0.00060	-52.2± 181.2
		NaI	-295.8	1.42± 0.61	2.34	-0.00098±0.00014	-317.6± 47.6	0.69± 0.61	-0.00100±0.00020	-322.6± 64.7
		CaII	-28.2	0.25± 0.10	2.45	-0.00010±0.00051	-51.6± 153.6	0.21± 0.10	-0.00009±0.00055	-50.0± 167.0
		CaII	-43.6	0.26± 0.23	1.16	-0.00015±0.00049	-67.0± 149.8	0.39± 0.21	-0.00003±0.00041	-32.5± 123.6
		CaII	31.9	0.80± 0.29	2.77	0.00010±0.00028	8.3± 87.8	0.39± 0.23	-0.00011±0.00040	-56.9± 122.8
		CaII	69.9	0.61± 0.30	2.05	0.00023±0.00032	47.1± 99.5	0.25± 0.23	0.00006±0.00050	-4.7± 151.8
		CaII	27.6	0.54± 0.24	2.29	0.00009±0.00034	3.5± 105.6	0.58± 0.23	-0.00026±0.00033	-100.1± 101.8
SDSS J114313.05+193646.9	0.02085±0.00009	NaI	6738.8	1.10± 0.25	4.33	0.02246±0.00016	481.2± 55.1	–	–	–
SDSS J114318.07+193401.3	0.02262±0.00015	NaI	6741.0	1.14± 0.24	4.79	0.02246±0.00016	-46.3± 66.2	–	–	–
SDSS J114336.98+193616.7	0.02201±0.00019	NaI	6740.7	1.14± 0.24	4.75	0.02246±0.00016	135.7± 74.9	–	–	–
SDSS J114637.59+405036.6	0.00280±0.00002	CaII	788.4	1.28± 0.58	2.22	0.00261±0.00022	-55.2± 67.7	1.05± 0.89	0.00227±0.00025	-157.0± 74.1
SDSS J115115.25+485331.0	0.02565±0.00011	NaI	7478.1	1.13± 0.61	1.86	0.02491±0.00016	-221.3± 57.7	0.72± 0.46	0.02464±0.00020	-302.4± 68.0
SDSS J121323.27+295518.4	0.00042±0.00001	CaII	-26.6	0.32± 0.14	2.34	-0.00011±0.00045	-158.0± 135.2	0.49± 0.17	-0.00031±0.00036	-217.7± 107.7
SDSS J121344.76+363802.4	0.00045±0.00018	CaII	-7.5	0.27± 0.12	2.37	-0.00005±0.00049	-148.2± 155.1	0.37± 0.12	-0.00011±0.00042	-168.5± 135.9

Continued on next page ...

Table D2 – continued

Galaxy	z_{abs}	Ion	v_{LSR} [km s^{-1}]	rEW_1 Å	rEW_1/σ_{rEW_1}	z_{line1}	Δv_1 [km s^{-1}]	rEW_2 Å	z_{line2}	Δv_2 [km s^{-1}]
SDSS J121633.70+130153.6	0.00006±0.00007	CaII	-36.8	0.32± 0.10	3.31	-0.00011±0.00045	-50.9± 136.6	0.11± 0.10	-0.00035±0.00075	-122.8± 225.6
		CaII	-37.1	0.14± 0.08	1.68	-0.00012±0.00069	-51.5± 206.6	0.18± 0.08	-0.00005±0.00059	-32.2± 179.4
		CaII	10.2	0.55± 0.15	3.62	0.00004±0.00034	-5.3± 104.4	0.23± 0.13	0.00012±0.00053	20.2± 159.6
		CaII	-26.2	0.40± 0.09	4.20	-0.00008±0.00040	-41.5± 122.6	0.31± 0.11	-0.00003±0.00045	-24.9± 136.6
		CaII	-24.2	0.24± 0.07	3.54	-0.00008±0.00052	-40.6± 157.4	0.19± 0.07	-0.00023±0.00057	-86.0± 172.7
		CaII	34.4	0.35± 0.09	4.11	0.00012±0.00043	20.0± 129.7	0.19± 0.08	0.00007±0.00057	3.2± 172.7
		CaII	-8.5	0.26± 0.13	2.10	-0.00003±0.00049	-26.7± 149.7	0.33± 0.14	-0.00018±0.00044	-69.1± 133.6
		CaII	-16.7	0.21± 0.06	3.33	-0.00007±0.00055	-36.2± 165.6	0.10± 0.07	-0.00001±0.00081	-18.7± 243.8
		CaII	15.9	0.19± 0.08	2.34	0.00005±0.00059	-1.1± 177.8	0.17± 0.09	-0.00010±0.00061	-46.4± 184.3
		CaII	-42.9	0.25± 0.11	2.30	-0.00014±0.00050	-59.9± 152.6	0.21± 0.10	-0.00009±0.00055	-43.5± 165.6
		CaII	68.0	0.60± 0.30	2.04	0.00023±0.00033	51.5± 100.1	0.24± 0.23	0.00006±0.00051	2.8± 155.1
		CaII	-32.6	0.26± 0.09	2.82	-0.00012±0.00050	-51.9± 150.5	0.24± 0.10	0.00001±0.00052	-13.6± 156.4
		CaII	-12.1	0.47± 0.16	2.87	-0.00005±0.00037	-31.5± 113.2	0.28± 0.14	0.00001±0.00048	-12.9± 144.3
		CaII	-26.3	0.33± 0.13	2.51	-0.00011±0.00044	-48.7± 133.5	0.47± 0.17	-0.00031±0.00037	-110.2± 112.3
		CaII	-10.2	0.26± 0.10	2.66	-0.00005±0.00050	-32.5± 150.3	0.31± 0.11	-0.00016±0.00046	-65.5± 138.0
		CaII	-47.4	0.47± 0.16	2.88	-0.00017±0.00037	-68.2± 113.3	0.27± 0.16	0.00004±0.00049	-3.8± 147.0
		CaII	5.1	0.30± 0.09	3.27	-0.00000±0.00047	-17.4± 141.5	0.10± 0.08	-0.00004±0.00079	-27.6± 238.5
		CaII	518.6	1.29± 0.32	4.03	0.00171±0.00022	497.6± 69.9	0.95± 0.32	0.00206±0.00026	601.9± 80.1
		CaII	-44.4	0.27± 0.08	3.24	-0.00017±0.00049	-66.9± 146.9	0.21± 0.08	-0.00013±0.00056	-56.3± 167.7
		CaII	-12.4	0.23± 0.10	2.18	-0.00006±0.00054	-34.5± 161.9	0.13± 0.09	-0.00019±0.00071	-74.2± 213.8
		CaII	-57.7	0.18± 0.09	2.06	-0.00022±0.00059	-82.7± 179.2	0.17± 0.08	0.00000±0.00061	-15.7± 184.0
SDSS J122037.63+283803.3	0.02764±0.00011	NaI	8379.1	1.08± 0.25	4.38	0.02791±0.00016	82.9± 58.2	–	–	–
SDSS J122843.30+114518.1	0.00054±0.00007	CaII	-55.2	0.57± 0.23	2.47	-0.00020±0.00034	-219.6± 103.1	0.41± 0.25	-0.00040±0.00039	-281.0± 119.0
SDSS J122844.91+124835.1	0.00004±0.00033	CaII	-7.3	0.57± 0.36	1.56	-0.00001±0.00034	-15.7± 140.7	0.67± 0.35	0.00001±0.00031	-10.5± 134.3
		CaII	-35.1	0.31± 0.12	2.72	-0.00011±0.00045	-44.2± 167.3	0.22± 0.10	-0.00012±0.00054	-48.0± 189.0
		CaII	-36.0	0.38± 0.17	2.28	-0.00012±0.00041	-46.9± 157.9	0.39± 0.18	-0.00023±0.00040	-82.5± 155.8
		CaII	12.7	0.38± 0.16	2.29	0.00005±0.00041	4.3± 158.0	0.25± 0.15	-0.00009±0.00050	-39.8± 179.2
		CaII	30.1	0.45± 0.15	3.04	0.00011±0.00038	22.0± 149.8	0.28± 0.14	0.00019±0.00048	44.1± 173.6
		CaII	0.5	0.52± 0.15	3.37	0.00001±0.00035	-10.1± 143.8	0.26± 0.15	-0.00010±0.00050	-41.7± 178.0
		CaII	-20.2	0.36± 0.10	3.64	-0.00007±0.00043	-32.1± 160.7	0.29± 0.10	-0.00016±0.00047	-60.9± 171.9
		NaI	-215.4	0.78± 0.38	2.08	-0.00072±0.00019	-227.4± 113.4	0.57± 0.28	-0.00046±0.00022	-150.6± 118.5
		CaII	-99.2	0.24± 0.17	1.41	-0.00033±0.00052	-110.4± 184.2	0.18± 0.17	0.00007±0.00060	9.5± 204.9
		CaII	-36.8	0.32± 0.10	3.31	-0.00011±0.00045	-46.4± 166.8	0.16± 0.09	-0.00007±0.00063	-34.4± 212.2
		CaII	-27.2	0.24± 0.09	2.61	-0.00009±0.00051	-39.6± 182.8	0.26± 0.10	-0.00025±0.00050	-88.0± 178.6
		CaII	-37.1	0.14± 0.08	1.68	-0.00012±0.00069	-47.0± 227.6	0.18± 0.08	-0.00005±0.00059	-27.7± 203.3
		CaII	6.5	0.55± 0.16	3.31	0.00002±0.00034	-4.6± 142.1	0.23± 0.13	0.00012±0.00053	24.7± 186.1
		CaII	-26.2	0.40± 0.09	4.20	-0.00008±0.00040	-37.0± 155.5	0.32± 0.10	-0.00003±0.00045	-22.3± 166.3
		CaII	-24.2	0.24± 0.07	3.54	-0.00008±0.00052	-36.1± 184.2	0.19± 0.07	-0.00023±0.00057	-81.5± 197.4
		CaII	-27.4	0.36± 0.10	3.56	-0.00010±0.00042	-41.5± 160.1	0.25± 0.11	0.00004±0.00050	0.4± 179.9
		CaII	34.4	0.35± 0.09	4.11	0.00012±0.00043	24.5± 161.1	0.16± 0.07	-0.00005±0.00063	-27.5± 213.5
		CaII	-36.6	0.49± 0.18	2.68	-0.00012±0.00036	-46.8± 146.2	0.52± 0.18	-0.00021±0.00035	-73.9± 143.0
		CaII	-23.8	0.17± 0.08	2.14	-0.00009±0.00061	-39.3± 207.8	0.34± 0.11	-0.00041±0.00043	-134.5± 162.8
		CaII	-47.6	0.33± 0.08	3.97	-0.00017±0.00044	-63.7± 164.3	0.20± 0.09	-0.00037±0.00057	-121.8± 196.9
		CaII	-8.5	0.26± 0.13	2.10	-0.00003±0.00049	-22.2± 177.6	0.32± 0.13	-0.00019±0.00045	-69.9± 165.5
		CaII	-38.9	0.45± 0.14	3.15	-0.00013±0.00038	-51.5± 149.4	0.35± 0.16	0.00008±0.00043	13.4± 161.0
		CaII	-16.7	0.21± 0.06	3.33	-0.00007±0.00055	-31.7± 191.3	0.10± 0.07	-0.00001±0.00081	-14.2± 261.9
		CaII	-3.7	0.17± 0.10	1.75	-0.00001±0.00062	-16.2± 210.6	0.17± 0.08	-0.00010±0.00061	-41.0± 207.3
		CaII	-42.9	0.25± 0.11	2.30	-0.00014±0.00050	-55.5± 180.1	0.21± 0.10	-0.00009±0.00055	-39.0± 191.2
		CaII	-14.4	0.46± 0.15	3.14	-0.00006±0.00037	-29.3± 148.7	0.28± 0.14	0.00001±0.00048	-8.5± 173.1

Continued on next page . . .

Table D2 – continued

Galaxy	z_{abs}	Ion	v_{LSR} [km s^{-1}]	rEW_1 Å	rEW_1/σ_{rEW_1}	z_{line1}	Δv_1 [km s^{-1}]	rEW_2 Å	z_{line2}	Δv_2 [km s^{-1}]
		CaII	-56.8	0.30± 0.14	2.12	-0.00019±0.00047	-69.9± 170.9	0.24± 0.11	-0.00001±0.00052	-14.1± 182.9
		CaII	398.4	0.41± 0.15	2.75	0.00132±0.00040	385.2± 153.7	0.17± 0.13	0.00136±0.00061	396.1± 206.1
		CaII	-10.3	0.29± 0.12	2.45	-0.00006±0.00047	-28.8± 172.0	0.33± 0.12	-0.00011±0.00044	-46.2± 164.3
		CaII	-10.2	0.26± 0.10	2.66	-0.00005±0.00050	-28.1± 178.1	0.31± 0.11	-0.00016±0.00046	-61.0± 167.9
		CaII	-55.6	0.36± 0.14	2.63	-0.00021±0.00043	-75.2± 160.7	0.29± 0.14	-0.00012±0.00047	-48.8± 170.8
		CaII	-19.5	0.18± 0.07	2.44	-0.00008±0.00060	-37.1± 204.6	0.09± 0.07	-0.00002±0.00083	-16.7± 268.3
		CaII	-47.4	0.47± 0.16	2.88	-0.00017±0.00037	-63.8± 148.2	0.25± 0.15	-0.00000±0.00051	-13.5± 180.5
		CaII	8.4	0.30± 0.08	3.55	0.00001±0.00046	-9.7± 170.1	0.10± 0.07	-0.00002±0.00078	-18.6± 254.3
		CaII	-67.8	0.36± 0.12	3.01	-0.00025±0.00042	-88.3± 160.1	0.27± 0.12	0.00003±0.00049	-3.4± 175.4
		CaII	530.1	1.35± 0.29	4.61	0.00175±0.00022	513.6± 117.7	1.04± 0.27	0.00205±0.00025	602.3± 122.5
		CaII	-44.4	0.27± 0.08	3.24	-0.00017±0.00049	-62.4± 175.3	0.21± 0.08	-0.00013±0.00056	-51.8± 193.1
		CaII	-12.4	0.23± 0.10	2.18	-0.00006±0.00054	-30.0± 188.0	0.15± 0.10	-0.00011±0.00066	-46.0± 219.8
		CaII	-17.4	0.22± 0.08	2.66	-0.00009±0.00055	-38.0± 190.7	0.17± 0.08	0.00000±0.00061	-11.3± 207.4
		CaII	12.6	0.25± 0.11	2.20	0.00002±0.00051	-7.5± 180.6	0.17± 0.11	0.00012±0.00062	25.0± 209.8
		CaII	-62.9	0.41± 0.11	3.77	-0.00025±0.00040	-86.2± 154.1	0.23± 0.11	-0.00033±0.00053	-110.6± 185.5
		CaII	-46.5	0.20± 0.07	2.97	-0.00019±0.00057	-69.9± 197.1	0.20± 0.07	-0.00026±0.00057	-89.0± 195.7
SDSS J123745.22+070618.3	0.00011±0.00032	CaII	11.0	0.29± 0.09	3.32	0.00002±0.00047	-28.0± 172.3	0.11± 0.07	-0.00003±0.00075	-42.1± 246.1
		CaII	-43.3	0.27± 0.08	3.18	-0.00016±0.00049	-82.2± 176.4	0.21± 0.08	-0.00013±0.00055	-72.8± 191.2
		CaII	-10.4	0.22± 0.11	2.07	-0.00005±0.00054	-48.8± 190.2	0.13± 0.09	-0.00019±0.00069	-91.3± 229.2
SDSS J124006.10+613609.5	0.00026±0.00017	NaI	-192.2	1.32± 0.64	2.05	-0.00067±0.00015	-280.1± 67.7	0.45± 0.42	-0.00061±0.00025	-262.2± 91.3
SDSS J140613.22+153035.5	0.06040±0.00018	NaI	18378.9	1.16± 0.37	3.16	0.06123±0.00015	247.5± 71.9	0.63± 0.32	0.06132±0.00021	273.9± 83.2
SDSS J141745.62+162509.3	0.24229±0.00015	CaII	72436.1	0.50± 0.15	3.31	0.24142±0.00032	-260.6± 107.1	0.31± 0.14	0.24162±0.00041	-199.8± 130.9
SDSS J142009.64+132626.7	0.14152±0.00020	NaI	42222.9	0.63± 0.22	2.89	0.14071±0.00020	-243.0± 84.3	0.32± 0.25	0.14065±0.00028	-259.2± 102.3
SDSS J150400.94+240437.1	0.06894±0.00010	NaI	20924.7	2.38± 0.69	3.47	0.06971±0.00011	229.0± 42.9	0.93± 0.57	0.06986±0.00017	276.6± 58.6
SDSS J150403.17+240559.8	0.06997±0.00019	NaI	20925.9	2.42± 0.68	3.56	0.06971±0.00011	-77.4± 65.3	1.02± 0.64	0.06989±0.00016	-22.8± 75.0
SDSS J151145.63+071510.6	0.04393±0.00019	NaI	13364.4	1.24± 0.37	3.37	0.04451±0.00015	173.0± 71.9	–	–	–
SDSS J155752.51+342142.8	0.11366±0.00006	CaII	34190.7	0.59± 0.17	3.50	0.11392±0.00031	78.3± 96.4	0.51± 0.23	0.11408±0.00033	125.6± 102.3
		Both_{NaI}	34319.8	0.96± 0.26	3.73	0.11435±0.00016	207.4± 52.8	–	–	–
		Both_{CaII}	34319.8	0.59± 0.17	3.50	0.11392±0.00031	78.3± 96.4	0.51± 0.23	0.11408±0.00033	125.6± 102.3

APPENDIX E

CORRELATION TABLES FOR SAMPLE SUBSETS

Table E1 Spearman's Rank Correlation Coefficients for different subsets of the 19 Ca II absorbers. The different subsets are based on r-band concentration index, the fracdev parameter, and a red/blue color cut based on the g-r, M_r plot of Yan et al. (2006). The number in parentheses is the number of absorbers in each sample.

	$C_r \geq 2.6$; Elliptical Galaxies (5)								$C_r < 2.6$; Disk Galaxies (14)							
	rEW				Δv				rEW				Δv			
Property Name	ρ	p-value	N_σ	✓	ρ	p-value	N_σ	✓	ρ	p-value	N_σ	✓	ρ	p-value	N_σ	✓
$g-r$	-0.359	0.553	0.59		-0.103	0.870	0.16		-0.455	0.102	1.63		0.0945	0.748	0.32	
$u-r$	-0.359	0.553	0.59		-0.103	0.870	0.16		-0.538	0.0470	1.99		-0.0681	0.817	0.23	
$r-i$	-0.359	0.553	0.59		-0.103	0.870	0.16		-0.222	0.446	0.76		0.262	0.366	0.90	
M_r	0.359	0.553	0.59		0.103	0.870	0.16		0.323	0.260	1.13		-0.204	0.483	0.70	
L_r^*	-0.359	0.553	0.59		-0.103	0.870	0.16		-0.323	0.260	1.13		0.204	0.483	0.70	
b [kpc]	0.667	0.219	1.23		-0.103	0.870	0.16		0.0286	0.923	0.10		-0.679	0.00756	2.67	
$b/r_{\rm Petro}$	0.359	0.553	0.59		0.103	0.870	0.16		0.235	0.418	0.81		-0.538	0.0470	1.99	
C_r	-0.975	0.00482	2.82		0.308	0.614	0.50		-0.187	0.523	0.64		0.0637	0.829	0.22	
$fracdev$	-0.359	0.553	0.59		-0.103	0.870	0.16		-0.415	0.141	1.47		0.305	0.290	1.06	
i	-0.154	0.805	0.25		0.103	0.870	0.16		-0.0857	0.771	0.29		-0.160	0.584	0.55	
z	-0.667	0.219	1.23		0.103	0.870	0.16		-0.182	0.533	0.62		0.336	0.240	1.18	
R_{50}^r	0.975	0.00482	2.82		-0.308	0.614	0.50		-0.130	0.659	0.44		-0.341	0.233	1.19	
$E(B-V)_{QSO}$	-0.154	0.805	0.25		0.103	0.870	0.16		0.411	0.144	1.46		0.380	0.180	1.34	
b/a	0.154	0.805	0.25		-0.103	0.870	0.16		0.0769	0.794	0.26		0.226	0.436	0.78	
Θ	0.154	0.805	0.25		-0.103	0.870	0.16		-0.0901	0.759	0.31		-0.0725	0.805	0.25	
g_{QSO}	0.154	0.805	0.25		-0.103	0.870	0.16		0.836	0.000195	3.73		-0.0418	0.887	0.14	
rEW	1.00	–	–		-0.500	0.391	0.86		1.00	–	–		-0.134	0.648	0.46	
Δv	-0.500	0.391	0.86		1.00	–	–		-0.134	0.648	0.46		1.00	–	–	
	fracdev$\geq$0.8; Elliptical Galaxies (4)								fracdev$<$0.8; Disk Galaxies (15)							
	rEW				Δv				rEW				Δv			
Property Name	ρ	p-value	N_σ	✓	ρ	p-value	N_σ	✓	ρ	p-value	N_σ	✓	ρ	p-value	N_σ	✓
$g-r$	0.400	0.600	0.52		-0.400	0.600	0.52		-0.0733	0.795	0.26		-0.166	0.554	0.59	
$u-r$	0.400	0.600	0.52		-0.400	0.600	0.52		-0.127	0.652	0.45		-0.256	0.358	0.92	
$r-i$	0.400	0.600	0.52		-0.400	0.600	0.52		0.109	0.699	0.39		0.0125	0.965	0.04	
M_r	0.200	0.800	0.25		0.200	0.800	0.25		-0.220	0.431	0.79		0.113	0.689	0.40	
L_r^*	-0.200	0.800	0.25		-0.200	0.800	0.25		0.220	0.431	0.79		-0.113	0.689	0.40	
b [kpc]	0.800	0.200	1.28		-0.800	0.200	1.28		-0.320	0.245	1.16		-0.520	0.0469	1.99	
$b/r_{\rm Petro}$	0.400	0.600	0.52		-0.400	0.600	0.52		-0.241	0.386	0.87		-0.391	0.149	1.44	
C_r	0.400	0.600	0.52		-0.400	0.600	0.52		-0.309	0.262	1.12		-0.245	0.379	0.88	
$fracdev$	0.258	0.742	0.33		-0.775	0.225	1.21		-0.220	0.431	0.79		-0.174	0.536	0.62	
i	-0.400	0.600	0.52		0.400	0.600	0.52		-0.170	0.545	0.60		-0.0268	0.924	0.09	
z	-0.400	0.600	0.52		-0.400	0.600	0.52		0.320	0.245	1.16		0.324	0.240	1.18	
R_{50}^r	-0.400	0.600	0.52		0.400	0.600	0.52		-0.234	0.401	0.84		-0.252	0.365	0.91	
$E(B-V)_{QSO}$	0.00	1.00	0.00		0.800	0.200	1.28		0.209	0.454	0.75		0.713	0.00284	2.98	
b/a	0.400	0.600	0.52		-0.400	0.600	0.52		0.170	0.545	0.60		0.0268	0.924	0.09	
Θ	0.400	0.600	0.52		0.400	0.600	0.52		-0.241	0.386	0.87		0.0912	0.747	0.32	
g_{QSO}	0.400	0.600	0.52		-0.400	0.600	0.52		0.565	0.0281	2.20		0.218	0.435	0.78	
rEW	1.00	–	–		-0.600	0.400	0.84		1.00	–	–		0.154	0.585	0.55	
Δv	-0.600	0.400	0.84		1.00	–	–		0.154	0.585	0.55		1.00	–	–	
	Red Galaxies (4)								Blue Galaxies (15)							
	rEW				Δv				rEW				Δv			
Property Name	ρ	p-value	N_σ	✓	ρ	p-value	N_σ	✓	ρ	p-value	N_σ	✓	ρ	p-value	N_σ	✓
$g-r$	0.800	0.200	1.28		-0.800	0.200	1.28		-0.395	0.145	1.46		0.0858	0.761	0.30	
$u-r$	-0.200	0.800	0.25		0.00	1.00	0.00		-0.366	0.179	1.34		-0.147	0.602	0.52	
$r-i$	0.400	0.600	0.52		-0.400	0.600	0.52		-0.0983	0.727	0.35		0.254	0.361	0.91	
M_r	0.00	1.00	0.00		0.800	0.200	1.28		0.163	0.562	0.58		-0.304	0.271	1.10	
L_r^*	0.00	1.00	0.00		-0.800	0.200	1.28		-0.163	0.562	0.58		0.304	0.271	1.10	
b [kpc]	1.00	0.00	5.42	✓	-0.400	0.600	0.52		-0.177	0.528	0.63		-0.547	0.0349	2.11	
$b/r_{\rm Petro}$	0.800	0.200	1.28		-0.200	0.800	0.25		0.105	0.708	0.37		-0.533	0.0409	2.04	
C_r	-0.600	0.400	0.84		-0.400	0.600	0.52		-0.141	0.616	0.50		-0.454	0.0892	1.70	
$fracdev$	-0.800	0.200	1.28		-0.200	0.800	0.25		-0.386	0.155	1.42		-0.0856	0.762	0.30	
i	-0.400	0.600	0.52		0.400	0.600	0.52		-0.0912	0.747	0.32		-0.0357	0.899	0.13	
z	0.400	0.600	0.52		-0.600	0.400	0.84		-0.0697	0.805	0.25		0.618	0.0140	2.46	
R_{50}^r	-0.400	0.600	0.52		0.600	0.400	0.84		-0.223	0.423	0.80		-0.386	0.155	1.42	
$E(B-V)_{QSO}$	0.00	1.00	0.00		0.800	0.200	1.28		0.309	0.262	1.12		0.475	0.0733	1.79	
b/a	-0.200	0.800	0.25		0.00	1.00	0.00		0.105	0.708	0.37		0.0500	0.859	0.18	
Θ	0.400	0.600	0.52		0.400	0.600	0.52		-0.0447	0.874	0.16		0.0214	0.940	0.08	
g_{QSO}	0.400	0.600	0.52		-0.400	0.600	0.52		0.726	0.00217	3.07		-0.0161	0.955	0.06	
rEW	1.00	–	–		-0.400	0.600	0.52		1.00	–	–		-0.0107	0.970	0.04	
Δv	-0.400	0.600	0.52		1.00	–	–		-0.0107	0.970	0.04		1.00	–	–	

Table E2 Spearman's Rank Correlation Coefficients for different subsets of the 36 Na I absorbers. The different subsets are based on r-band concentration index, the $fracdev$ parameter, and a red/blue color cut based on the $g-r$, M_r plot of Yan et al. (2006). The number in parentheses is the number of absorbers in each sample.

	rc								bc							
	$C_r \geq 2.6$; Elliptical Galaxies (13)								$C_r < 2.6$; Disk Galaxies (23)							
Property Name	ρ	p-value	N_σ	✓	ρ	p-value	N_σ	✓	ρ	p-value	N_σ	✓	ρ	p-value	N_σ	✓
$g-r$	0.0220	0.943	0.07		0.434	0.138	1.48		0.208	0.340	0.95		-0.0682	0.757	0.31	
$u-r$	0.0879	0.775	0.29		0.429	0.144	1.46		0.303	0.159	1.41		-0.0316	0.886	0.14	
$r-i$	-0.154	0.616	0.50		0.330	0.271	1.10		0.281	0.195	1.30		-0.147	0.503	0.67	
M_r	-0.346	0.247	1.16		-0.264	0.384	0.87		0.144	0.511	0.66		0.288	0.183	1.33	
L_r^*	0.346	0.247	1.16		0.264	0.384	0.87		-0.144	0.511	0.66		-0.288	0.183	1.33	
b [kpc]	0.0385	0.901	0.12		0.538	0.0576	1.90		0.324	0.131	1.51		-0.131	0.550	0.60	
$b/r_{\rm Petro}$	-0.187	0.541	0.61		0.110	0.721	0.36		0.196	0.371	0.89		0.120	0.587	0.54	
C_r	0.0330	0.915	0.11		0.0385	0.901	0.12		0.00296	0.989	0.01		-0.0751	0.733	0.34	
$fracdev$	0.0170	0.956	0.05		0.187	0.542	0.61		-0.150	0.495	0.68		0.0707	0.749	0.32	
i	0.0220	0.943	0.07		-0.253	0.405	0.83		0.591	0.00299	2.97		0.145	0.508	0.66	
z	0.154	0.616	0.50		0.126	0.681	0.41		0.168	0.444	0.77		-0.310	0.150	1.44	
R_{50}^r	-0.0659	0.831	0.21		-0.308	0.306	1.02		-0.165	0.452	0.75		0.0830	0.707	0.38	
$E(B-V)_{QSO}$	0.0165	0.957	0.05		-0.258	0.394	0.85		0.257	0.237	1.18		-0.125	0.568	0.57	
b/a	0.0659	0.831	0.21		0.181	0.553	0.59		-0.591	0.00299	2.97		-0.145	0.508	0.66	
Θ	0.440	0.133	1.50		-0.0714	0.817	0.23		-0.00988	0.964	0.04		-0.210	0.335	0.96	
g_{QSO}	0.538	0.0576	1.90		-0.505	0.0780	1.76		0.906	2.76E-09	5.42	✓	0.353	0.0981	1.65	
rEW	1.00	–	–		-0.104	0.734	0.34		1.00	–	–		0.343	0.109	1.60	
Δv	-0.104	0.734	0.34		1.00	–	–		0.343	0.109	1.60		1.00	–	–	
	fracdev$\geq$0.8; Elliptical Galaxies (12)								fracdev$<$0.8; Disk Galaxies (24)							
	rEW				Δv				rEW				Δv			
Property Name	ρ	p-value	N_σ	✓	ρ	p-value	N_σ	✓	ρ	p-value	N_σ	✓	ρ	p-value	N_σ	✓
$g-r$	0.350	0.265	1.11		0.476	0.118	1.56		0.170	0.428	0.79		-0.0496	0.818	0.23	
$u-r$	0.350	0.265	1.11		0.476	0.118	1.56		0.212	0.320	1.00		-0.0522	0.809	0.24	
$r-i$	0.189	0.557	0.59		0.294	0.354	0.93		0.202	0.344	0.95		-0.0870	0.686	0.40	
M_r	-0.301	0.342	0.95		-0.175	0.587	0.54		-0.0383	0.859	0.18		0.123	0.568	0.57	
L_r^*	0.301	0.342	0.95		0.175	0.587	0.54		0.0383	0.859	0.18		-0.123	0.568	0.57	
b [kpc]	0.133	0.681	0.41		0.301	0.342	0.95		0.286	0.175	1.36		-0.0322	0.881	0.15	
$b/r_{\rm Petro}$	-0.0629	0.846	0.19		0.112	0.729	0.35		0.141	0.511	0.66		0.0896	0.677	0.42	
C_r	0.252	0.430	0.79		0.252	0.430	0.79		0.0513	0.812	0.24		-0.143	0.504	0.67	
$fracdev$	0.142	0.660	0.44		-0.0149	0.963	0.05		0.0465	0.829	0.22		0.151	0.480	0.71	
i	0.217	0.499	0.68		0.0140	0.966	0.04		0.477	0.0186	2.35		0.0383	0.859	0.18	
z	0.0839	0.795	0.26		-0.217	0.499	0.68		0.253	0.233	1.19		-0.0374	0.862	0.17	
R_{50}^r	-0.0490	0.880	0.15		0.0210	0.948	0.06		-0.227	0.286	1.07		-0.0452	0.834	0.21	
$E(B-V)_{QSO}$	-0.0909	0.779	0.28		-0.210	0.513	0.65		0.255	0.230	1.20		-0.0948	0.660	0.44	
b/a	-0.147	0.649	0.46		-0.161	0.618	0.50		-0.477	0.0186	2.35		-0.0383	0.859	0.18	
Θ	0.427	0.167	1.38		0.0699	0.829	0.22		-0.0357	0.869	0.17		-0.260	0.220	1.23	
g_{QSO}	0.664	0.0185	2.36		-0.566	0.0548	1.92		0.795	3.40E-06	4.65	✓	0.294	0.163	1.39	
rEW	1.00	–	–		-0.0699	0.829	0.22		1.00	–	–		0.306	0.146	1.45	
Δv	-0.0699	0.829	0.22		1.00	–	–		0.306	0.146	1.45		1.00	–	–	
	Red Galaxies (2)								Blue Galaxies (34)							
	rEW				Δv				rEW				Δv			
Property Name	ρ	p-value	N_σ	✓	ρ	p-value	N_σ	✓	ρ	p-value	N_σ	✓	ρ	p-value	N_σ	✓
$g-r$	1.00	0.00	5.42	✓	1.00	0.00	5.42	✓	0.186	0.293	1.05		-0.0539	0.762	0.30	
$u-r$	1.00	0.00	5.42	✓	1.00	0.00	5.42	✓	0.227	0.196	1.29		-0.0475	0.790	0.27	
$r-i$	1.00	0.00	5.42	✓	1.00	0.00	5.42	✓	0.217	0.217	1.23		-0.146	0.411	0.82	
M_r	-1.00	0.00	5.42	✓	-1.00	0.00	5.42	✓	0.0289	0.871	0.16		0.211	0.231	1.20	
L_r^*	1.00	0.00	5.42	✓	1.00	0.00	5.42	✓	-0.0289	0.871	0.16		-0.211	0.231	1.20	
b [kpc]	1.00	0.00	5.42	✓	1.00	0.00	5.42	✓	0.231	0.189	1.31		0.0585	0.742	0.33	
$b/r_{\rm Petro}$	-1.00	0.00	5.42	✓	-1.00	0.00	5.42	✓	0.100	0.572	0.56		0.221	0.209	1.26	
C_r	1.00	0.00	5.42	✓	1.00	0.00	5.42	✓	0.0133	0.941	0.07		-0.110	0.534	0.62	
$fracdev$	1.00	0.00	5.42	✓	1.00	0.00	5.42	✓	-0.0725	0.683	0.41		-0.0581	0.744	0.33	
i	-1.00	0.00	5.42	✓	-1.00	0.00	5.42	✓	0.469	0.00519	2.80		0.121	0.495	0.68	
z	1.00	0.00	5.42	✓	1.00	0.00	5.42	✓	0.150	0.398	0.84		-0.243	0.166	1.39	
R_{50}^r	-1.00	0.00	5.42	✓	-1.00	0.00	5.42	✓	-0.132	0.455	0.75		0.0426	0.811	0.24	
$E(B-V)_{QSO}$	1.00	0.00	5.42	✓	1.00	0.00	5.42	✓	0.156	0.379	0.88		-0.177	0.316	1.00	
b/a	1.00	0.00	5.42	✓	1.00	0.00	5.42	✓	-0.445	0.00830	2.64		-0.151	0.393	0.85	
Θ	1.00	0.00	5.42	✓	1.00	0.00	5.42	✓	0.0643	0.718	0.36		-0.142	0.422	0.80	
g_{QSO}	-1.00	0.00	5.42	✓	-1.00	0.00	5.42	✓	0.877	9.99E-12	5.42	✓	0.0614	0.730	0.34	
rEW	1.00	–	–		1.00	0.00	5.42	✓	1.00	–	–		0.190	0.281	1.08	
Δv	1.00	0.00	5.42	✓	1.00	–	–		0.190	0.281	1.08		1.00	–	–	

APPENDIX F

K-S AND U TEST TABLES FOR SAMPLE SUBSETS

Table F1 Results for the K-S and U tests for the Ca II absorber and non-absorber galaxies, divided into our morphological subsets.

	$C_r \geq 2.6$; Elliptical Galaxies (5)					$C_r < 2.6$; Disk Galaxies (14)				
	K-S		U		✓	K-S		U		✓
Property Name	p-value	N_σ	p-value	N_σ		p-value	N_σ	p-value	N_σ	
$g-r$	0.227	1.21	0.0758	1.78		0.102	1.64	0.0537	1.93	
$u-r$	0.250	1.15	0.0756	1.78		0.198	1.29	0.171	1.37	
$r-i$	0.107	1.61	0.0972	1.66		0.134	1.50	0.0646	1.85	
M_r	0.132	1.51	0.138	1.48		0.0201	2.32	0.0173	2.38	
L_r^*	0.218	1.23	0.134	1.50		0.0204	2.32	0.0168	2.39	
b [kpc]	0.463	0.734	0.225	1.21		0.0168	2.39	0.0208	2.31	
$b/r_{\rm Petro}$	0.429	0.790	0.206	1.26		6.45E-05	4.00	1.40E-05	4.34	✓
C_r	0.211	1.25	0.113	1.58		0.0933	1.68	0.0653	1.84	
$fracdev$	0.0495	1.97	0.0247	2.25		0.00791	2.66	0.211	1.25	
i	0.117	1.57	0.186	1.32		0.368	0.900	0.221	1.22	
z	0.0739	1.79	0.0413	2.04		0.0161	2.41	0.0154	2.42	
R_{50}^r	0.0425	2.03	0.0500	1.96		0.136	1.49	0.183	1.33	
$E(B-V)_{QSO}$	0.348	0.939	0.0666	1.83		0.0331	2.13	0.0147	2.44	
b/a	0.100	1.64	0.173	1.36		0.421	0.805	0.214	1.24	
Θ	0.157	1.41	0.194	1.30		0.0749	1.78	0.100	1.65	
g_{QSO}	0.439	0.774	0.300	1.04		0.195	1.30	0.212	1.25	
	fracdev$\geq$0.8; Elliptical Galaxies (4)					fracdev$<$0.8; Disk Galaxies (15)				
	K-S		U		✓	K-S		U		✓
Property Name	p-value	N_σ	p-value	N_σ		p-value	N_σ	p-value	N_σ	
$g-r$	0.380	0.878	0.164	1.39		0.306	1.02	0.242	1.17	
$u-r$	0.419	0.808	0.182	1.33		0.293	1.05	0.216	1.24	
$r-i$	0.335	0.964	0.207	1.26		0.311	1.01	0.238	1.18	
M_r	0.129	1.52	0.0135	2.47		0.179	1.35	0.202	1.28	
L_r^*	0.0895	1.70	0.0132	2.48		0.178	1.35	0.203	1.27	
b [kpc]	0.0181	2.36	0.0115	2.53		0.141	1.47	0.108	1.61	
$b/r_{\rm Petro}$	0.0341	2.12	0.00143	3.19		0.00831	2.64	0.00716	2.69	
C_r	0.0307	2.16	0.0225	2.28		0.145	1.46	0.169	1.38	
$fracdev$	0.668	0.429	0.272	1.10		0.0116	2.52	0.184	1.33	
i	0.509	0.660	0.267	1.11		0.230	1.20	0.198	1.29	
z	0.00259	3.01	0.00332	2.94		0.232	1.20	0.204	1.27	
R_{50}^r	0.0765	1.77	0.109	1.60		0.0428	2.03	0.0820	1.74	
$E(B-V)_{QSO}$	0.440	0.772	0.362	0.912		0.0949	1.67	0.0743	1.79	
b/a	0.448	0.758	0.212	1.25		0.232	1.20	0.200	1.28	
Θ	0.461	0.738	0.251	1.15		0.0526	1.94	0.0806	1.75	
g_{QSO}	0.0595	1.89	0.0254	2.24		0.215	1.24	0.219	1.23	
	Red Galaxies (4)					Blue Galaxies (15)				
	K-S		U		✓	K-S		U		✓
Property Name	p-value	N_σ	p-value	N_σ		p-value	N_σ	p-value	N_σ	
$g-r$	0.143	1.47	0.0814	1.74		0.293	1.05	0.210	1.25	
$u-r$	0.214	1.24	0.230	1.20		0.109	1.60	0.0904	1.69	
$r-i$	0.620	0.495	0.224	1.22		0.220	1.23	0.241	1.17	
M_r	0.483	0.701	0.253	1.14		0.169	1.37	0.167	1.38	
L_r^*	0.476	0.712	0.257	1.13		0.182	1.33	0.160	1.41	
b [kpc]	0.172	1.36	0.0408	2.05		0.110	1.60	0.0666	1.83	
$b/r_{\rm Petro}$	0.733	0.341	0.148	1.45		0.00280	2.99	0.00160	3.16	
C_r	0.103	1.63	0.0424	2.03		0.217	1.23	0.109	1.60	
$fracdev$	0.559	0.584	0.118	1.56		0.0558	1.91	0.164	1.39	
i	0.506	0.665	0.332	0.971		0.143	1.47	0.188	1.32	
z	0.244	1.17	0.172	1.37		0.0795	1.75	0.188	1.32	
R_{50}^r	0.0411	2.04	0.0617	1.87		0.0128	2.49	0.00951	2.59	
$E(B-V)_{QSO}$	0.410	0.824	0.297	1.04		0.206	1.26	0.149	1.44	
b/a	0.536	0.619	0.334	0.966		0.153	1.43	0.178	1.35	
Θ	0.412	0.820	0.140	1.48		0.120	1.55	0.192	1.30	
g_{QSO}	0.577	0.558	0.324	0.987		0.259	1.13	0.245	1.16	

Table F2 Results for the K-S and U tests for the Na I absorber and non-absorber galaxies, divided into our morphological subsets. Note that the K-S test for the 'Red' sample of Na I absorbers failed due to the low sample size in that subset.

	$C_r \geq 2.6$; Elliptical Galaxies (13)					$C_r < 2.6$; Disk Galaxies (23)				
	K-S		U		✓	K-S		U		✓
Property Name	p-value	N_σ	p-value	N_σ		p-value	N_σ	p-value	N_σ	
$g-r$	0.355	0.925	0.256	1.14		0.0907	1.69	0.221	1.22	
$u-r$	0.326	0.983	0.257	1.13		0.145	1.46	0.213	1.25	
$r-i$	0.263	1.12	0.234	1.19		0.174	1.36	0.186	1.32	
M_r	0.343	0.949	0.273	1.10		0.268	1.11	0.267	1.11	
L_r^*	0.342	0.949	0.267	1.11		0.274	1.09	0.268	1.11	
b [kpc]	0.109	1.60	0.0658	1.84		0.226	1.21	0.210	1.25	
$b/r_{\rm Petro}$	0.219	1.23	0.194	1.30		0.176	1.35	0.174	1.36	
C_r	0.00632	2.73	0.0168	2.39		0.218	1.23	0.132	1.51	
$fracdev$	0.165	1.39	0.224	1.22		0.00578	2.76	0.240	1.17	
i	0.356	0.923	0.292	1.05		0.0453	2.00	0.0449	2.01	
z	0.382	0.874	0.180	1.34		0.135	1.50	0.181	1.34	
R_{50}^r	0.121	1.55	0.128	1.52		0.0575	1.90	0.107	1.61	
$E(B-V)_{QSO}$	0.0798	1.75	0.167	1.38		0.00126	3.23	0.0111	2.54	
b/a	0.384	0.870	0.284	1.07		0.0431	2.02	0.0477	1.98	
Θ	0.278	1.08	0.185	1.32		0.302	1.03	0.195	1.30	
g_{QSO}	0.207	1.26	0.218	1.23		0.233	1.19	0.221	1.22	
	fracdev$\geq$0.8; Elliptical Galaxies (12)					fracdev$<$0.8; Disk Galaxies (24)				
	K-S		U		✓	K-S		U		✓
Property Name	p-value	N_σ	p-value	N_σ		p-value	N_σ	p-value	N_σ	
$g-r$	0.0968	1.66	0.0594	1.89		0.0872	1.71	0.204	1.27	
$u-r$	0.157	1.41	0.0809	1.75		0.117	1.57	0.188	1.32	
$r-i$	0.182	1.34	0.150	1.44		0.124	1.54	0.183	1.33	
M_r	0.278	1.08	0.281	1.08		0.179	1.34	0.247	1.16	
L_r^*	0.235	1.19	0.280	1.08		0.182	1.33	0.249	1.15	
b [kpc]	0.162	1.40	0.112	1.59		0.294	1.05	0.234	1.19	
$b/r_{\rm Petro}$	0.325	0.984	0.169	1.37		0.173	1.36	0.169	1.38	
C_r	0.0117	2.52	0.0370	2.09		0.292	1.05	0.271	1.10	
$fracdev$	0.0111	2.54	0.277	1.09		0.00739	2.68	0.180	1.34	
i	0.399	0.843	0.278	1.09		0.0207	2.31	0.0222	2.29	
z	0.274	1.09	0.233	1.19		0.236	1.19	0.284	1.07	
R_{50}^r	0.236	1.19	0.195	1.30		0.140	1.48	0.177	1.35	
$E(B-V)_{QSO}$	0.0542	1.93	0.120	1.55		0.00548	2.78	0.0222	2.29	
b/a	0.349	0.936	0.259	1.13		0.0204	2.32	0.0226	2.28	
Θ	0.144	1.46	0.158	1.41		0.357	0.922	0.210	1.25	
g_{QSO}	0.0802	1.75	0.135	1.50		0.183	1.33	0.163	1.39	
	Red Galaxies (2)					Blue Galaxies (34)				
	K-S		U		✓	K-S		U		✓
Property Name	p-value	N_σ	p-value	N_σ		p-value	N_σ	p-value	N_σ	
$g-r$	0.00	0.00	0.0289	2.19		0.0739	1.79	0.190	1.31	
$u-r$	0.00	0.00	0.0337	2.12		0.0990	1.65	0.179	1.34	
$r-i$	0.00	0.00	0.0753	1.78		0.113	1.58	0.151	1.44	
M_r	0.00	0.00	0.467	0.727		0.251	1.15	0.226	1.21	
L_r^*	0.00	0.00	0.469	0.723		0.263	1.12	0.228	1.21	
b [kpc]	0.00	0.00	0.154	1.43		0.229	1.20	0.213	1.25	
$b/r_{\rm Petro}$	0.00	0.00	0.385	0.868		0.264	1.12	0.263	1.12	
C_r	0.00	0.00	0.340	0.954		0.151	1.44	0.113	1.59	
$fracdev$	0.00	0.00	0.0980	1.65		0.0161	2.41	0.207	1.26	
i	0.00	0.00	0.0825	1.74		0.146	1.45	0.0926	1.68	
z	0.00	0.00	0.0713	1.80		0.246	1.16	0.217	1.23	
R_{50}^r	0.00	0.00	0.370	0.896		0.186	1.32	0.180	1.34	
$E(B-V)_{QSO}$	0.00	0.00	0.139	1.48		0.000484	3.49	0.0108	2.55	
b/a	0.00	0.00	0.460	0.738		0.182	1.33	0.111	1.59	
Θ	0.00	0.00	0.166	1.39		0.315	1.00	0.182	1.33	
g_{QSO}	0.00	0.00	0.427	0.794		0.221	1.22	0.231	1.20	

BIBLIOGRAPHY

Abazajian, K. N., Adelman-McCarthy, J. K., Agüeros, M. A., et al. 2009, The Astrophysical Journal Supplement Series, 182, 543

Adelman-McCarthy, J. K., Agüeros, M. A., Allam, S. S., et al. 2008, Astrophysical Journal Supplement Series, 175, 297

Alpher, R. A., Bethe, H., & Gamow, G. 1948, Physical Review, 73, 803

Baldry, I. K., Glazebrook, K., Brinkmann, J., et al. 2004, The Astrophysical Journal, 600, 681

Barlow, M. J. 1978, Monthly Notices of the Royal Astronomical Society, 183, 417

Ben Bekhti, N., Richter, P., Westmeier, T., & Murphy, M. T. 2008, Astronomy and Astrophysics, 487, 583

Benson, A. J., Bower, R. G., Frenk, C. S., et al. 2003, The Astrophysical Journal, 599, 38

Bergeron, J., Kunth, D., & D'Odorico, S. 1987, Astronomy and Astrophysics, 180, 1, provided by the SAO/NASA Astrophysics Data System

Bertin, P., Lallement, R., Ferlet, R., & Vidal-Madjar, A. 1993, Astronomy and Astrophysics (ISSN 0004-6361), 278, 549

Bertone, G., Hooper, D., & Silk, J. 2005, Physical Reports, 405, 279

Binggeli, B., Popescu, C. C., & Tammann, G. A. 1993, Astronomy and Astrophysics Supplement Series, 98, 275

Blades, J. C., Hunstead, R. W., & Murdoch, H. S. 1981, Royal Astronomical Society, 194, 669

Blanton, M. R., & Hogg, D. 2009

Blanton, M. R., Lin, H., Lupton, R. H., et al. 2003a, The Astronomical Journal, 125, 2276

Blanton, M. R., Lupton, R. H., Schlegel, D. J., et al. 2005, The Astrophysical Journal, 631, 208

Blanton, M. R., & Roweis, S. 2007, The Astronomical Journal, 133, 734, provided by the SAO/NASA Astrophysics Data System

Blanton, M. R., Hogg, D. W., Bahcall, N. A., et al. 2003b, The Astrophysical Journal, 594, 186

—. 2003c, The Astrophysical Journal, 592, 819

Boissier, S., Péroux, C., & Pettini, M. 2003, Monthly Notices of the Royal Astronomical Society, 338, 131

Boksenberg, A., Danziger, I. J., Fosbury, R. A. E., & Goss, W. M. 1980, The Astrophysical Journal, 242, L145

Boksenberg, A., & Sargent, W. L. W. 1978, The Astrophysical Journal, 220, 42

Boquien, M., Duc, P.-A., Braine, J., et al. 2007, Astronomy and Astrophysics, 467, 93

Bouche, N., Hohensee, W., Vargas, R., et al. 2011, ArXiv e-prints

Bowen, D. V. 1991, Royal Astronomical Society, 251, 649

Bowen, D. V., Huchtmeier, W., Brinks, E., Tripp, T. M., & Jenkins, E. B. 2001a, Astronomy and Astrophysics, 372, 820

Bowen, D. V., Jenkins, E. B., Pettini, M., & Tripp, T. M. 2005, The Astrophysical Journal, 635, 880, provided by the SAO/NASA Astrophysics Data System

Bowen, D. V., Tripp, T. M., & Jenkins, E. B. 2001b, The Astronomical Journal, 121, 1456

Bowen, David V., Pettini, Max, Penston, Michael V., & Blades, Chris. 1991, Royal Astronomical Society, 249, 145

Briggs, F. H., & Barnes, D. G. 2006, The Astrophysical Journal, 640, L127, provided by the SAO/NASA Astrophysics Data System

Broeils, A. H., & Rhee, M.-H. 1997, Astronomy and Astrophysics

Bukhmastova, Y. L. 2001, Astronomy Reports, 45, 581, provided by the SAO/NASA Astrophysics Data System

Burbidge, G., Hewitt, A., Narlikar, J. V., & Gupta, P. D. 1990, The Astrophysical Journal Supplement Series, 74, 675

Burstein, D., & Krumm, N. 1981, The Astrophysical Journal, 250, 517, provided by the SAO/NASA Astrophysics Data System

Calzetti, D., Armus, L., Bohlin, R. C., et al. 2000, The Astrophysical Journal, 533, 682, provided by the SAO/NASA Astrophysics Data System

Cardelli, J. A., Clayton, G. C., & Mathis, J. S. 1989, The Astrophysical Journal, 345, 245

Carilli, C. L., & van Gorkom, J. H. 1987, The Astrophysical Journal, 319, 683, provided by the SAO/NASA Astrophysics Data System

Carilli, C. L., van Gorkom, J. H., & Stocke, J. T. 1989, Nature, 338, 134, provided by the SAO/NASA Astrophysics Data System

Carroll, B. W., & Ostlie, D. A. 1996, An Introduction to Modern Astrophysics, ed. Carroll, B. W. & Ostlie, D. A.

Carroll, S. M., Press, W. H., & Turner, E. L. 1992, Annual Review of Astronomy and Astrophysics, 30, 499

Cayatte, V., Kotanyl, C., Balkowski, C., & van Gorkom, J. H. 1994, The Astronomical Journal, 107, 1003

Charlton, J., Churchill, C., & Murdin, P. 2000, Quasistellar Objects: Intervening Absorption Lines, ed. Murdin, P.

Chen, H.-W., Kennicutt, Jr., R. C., & Rauch, M. 2005, The Astrophysical Journal, 620, 703

Chen, H.-W., & Lanzetta, K. M. 2003, The Astrophysical Journal, 597, 706, provided by the SAO/NASA Astrophysics Data System

Chen, Y.-M., Tremonti, C. A., Heckman, T. M., et al. 2010, The Astronomical Journal, 140, 445

Chengalur, J. N., & Kanekar, N. 2002, Astronomy and Astrophysics, 388, 383

Cherinka, B., Schulte-Ladbeck, R., & Rosenberg, J. 2009, The Astronomical Journal, 139, 12

Cherinka, B., & Schulte-Ladbeck, R. E. 2011, The Astronomical Journal, 142, 122

Christensen, L., Wisotzki, L., Roth, M. M., et al. 2007, Astronomy and Astrophysics, 468, 587

Churchill, C. 2009, In Preparation

Clowe, D., Bradač, M., Gonzalez, A. H., et al. 2006, The Astrophysical Journal Letters, 648, L109

Crampton, D., Gussie, G., Cowley, A. P., & Schmidtke, P. C. 1997, The Astronomical Journal, 114, 2353, provided by the SAO/NASA Astrophysics Data System

Crawford, I. A. 1992, Royal Astronomical Society, 259, 47

de Blok, W. J. G., McGaugh, S. S., & van der Hulst, J. M. 1996, Monthly Notices of the Royal Astronomical Society, 283, 18

Dekel, A., & Birnboim, Y. 2006, Monthly Notices of the Royal Astronomical Society, 368, 2

Dicke, R. H., Peebles, P. J. E., Roll, P. G., & Wilkinson, D. T. 1965, Astrophysical Journal, 142, 414

Dobos, L., Csabai, I., Yip, C.-W., et al. 2011, ArXiv e-prints

Ferlet, R., Dennefeld, M., & Maurice, E. 1985a, Astronomy and Astrophysics, 152, 151, provided by the SAO/NASA Astrophysics Data System

Ferlet, R., Vidal-Madjar, A., & Gry, C. 1985b, The Astrophysical Journal, 298, 838, provided by the SAO/NASA Astrophysics Data System

Field, G. B. 1974, The Astrophysical Journal, 187, 453

Field, G. B., & Cameron, A. G. W. 1975, The dusty universe, ed. Field, G. B. & Cameron, A. G. W.

Fisher, J. R., Norrod, R. D., & Balser, D. S. 2003, Investigation of Spectral Baseline Properties of the Green Bank Telescope

Frei, Z., & Gunn, J. E. 1994, The Astronomical Journal, 108, 1476

Frisch, P. C. 2001, The interstellar medium of our Galaxy, 647–675

Gardner, J. P., Katz, N., Hernquist, L., & Weinberg, D. H. 2001, The Astrophysical Journal, 559, 131, provided by the SAO/NASA Astrophysics Data System

Haan, S., Schinnerer, E., Mundell, C. G., García-Burillo, S., & Combes, F. 2008, The Astronomical Journal, 135, 232, provided by the SAO/NASA Astrophysics Data System

Haehnelt, M. G., Steinmetz, M., & Rauch, M. 1998, Astrophysical Journal, 495, 647, provided by the SAO/NASA Astrophysics Data System

Hazard, C., Mackey, M. B., & Shimmins, A. J. 1963, Nature, 197, 1037

Heckman, T. M., Lehnert, M. D., Strickland, D. K., & Armus, L. 2000, The Astrophysical Journal Supplement Series, 129, 493

Helou, G., Khan, I. R., Malek, L., & Boehmer, L. 1988, The Astrophysical Journal Supplement Series, 68, 151

Hewett, P. C., & Wild, V. 2007, Monthly Notices of the Royal Astronomical Society, 379, 738

Hewett, P. C., Irwin, M. J., Bunclark, P., et al. 1985, Royal Astronomical Society, 213, 971

Hinshaw, G., Weiland, J. L., Hill, R. S., et al. 2009, The Astrophysical Journal Supplement Series, 180, 225

Hogg, D. W., Blanton, M., Strateva, I., et al. 2002, The Astronomical Journal, 124, 646

Holmberg, J., Flynn, C., & Portinari, L. 2006, Monthly Notices of the Royal Astronomical Society, 367, 449

Holweger, H. 2001, in American Institute of Physics Conference Series, Vol. 598, Joint SOHO/ACE workshop "Solar and Galactic Composition", ed. R. F. Wimmer-Schweingruber, 23–30, provided by the SAO/NASA Astrophysics Data System

Hopkins, A. M., Miller, C. J., Nichol, R. C., et al. 2003, The Astrophysical Journal, 599, 971

Hoyle, F. 1953, The Astrophysical Journal, 118, 513

Jarosik, N., Bennett, C. L., Dunkley, J., et al. 2011, The Astrophysical Journal Supplement, 192, 14

Johansson, P. H., & Efstathiou, G. 2006, Monthly Notices of the Royal Astronomical Society, 371, 1519, provided by the SAO/NASA Astrophysics Data System

Junkkarinen, V. T., & Barlow, T. A. 1994, in Bulletin of the American Astronomical Society, Vol. 26, American Astronomical Society Meeting Abstracts, 1330–+, provided by the SAO/NASA Astrophysics Data System

Kacprzak, G. G., Churchill, C. W., Evans, J. L., Murphy, M. T., & Steidel, C. C. 2011, Monthly Notices of the Royal Astronomical Society: Letters, 416, 3118

Kanekar, N., & Chengalur, J. N. 2005, Astronomy and Astrophysics, 429, L51, provided by the SAO/NASA Astrophysics Data System

Kanekar, N., Chengalur, J. N., Subrahmanyan, R., & Petitjean, P. 2001, Astronomy and Astrophysics, 367, 46, provided by the SAO/NASA Astrophysics Data System

Kannappan, S. J. 2004, The Astrophysical Journal, 611, L89, provided by the SAO/NASA Astrophysics Data System

Kennicutt, Jr., R. C. 1983, The Astrophysical Journal, 272, 54, provided by the SAO/NASA Astrophysics Data System

—. 1992, Astrophysical Journal Supplement Series, 79, 255, provided by the SAO/NASA Astrophysics Data System

—. 1998, Annual Review of Astronomy and Astrophysics, 36, 189, provided by the SAO/NASA Astrophysics Data System

Kereš, D., Katz, N., Fardal, M., Davé, R., & Weinberg, D. H. 2009, Monthly Notices of the Royal Astronomical Society, 395, 160

Kereš, D., Katz, N., Weinberg, D. H., & Davé, R. 2005, Monthly Notices of the Royal Astronomical Society, 363, 2

Kobulnicky, H. A., Kennicutt, Jr., R. C., & Pizagno, J. L. 1999, The Astrophysical Journal, 514, 544, provided by the SAO/NASA Astrophysics Data System

Kollmeier, J. A., Weinberg, D. H., Dave, R., & Katz, N. 2003, The Astrophysical Journal, 594, 75

Komatsu, E., Smith, K. M., Dunkley, J., et al. 2011, The Astrophysical Journal Supplement, 192, 18

Kondo, S., Kobayashi, N., Minowa, Y., et al. 2006, The Astrophysical Journal, 643, 22

König, B., Schulte-Ladbeck, R. E., & Cherinka, B. 2006, The Astronomical Journal, 132, 1844, provided by the SAO/NASA Astrophysics Data System

Kozłowski, S., & Kochanek, C. S. 2009, The Astrophysical Journal, 701, 508, provided by the SAO/NASA Astrophysics Data System

Kulkarni, V. P. 2007, in Astronomical Society of the Pacific Conference Series, Vol. 380, Deepest Astronomical Surveys, ed. J. Afonso, H. C. Ferguson, B. Mobasher, & R. Norris, 455

Kulkarni, V. P., Fall, S. M., Lauroesch, J. T., et al. 2005, The Astrophysical Journal, 618, 68

Kulkarni, V. P., Khare, P., Som, D., et al. 2010, New Astronomy, 15, 735

Kunth, D., & Bergeron, J. 1984, Royal Astronomical Society, 210, 873

Kwok, S. 2007, Physics and Chemistry of the Interstellar Medium, ed. Kwok, S.

Lane, W. M., Briggs, F. H., & Smette, A. 2000, Astrophysical Journal, 532, 146, provided by the SAO/NASA Astrophysics Data System

Larson, D., Dunkley, J., Hinshaw, G., et al. 2011, The Astrophysical Journal Supplement, 192, 16

Le Brun, V., Bergeron, J., Boisse, P., & Deharveng, J. M. 1997, Astronomy and Astrophysics, 321, 733, provided by the SAO/NASA Astrophysics Data System

Loveday, J. 2000, Monthly Notices of the Royal Astronomical Society, 312, 557

Marinoni, C., Monaco, P., Giuricin, G., & Costantini, B. 1999, The Astrophysical Journal, 521, 50, provided by the SAO/NASA Astrophysics Data System

Martel, A., & Osterbrock, D. E. 1994, The Astronomical Journal, 107, 1283, provided by the SAO/NASA Astrophysics Data System

McGaugh, S. S. 1991, The Astrophysical Journal, 380, 140, provided by the SAO/NASA Astrophysics Data System

Merchán, M. E., & Zandivarez, A. 2005, The Astrophysical Journal, 630, 759, provided by the SAO/NASA Astrophysics Data System

Miller, E. D., Knezek, P. M., & Bregman, J. N. 1999, The Astrophysical Journal Letters, 510, L95

Mo, H. J., & Mao, S. 2002, Monthly Notices of the Royal Astronomical Society, 333, 768

Nagamine, K., Wolfe, A. M., Hernquist, L., & Springel, V. 2007, The Astrophysical Journal, 660, 945, provided by the SAO/NASA Astrophysics Data System

Nestor, D. B., Pettini, M., Hewett, P. C., Rao, S., & Wild, V. 2008, Monthly Notices of the Royal Astronomical Society, 390, 1670

Nestor, D. B., Rao, S. M., Turnshek, D. A., & Vanden Berk, D. 2003, The Astrophysical Journal, 595, L5

Nestor, D. B., Turnshek, D. A., Rao, S. M., & Quider, A. M. 2007, The Astrophysical Journal, 658, 185

Okoshi, K., & Nagashima, M. 2005, The Astrophysical Journal, 623, 99, provided by the SAO/NASA Astrophysics Data System

Oort, J. H. 1932, Bulletin of the Astronomical Institute of the Netherlands, 6, 249

Padilla, N. D., & Strauss, M. A. 2008, Monthly Notices of the Royal Astronomical Society, 388, 1321

Park, C., & Choi, Y.-Y. 2005, The Astrophysical Journal, 635, L29

Paturel, G., Petit, C., Prugniel, P., et al. 2003, Astronomy and Astrophysics, 412, 45, provided by the SAO/NASA Astrophysics Data System

Peebles, P. J. E. 1980, The large-scale structure of the universe, ed. Peebles, P. J. E.

Penzias, A. A., & Wilson, R. W. 1965a, Astrophysical Journal, 142, 419

—. 1965b, Astrophysical Journal, 142, 1149

Perlmutter, S., Aldering, G., Goldhaber, G., et al. 1999, Astrophysical Journal, 517, 565

Petitjean, P., Theodore, B., Smette, A., & Lespine, Y. 1996, Astronomy and Astrophysics, 313, L25

Pettini, M., & Pagel, B. E. J. 2004, Monthly Notices of the Royal Astronomical Society, 348, L59, provided by the SAO/NASA Astrophysics Data System

Phillips, A. P., Gondhalekar, P. M., & Pettini, M. 1982, Monthly Notices of the Royal Astronomical Society, 200, 687

Phillips, A. P., Pettini, M., & Gondhalekar, P. M. 1984, Royal Astronomical Society, 206, 337

Pieri, M. M., Frank, S., Weinberg, D. H., Mathur, S., & York, D. G. 2010, The Astrophysical Journal Letters, 724, L69

Poggianti, B. M. 1997, A & A Supplement Series, 122, 399, provided by the SAO/NASA Astrophysics Data System

Press, W. H., & Schechter, P. 1974, The Astrophysical Journal, 187, 425

Prochaska, J. X., Hennawi, J. F., & HerbertFort, S. 2008, The Astrophysical Journal, 675, 1002

Prochaska, J. X., O'Meara, J. M., & Worseck, G. 2010, Astrophysical Journal, 718, 392

Prochaska, J. X., Weiner, B., Chen, H.-W., Mulchaey, J., & Cooksey, K. 2011, Astrophysical Journal, 740, 91

Prochaska, J. X., & Wolfe, A. M. 1997, The Astrophysical Journal, 487, 73

Rao, S. M., Belfort-Mihalyi, M., Turnshek, D. A., et al. 2011, Monthly Notices of the Royal Astronomical Society, 416, 1215

Rao, S. M., Nestor, D. B., Turnshek, D. A., et al. 2003, The Astrophysical Journal, 595, 94

Rao, S. M., & Turnshek, D. A. 1998, The Astrophysical Journal, 500, L115

Rauch, M. 1998, Annual Review of Astronomy and Astrophysics, 36, 267

Rees, M. J., & Ostriker, J. P. 1977, Monthly Notices of the Royal Astronomical Society, 179, 541

Reimers, D., & Hagen, H. 1998, Astronomy and Astrophysics, 329, L25, provided by the SAO/NASA Astrophysics Data System

Richards, G. T., Fan, X., Newberg, H. J., et al. 2002, Astronomy, 62

Richter, P., Krause, F., Fechner, C., Charlton, J. C., & Murphy, M. T. 2011, Astronomy and Astrophysics, 528, A12+

Riess, A. G., Filippenko, A. V., Challis, P., et al. 1998, The Astronomical Journal, 116, 1009

Roberts, M. S., & Haynes, M. P. 1994, Annual Review of Astronomy and Astrophysics, 32, 115, provided by the SAO/NASA Astrophysics Data System

Rosenberg, J. L., Bowen, D. V., Tripp, T. M., & Brinks, E. 2006, The Astronomical Journal, 132, 478

Rosenberg, J. L., & Schneider, S. E. 2003, The Astrophysical Journal, 585, 256

Routly, P. M., & Spitzer, Jr., L. 1952, The Astrophysical Journal, 115, 227, provided by the SAO/NASA Astrophysics Data System

Rubin, V. C., Burstein, D., Ford, Jr., W. K., & Thonnard, N. 1985, The Astrophysical Journal, 289, 81, provided by the SAO/NASA Astrophysics Data System

Rubin, V. C., Ford, W. K. J., & . Thonnard, N. 1980, Astrophysical Journal, 238, 471

Ryan-Weber, E. V., Webster, R. L., & Staveley-Smith, L. 2003, Monthly Notices of the Royal Astronomical Society, 343, 1195, provided by the SAO/NASA Astrophysics Data System

Salpeter, E. E., & Hoffman, G. L. 1996, The Astrophysical Journal, 465, 595, provided by the SAO/NASA Astrophysics Data System

Sandage, A., & Bedke, J. 1988, NASA Special Publication, 496, provided by the SAO/NASA Astrophysics Data System

Schlegel, D. J., Finkbeiner, D. P., & Davis, M. 1998, The Astrophysical Journal, 500, 525, provided by the SAO/NASA Astrophysics Data System

Schmidt, B. P., Suntzeff, N. B., Phillips, M. M., et al. 1998, The Astrophysical Journal, 507, 46

Schmidt, M. 1963, Nature, 197, 1040

Schneider, D. P., Hartig, G. F., Jannuzi, B. T., et al. 1993, The Astrophysical Journal Supplement Series, 87, 45

Schneider, D. P., Hall, P. B., Richards, G. T., et al. 2005, The Astronomical Journal, 130, 367

Schneider, D. P., Richards, G. T., Hall, P. B., et al. 2010, The Astronomical Journal, 139, 2360

Schulte-Ladbeck, R. E., König, B., & Cherinka, B. 2005, Proceedings of the International Astronomical Union, 1, 319

Schulte-Ladbeck, R. E., Rao, S. M., Drozdovsky, I. O., et al. 2004, The Astrophysical Journal, 600, 613

Shapley, A. E., Steidel, C. C., Adelberger, K. L., et al. 2001, The Astrophysical Journal, 562, 95

Shapley, A. E., Steidel, C. C., Erb, D. K., et al. 2005, The Astrophysical Journal, 626, 698

Shimasaku, K., Fukugita, M., Doi, M., et al. 2001, The Astronomical Journal, 122, 1238

Silk, J. 1977, The Astrophysical Journal, 211, 638

Siluk, R. S., & Silk, J. 1974, The Astrophysical Journal, 192, 51

Smith, J. A., Tucker, D. L., Kent, S., et al. 2002, The Astronomical Journal, 123, 2121, provided by the SAO/NASA Astrophysics Data System

Springel, V., White, S. D. M., Jenkins, A., et al. 2005, Nature, 435, 629

Steidel, C. C. 1995, in QSO Absorption Lines, ed. G. Meylan, 139

Steidel, C. C., Dickinson, M., & Persson, S. E. 1994, The Astrophysical Journal Letters, 437, L75, provided by the SAO/NASA Astrophysics Data System

Stewart, K. R., Kaufmann, T., Bullock, J. S., et al. 2011, The Astrophysical Journal Letters, 735, L1+

Stoughton, C., Lupton, R. H., Bernardi, M., et al. 2002, The Astronomical Journal, 123, 485

Strateva, I., Ivezić, v., Knapp, G. R., et al. 2001, The Astronomical Journal, 122, 1861

Strauss, M. A., Weinberg, D. H., Lupton, R. H., et al. 2002, The Astronomical Journal, 124, 1810

Swaters, R. A., van Albada, T. S., van der Hulst, J. M., & Sancisi, R. 2002, Astronomy and Astrophysics, 390, 829

Timmes, F. X., Woosley, S. E., & Weaver, T. A. 1995, The Astrophysical Journal Supplement Series, 98, 617

Tripp, T. M., Jenkins, E. B., Bowen, D. V., et al. 2005, The Astrophysical Journal, 619, 714

Tripp, T. M., Sembach, K. R., Bowen, D. V., et al. 2008, Astrophysical Journal Supplement Series, 177, 39

Tully, R. B., Pierce, M. J., Huang, J., et al. 1998, The Astronomical Journal, 115, 2264, provided by the SAO/NASA Astrophysics Data System

Tumlinson, J., Shull, J. M., Giroux, M. L., & Stocke, J. T. 2005, Astrophysical Journal, 620, 95

Tumlinson, J., Thom, C., Werk, J. K., et al. 2011, Science, 334, 948

Turnshek, D. A., Rao, S., Nestor, D., et al. 2001, The Astrophysical Journal, 553, 288, provided by the SAO/NASA Astrophysics Data System

van Driel, W., van Woerden, H., Schwarz, U. J., & Gallagher, III, J. S. 1988a, Astronomy and Astrophysics, 191, 201

—. 1988b, Astronomy and Astrophysics, 191, 201, provided by the SAO/NASA Astrophysics Data System

Verner, D. A., Barthel, P. D., & Tytler, D. 1994, Astronomy and Astrophysics Supplement Series, 108, 287

Verschuur, G. L., Kellermann, K. I., & van Brunt, V. 1974, Galactic and Extra-Galactic Radio Astronomy, ed. Verschuur, G. L., Kellermann, K. I., & van Brunt, V., provided by the SAO/NASA Astrophysics Data System

Vladilo, G., Molaro, P., Monai, S., et al. 1993, Astronomy and Astrophysics, 274, 37, provided by the SAO/NASA Astrophysics Data System

Wakker, B. P., & Mathis, J. S. 2000, The Astrophysical Journal Letters, 544, L107

Wakker, B. P., & van Woerden, H. 1991, Astronomy and Astrophysics (ISSN 0004-6361), 250, 509

Welsh, B. Y., Lallement, R., Vergely, J.-L., & Raimond, S. 2009a, Astronomy and Astrophysics, 510, A54

Welsh, B. Y., Lallement, R., Vergely, J.-L., & Raimond, S. 2010, Astronomy and Astrophysics, 510, A54+

Welsh, B. Y., Wheatley, J. M., & Lallement, R. 2009b, Publications of the Astronomical Society of the Pacific, 121, 606

Welty, D. E., Morton, D. C., & Hobbs, L. M. 1996, The Astrophysical Journal Supplement, 106, 533, provided by the SAO/NASA Astrophysics Data System

West, A. A. 2005, PhD thesis, University of Washington, United States – Washington, provided by the SAO/NASA Astrophysics Data System

West, A. A., Garcia-Appadoo, D. A., Dalcanton, J. J., et al. 2009, The Astronomical Journal, 138, 796

White, S. D. M., & Frenk, C. S. 1991, The Astrophysical Journal, 379, 52

White, S. D. M., & Rees, M. J. 1978, Monthly Notices of the Royal Astronomical Society, 183, 341

Wild, V., Hewett, P., & Pettini, M. 2006a, 6

Wild, V., & Hewett, P. C. 2005a, Monthly Notices of the Royal Astronomical Society: Letters, 361, L30

—. 2005b, Monthly Notices of the Royal Astronomical Society, 358, 1083

Wild, V., Hewett, P. C., & Pettini, M. 2006b, Monthly Notices of the Royal Astronomical Society, 367, 211

—. 2007, Monthly Notices of the Royal Astronomical Society, 374, 292

Wilson, A. S., & Penston, M. V. 1979, The Astrophysical Journal, 232, 389

Wolfe, A. M., Gawiser, E., & Prochaska, J. X. 2005, Annual Review of Astronomy and Astrophysics, 43, 861, provided by the SAO/NASA Astrophysics Data System

Wolfe, A. M., Turnshek, D. A., Smith, H. E., & Cohen, R. D. 1986, Astrophysical Journal Supplement Series, 61, 249, provided by the SAO/NASA Astrophysics Data System

Womble, D. S. 1993, Publications of the Astronomical Society of the Pacific, 105, 1043

Womble, D. S., Junkkarinen, V. T., & Burbidge, E. M. 1992, The Astrophysical Journal, 388, 55

Womble, D. S., Junkkarinen, V. T., Cohen, R. D., & Burbidge, E. M. 1990, The Astronomical Journal, 100, 1785

Womble, D. S., Junkkarinen, V. T., & Burbidge, E. M. 1991, Bulletin of the American Astronomical Society, 23

Woosley, S. E., & Weaver, T. A. 1995, The Astrophysical Journal Supplement Series, 101, 181

Yan, R., Newman, J. A., Faber, S. M., et al. 2006, The Astrophysical Journal, 648, 281

Young, C. K., & Currie, M. J. 1995, Monthly Notices of the Royal Astronomical Society, 273, 1141, provided by the SAO/NASA Astrophysics Data System

Yun, M. S., Ho, P. T. P., & Lo, K. Y. 1994, Nature, 372, 530

Zwaan, M. A., van der Hulst, J. M., Briggs, F. H., Verheijen, M. A. W., & Ryan-Weber, E. V. 2005, Monthly Notices of the Royal Astronomical Society, 364, 1467, provided by the SAO/NASA Astrophysics Data System

Zwicky, F. 1937, Astrophysical Journal, 86, 217

Zych, B. J., Murphy, M. T., Hewett, P. C., & Prochaska, J. X. 2009, Monthly Notices of the Royal Astronomical Society, 392, 1429, provided by the SAO/NASA Astrophysics Data System

Zych, B. J., Murphy, M. T., Pettini, M., et al. 2007, Monthly Notices of the Royal Astronomical Society, 379, 1409